Università
di Catania

Department of Civil Engineering and Architecture

Doctoral Program of National Interest in
Defense against natural risks and ecological transition
of built environment

Cycle XXXVIII

Enhanced Dissipation for Improved Mechanical Performance: A Journey from Concrete Structures to Functional Materials

Doctoral Thesis
Curriculum "*Resilience and Assessment of Infrastructures*"

Author
Christian Cardillo

Supervisor
Prof. Ivan Giorgio

Course Coordinator
Prof. Massimo Cuomo

Cosupervisor
Prof. Roberto Fedele

ACADEMIC YEAR 2024/2025

Christian CARDILLO

ENHANCED DISSIPATION FOR IMPROVED MECHANICAL PERFORMANCE: A JOURNEY FROM CONCRETE STRUCTURES TO FUNCTIONAL MATERIALS

Doctoral Thesis

UNIVERSITY OF CATANIA

September 2025

"*Science teaches us to be neglectful of nothing — not to despise the small beginnings, for they precede of necessity all great things in the knowledge of science, either pure or applied... the small as often contains the great in principle, as the great does the small; and thus the mind becomes comprehensive.*"

Michael Faraday

UNIVERSITÀ DEGLI STUDI DI CATANIA

Defense against natural risks and ecological transition of built environment

Cycle XXXVIII

Enhanced Dissipation for Improved Mechanical Performance: A Journey from Concrete Structures to Functional Materials

by Christian CARDILLO

ABSTRACT

The mechanical response of real-world materials is often governed by microscopic mechanisms, such as microcrack sliding, viscoelastic relaxation, multiphase flow instabilities, or coupled electromechanical effects, that are absent from classical continuum models. This thesis develops a unified modeling framework to incorporate such mechanisms explicitly, beginning with a focused study on dissipation in cementitious materials and progressively generalizing to a variety of materials and multiphysics systems. The approach enriches established continuum theories with targeted kinematic or constitutive variables, formulates the resulting models variationally for physical and numerical consistency, and validates predictions through finite element simulations, experiments, and parametric studies. In the first stage, the classical Timoshenko beam model is extended to capture frictional sliding within microcracks in concrete, enabling accurate prediction of hysteresis loops under cyclic bending and shear. This strategy is then adapted to corneal biomechanics, combining finite element modeling with shear wave elastography to identify viscoelastic parameters in both healthy and keratoconus-affected corneas, with applications in early diagnosis and treatment optimization. The methodology is further applied to multiphase and thermomechanical problems, including experimental and numerical analysis of viscous fingering in fractured porous media, and process modeling of laser powder bed fusion for Inconel 718 alloys with and without nanoparticle dispersion. Finally, the framework is generalized to nanoscale functional materials, producing a higher-order variational model for coupled flexoelectric-photovoltaic effects in $BaTiO_3$ thin plates, with implications for energy harvesting and multifunctional MEMS devices. Across these diverse domains, the research demonstrates how a consistent variational enrichment philosophy can be transferred from a specific structural application to widely different material systems. The result is a versatile set of modeling tools that advance both the scientific understanding and the engineering design of complex, multiscale materials in civil, biomedical, environmental, manufacturing, and nanotechnological applications.

Contents

Chapter 1

Introduction

1.1 Motivation and Background

The prediction of material behavior under service conditions remains one of the central challenges in engineering science. In structural design, biomedical applications, manufacturing, and nanotechnology alike, materials are rarely homogeneous or perfectly elastic; rather, their responses emerge from a complex interplay of microscopic defects, heterogeneities, and coupled physical fields. Microcracks in quasi-brittle solids, viscoelastic relaxation in soft tissues, capillary and viscous instabilities in porous media, thermal and phase-transition effects in alloys, and electromechanical coupling in functional nanomaterials all exemplify systems in which microscopic physics drives macroscopic performance.

Over the past decades, continuum mechanics has provided a powerful framework for linking scales, with classical theories, such as the Euler–Bernoulli and Timoshenko beam models, linear viscoelasticity, Darcy's law, and Fourier heat conduction, forming the backbone of engineering analysis. However, while these models offer analytical tractability and efficient computation, they often rely on constitutive simplifications that fail to capture key nonlinear and dissipative mechanisms. In quasi-brittle materials, for example, classical beam theories ignore the irreversible frictional sliding that occurs along microcrack interfaces, leading to inaccurate predictions under cyclic loading. Similarly, in biological soft tissues, purely elastic models cannot reproduce the rate-dependent deformation observed experimentally, limiting their diagnostic utility. In porous media and additive manufacturing, neglecting the coupled dynamics between phases or ignoring residual stresses can result in substantial errors in performance prediction.

Addressing these shortcomings has motivated the development of enriched continuum models, micromorphic and higher-order theories, and multiphysics formulations that explicitly account for microstructural mechanisms. Such approaches have been explored in micromechanics of composites, damage mechanics, generalized continua, and coupled-field modeling. Generalized continuum models are an extension of classical continuum mechanics designed to capture effects that the traditional framework cannot describe accurately. In classical mechanics, materials are treated as continuous media without any internal structure, and the deformation at a point depends only on the displacement field and its first derivatives. This works well for many engineering applications, but it can fail when the material has an underlying microstructure, such as grains in polycrystals, fibers in composites, or cells in biological tissues, that significantly influences its behavior. Generalized continuum theories incorporate additional degrees of freedom or higher-order kinematic measures to represent these microstructural effects, allowing for a more refined description of phenomena like size-dependence, dispersion, and localized deformation patterns. Micromorphic theory is a specific type of generalized continuum model in which each material point is endowed not only with the usual macroscopic displacement but also with independent micro-deformation variables. These variables represent the motion, rotation, or distortion of an internal microstructure relative to the bulk material, and they can vary continuously across the domain. In this way, micromorphic theory bridges the gap between purely microscopic models, which track individual particles or constituents, and classical macroscopic models, which ignore microstructural dynamics. This approach can capture complex behaviors such as micro-rotation, micro-shear, and anisotropic micro-deformation that would be invisible to a classical continuum description. Higher-order continuum theories, which include strain-gradient and couple-stress models, extend the kinematic description further by making the stored energy or the stress field depend on higher derivatives of the displacement or other kinematic measures. This means that not only the local strain but also its spatial variation contributes to the mechanical response. Such models naturally introduce internal length scales into the theory, enabling them to describe phenomena like size effects in small-scale structures, boundary layer stiffening, and wave dispersion in heterogeneous materials. In essence, micromorphic theory can be seen as one branch within the broader family of generalized continuum theories, while higher-order theories represent another branch that enriches the material description by considering derivatives of strain or other fields beyond the first order. Together, these frameworks provide powerful tools to model materials whose macroscopic behavior is strongly influenced by their microstructure or by small-scale physical processes. Yet, the efforts introduced to model complex continua often remain specialized, tailored to a single material class or physical process, making cross-domain transfer difficult. There is thus a pressing need for a unified modeling philosophy, one that is firmly rooted in continuum mechanics, capable of incorporating targeted microstructural descriptors, and versatile enough to be adapted to disparate materials and applications.

1.2 Aim of the research

The present thesis responds to this need by proposing and applying a unifying strategy that starts with a concrete, domain-specific problem, energy dissipation in cementitious structural elements, and progressively generalizes to increasingly complex material systems and multiphysics interactions. The core methodology follows four interconnected steps: i) *Mechanism identification*, determining the microstructural or multiphysics phenomenon controlling macroscopic behavior; ii) *Model enrichment*, extending classical models with additional kinematic or constitutive variables to represent the identified mechanisms; iii) *Variational formulation*, deriving governing equations through generalized principles of virtual work, ensuring theoretical consistency and compatibility with numerical methods;

iv) *Validation and exploration*, testing the models through finite element simulations, experimental data, and parametric studies to assess predictive capacity and sensitivity.

This systematic approach not only advances understanding within each studied material class but also demonstrates how conceptual tools developed in one context can be adapted to others, ultimately enabling transferable and scalable modeling strategies.

The thesis opens with cement-based materials, an enduring cornerstone of civil engineering whose structural integrity and durability depend critically also on their ability to dissipate energy without catastrophic damage. While classical Timoshenko beam theory captures bending and shear deformation, it omits the microcrack-induced frictional dissipation that governs hysteresis in cyclic loading. In the first group of studies (see papers [1–3] in chapter 11), the beam model is augmented with a kinematic descriptor for average microcrack sliding, framed within a variational principle that accounts for elastic storage, external work, and Rayleigh-type frictional dissipation. This is further refined with a dynamic hysteresis mechanism based on Dahl's theory of solid friction, allowing for realistic elastoplastic-like loops in bending-shear interactions. Finite element simulations, benchmarked against experimental bending tests, highlight how microstructural friction parameters influence the energy dissipation capacity of structural members. These results inform the design of seismic-resistant concrete elements, enhance fatigue life prediction, and support rehabilitation strategies for aging infrastructure.

Building on the cementitious material framework, the methodology is transferred to a very different domain: corneal biomechanics [4,5]. Here, dissipation arises from viscoelastic relaxation within the corneal stroma, rather than from frictional sliding. Finite element models coupled with shear wave elastography measurements enable the quantification of viscoelastic constants in both healthy and keratoconus-affected corneas. Sensitivity analyses and optimization techniques reveal the biomechanical parameters most critical to diagnostic readings, paving the way for non-invasive early detection of keratoconus, treatment planning, and patient-specific therapeutic optimization. Despite the radical shift in material class and scale, the variational enrichment strategy proves equally effective, underscoring its generality.

The scope then broadens to processes where mechanics is inherently coupled with fluid flow or thermal effects. In fractured porous media [6], experiments on miscible viscous fingering reveal how fracture geometry and viscosity ratio govern sweep efficiency, tip velocity, and pattern complexity, key considerations in enhanced oil recovery, CO_2 sequestration, and groundwater remediation. In additive manufacturing [7], a coupled transient thermomechanical finite element model of laser powder bed fusion captures phase changes, melt pool dynamics, and residual stress development in Inconel 718 alloys with and without nanoparticle dispersion. The simulations guide the selection of process parameters to minimize residual stresses and defects, advancing the design of high-performance aerospace components.

The final contribution [8] demonstrates the adaptability of the approach at the nanoscale, where mechanical, electrical, and optical interactions are intertwined. A higher-order variational framework models coupled flexoelectric-photovoltaic effects in $BaTiO_3$ thin plates, incorporating strain-gradient polarization, curvature-induced photocurrents, and dynamic loading effects. Analytical and numerical solutions identify configurations that optimize energy harvesting performance, informing the design of self-powered nanosensors, multifunctional MEMS devices, and photonic-mechanical energy harvesters.

Across these diverse applications, the thesis maintains a coherent intellectual trajectory: starting from a single, well-characterized dissipation mechanism in a traditional structural material, and step by step, expanding the modeling paradigm to encompass soft tissues, multiphase flow systems, thermomechanical processes, and functional nanomaterials. The result is a robust, versatile methodology for developing enriched continuum models that faithfully capture complex, multiscale material behavior, advancing both the scientific foundations of continuum mechanics and its practical applications across civil, biomedical, environmental, manufacturing, and nanoscale engineering.

Chapter 2

A simple extension of Timoshenko beam model to describe dissipation in cementitious elements

Chapter abstract

In this chapter, the Timoshenko model for plane beams is adapted to capture dissipative behaviors in cement-based materials subject to small displacements and strains. Drawing on the concept of micromorphic continua, a new kinematic measure is introduced to represent average sliding correlated with a stable micro-crack density. The approach considers elastic deformations and friction loss on rough micro-crack faces, similar to configurations with saw-tooth joints. Using a variational approach within the Hamilton–Rayleigh framework, second-order differential equations are derived based on a generalized virtual work principle. These include: (i) variation of inner elastic energy due to elasticity and nonlinear asperity deformation; (ii) virtual work related to external forces and moments; and (iii) frictional dissipation characterized through a Rayleigh potential incorporating nonlinear viscous and Coulomb friction effects. One-dimensional finite element simulations conducted in COMSOL Multiphysics explore the behavior of structural components under cyclic three- and four-point bending tests. The study of energy dissipation through changing model parameters aligns with initial experimental observations, demonstrating this method as a quantitative tool for evaluating hysteresis cycles and guiding the development of cementitious materials.

Z. Angew. Math. Phys. (2024) 75:166
© 2024 The Author(s)
https://doi.org/10.1007/s00033-024-02304-w

Zeitschrift für angewandte Mathematik und Physik ZAMP

A simple extension of Timoshenko beam model to describe dissipation in cementitious elements

Giuliano Aretusi, Christian Cardillo, Antonello Salvatori, Ewa Bednarczyk and Roberto Fedele

Abstract. In this paper, an extension of the Timoshenko model for plane beams is outlined, with the aim of describing, under the assumption of small displacements and strains, a class of dissipative mechanisms observed in cementitious materials. In the spirit of micromorphic continua, the modified beam model includes a novel kinematic descriptor, conceived as an average sliding relevant to a density of micro-cracks not varying along time. For the pairs of rough surfaces, in which such a distribution of micro-cracks is articulated, both an elastic deformation and a frictional dissipation are considered, similarly to what occurs for the fingers of the joints having a tooth saw profile. The system of governing differential equations, of the second order, is provided by a variational approach, endowed by standard boundary conditions. To this purpose, a generalized version of the principle of virtual work is used, in the spirit of Hamilton–Rayleigh approach, including as contributions: (i) the variation of the inner elastic energy, generated by the linear elasticity of the sound material and, in a nonlinear way, by the mutual, reversible deformation of the asperities inside the micro-cracks; (ii) the virtual work of the external actions consistent with the beam model, i.e., the distributed transversal forces and the moments per unit lengths; besides these two contributions, constituting the conservative part of the system, (iii) the dissipation due to friction specified through a smooth Rayleigh potential, entering a nonlinear dependence of viscous and Coulomb type on the sliding rate. Through a COMSOL Multiphysics® implementation, 1D finite element analyses are carried out to simulate structural elements subjected to three- and four-point bending tests with alternating loading cycles. The dissipation of energy is investigated at varying the model parameters, and the predictions turn out to be in agreement with preliminary data from an experimental campaign. The present approach is expected to provide a valuable tool for the quantitative and comparative assessment of the hysteresis cycles, favoring the robust design of cementitious materials.

Mathematics Subject Classification. 74K10, 74B20, 74A60, 65M60.

Keywords. Enhanced Timoshenko beam model, 1D continua with microstructure, Micro-cracks, Cementitious materials, Dissipated energy, Friction, Hysteresis cycles.

1. Introduction

Concrete is a multiphase and multiscale composite material that plays a fundamental and pivotal role in shaping our built environment, providing stability, durability, and versatility in a wide range of construction projects. Research in concrete technology is crucial to promote sustainability, enhance safety, and hence turns out to be of prominent interest for the construction industry. Concrete properties stem from its highly heterogeneous microstructure, including constituents of diverse typologies with various sizes and shapes which are subjected to chemical-physical processes not only during curing but along the entire service life, depending on the water-to-cement ratio and other possible additives as well as on the environmental conditions (in primis the history of temperature and of relative humidity, but also the possible diffusion of aggressive compounds). At the macroscale, the mechanical behavior of concrete results to be extremely complex, characterized by the superposition of an instantaneous response, which can be modeled by nonlinear elasticity, plasticity and damage, leading to hysteresis under cyclic loading,

Birkhäuser

and of deferred phenomena, such as shrinkage and creep. A network of very small cracks, not visible by eyes, is usually present in concrete as a consequence of the cement hydration, shrinkage and loading.

The most recent research topics on concrete concern the study of supplementary cementitious materials, also of nanometer size, the long-term chemical physical deterioration processes and self-healing provisions. Materials like fly ash, slag and silica fume can be added to concrete, in order to improve some of its features and reduce its carbon footprint [1–3], contributing to more sustainable and environmentally friendly construction practices. As an alternative, the mechanical properties and the longevity of the material can be enhanced also by incorporating nanomaterials, see, e.g., [4,5]. Nanoparticles are much smaller in size than conventional concrete constituents, and hence they fill in the gaps between larger particles, improving packing and the overall strength with it, and reducing permeability and porosity. Furthermore, nanomaterials such as nano-silica or nanotubes have a high surface-to-volume ratio [6], allowing for a better bonding with cement particles and favoring the chemical reactivity. Nanomaterials can contribute to mitigate early-age cracking in concrete by reducing the heat of hydration, controlling the formation of micro-cracks and improving the curing process. After decades of services life, chemical physical processes, such as the alkali silica reaction and the sulfate attack, promoted by specific ions already present in the constituents or diffusing from outside, accomplices the environmental conditions, can cause local swelling phenomena in the concrete elements endowed by cracking, with a correlated decrease in mechanical stiffness and strength, see e.g. [7–10]. Research on self-healing concrete focuses on strategies to repair cracks autonomously, mimicking the behavior of biological tissues, such as bone (see, e.g., [11–13]). Key aspects of this research are the development of healing agents that react and seal the crack, such as bacteria, polymers or organic and inorganic materials. At the same time, concrete-based materials with ultra-high-performance are being conceived, characterized by exceptional strength and durability, e.g., see [14–16].

In this scenario, computer simulations and digital modeling can play an increasing role in designing and optimizing the concrete structures, allowing one to carry out virtual tests very rapidly and at low costs, and contributing to a better understanding of the complex mechanisms which turn out to be multiphase and multiscale. This knowledge allows researchers for a more sustainable design, reduced construction costs, improved safety, enhanced durability, ultimately leading to better-engineered structures [17–21]. Moreover, due to a widespread use of cementitious materials in civil engineering, macroscopic models are supposed to be used also by not specialized personnel, implemented in commercial software, and hence they must be conceived as a compromise between simplicity and accuracy, hopefully including a low number of parameters to identify.

From a modeling perspective, the behavior of concrete poses numerous challenges. Crucial issues concern its nonlinear behavior [22–26] even under small strains, the dissipative effects stemming from its microstructure in both elastic and plastic regime [27–31], and the evolution of cracks [32]. Recent studies have explored innovative approaches using material particles akin to swarm robotics, offering promising computational efficiency [33,34]. As an alternative to Cauchy media, generalized continua have been investigated, see e.g. [35–41]. Among them, Cosserat-type models account for the presence of stiff aggregates, and higher gradient continua can address strong heterogeneities (see, e.g., [42–47]). Furthermore, due to the presence of voids generated during the curing process and of micro-cracks, concrete can be treated as a porous material (see, e.g., [48–50]). In particular, micro-cracks affect concrete behavior by introducing asymmetry in its mechanical response and generating internal friction under cyclic loads.

In modeling the hysteresis cycles, commonly adopted viscous models rest on a linearization of the dissipative actions. Alternatively, Coulomb-type friction between bumpy surfaces in the micro-cracks can be used, providing a response nearly independent of the frequency. Rheological models and thermodynamic frameworks with diffusive internal variables are also employed to address dissipation in solid materials.

Finally, it is important to acknowledge ongoing research efforts related to plasticity and damage evolution [51–53]. Variational formulations are favored for their logical consistency and ability to minimize unnecessary assumptions [54–57].

This work aims at investigating from the numerical standpoint the role played in concrete beams by the existing micro-cracks as a possible source of dissipation, especially during cyclic loading. To this purpose, an enhanced version of the Timoshenko beam model is proposed [58,59], inspired by a 3D continuum formulation endowed with a Coulomb-like dissipation potential (see, e.g., [60,61]), which turns out to predict more effectively the hysteresis cycles under moment and shear actions. The paper is organized as follows. Section 2 is devoted to the postulation of the elastic energy and of a Rayleigh dissipation potential for the beam and to the variational deduction of the governing equations. Details for the finite element implementation in COMSOL Multiphysics are outlined in Sect. 3. In Sect. 4, numerical results are discussed, at varying the model parameters. Section 4 outlines the pros and cons of the proposed approach and presents future developments.

A punctualization about the notation. Since a 1D description is considered in what follows, for the sake of brevity the first spatial derivative with respect to the x-coordinate of a function $a(x,t)$ is denoted by the symbol $a' = \partial a/\partial x$, while $\dot{a} = \partial a/\partial t$ indicates the first derivative of the same function with respect to time t. This notation is extended in a consistent way to the higher order derivatives.

2. Beam model with micro-slips and friction

Let us consider a 1D model of a cementitious structural element in the plane xy, lying along the x-axis in its undeformed configuration and whose length is indicated by L. For the sake of simplicity, we will not introduce a curvilinear abscissa, although the results to be discussed hold for any curved plane beam. As well known, in the standard Timoshenko model, the cross sections remain plane during the deformation process but the orthogonality assumption between the longitudinal beam line and the cross section is not retained: the effect of shear, implying also warping, is accounted for by an equivalent rotation with respect to the neutral axis. Hence, the cross section can translate and rotate around the neutral axis. We assume that at the considered scale a random distribution of micro-cracks variously oriented is in place [62]. Let us introduce a further kinematic descriptor aiming to describe, as a volume average, sliding between pairs of rough surfaces inside the micro-cracks, see, e.g., [29]. Neglecting the axial strain, the complete set of kinematic descriptors is constituted of the three functions $v(x)$, $\varphi(x)$ and $\gamma(x)$, representing in turn the transverse displacement (along y) of the beam longitudinal axis and hence of the centroid, the cross section rotation around the neutral axis and an average relative sliding between the pairs of faces constituting the distribution of micro-cracks. Under small displacements, rotations and strains, the current configuration of the beam is specified by the vector map $\boldsymbol{\chi}_t$ depending on the generic abscissa $x \in [0, L]$ and on the time variable t, as illustrated in Fig. 1. By symbols

$$\boldsymbol{\chi}_t(x) := \begin{cases} \boldsymbol{r}(t) \equiv (x, y = v(x,t)) \\ \varphi = \varphi(x,t) \\ \gamma = \gamma(x,t) \end{cases} \quad . \tag{1}$$

Vector $\boldsymbol{r}(x,t)$ specifies the position of the cross section centroid along the loading history, and $\varphi(x,t)$ [rad] and $\gamma(x,t)$ [L] indicate the slope of the cross section and the average microscopic sliding in the sense explained above.

To seek the equilibrium configuration, a generalized version of the principle of virtual work is considered herein. This principle states that, for any virtual perturbation of the equilibrium configuration, the virtual variation of the elastic energy within the system, say $\delta\mathcal{W}^{\text{el}}$, must equal the virtual work made by the external forces acting on the system plus any other virtual dissipation, indicated in turn by $\delta\mathcal{W}^{\text{ext}}$ and

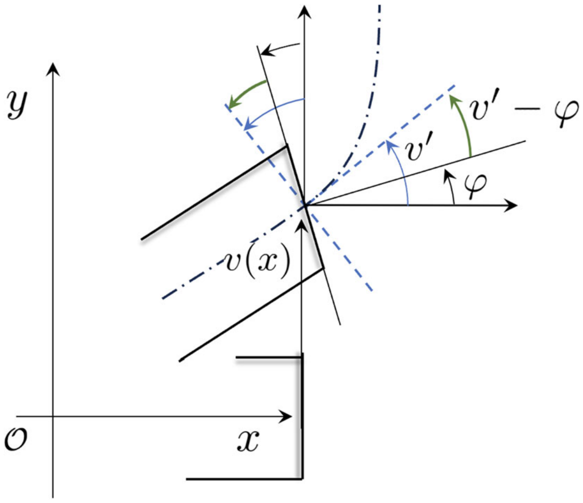

FIG. 1. Macroscopic kinematic descriptors of the beam

$\delta\mathcal{D}^{\,\mathrm{diss}}$. One has

$$\delta\mathcal{W}^{\,\mathrm{el}}(t) = \delta\mathcal{W}^{\,\mathrm{ext}}(t) + \delta\mathcal{D}^{\,\mathrm{diss}}(t), \tag{2}$$

for each time instant t. Quasi-static conditions are assumed herein, neglecting the inertial effects. We postulate the following expression of the elastic energy based on the above mentioned kinematic fields, namely

$$\begin{aligned}\mathcal{W}^{\,\mathrm{el}} &= \int_0^L \frac{1}{2}\mathrm{k}_b\,(\varphi')^2\,\mathrm{d}x + \int_0^L \frac{1}{2}\mathrm{k}_s\,(v'-\varphi)^2\,\mathrm{d}x \\ &\quad + \int_0^L \frac{1}{2}\mathrm{k}_{m1}\,\gamma^2\,\mathrm{d}x + \int_0^L \frac{1}{4}\mathrm{k}_{m2}\,\gamma^4\,\mathrm{d}x - \int_0^L \alpha_b\,\gamma\,\varphi'\,\mathrm{d}x - \int_0^L \alpha_s\,\gamma\,(v'-\varphi)\,\mathrm{d}x\ .\end{aligned} \tag{3}$$

The arguments of the integrals represent an energy density (per unit length), i.e. with the dimension of a force: the material parameters have the meaning of generalized stiffnesses. In particular, symbols k_b [FL^2], k_s [F], k_{m1} [F/L^2] and k_{m2} [F/L^4] denote direct stiffnesses associated with diverse deformation mechanisms, while α_b and α_s (in turn with dimensions [F] and [F/L]) govern their coupling. Parameters k_{m1} and k_{m2} control the energy stored by the micro-cracks. From the theoretical standpoint, the stored energy of Eq. (3) must be positive defined and strictly convex, to ensure existence and uniqueness of the minimum point. As well known, for quadratic forms these two properties coincide. If we neglect for a while the quartic contribution of the micro-slip, the coefficient matrix of the quadratic form Eq. (3) can be easily specified. Through the Sylvester's theorem, the admissible set of parameters can be specified through the constraints $\mathrm{k}_b > 0$, $\mathrm{k}_s > 0$, $\mathrm{k}_b\,\mathrm{k}_s\mathrm{k}_{m1} > \mathrm{k}_s\,\alpha_b^2 + \mathrm{k}_b\,\alpha_s^2$. All these parameters can be estimated on the basis of suitable experimental data, or through a micro–macro identification strategy, see e.g. [63–67]. Furthermore, if we assume both the coefficients of the micro-slips k_{m1} k_{m2} to be nonnegative, the nonlinear elastic contribution corresponding to the average micro-slip turns out to be positive defined and strictly convex, exhibiting two coinciding real minimum points in the origin and other two complex conjugates. If we image to integrate such a polynomial expression in γ, the odd terms cannot be included since they would provide non-symmetric contributions to the elastic energy, which in this circumstance does not appear mechanically based.

The first two contributions of the energy in Eq. (3), representing bending and shear, coincide with those of the standard Timoshenko model. The first two addends along the second row, which exhibit a polynomial dependence (quadratic and quartic) on γ, govern the amount of elastic energy stored by the pairs of surfaces constituting the distribution of micro-cracks. In fact, from a geometric standpoint, the lips of a micro-crack, which exhibit bumps or asperities, interact with each other. When these asperities come into contact, similarly to the teeth of a saw profile, they can bend like cantilevers, and hence, their relative sliding induces a fully reversible amount of deformation energy. Experimental studies, see, e.g., [68], stated that in cement-based materials sliding of micro-cracks can induce a macroscopic nonlinear response, even under small displacements and strains. The last two contributions of Eq. (3) govern the mutual energy between the beam bending and the relative slip of the asperities within the micro-cracks, as well as between the macroscopic shear distortion of the beam and the asperity deformation. To clarify this concept, let us indicate by $\mathbf{n}$ and $\mathbf{m}$ the unit vectors normal and tangential to an ideally flat micro-crack. Locally, one would expect that the Cauchy stress component $\sigma_{nm} = \boldsymbol{\sigma} : \mathbf{n} \otimes \mathbf{m}$ were responsible for the relative sliding of the opposite surfaces, while the stress component $\sigma_{nn} = \boldsymbol{\sigma} : \mathbf{n} \otimes \mathbf{n}$, if compressive, caused the unilateral closure of that crack and an increase in the frictional dissipation as stated by Coulomb. Due to the random orientation of the micro-cracks within the bulk, we reasonably expect that both the shear action and the bending moment contribute to such a relative sliding, i.e. to σ_{nm}, although not everywhere one has $\sigma_{nn} < 0$ and the frictional dissipation occurs. Therefore, we assume that coupling occurs between the micro-slips and both the shear deformation and the bending curvature.

By differentiating the energy in Eq. (3) with respect to the kinematic descriptors, we obtain the dual generalized stresses of the beam

$$\begin{aligned} M(x,t) &= \frac{\partial \mathcal{W}^{\,\mathrm{el}}}{\partial\, \varphi'} = \mathrm{k}_b \varphi' - \alpha_b \gamma \ \ , \ \ T(x,t) = \frac{\partial \mathcal{W}^{\mathrm{el}}}{\partial\, (v' - \varphi)} = \mathrm{k}_s\, (v' - \varphi) - \alpha_s \gamma, \\ \mathfrak{T}(x,t) &= \frac{\partial \mathcal{W}^{\,\mathrm{el}}}{\partial\, \gamma} = \mathrm{k}_{m1}\, \gamma + \mathrm{k}_{m2}\, \gamma^3 - \alpha_b\, \varphi' - \alpha_s\, (v' - \varphi) \\ &= \left(\mathrm{k}_{m1} - \frac{\alpha_b^2}{\mathrm{k}_b} - \frac{\alpha_s^2}{\mathrm{k}_s} \right) \gamma + \mathrm{k}_{m2}\, \gamma^3 - \frac{\alpha_b}{\mathrm{k}_b}\, M - \frac{\alpha_s}{\mathrm{k}_s}\, T \ \ . \end{aligned} \tag{4}$$

The virtual work made by the inner forces is straightforwardly computed by the first variation of the elastic energy (3) as:

$$\begin{aligned} \delta \mathcal{W}^{\,\mathrm{el}} = &\int_0^L \mathrm{k}_b \varphi'\, \delta\varphi'\, \mathrm{d}x + \int_0^L \mathrm{k}_s\, (v' - \varphi)\, \delta\, (v' - \varphi)\, \mathrm{d}x \\ &+ \int_0^L \mathrm{k}_{m1} \gamma\, \delta\gamma\, \mathrm{d}x + \int_0^L \mathrm{k}_{m2} \gamma^3\, \delta\gamma\, \mathrm{d}x + \\ &- \int_0^L \alpha_b\, (\varphi'\, \delta\gamma + \gamma\, \delta\varphi')\, \mathrm{d}x - \int_0^L \alpha_s\, [(v' - \varphi)\, \delta\gamma + \gamma\, (\delta v' - \delta\varphi)]\, \mathrm{d}x\,, \end{aligned} \tag{5}$$

where symbol $'$ denotes as usual the derivative with respect to the spatial coordinate x. Integrating by parts and applying the fundamental lemma of the integral calculus (as 1D counterpart of the divergence theorem), the contributions of the internal elastic energy can be grouped on the basis of the kinematic descriptor appearing as test function,

$$\begin{aligned}\delta\mathcal{W}^{\mathrm{el}} = &-\int_0^L \Big[\,(\mathrm{k}_b\varphi')' + \mathrm{k}_s\,(v'-\varphi) - (\alpha_b\gamma)' - \alpha_s\gamma\,\Big]\,\delta\varphi\,\mathrm{d}x + \left[(\mathrm{k}_b\varphi' - \alpha_b\gamma)\;\delta\varphi\right]_0^L \\ &+ \int_0^L \Big[\,\mathrm{k}_{m1}\gamma + \mathrm{k}_{m2}\gamma^3 - \alpha_b\,\varphi' - \alpha_s\,(v'-\varphi)\,\Big]\,\delta\gamma\,\mathrm{d}x + \\ &- \int_0^L \Big\{\,\Big[\mathrm{k}_s\,(v'-\varphi)\,\Big]' - (\alpha_s\,\gamma)'\,\Big\}\delta v\,\mathrm{d}x + \Big[\,\Big\{\mathrm{k}_s\,(v'-\varphi) - \alpha_s\gamma\,\Big\}\delta v\,\Big]_0^L\,, \end{aligned} \tag{6}$$

being as usual $[a(x)]_0^L = a(L) - a(0)$. The above equations describes the conservative part of the system. To simulate the dissipation mechanisms at the macroscale due to microscopic tangential slip with friction, in the spirit of Hamilton–Rayleigh principle a dissipation potential is introduced, see, e.g., [69]. A nonnegative Rayleigh function can be postulated as follows:

$$\mathfrak{R}(x,t) = \frac{\zeta}{\eta}\,\ln\left[\cosh(\eta\,\dot{\gamma})\right]\,|\varphi'| \geq 0\,, \tag{7}$$

having the dimension of a power density, namely [F/t]. Symbol $\dot{\gamma}$ [L/t] denotes as usual the time derivative of the average slip in argument, being the product $\eta\,\dot{\gamma}$ non-dimensional, and ζ has dimension [F]. By differentiating the Rayleigh potential $\mathfrak{R}$ in Eq. (7) with respect to the average slip rate $\dot{\gamma}$, by changing the sign we obtain the dual friction force density, exerted between the opposite faces of the micro-cracks

$$\tau_{\mathrm{diss}} = -\frac{\partial\,\mathfrak{R}}{\partial\,\dot{\gamma}} = -\zeta\;\tanh\left[\eta\,\dot{\gamma}\right]\,|\varphi'|\,, \tag{8}$$

having dimension [F/L]. As anticipated in Eq. (2), we can take into account the virtual work carried out by the friction force density at the level of the micro-cracks, as follows:

$$\delta\mathcal{D}^{\mathrm{diss}}(t) = -\int_0^L \mathrm{d}x\;\zeta|\varphi'(x,t)|\tanh[\,\eta\,\dot{\gamma}(x,t)]\,\delta\gamma\;. \tag{9}$$

Basically, any friction force can be described through a standard Coulomb behavior. However, due to the non-Lipschitz continuity of the forcing term, including the signum function, the uniqueness of the solution would be lost. To overcome this drawback, the hyperbolic function $\tanh[\eta\,\dot{\gamma}]$, with asymptotes ±1 for $\eta\dot{\gamma} \to \pm\infty$, can be utilized to mimic the Coulomb behavior while avoiding the aforementioned issue, assuming η sufficiently large, see e.g. [70,71]. This approach turns out to work effectively in a variety of applications: moreover, it introduces a viscous behavior for small velocities $\dot{\gamma}$, which plays a stabilization role in several contexts, without mentioning that η can be tuned on the basis of the experimental data. The appearance in Eq. (9) of the derivative of the cross section rotation in absolute value, $|\varphi'|$, is related to the fact that, by increasing the bending curvature, compressive states become more significant at least in one part of the cross section, favoring the closure of the micro-cracks. The intensity of the friction force is governed also by the parameter ζ, independent of the term $|\varphi'|$. For a comprehensive description of the dissipation in a Lagrangian approach, the reader is referred to [69,72].

The external virtual work, including the distributed forces b_y in the y-direction and the moment per unit length μ, is expressed as:

$$\begin{aligned}\delta\mathcal{W}^{\mathrm{ext}}(t) = &\int_0^L \mathrm{d}x\;b_y(x,t)\,\delta v + \int_0^L \mathrm{d}x\;\mu(x,t)\,\delta\varphi \\ &+ F_{y0}(t)\,\delta v(0,t) + W_0(t)\,\delta\varphi(0,t) + F_y(t)\,\delta v(L,t) + W_L(t)\,\delta\varphi(L,t)\;\;,\;\forall\,t,\end{aligned} \tag{10}$$

where concentrated vertical forces F_y and moments W can be applied at both the ends of the beam, at each instant t. We remark that Eq. (6) cannot provide any boundary condition for γ since this variable does not appear under a spatial derivative.

By substituting into Eqs. (2) the expressions in Eqs. (6), (9) and (10), by the fundamental lemma of the variational calculus the governing equations in strong form are as follows

$$\begin{cases} -\left[\mathrm{k}_s\left(v'-\varphi\right)\right]'+\left(\alpha_s\,\gamma\right)'=-T'=b_y(x,t) \\ \quad \mathrm{k}_{m1}\gamma+\mathrm{k}_{m2}\gamma^3-\alpha_b\,\varphi'-\alpha_s\left(v'-\varphi\right)=\mathfrak{T}=-\zeta|\varphi'|\tanh[\,\eta\,\dot{\gamma}] \\ -\left[(\mathrm{k}_b\varphi')'+\mathrm{k}_s\left(v'-\varphi\right)-(\alpha_b\gamma)'-\alpha_s\gamma\right]=-M'-T=\mu(x,t) \end{cases} \quad . \tag{11}$$

to hold $\forall\, x\in]0,L[$ and $\forall\, t$. At the beam ends, with abscissae $x=0$ and $x=L$, values of $v(0,t)$, $v(L,t)$ and $\varphi(0,t)$, $\varphi(L,t)$ can be prescribed (essential boundary conditions), or, dually, the history of the shear force $T(0,t)$, $T(L,t)$ and of the bending moment $M(0,t)$, $M(L,t)$ (natural boundary conditions) in equilibrium with the external loading Eq. (10). Initial conditions at $t=0$ must be considered, assuming for instance $v(x,0)=\varphi(x,0)=\gamma(x,0)=0$, $\forall\, x\in]0,L[$.

The above equalities in Eq. (11), endowed by the boundary and the initial conditions, represent a system of nonlinear partial differential equations dependent on space and time, i.e., within the strip $[0,L]\times[0,t]$. The second equation from above includes first order derivatives as maximum order, and exhibits a nonlinear dependence on the micro-crack slip γ, which appears at the maximum power 3, and on time also, through the slip rate $\dot{\gamma}$. The remaining equations are linear in the derivatives: In the first equation, an equivalent or effective distributed transversal loading can be considered, equal to $b_y-(\alpha_s\gamma)'$, while in the last equation an equivalent or effective moment per unit length can be specified, namely $\mu-(\alpha_b\gamma)'-(\alpha_s\gamma)$. If we assume the coupling stiffnesses α_b and α_s to vanish, the second equation becomes decoupled from the remaining ones and the standard Timoshenko beam model is retrieved.

It is worth noting that the average micro-slips can affect both the shear action and the bending moment: it acts like a microrotation of the generic cross section. If we differentiate the constitutive relationships for the shear actions and the bending moment in Eq. (4), in the absence of distributed loading one obtains

$$T'=\mathrm{k}_s\left(v''-\varphi'\right)-\alpha_s\gamma', \qquad M'=\mathrm{k}_b\varphi''-\alpha_b\gamma'\,. \tag{12}$$

Hence, at locations where the moment is constant with the abscissa and the shear action T is null, namely $M=c$ and $T=0$, one has

$$\mathrm{k}_s\left(v'-\varphi\right)=\alpha_s\gamma, \qquad \mathrm{k}_b\varphi''=\alpha_b\gamma'\,. \tag{13}$$

Concentrated jumps in the diagram of the shear action cause cusps in the plots of γ (with right and left derivatives tending to $\pm\infty$), while angular points for T or M cause angular points in turn for $v'-\varphi$ and γ, and for φ' and γ.

3. Virtual tests

To assess the dissipative behavior of a cementitious material under small displacements and strains, we make reference to standard experimental configurations under bending, commonly referred to as three-point and four-point bending tests. The sample has a rectangular parallelepiped shape, with sides $d\times d\times L$, and is placed on two supports located symmetrically with respect to the beam center, at a distance ℓ from each other: a vertical force is applied at the center, for the three-point test, or at two specific locations on the top for the four-point bending test (see Figs. 2, 3). Due to the presence of unilateral constraints, exclusively alternating (i.e. pulsating, with non-null mean value) loading cycles have been applied, besides a monotonic history. The preliminary numerical exercises discussed in what follows are intended to provide a basis for the model validation, and the reference for an experimental campaign on course.

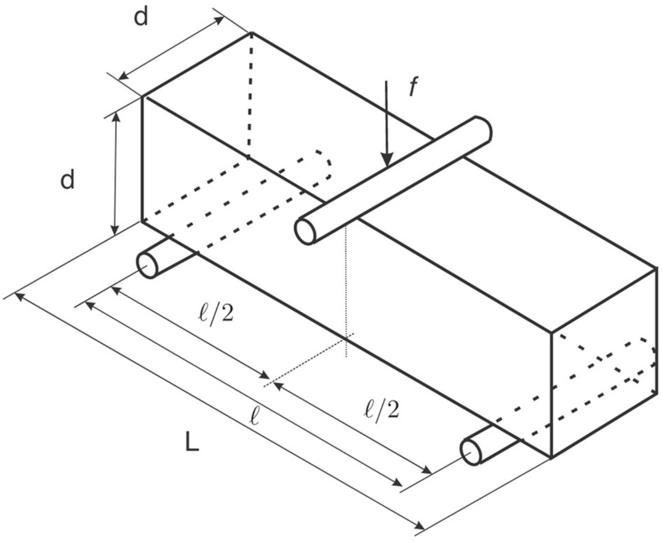

FIG. 2. Experimental configuration for three-point bending test and sample geometry

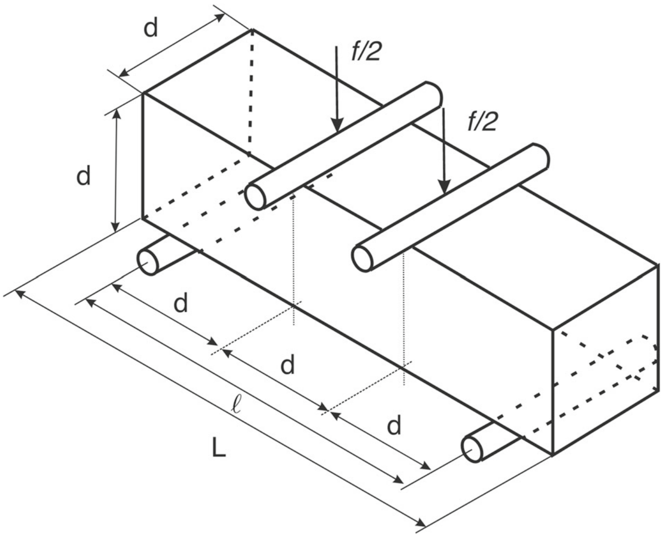

FIG. 3. Experimental configuration for the four-point bending, and sample geometry

The 1D finite element analyses are carried out by the commercial software COMSOL Multiphysics® [73], which enables the direct implementation of the weak formulation Eq. (2) through a package for partial differential equations. Since the proposed model includes the first gradient of the three kinematic descriptors, see Eq. (5), it represents a higher order model of first grade: hence, C^0 conformity at for the finite element discretization is sufficient, guaranteed by standard Lagrangian quadratic polynomials as shape functions. The adopted discretization consists of 121 quadratic finite elements, each one including three nodes, corresponding to 720 overall degrees of freedom when considering the nodal values for the three fields and the constraints. An implicit time integration scheme has been utilized, referred to as backward differentiation formula (BDF) method. For further details on the numerical implementation even under geometric nonlinearity, we forward the interested reader to [74–79].

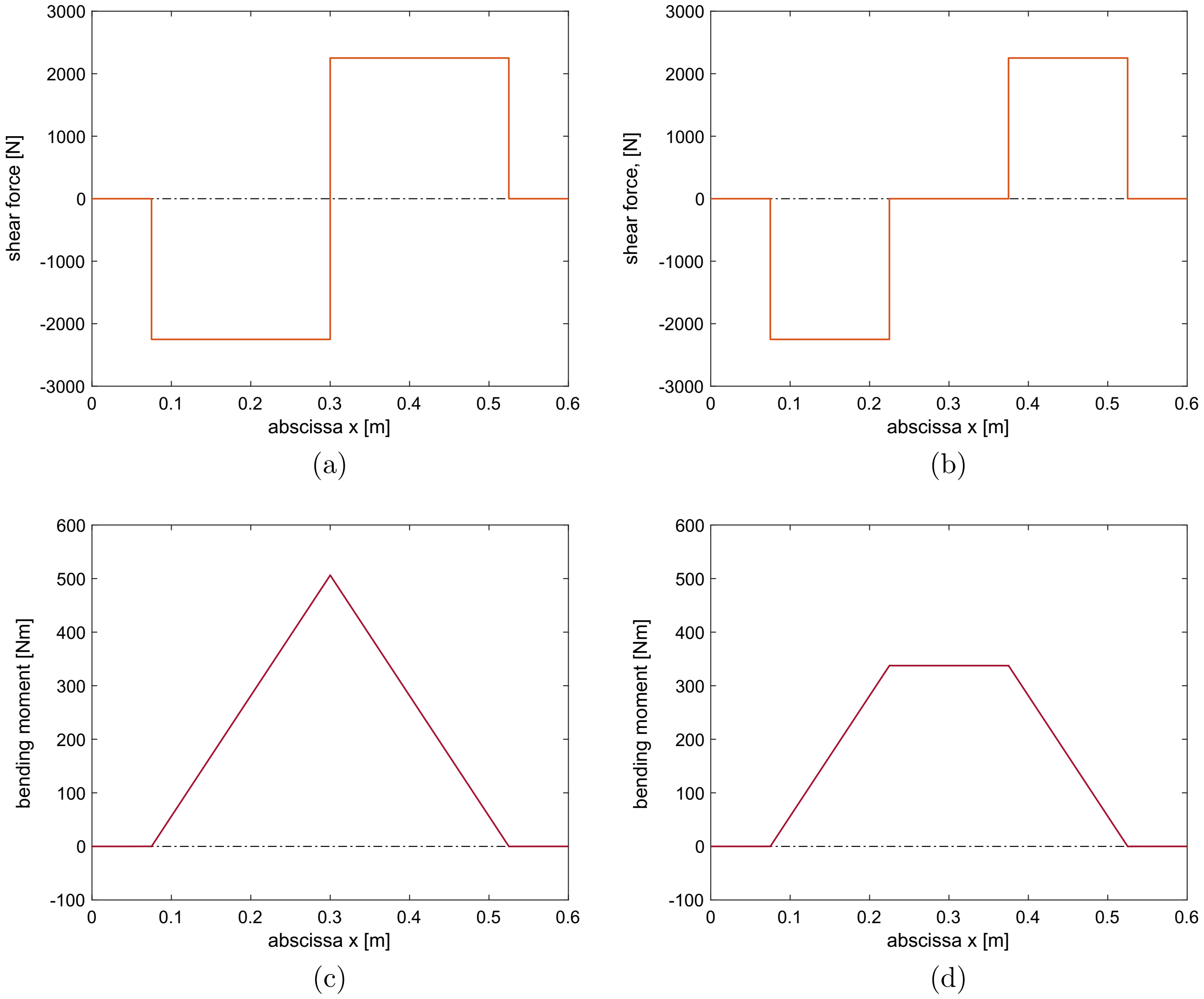

(a) (b)

(c) (d)

Fig. 4. Profiles of the shear force T, in (**a**) and (**b**), and of the bending moment M, in (**c**) and (d), concerning the three-point bending test (first column) and the four-point bending configuration (second column)

We have assumed Young's modulus E=31.45 (GPa), and Poisson ratio $\nu = 0.15$. The standard bending stiffness can be retrieved as $\mathrm{k}_b = E\,J$, being J the second inertia moment of the cross section, while for the shear stiffness one has $\mathrm{k}_s = 5/6\,G_c\,d^2$, where $G_c = E/[2\,(1+\nu)]$ is the shear modulus. The set of parameter values needed for the simulations is reported in the synoptic Table 1. Alternatively, these parameters can be identified through micro–macro-approaches, or on the basis of experimental data through the minimization of a suitable discrepancy norm. Instead of lengthy minimization procedures requiring numerous forward analyses, artificial neural networks (ANN), once trained and tested on the basis of synthetic data corrupted by noise, can provide very rapidly at negligible cost the solution of the inverse problem in terms of parameter estimates, see, e.g., [80–84]. As external loading an alternating force with a sinusoidal trend was considered, namely

$$f(t) = \frac{F_0}{2}\left[\,1 - \cos\left(2\pi f_q\, t\right)\,\right]. \tag{14}$$

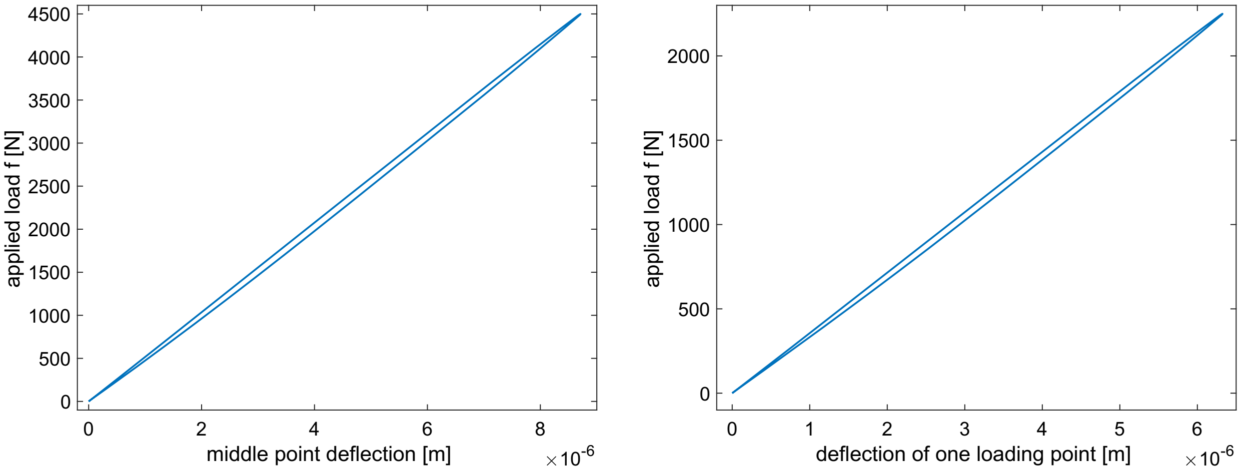

(a) (b)

Fig. 5. Hysteresis cycle under three-point bending test, in (**a**), and four-point bending test, in (**b**). Beam geometry and model parameters are assumed as in Table 1

The amplitude was assumed as $F_0 = 4.5$ (kN) for the three-point bending test, and one half of it for the four-point bending configuration. The frequency f_q was set to 10 (Hz).

3.1. Discussion of the results

In this section, the response of the proposed beam model is analyzed critically and comparatively when subjected to three- and four-point bending tests. Parameters, assumed as in Table 1, have been selected by trial and error to fit preliminary data on plain concrete samples. Moreover, we assess the resulting dissipation during cyclic loading.

The diagrams of the generalized stresses of the beam, namely the bending moment M and the shear action T, evaluated at the force peak, are drawn in Fig. 4: those in the first column concern the three-point bending test and those in the second column the four-point bending configuration. All of them can be computed on the basis of equilibrium conditions in the isostatic structural schemes.

Figure 5 shows a complete hysteresis cycle, consisting of a loading and an unloading branch, in terms of vertical force and displacement of the application point for the two configurations. The dissipated energy, corresponding to the area within the cycle for the three-point bending test, and to the double of it for the four bending configuration (in which two identical forces are applied), has been computed by numerical quadrature: the energy loss amounts to 6.212×10^{-4} (J) and to 4.445×10^{-4} (J) for three- and four-point bending tests, respectively.

The spatial profile of the three kinematical descriptors is depicted in Fig. 6: they are evaluated at the force peak, corresponding to the time instant $t = 0.05$ (s). Along the beam axis, run by abscissa x, we report the transverse displacement v (i.e., the deformed configuration), the slope of the cross section φ, and the average sliding at the level of the micro-cracks γ. In the synoptical view of Fig. 6, arranged as a 3×2 matrix, the first column concerns the three-point bending test, the second column the four-point configuration. In the first row, showing the vertical displacement profiles, the location of the hinges is marked by circles $\circ$ along the curve, while the loading application points are marked by rhombs $\diamond$. By visual inspection, spatial profiles of the variables v and φ coincide with those expected by the standard Timoshenko model. For the assigned parameter set of Table 1, the intensity of average micro-slip γ

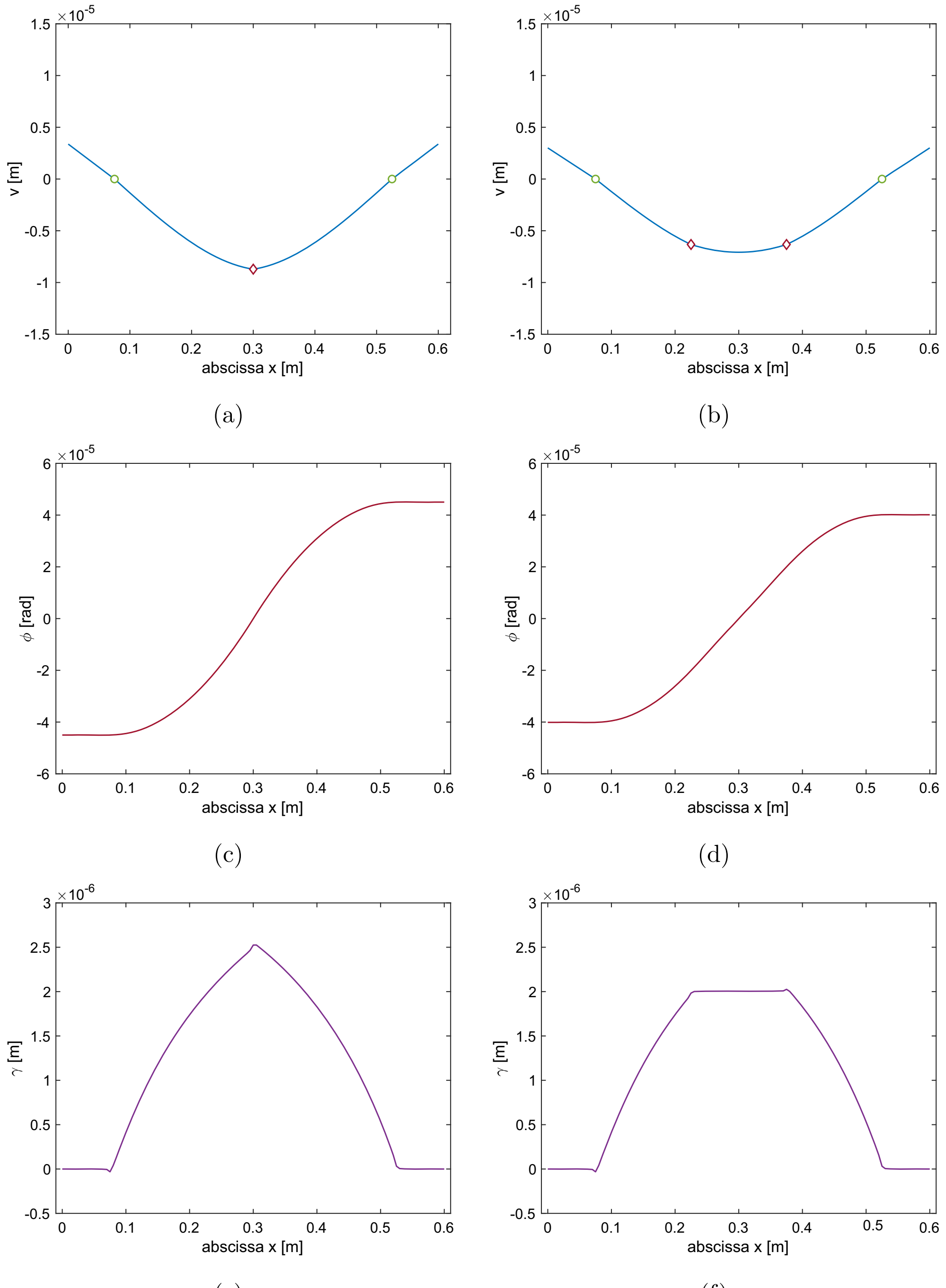

(a) (b)

(c) (d)

(e) (f)

Fig. 6. Three point bending (in the first column) and four-point bending configurations (in the second column). Profiles along the beam axis, evaluated at the force peak (time instant $t = 0.05$ (s)), of the three field variables: the transverse displacement, v, (**a**) and (**b**); the slope of the cross section, φ, (**c**) and (**d**); and the relative sliding at the level of micro-cracks, γ, (**e**) and (**f**). In plots (**a**) and (**b**), the locations of the supports are marked by circles $\circ$, while the application points of the force by rhombs $\diamond$

approximately follows the profile of the bending moment. Moreover, the plot of γ exhibits angular points and cusps at locations where the shear action undergoes jumps.

Table 1. *Beam geometry and model parameters used as a reference in the numerical exercises*

	Geometry	
d	L	ℓ
150 (mm)	600 (mm)	450 (mm)
	Material parameters	
k_b	k_s	k_{m1}
1.33×10^6 (N m^2)	2.56×10^8 (N)	7.5×10^8 (N/m^2)
k_{m2}	α_b	α_s
1.00×10^8 (N/m^4)	8.05×10^6 (N)	0.5×10^7 (N/m)
ζ	η	E_c
2.95×10^8 (N)	225 (s/m)	31.45 (GPa)

To favor a huge comprehension of the proposed model, Figs. 7 and 8 depict the time histories of the relative micro-slip γ and of the density of friction force $\tau_{\text{diss}} = -\zeta|\varphi'|\tanh[\eta\,\dot{\gamma}]$, evaluated at the application point of the external force for both the test configurations. It is worth noting that the time response of these quantities is nonlinear with respect to the evolution of the loading multiplier, varying according to the law in Eq. (14).

To assess the role played by the amplitude of the friction force, we have run several analyses by scaling the parameter ζ in Eq. (8) through a factor q. Figure 9 shows the energy lost by the system along one complete cycle at varying the scale factor through the values $q = (0.25, 0.5, 1, 2, 4)$. As a result, we have obtained for the dissipated energy values in the interval $[3.1 \times 10^{-4}, 6.2 \times 10^{-4}]$ (J) for the three-point bending test, and slightly smaller values, within the interval $[1.9 \times 10^{-4}, 4.7 \times 10^{-4}]$ (J), for the four-point configuration. The dotted lines indicate regression curves fitting these data, relevant to each test configuration. The observed trends are qualitatively similar, revealing the presence of a maximum of the dissipated energy. This behavior typically denotes the presence of two conflicting features. In fact, on the one hand, when the amplitude of the friction force density is low, there is less dissipation within a hysteresis cycle. On the other hand, if the amplitude of the friction force exceeds a threshold, the average relative sliding inside the distribution of micro-cracks cannot increase, and with it the dissipation necessarily decreases. Therefore, it is possible to select a value of the friction coefficient as the point which maximizes the dissipated energy.

To assess the role played by the coupling parameters, we have increase the value of the coefficient α_b in Table 1 by 30% and 60%. Figure 10 shows the hysteresis cycles predicted by the finite element analyses for the selected configurations. In particular, for the three-point bending test, starting from 6.212×10^{-4} (J) the dissipated energy is increased up to 0.0011 (J) and 0.0019 (J), respectively. Similarly, in the four-point configuration, for the same percentage increment of the parameter α_b, starting from 4.445×10^{-4} (J) the dissipated energy is increased up to 8.136×10^{-4} (J) and 0.0014 (J), in the order for the two levels of considered increase.

The same analysis has been carried out for the coupling coefficient α_s. However, since this coefficient affects less the overall behavior, the changes in percentage observed with respect to the reference set of parameters are negligible. In the case of the three-point bending test, the 30% increase in this coupling stiffness results into an energy loss of 6.215×10^{-4} (J), and a 60% increase causes a dissipation of 6.219×10^{-4} (J). In the four-point bending test, a 30% increase corresponds to an energy loss of 4.449×10^{-4} (J), while the 60% increase gives rise to a dissipation of 4.453×10^{-4} (J). After that, we increased the value of α_s by five times. Firstly, we have obtained hysteresis cycles very close to those provided by the reference parameters of Table 1, confirming that the impact of α_s is less significant with respect to α_b. The energy loss for the three-point and four-point bending configurations amounts to 6.314×10^{-4} (J) and 4.534×10^{-4} (J), respectively. Secondly, analyzing the distribution of the average sliding γ at the peak, as shown in Fig. 11, due to the linear coupling between γ and the shear deformation $(v' - \varphi)$, one can easily recognize an increase of the average sliding in one side of the beam and the opposite behavior

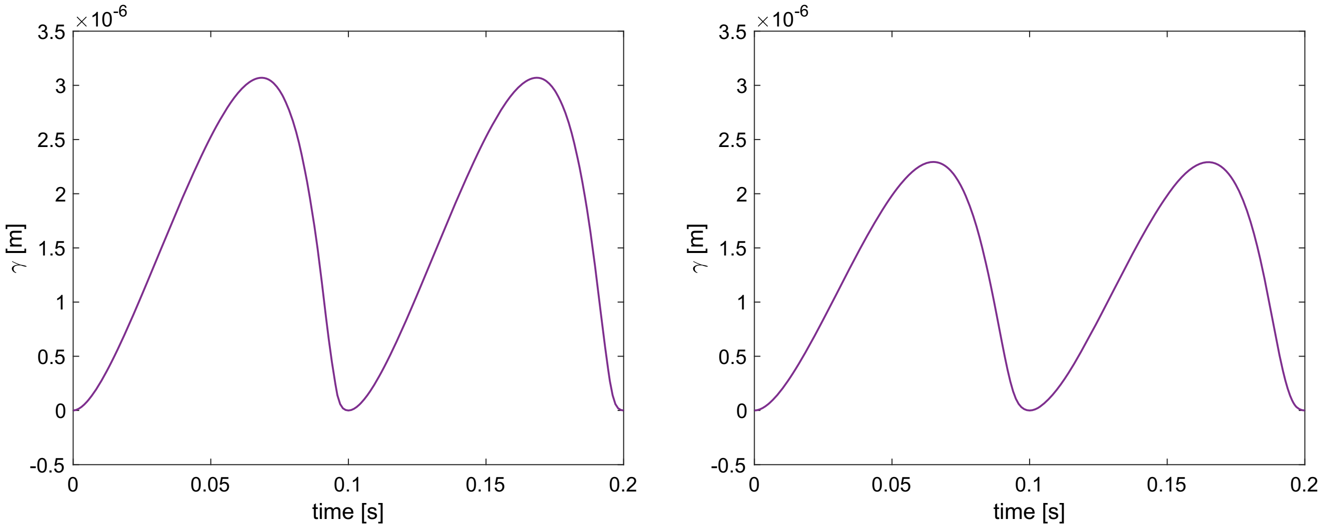

(a)

(b)

FIG. 7. Time history of the micro-slip γ for the three-point bending test evaluated at the middle point, in (**a**), and for the four-point bending test evaluated at one loading point, in (**b**)

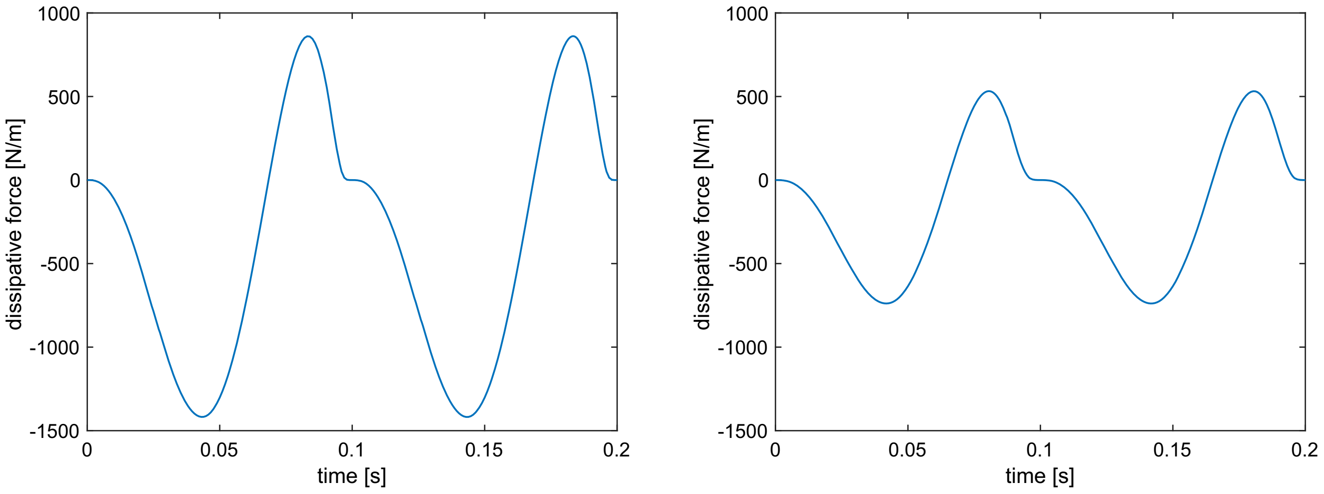

(a)

(b)

FIG. 8. Time history of the friction force density, $\tau_{\text{diss}} = -\zeta|\varphi'|\tanh[\eta\dot{\gamma}]$, evaluated at the middle point of the beam in the three-point bending configuration, in (**a**), and at one of the force application points for the four-point bending test, in (**b**)

in the remaining part, so that the distribution of the average sliding of micro-cracks turns out to be not symmetric. This asymmetric behavior can be noticed also for the distribution of the dissipated power density, as reported in Fig. 12.

Let us consider the stiffness k_{m2}, multiplying γ^4 in the expression of elastic energy Eq. (3). Figure 13 shows the hysteresis cycles corresponding to $\mathrm{k}_{m2} = 0$ (N/m^4) (subfigures (a) and (b)) and $\mathrm{k}_{m2} = 1 \times 10^{20}$ (N/m^4) (subfigures (c) and (d)). The first and second column of the composite figure correspond in the order to the three-point and to the four-point bending test. When we set $\mathrm{k}_{m2} = 0$ (N/m^4), we obtain

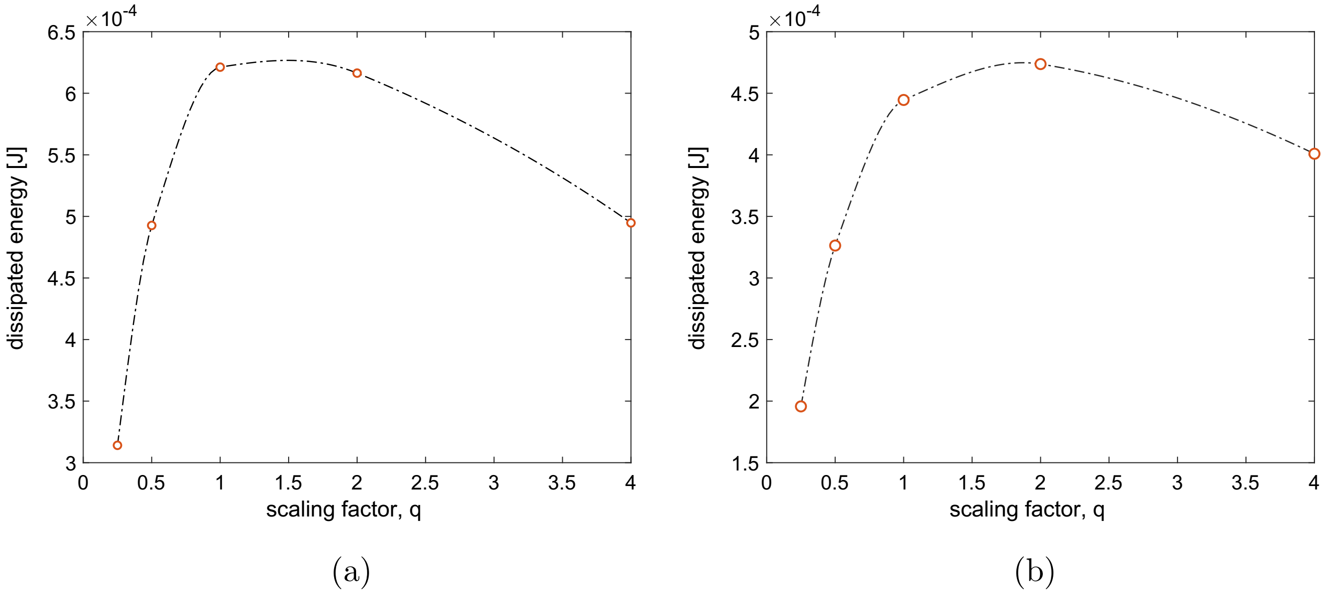

FIG. 9. Dissipated energy at varying the scaling factor q (multiplying parameter ζ), for the three-point bending test, in (**a**), and for the four-point configuration, in (**b**). The dashed line indicate a regression curve, interpolating the results of the simulations marked by red circles ○

for the three-point bending test an energy loss of 6.212×10^{-4} (J), while for the four-point bending test the dissipated energy per cycle amount to 4.445×10^{-4} (J), almost unchanged with respect to the above mentioned cases, with parameters corresponding to Table 1. By setting $\mathrm{k}_{m2} = 1 \times 10^{20}$ (N/m^4), for the three-point bending test the energy loss in the loading–unloading cycle amounts to 3.423×10^{-4} (J), while for the four-point configuration equals 2.605×10^{-4} (J). Thus, a higher stiffness of the asperities inside the micro-cracks leads to a substantial decrease of the dissipation.

4. Closing remarks and future prospects

In this study, a novel beam model especially suitable for cementitious structural elements is outlined, which generalizes the standard Timoshenko beam by a high order strategy. In the mechanical formulation, an additional kinematic descriptor has been considered, which represents an average sliding between the pairs of rough surfaces constituting a density of micro-cracks. Such a distributions of micro-cracks, randomly oriented within the beam volume, is assumed to remain constant during the entire loading process. The additional field variable, rooted in the meso-structure, generates both an elastic energy and a nonlinear dissipation, defined through a smooth Rayleigh potential which induces a Coulomb-like friction force with a viscous dependence on the rate of deformation. The expression of the stored energy associated with these micro-slips has been enriched up to include a quartic term, and represents the conservative part of the system. The coefficients weighting the diverse contributions are subjected to constraints, deduced by the Sylvester criterion, to guarantee positive definition and strict convexity of the energy functional. This formulation, deduced by a variational approach based on the principle of virtual work in the spirit of Hamilton–Rayleigh approach, provides a simple but effective framework to describe dissipative mechanisms in cementitious elements, which imply an energy loss during cycling loading. The response of the extended Timoshenko beam can be described through a system of three nonlinear partial different equations, depending on space and time, endowed by boundary and initial conditions: at the beam ends, one can prescribe the history of the transversal displacement and of the rotation of the cross

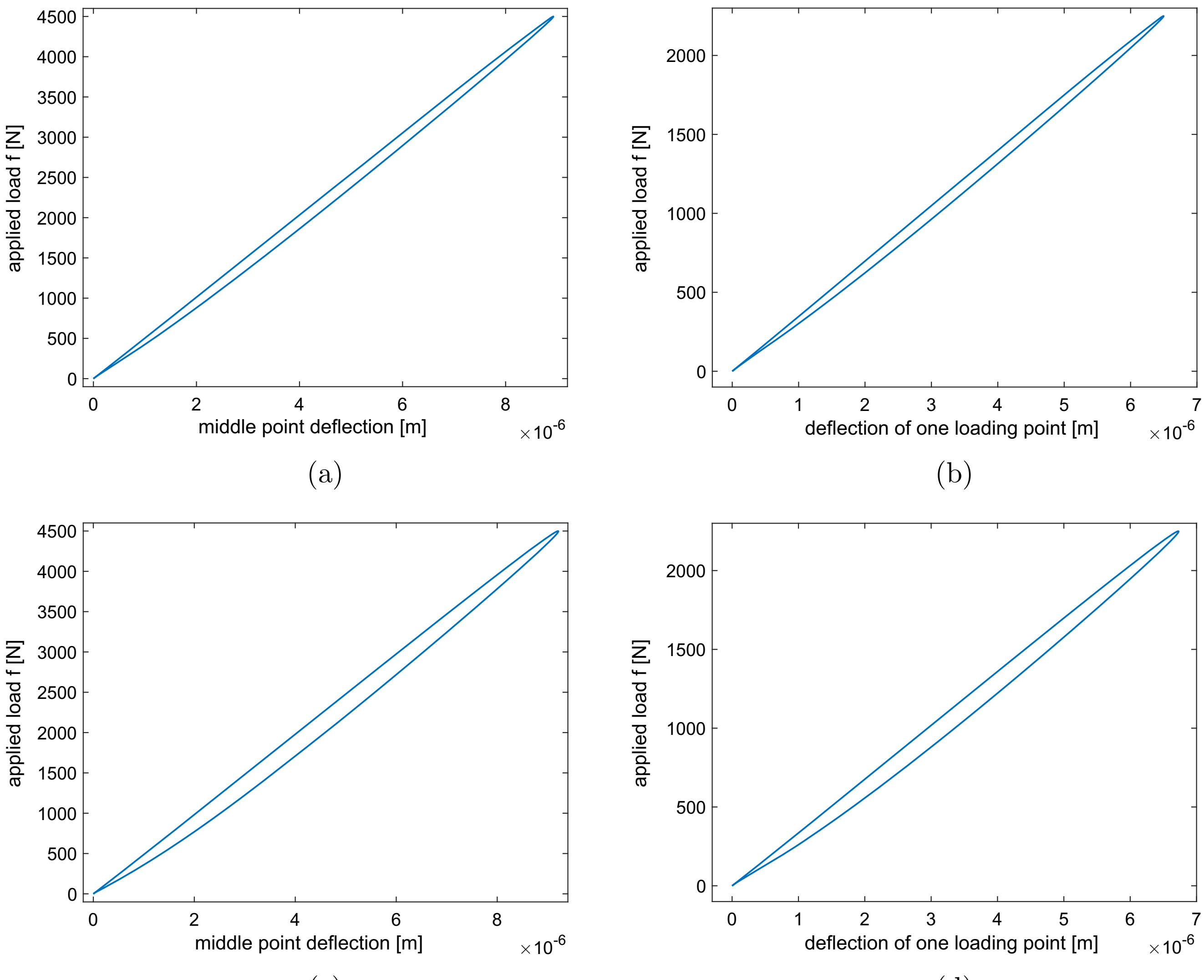

(a) (b)

(c) (d)

Fig. 10. Hysteresis cycles in the three-point bending test, when scaling the coupling stiffness α_b by factors 1.3 and 1.6, in (**a**) and (**c**), respectively, and in the four-point bending test, in (**b**) and (**d**) with the same scaling

section (but not the average sliding), or, alternatively, of their dual actions, while at the initial time instant the three fields are assumed to be null along the entire beam.

Starting from the weak formulation of this model, 1D finite element analyses have been carried out by COMSOL Multiphysics®, describing the three-point and the four-point bending tests as reference configurations under alternating cycles. At varying the governing parameters, the extended beam model turns out to describe in a satisfactory manner hysteresis cycles, in agreement with literature data (see, e.g., [85,86]) and with preliminary experiments carried out by the authors on plain concrete samples. The nonlinear relationship between the amplitude of the frictional force and the energy loss during the hysteresis cycles has been investigated, revealing the existence of a critical intensity at which the dissipation is maximized.

The proposed model is expected to provide useful insights for the optimal design of cementitious structural elements, particularly in those applications where both the energy dissipation and the mechanical stiffness represent critical factors. For instance, in the seismic structural design, building materials must

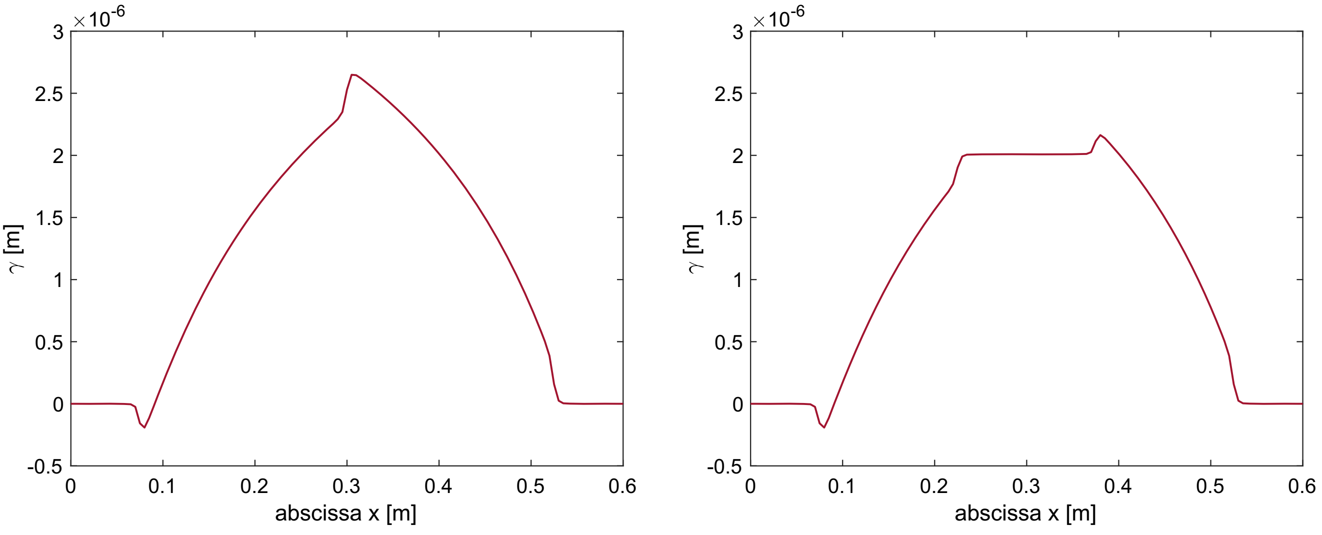

(a) (b)

Fig. 11. Distribution of the micro-crack average sliding γ along the beam for the three-point bending test, in (**a**), and for the four-point configuration, in (**b**), relevant to $\alpha_s = 2.5 \times 10^7$ (N/m). For this value of α_s, the profile of γ turns out to be non-symmetric with respect to the center of the beam, exhibiting a stronger dependence on the sign of the shear action T

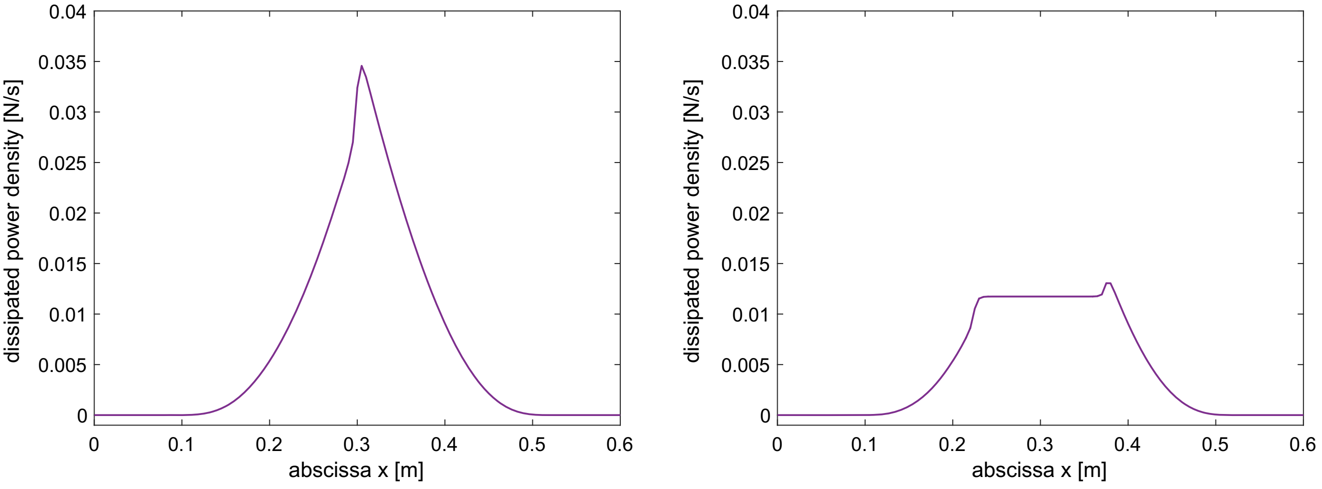

(a) (b)

Fig. 12. Distribution of the dissipated power density $\mathfrak{R}$ for the three-point bending test, in (**a**), and for the four-point configuration, in (**b**), relevant to $\alpha_s = 2.5 \times 10^7$ (N/m). For this value of α_s, the distribution of the power density turns out to be non-symmetric with respect to the center of the beam, exhibiting a stronger dependence on the sign of the shear action T

be able of dissipating the highest amount of energy without decreasing the mechanical stiffness; analogous considerations can be referred to structures subjected to dynamic impact. The present formulation allows one to compare the dissipation capabilities of cementitious elements, for instance, at varying the typology and the percentage of additives.

As a possible improvement, the interactions among the micro-cracks can be investigated on a statistical basis, deducing the energy dissipated by friction. As discussed in [87,88], for moderate crack densities, the interaction effects inside the population of cracks can be approximated assuming that the influence of the

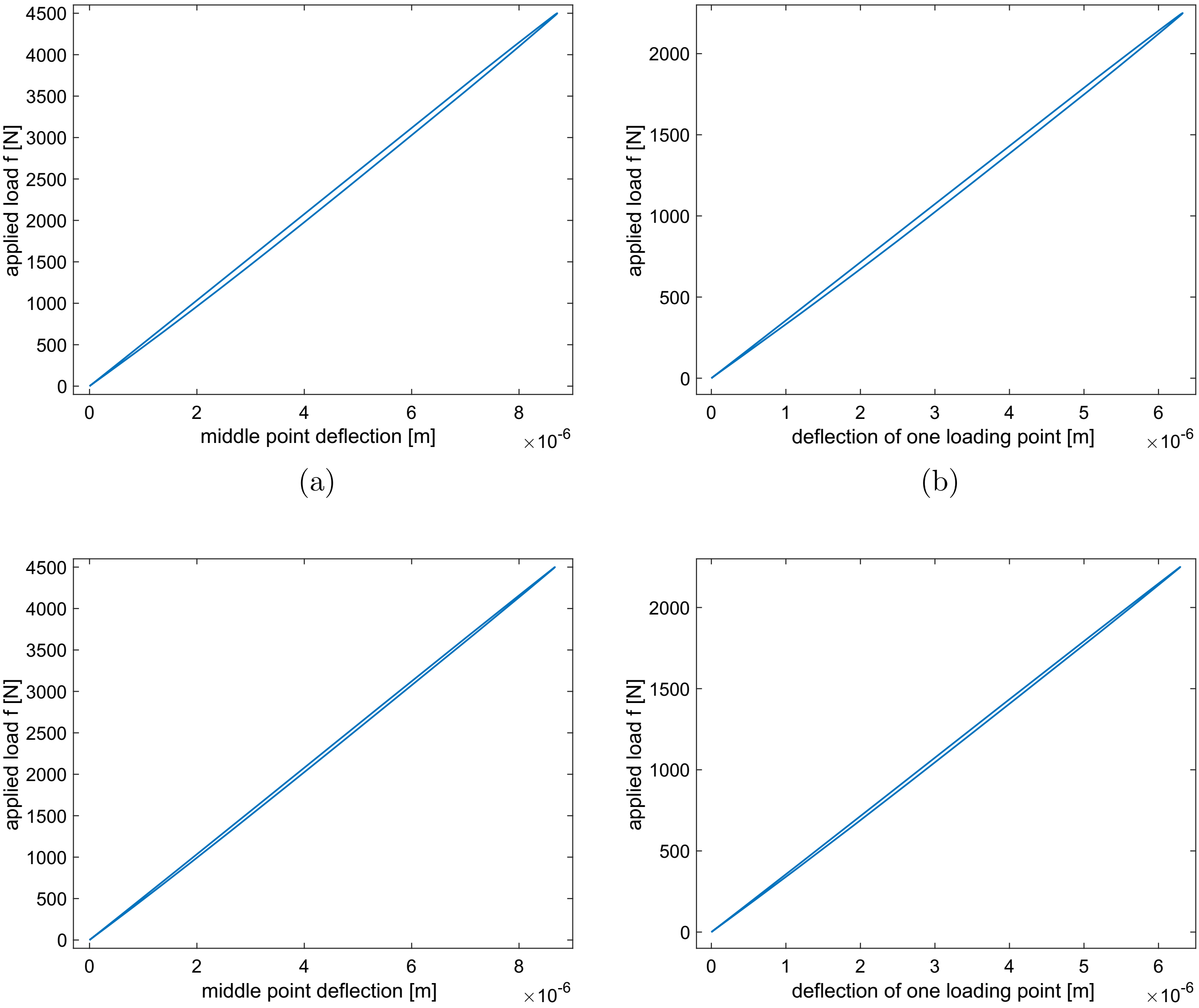

(a) (b)

(c) (d)

FIG. 13. Hysteresis cycles in the three-point bending test, for $k_{m2} = 0$ (N/m^4) and $k_{m2} = 1 \times 10^{20}$ (N/m^4), in (**a**) and (**c**) respectively, and in the four-point bending test, in (**b**) and (**d**) with the corresponding values of k_{m2} on the same row

deformation at one crack on the stress field in the neighborhood of another crack remains spatially uniform (Kachanov model). This model would allow to provide through a micro–macro-approach estimations of the coupling stiffnesses in Eq. (3), to be compared with those identified by inverse analyses on the basis of experimental data at the macroscale. Moreover, by properly describing the growth of the population of micro-cracks as well as the propagation and coalescence of cracks (see, e.g., [89]), also damage and fatigue phenomena can be modeled.

In this scenario, robust identification procedures are required, exploiting sensitivity analysis to realize non-trivial tests and selecting a suitable discrepancy function to minimize. For instance, the response in terms of displacements and rotations predicted by the proposed model can be validated experimentally by means of full-field measurements, see, e.g., [90,91]. As well known, kinematic data within a region of interest can be obtained through multiscale digital image correlation (DIC) techniques by processing digital images monitoring the sample deformation during the tests. Such images can be provided by a single optical camera, and in this case they provide information about plane displacements over the outer flat surface of the sample (2D DIC); alternatively, three dimensional tomographic reconstructions can be acquired within a X-ray tomograp coupled with an “in situ” mechanical apparatus, and in this case they provide information about three dimensional displacements within the bulk of the sample (3D-Volume DIC). As measurable quantities in the identification procedures one could process also the temperature fields provided, for instance, by a thermal imaging camera, since the temperature distribution over the outer surface is expected to be correlated with the dissipated power density generated by the micro-slips. Moreover, recourse can be made to micro–macro computational strategies starting from simplified mechanical assumptions on the meso-structure, apt to compute the stiffnesses appearing in the expression of the energy Eq. (3).

Funding Open access funding provided by Politecnico di Milano within the CRUI-CARE Agreement.

References

[1] Misra, A., Biswas, D., Upadhyaya, S.: Physico-mechanical behavior of self-cementing class C fly ash-clay mixtures. Fuel **84**(11), 1410–1422 (2005). https://doi.org/10.1016/j.fuel.2004.10.018

[2] Contrafatto, L., Danzuso, C.L., Gazzo, S., Greco, L.: Physical, mechanical and thermal properties of lightweight insulating mortar with recycled Etna volcanic aggregates. Constr. Build. Mater. **240**, 117917 (2020). https://doi.org/10.1016/j.conbuildmat.2019.117917

[3] Sclofani, D.A.S., Contrafatto, L.: Experimental behaviour of polyvinyl-alcohol modified concrete. Adv. Mater. Res. **687**, 155–160 (2013). https://doi.org/10.4028/www.scientific.net/AMR.687.155

[4] Spagnuolo, M.: Symmetrization of mechanical response in fibrous metamaterials through micro-shear deformability. Symmetry **14**(12), 2660 (2022). https://doi.org/10.3390/sym14122660

[5] Javili, A., dell’Isola, F., Steinmann, P.: Geometrically nonlinear higher-gradient elasticity with energetic boundaries. J. Mech. Phys. Solids **61**(12), 2381–2401 (2013). https://doi.org/10.1016/j.jmps.2013.06.005

[6] Abhilash, P., Nayak, D.K., Sangoju, B., Kumar, R., Kumar, V.: Effect of nano-silica in concrete: a review. Constr. Build. Mater. **278**, 122347 (2021). https://doi.org/10.1016/j.conbuildmat.2021.122347

[7] Comi, C., Fedele, R., Perego, U.: A chemo-thermo-damage model for the analysis of concrete dams affected by alkali-silica reaction. Mech. Mater. **41**(3), 210–230 (2009). https://doi.org/10.1016/j.mechmat.2008.10.010

[8] Cefis, N., Tedeschi, C., Comi, C.: External sulfate attack in structural concrete made with Portland-limestone cement: an experimental study. Can. J. Civ. Eng. **48**(7), 731–739 (2021). https://doi.org/10.1139/cjce-2019-0354

[9] Scrofani, A., Barchiesi, E., Chiaia, B., Misra, A., Placidi, L.: Fluid diffusion related aging effect in a concrete dam modeled as a Timoshenko beam. Math. Mech. Complex Syst. **11**(2), 313–334 (2023). https://doi.org/10.2140/memocs.2023.11.313

[10] Barchiesi, E., Hamila, N.: Maximum mechano-damage power release-based phase-field modeling of mass diffusion in damaging deformable solids. Z. Angew. Math. Phys. **73**(1), 35 (2022). https://doi.org/10.1007/s00033-021-01668-7

[11] Sangadji, S., Schlangen, E.: Mimicking bone healing process to self repair concrete structure novel approach using porous network concrete. Procedia Engn. **54**, 315–326 (2013). https://doi.org/10.1016/j.proeng.2013.03.029

[12] Bednarczyk, E.I., Lekszycki, T., Glinkowski, W.: Effect of micro-cracks on the angiogenesis and osteophyte development during degenerative joint disease. Comput. Assist. Methods Eng. Sci. **24**(3), 149–156 (2018)

[13] Giorgio, I., Spagnuolo, M., Andreaus, U., Scerrato, D., Bersani, A.M.: In-depth gaze at the astonishing mechanical behavior of bone: a review for designing bio-inspired hierarchical metamaterials. Math. Mech. Solids **26**(7), 1074–1103 (2021). https://doi.org/10.1177/1081286520978516

[14] Xue, J., Briseghella, B., Huang, F., Nuti, C., Tabatabai, H., Chen, B.: Review of ultra-high performance concrete and its application in bridge engineering. Constr. Build. Mater. **260**, 119844 (2020). https://doi.org/10.1016/j.conbuildmat.2018.08.036

[15] Khristenko, U., Schuß, S., Krüger, M., Schmidt, F., Wohlmuth, B., Hesch, C.: Multidimensional coupling: a variationally consistent approach to fiber-reinforced materials. Comput. Methods Appl. Mech. Eng. **382**, 113869 (2021). https://doi.org/10.1016/j.cma.2021.113869

[16] Lamzin, D.A., Bragov, A., Lomunov, A., Konstantinov, A.Y., dell'Isola, F.: Analysis of the dynamic behavior of sand-lime and ceramic bricks. Mater. Phys. Mech. **42**(6), 691 (2019). https://doi.org/10.18720/MPM.4262019_1

[17] Kezmane, A., Chiaia, B., Kumpyak, O., Maksimov, V., Placidi, L.: 3D modelling of reinforced concrete slab with yielding supports subject to impact load. Eur. J. Environ. Civ. Eng. **21**(7–8), 988–1025 (2017). https://doi.org/10.1080/19648189.2016.1194330

[18] Funari, M.F., Spadea, S., Fabbrocino, F., Luciano, R.: A moving interface finite element formulation to predict dynamic edge debonding in FRP-strengthened concrete beams in service conditions. Fibers **8**(6), 42 (2020). https://doi.org/10.3390/fib8060042

[19] Augello, R., Carrera, E., Pagani, A., Arruda, M.R., Shen, J.: Node-dependent kinematic models applied to reinforced concrete structures. Math. Mech. Complex Syst. **11**(1), 19–43 (2023). https://doi.org/10.2140/memocs.2023.11.19

[20] Rezaei, N., Barchiesi, E., Timofeev, D., Tran, C.A., Misra, A., Placidi, L.: Solution of a paradox related to the rigid bar pull-out problem in standard elasticity. Mech. Res. Commun. **126**, 104015 (2022). https://doi.org/10.1016/j.mechrescom.2022.104015

[21] Rezaei, N., Yildizdag, M.E., Turco, E., Misra, A., Placidi, L.: Strain-gradient finite elasticity solutions to rigid bar pull-out test. Contin. Mech. Thermodyn. **36**, 607–617 (2024). https://doi.org/10.1007/s00161-024-01285-5

[22] Pietraszkiewicz, W., Eremeyev, V.A.: On vectorially parameterized natural strain measures of the non-linear Cosserat continuum. Int. J. Solids Struct. **46**(11–12), 2477–2480 (2009). https://doi.org/10.1016/j.ijsolstr.2009.01.030

[23] Giorgio, I., De Angelo, M., Turco, E., Misra, A.: A Biot–Cosserat two-dimensional elastic nonlinear model for a micromorphic medium. Contin. Mech. Thermodyn. **32**(5), 1357–1369 (2020). https://doi.org/10.1007/s00161-019-00848-1

[24] Turco, E., dell'Isola, F., Misra, A.: A nonlinear Lagrangian particle model for grains assemblies including grain relative rotations. Int. J. Numer. Anal. Methods Geomech. **43**(5), 1051–1079 (2019). https://doi.org/10.1002/nag.2915

[25] Spagnuolo, M., Franciosi, P., Dell'Isola, F.: A Green operator-based elastic modeling for two-phase pantographic-inspired bi-continuous materials. Int. J. Solids Struct. **188**, 282–308 (2020). https://doi.org/10.1016/j.ijsolstr.2019.10.018

[26] Ciallella, A., Giorgio, I., Eugster, S.R., Rizzi, N.L., dell'Isola, F.: Generalized beam model for the analysis of wave propagation with a symmetric pattern of deformation in planar pantographic sheets. Wave Motion **113**, 102986 (2022). https://doi.org/10.1016/j.wavemoti.2022.102986

[27] Vaiana, N., Sessa, S., Rosati, L.: A generalized class of uniaxial rate-independent models for simulating asymmetric mechanical hysteresis phenomena. Mech. Syst. Signal Process. **146**, 106984 (2021). https://doi.org/10.1016/j.ymssp.2020.106984

[28] Vaiana, N., Sessa, S., Marmo, F., Rosati, L.: A class of uniaxial phenomenological models for simulating hysteretic phenomena in rate-independent mechanical systems and materials. Nonlinear Dyn. **93**, 1647–1669 (2018). https://doi.org/10.1016/j.cemconres.2016.03.002

[29] Scerrato, D., Giorgio, I., Della Corte, A., Madeo, A., Dowling, N.E., Darve, F.: Towards the design of an enriched concrete with enhanced dissipation performances. Cem. Concr. Res. **84**, 48–61 (2016). https://doi.org/10.1016/j.cemconres.2016.03.002

[30] Cuomo, M.: Forms of the dissipation function for a class of viscoplastic models. Math. Mech. Complex Syst. **5**(3), 217–237 (2017). https://doi.org/10.2140/memocs.2017.5.217

[31] Ciallella, A., Pasquali, D., Gołaszewski, M., D'Annibale, F., Giorgio, I.: A rate-independent internal friction to describe the hysteretic behavior of pantographic structures under cyclic loads. Mech. Res. Commun. **116**, 103761 (2021). https://doi.org/10.1016/j.mechrescom.2021.103761

[32] Giorgio, I., Scerrato, D.: Multi-scale concrete model with rate-dependent internal friction. Eur. J. Environ. Civ. Eng. **21**(7–8), 821–839 (2017). https://doi.org/10.1080/19648189.2016.1144539

[33] dell'Erba, R.: Swarm robotics and complex behaviour of continuum material. Contin. Mech. Thermodyn. **31**(4), 989–1014 (2019). https://doi.org/10.1007/s00161-018-0675-1

[34] Della Corte, A., Battista, A., Dell'Isola, F., Giorgio, I.: Modeling deformable bodies using discrete systems with centroid-based propagating interaction: fracture and crack evolution. In: Dell'Isola, F., Sofonea, M., Steigmann, D. (eds.) Mathematical Modelling in Solid Mechanics. Advanced Structured Materials, vol. 69, pp. 59–88. Springer, Singapore (2017). https://doi.org/10.1007/978-981-10-3764-1_5

[35] Auffray, N., dell'Isola, F., Eremeyev, V.A., Madeo, A., Rosi, G.: Analytical continuum mechanics à la Hamilton–Piola least action principle for second gradient continua and capillary fluids. Math. Mech. Solids **20**(4), 375–417 (2015). https://doi.org/10.1177/1081286513497616

[36] dell'Isola, F., Eugster, S.R., Fedele, R., Seppecher, P.: Second-gradient continua: from Lagrangian to Eulerian and back. Math. Mech. Solids **17**(12), 2715–2750 (2022). https://doi.org/10.1177/10812865221078

[37] Fedele, R.: Third gradient continua: nonstandard equilibrium equations and selection of work conjugate variables. Math. Mech. Solids **27**(10), 2046–2072 (2022). https://doi.org/10.1177/10812865221098966

[38] dell'Isola, F., Andreaus, U., Placidi, L.: At the origins and in the vanguard of peridynamics, non-local and higher-gradient continuum mechanics: an underestimated and still topical contribution of Gabrio Piola. Math. Mech. Solids **20**(8), 887–928 (2015). https://doi.org/10.1177/1081286513509811

[39] Alibert, J.J., Seppecher, P., dell'Isola, F.: Truss modular beams with deformation energy depending on higher displacement gradients. Math. Mech. Solids **8**(1), 51–73 (2003). https://doi.org/10.1177/1081286503008001658

[40] Andreaus, U., dell'Isola, F., Giorgio, I., Placidi, L., Lekszycki, T., Rizzi, N.L.: Numerical simulations of classical problems in two-dimensional (non) linear second gradient elasticity. Int. J. Eng. Sci. **108**, 34–50 (2016). https://doi.org/10.1016/j.ijengsci.2016.08.003

[41] Fedele, R., Placidi, L., Fabbrocino, F.: A review of inverse problems for generalized elastic media: formulations, experiments, synthesis. Contin. Mech. Thermodyn. (2024). https://doi.org/10.1007/s00419-017-1266-5

[42] Giorgio, I., Hild, F., Gerami, E., dell'Isola, F., Misra, A.: Experimental verification of 2D Cosserat chirality with stretch-micro-rotation coupling in orthotropic metamaterials with granular motif. Mech. Res. Commun. **126**, 104020 (2022). https://doi.org/10.1016/j.mechrescom.2022.104020

[43] Fedele, R.: Piola's approach to the equilibrium problem for bodies with second gradient energies. Part I: first gradient theory and differential geometry. Contin. Mech. Thermodyn. **34**, 445–474 (2022). https://doi.org/10.1007/s00161-021-01064-6

[44] Fedele, R.: Approach à la Piola for the equilibrium problem of bodies with second gradient energies. Part II: variational derivation of second gradient equations and their transport. Contin. Mech. Thermodyn. **34**, 1087–1111 (2022). https://doi.org/10.1007/s00161-022-01100-z

[45] La Valle, G., Abali, B.E., Falsone, G., Soize, C.: Sensitivity of a homogeneous and isotropic second-gradient continuum model for particle-based materials with respect to uncertainties. J. Appl. Math. Mech. **103**(10), e202300068 (2023). https://doi.org/10.1002/zamm.202300068

[46] Chróścielewski, J., dell'Isola, F., Eremeyev, V.A., Sabik, A.: On rotational instability within the nonlinear six-parameter shell theory. Int. J. Solids Struct. **196**, 179–189 (2020). https://doi.org/10.1016/j.ijsolstr.2020.04.030

[47] Giorgio, I., Misra, A., Placidi, L.: Geometrically nonlinear Cosserat elasticity with chiral effects based upon granular micromechanics. In: Altenbach, H., Berezovski, A., Dell'Isola, F., Porubov, A. (eds.) Sixty Shades of Generalized Continua. Advanced Structured Materials, vol. 170, pp. 273–292. Springer, Cham (2023). https://doi.org/10.1007/978-3-031-26186-2_17

[48] dell'Isola, F., Madeo, A., Seppecher, P.: Boundary conditions at fluid-permeable interfaces in porous media: a variational approach. Int. J. Solids Struct. **46**(17), 3150–3164 (2009). https://doi.org/10.1016/j.ijsolstr.2009.04.008

[49] Madeo, A., dell'Isola, F., Darve, F.: A continuum model for deformable, second gradient porous media partially saturated with compressible fluids. J. Mech. Phys. Solids **61**(11), 2196–2211 (2013). https://doi.org/10.1016/j.jmps.2013.06.009

[50] Giorgio, I., dell'Isola, F., Andreaus, U., Misra, A.: An orthotropic continuum model with substructure evolution for describing bone remodeling: an interpretation of the primary mechanism behind Wolff's law. Biomech. Model. Mechanobiol. **22**(6), 2135–2152 (2023). https://doi.org/10.1007/s10237-023-01755-w

[51] Fabbrocino, F., Funari, M., Greco, F., Lonetti, P., Luciano, R., Penna, R.: Dynamic crack growth based on moving mesh method. Compos. Part B Eng. **174**, 107053 (2019). https://doi.org/10.1016/j.compositesb.2019.107053

[52] Placidi, L., Misra, A., Barchiesi, E.: Simulation results for damage with evolving microstructure and growing strain gradient moduli. Contin. Mech. Thermodyn. **31**, 1143–1163 (2019). https://doi.org/10.1007/s00161-018-0693-z

[53] Placidi, L., Barchiesi, E., Misra, A.: A strain gradient variational approach to damage: a comparison with damage gradient models and numerical results. Math. Mech. Complex Syst. **6**(2), 77–100 (2018). https://doi.org/10.2140/memocs.2018.6.77

[54] Placidi, L.: A variational approach for a nonlinear one-dimensional damage-elasto-plastic second-gradient continuum model. Contin. Mech. Thermodyn. **28**, 119–137 (2016). https://doi.org/10.1007/s00161-014-0405-2

[55] Luciano, R., Caporale, A., Darban, H., Bartolomeo, C.: Variational approaches for bending and buckling of non-local stress-driven Timoshenko nano-beams for smart materials. Mech. Res. Commun. **103**, 103470 (2020). https://doi.org/10.1016/j.mechrescom.2019.103470

[56] Giorgio, I.: A variational formulation for one-dimensional linear thermoviscoelasticity. Math. Mech. Complex Syst. **9**(4), 397–412 (2022). https://doi.org/10.2140/memocs.2021.9.397

[57] dell'Isola, F., Misra, A.: Principle of virtual work as foundational framework for metamaterial discovery and rational design. C. R Méc. **351**(S3), 1–25 (2023). https://doi.org/10.1016/10.5802/crmeca.151

[58] Bui, N.N., Ngo, M., Nikolic, M., Brancherie, D., Ibrahimbegovic, A.: Enriched Timoshenko beam finite element for modeling bending and shear failure of reinforced concrete frames. Comput. Struct. **143**, 9–18 (2014). https://doi.org/10.1016/j.compstruc.2014.06.004

[59] Endo, M.: Study on an alternative deformation concept for the Timoshenko beam and Mindlin plate models. Int. J. Eng. Sci. **87**, 32–46 (2015). https://doi.org/10.1016/j.ijengsci.2014.11.001

[60] Scerrato, D., Giorgio, I., Madeo, A., Limam, A., Darve, F.: A simple non-linear model for internal friction in modified concrete. Int. J. Eng. Sci. **80**, 136–152 (2014). https://doi.org/10.1016/j.ijengsci.2014.02.02

[61] Aretusi, G., Ciallella, A.: An application of Coulomb-friction model to predict internal dissipation in concrete. In: Marmo, F., Sessa, S., Barchiesi, E., Spagnuolo, M. (eds.) Mathematical Applications in Continuum and Structural Mechanics. Advanced Structured Materials, pp. 73–86. Springer, Cham (2021). https://doi.org/10.1007/978-3-030-42707-8_5

[62] Pensée, V., Kondo, D., Dormieux, L.: Micromechanical analysis of anisotropic damage in brittle materials. J. Eng. Mech. **128**(8), 889–897 (2002). https://doi.org/10.1061/(ASCE)0733-9399(2002)128:8(889)

[63] Fedele, R., Filippini, M., Maier, G.: Constitutive model calibration for railway wheel steel through tension-torsion tests. Comput. Struct. **83**(12), 1005–1020 (2005). https://doi.org/10.1016/j.compstruc.2004.10.006

[64] Fedele, R., Galantucci, L., Ciani, A., Casalegno, V., Ventrella, A., Ferraris, M.: Characterization of innovative CFC/Cu joints by full-field measurements and finite elements. Mat. Sci. Eng. A **595C**, 306–317 (2014). https://doi.org/10.1016/j.msea.2013.12.015

[65] Cefis, N., Fedele, R., Beghi, M.: An integrated methodology to estimate the effective elastic parameters of amorphous TiO_2 nanostructured films, combining SEM images, finite element simulations and homogenization techniques. Mech. Res. Commun. **131**, 104153 (2023). https://doi.org/10.1016/j.mechrescom.2023.104153

[66] Yang, H., Ganzosch, G., Giorgio, I., Abali, B.E.: Material characterization and computations of a polymeric metamaterial with a pantographic substructure. Z. Angew. Math. Phys. **69**, 1–16 (2018). https://doi.org/10.1007/s00033-018-1000-3

[67] Giorgio, I., Harrison, P., dell'Isola, F., Alsayednoor, J., Turco, E.: Wrinkling in engineering fabrics: a comparison between two different comprehensive modelling approaches. Proc. R. Soc. A Math. Phys. Eng. Sci. **474**(2216), 20180063 (2018). https://doi.org/10.1098/rspa.2018.0063

[68] Raveendra, B.R., Benipal, G.S., Singh, A.K.: Constitutive modelling of concrete: an overview. Asian J. Civ. Eng. **6**(4), 211–214 (2005)

[69] Bersani, A.M., Caressa, P.: Lagrangian descriptions of dissipative systems: a review. Math. Mech. Solids **26**(6), 785–803 (2021). https://doi.org/10.1177/1081286520971834

[70] Amir, M., Papakonstantinou, K., Warn, G.: A consistent Timoshenko hysteretic beam finite element model. Int. J. Nonlinear Mech. **119**, 103218 (2020). https://doi.org/10.1016/j.ijnonlinmec.2019.07.003

[71] Ismail, M., Ikhouane, F., Rodellar, J.: The hysteresis Bouc–Wen model, a survey. Arch. Comput. Methods Eng. **16**, 161–188 (2009). https://doi.org/10.1007/s11831-009-9031-8

[72] Ciallella, A., Scerrato, D., Spagnuolo, M., Giorgio, I.: A continuum model based on Rayleigh dissipation functions to describe a Coulomb-type constitutive law for internal friction in woven fabrics. Z. Angew. Math. Phys. **73**(5), 209 (2022). https://doi.org/10.1007/s00033-022-01845-2

[73] User's Guide: COMSOL Multiphysics® v. 6.2. COMSOL AB, Stockholm (2023)

[74] Greco, L., Cuomo, M., Contrafatto, L.: Two new triangular G1-conforming finite elements with cubic edge rotation for the analysis of Kirchhoff plates. Comput. Methods Appl. Mech. Eng. **356**, 354–386 (2019). https://doi.org/10.1016/j.cma.2019.07.026

[75] Greco, L., Castello, D., Cuomo, M.: An objective and accurate G1-conforming mixed Bézier FE-formulation for Kirchhoff–Love rods. Math. Mech. Solids **29**(4), 645–685 (2023). https://doi.org/10.1177/10812865231204972

[76] Eugster, S.R., Harsch, J.: A variational formulation of classical nonlinear beam theories. In: Abali, B., Giorgio, I. (eds.) Developments and Novel Approaches in Nonlinear Solid Body Mechanics. Advanced Structured Materials, vol. 130, pp. 95–121. Springer, Cham (2020). https://doi.org/10.1007/978-3-030-50460-1_9

[77] Balobanov, V., Niiranen, J.: Locking-free variational formulations and isogeometric analysis for the Timoshenko beam models of strain gradient and classical elasticity. Comput. Methods Appl. Mech. Eng. **339**, 137–159 (2018). https://doi.org/10.1016/j.cma.2018.04.028

[78] Giorgio, I.: A discrete formulation of Kirchhoff rods in large-motion dynamics. Math. Mech. Solids **25**(5), 1081–1100 (2020). https://doi.org/10.1177/1081286519900902

[79] Barchiesi, E., dell'Isola, F., Bersani, A.M., Turco, E.: Equilibria determination of elastic articulated duoskelion beams in 2D via a Riks-type algorithm. Int. J. Nonlinear Mech. **128**, 103628 (2021). https://doi.org/10.1016/j.ijnonlinmec.2020.103628

[80] Fedele, R., Maier, G., Miller, B.: Identification of elastic stiffness and local stresses in concrete dams by in situ tests and neural networks. Struct. Infrastruct. Eng. **1**(3), 165–180 (2005). https://doi.org/10.1080/15732470500030513

[81] Abali, B.E., Wu, C.C., Müller, W.H.: An energy-based method to determine material constants in nonlinear rheology with applications. Contin. Mech. Thermodyn. **28**, 1221–1246 (2016). https://doi.org/10.1007/s00161-015-0472-z

[82] De Angelo, M., Placidi, L., Nejadsadeghi, N., Misra, A.: Non-standard Timoshenko beam model for chiral metamaterial: identification of stiffness parameters. Mech. Res. Commun. **103**, 103462 (2020). https://doi.org/10.1016/j.mechrescom.2019.103462

[83] Ciallella, A., La Valle, G., Vintache, A., Smaniotto, B., Hild, F.: Deformation mode in 3-point flexure on pantographic block. Int. J. Solids Struct. **265**, 112129 (2023). https://doi.org/10.1016/j.ijsolstr.2023.112129

[84] Shekarchizadeh, N., Abali, B.E., Barchiesi, E., Bersani, A.M.: Inverse analysis of metamaterials and parameter determination by means of an automatized optimization problem. Z. Angew. Math. Mech. **101**(8), e202000277 (2021). https://doi.org/10.1002/zamm.202000277

[85] Tinoco, M.P., de Andrade Silva, F.: On the mechanical behavior of hybrid fiber reinforced strain hardening cementitious composites subjected to monotonic and cyclic loading. J. Mater. Res. Technol. **11**, 754–768 (2021). https://doi.org/10.1016/j.jmrt.2021.01.053

[86] Crambuer, R., Richard, B., Ile, N., Ragueneau, F.: Experimental characterization and modeling of energy dissipation in reinforced concrete beams subjected to cyclic loading. Eng. Struct. **56**, 919–934 (2013). https://doi.org/10.1016/j.engstruct.2013.06.024

[87] Jang, Y.H., Barber, J.: Frictional energy dissipation in materials containing cracks. J. Mech. Phys. Solids **59**(3), 583–594 (2011). https://doi.org/10.1016/j.jmps.2010.12.010

[88] Li, Y., Tham, L., Wang, Y., Tsui, Y.: A modified Kachanov method for analysis of solids with multiple cracks. Eng. Fract. Mech. **70**(9), 1115–1129 (2003). https://doi.org/10.1016/S0013-7944(02)00096-6

[89] Ray, S., Chandra Kishen, J.: Fatigue crack propagation model for plain concrete: an analogy with population growth. Eng. Fract. Mech. **77**(17), 3418–3433 (2010). https://doi.org/10.1016/j.engfracmech.2010.09.008

[90] Auger, P., Lavigne, T., Smaniotto, B., Spagnuolo, M., dell'Isola, F., Hild, F.: Poynting effects in pantographic metamaterial captured via multiscale DVC. J. Strain Anal. Eng. **56**(7), 462–477 (2021). https://doi.org/10.1177/0309324720976625

[91] Hild, F., Misra, A., dell'Isola, F.: Multiscale DIC applied to pantographic structures. Exp. Mech. **61**, 431–443 (2021). https://doi.org/10.1007/s11340-020-00636-y

Giuliano Aretusi and Antonello Salvatori
Department of Civil, Construction-Architectural and Environmental Engineering
Università dell'Aquila
P.zza Ernesto Pontieri 1, Monteluco di Roio
67100 L'Aquila
Italy

Christian Cardillo
Department of Civil Engineering and Architecture
Università di Catania
Via Santa Sofia, 64
95123 Catania
Italy

Ewa Bednarczyk
Faculty of Mechanical and Industrial Engineering
Warsaw University of Technology
Ludwika Narbutta 85
02-524 Warsaw
Poland

Roberto Fedele
Department of Civil and Environmental Engineering
Politecnico di Milano
Piazza Leonardo da Vinci 32
20133 Milan
Italy
e-mail: roberto.fedele@polimi.it

(Received: April 3, 2024; revised: July 21, 2024; accepted: July 23, 2024)

Chapter 3

A dissipation model for concrete based on an enhanced Timoshenko beam

Chapter abstract

This chapter introduces an advanced Timoshenko beam model that characterizes dissipation in cement-based materials, addressing both bending and axial effects to examine compression and combined compression-flexion phenomena. The model includes a parameter for relative sliding in microcracks, assuming a stable microcrack density under minor deformations. By applying an extended virtual work principle, it considers external loads, internal elasticity, and dissipation due to microcrack interactions, incorporating nonlinear characteristics. Finite element simulations evaluate the mechanical properties under three-point bending and compression, demonstrating energy loss during cyclic loading. A parametric analysis on the amplitude of friction force reveals a non-linear relationship with dissipation, pinpointing an optimal value. This model offers valuable insights into the behavior of cement-based materials, particularly in terms of dissipation, which is essential for structural uses.

Networks and
Heterogeneous Media

https://www.aimspress.com/journal/nhm

NHM, 19(2): 700–723.
DOI: 10.3934/nhm.2024031
Received: 11 May 2024
Revised: 27 June 2024
Accepted: 01 July 2024
Published: 11 July 2024

Research article

A dissipation model for concrete based on an enhanced Timoshenko beam

Giuliano Aretusi[1], Christian Cardillo[2,*], Larry Murcia Terranova[3] and Ewa Bednarczyk[4]

[1] Department of Civil, Construction-Architectural and Environmental Engineering, Università dell'Aquila, L'Aquila 67100, Italy

[2] Department of Civil Engineering and Architecture, Università di Catania, Catania 95100, Italy

[3] Department of Information Engineering, Computer Science and Mathematics, Università dell'Aquila, L'Aquila 67100, Italy

[4] Faculty of Mechanical and Industrial Engineering, Warsaw University of Technology, Warsaw 00-661, Poland

* **Correspondence:** Email: christian.cardillo@phd.unict.it.

Abstract: A novel Timoshenko beam model enriched to account for dissipation in cement-based materials was presented in this paper. The model introduced a new variable representing the relative sliding inside microcracks within the material. In the paper, the microcrack density was not supposed to increase, assuming a small deformation regime that implied no damage growth. The model utilized an expanded version of the principle of virtual work whose contributions came from external forces, internal elastic forces, and dissipation due to the microcrack's microstructure. The elastic energy included terms related to microcrack sliding and micro-macro interactions, accounting for nonlinearity in the material behavior. Numerical simulations, conducted using the finite element method, evaluated the mechanical properties of cement-based materials under three-point flexural tests and compression tests. These tests enabled the assessment of the material dissipative behavior under cyclic loading. Results showed dissipated energy cycles and mechanical responses influenced by the microcrack mechanics. Additionally, a parametric study, varying the friction force amplitude, revealed its impact on dissipated energy. The study highlighted a non-monotonic relationship between friction force amplitude and dissipated energy, with an optimal value maximizing dissipation. Overall, the model provided insights into the mechanics of cement-based materials, particularly regarding dissipation, which was essential for understanding their behavior in structural applications.

Keywords: enhanced Timoshenko beam model; 1D continua with microstructure; microcrack sliding; cement-based materials; dissipated energy

1. Introduction

It is remarkable that despite its widespread use in civil engineering, concrete remains relatively unknown. Indeed, in technical practice, oversimplified models that ignore some essential aspects are used. From ancient times to the present day, human structures have been crafted from concrete, initially comprising rudimentary cement made by crushing and burning gypsum or limestone. Over the course of civil engineering history, concrete has evolved into a sophisticated composite material. Nowadays, concrete is a fundamental construction material that plays a pivotal role in shaping our built environment, providing stability, durability, and versatility in a wide range of construction projects. Ongoing research in concrete technology is crucial for advancing the construction industry, promoting sustainability, enhancing safety, and meeting the evolving demands of our built environment.

Among some of the most significant current research areas concerning concrete, we can summarize the following categories: i) supplementary cementitious materials (SCMs); ii) nanotechnology; iii) self-healing concrete; iv) ultra-high-performance concrete (UHPC); v) digital tools in concrete design.

SCMs are materials like fly ash, slag, and silica fume that can be added to concrete in addition to Portland cement to improve its properties and reduce its carbon footprint [1–3]. By incorporating these SCMs into concrete mixtures, construction professionals can decrease the amount of Portland cement needed, a significant source of carbon emissions in concrete production. This substitution not only improves the technical properties of concrete but also contributes to more sustainable and environmentally friendly construction practices, making it an essential aspect of modern concrete research and construction [4].

Incorporating nanomaterials into concrete formulations represents a promising possibility for enhancing the mechanical properties and longevity of the material. This research area is continually evolving and has the potential to revolutionize the construction industry by producing stronger, more durable, and sustainable concrete structures. Potentially, the inclusions could be nanoparticles [5], fibers [6–8], and suitable complex microstructures enancing the performaces [9–11]. Nanotechnology applied to concrete can improve particle packing and reduce permeability. Nanoparticles are much smaller in size than traditional concrete materials. When incorporated into the concrete mix, they fill in the gaps between larger particles, improving particle packing. This denser packing enhances the concrete's overall strength and reduces porosity, increasing surface area. Nanomaterials, such as nano-silica or nanotubes, have a high surface area-to-volume ratio [12]. This increased surface area allows for better bonding with cement particles and enhances chemical reactions. Moreover, they can be employed to form additional cementitious compounds that contribute to increased strength and durability, increased flexural and compressive strength, and shifting of the mitigation of early-age cracking. Nanomaterials can help mitigate early-age cracking by reducing the heat of hydration, controlling the formation of microcracks, and improving the overall curing process.

Research on self-healing concrete focuses on developing innovative materials and techniques that allow it to repair its cracks autonomously [13]. This area of study is essential for improving the durability and longevity of concrete structures. The idea of self-healing originates from the aim to enhance the performance of building materials like concrete with extra features mimicking the behavior of biological tissues, such as bone (see, e.g., [14, 15] to exploite mechanical properties, and [16–19] for biologocal processes that allow the healing of the tissue). Key aspects of research on self-healing concrete are self-healing mechanisms, healing agents, and microstructural changes. Self-healing concrete typically relies on several mechanisms, including autogenous and encapsulated healing. Autogenous healing occurs when unhydrated cement particles in the presence of water fill small cracks through continued hydration, sealing the crack [20]. Encapsulated healing involves the use of microcapsules containing healing agents embedded in the concrete. When a crack forms, these capsules rupture, releasing healing agents that react and seal the crack [21]. Various healing agents can be embedded in self-healing concrete, such as bacteria, polymers, or organic and inorganic materials. Bacteria-based systems use specially designed bacteria that produce calcium carbonate ($CaCO_3$) when exposed to moisture and oxygen. This $CaCO_3$ seals cracks by precipitating in them. Polymer-based systems rely on the expansion of polymers to seal cracks. These polymers can be embedded within the concrete mix or applied as an external layer. This field of research aims to understand how self-healing affects the microstructure of concrete, ensuring that the healing process does not compromise the overall strength and durability of the material. Techniques like scanning electron microscopy (SEM) and X-ray micro-computed tomography (μ-CT) are used to analyze the effectiveness of self-healing mechanisms.

UHPC is a relatively recent development in the field of concrete technology [22]. It is characterized by its exceptional strength, durability, and unique properties that distinguish it from traditional concrete. UHPC typically comprises a precise blend of materials, including Portland cement, fine quartz or silica fume, very fine sand, high-range water-reducing admixtures, and sometimes steel fibers. The exact mix design can vary but is characterized by the use of outstanding materials and minimal water content.

Moreover, ultra high performance fiber-teinforced concrete (UHP FRC) is an advanced concrete variant that incorporates high-strength fibers to significantly enhance its mechanical and durability properties [23]. Characterized by a compressive strength greater than 150 MPa, UHP FRC surpasses conventional concrete, which typically ranges from 20 to 50 MPa. The inclusion of fibers like steel, glass, or synthetic materials boosts its tensile strength and ductility, enabling it to withstand greater tensile forces and deform more without cracking. UHP FRC features a dense matrix with very low porosity, making it highly resistant to water penetration and chemical attacks. This density is achieved through optimized particle packing and the use of fine powders such as silica fume, fly ash, and superplasticizers. The combination of a dense matrix and high fiber content results in exceptional durability, providing resistance to freeze-thaw cycles, abrasion, and aggressive environments. Typically self-consolidating, UHP FRC flows and fills complex molds without the need for mechanical vibration, facilitating the creation of intricate architectural elements. The components of UHP FRC include high-quality Portland cement as the primary binder, fine aggregates to ensure dense particle packing, silica fume to fill voids and increase strength, superplasticizers to enhance workability and fluidity without increasing water content, and high-strength fibers like steel, glass, polypropylene, or carbon to improve tensile strength and ductility. UHP FRC finds applications in bridges and infrastructure, architectural elements, repair and rehabilitation, and security and defense structures due to its high strength, durability, and impact resistance. Its advantages lie in its superior mechanical properties, exceptional durability, design flexibility, and potential contributions to sustainable construction through reduced material usage and longer lifespan. However, the production of UHP FRC is more costly than conventional concrete, requiring precise mix design, quality control, and specialized knowledge for design and construction. Despite these challenges, UHP FRC stands out as a cutting-edge material suitable for demanding applications in modern construction.

Computer simulations and modeling play a crucial role in designing and optimizing concrete structures. These tools provide technicians and engineers with valuable insights, enabling them to make informed decisions, improve designs, and enhance the overall performance of concrete structures. Computer simulations and modeling provide a comprehensive and detailed understanding of how concrete structures perform in real-world conditions. This knowledge allows for more efficient and sustainable designs, reduced construction costs, improved safety, and enhanced durability, ultimately leading to better-engineered concrete structures. For instance, potential applications of this method include 3D modeling of concrete [24, 25], research focused on optimizing key aspects of concrete performance or its internal structure [26–28], and aided design techniques [29–31].

Fundamentally, it is the internal microstructure of concrete that defines its unique properties. Comprising components like Portland cement, sand, and gravel of various sizes and shapes, concrete is a highly heterogeneous material. Its strength is significantly influenced by factors such as the water-to-cement ratio and the incorporation of additives that chemically or mechanically alter its properties.

Describing the behavior of concrete poses numerous challenges from a modeling perspective. Among these challenges, the key is its nonlinear behavior both at the macro level of observation, in a standard context [32–34], as well as in porous materials [35], and at the microscopic level [36, 37], even under small deformations. The dissipative effects stemming from its microstructure in both elastic and plastic regimes [38] and the evolution of cracks within it [39] are also crucial.

At its core, the microstructure of concrete consists of a matrix formed by the solid phase of the cement paste, interspersed with pieces of inert material of varying sizes. Additionally, the microstructure is further complicated by factors such as chemical species and thermal cycles during curing, which naturally give rise to microcracks within the material. While these microcracks impact the macroscopic behavior of concrete, their effects remain subdued unless subjected to significant external loads [40].

Various models have been explored in the literature to predict concrete behavior. In addition to traditional models like the Cauchy model, alternative approaches within the framework of generalized continua have been investigated. Among them, we recall the second-gradient continua [41–44] or even of higher order [45], micromorphic continua [46–48], and functionally graded materials [49]. These include also Cosserat-type models to account for the presence of stiff aggregates and higher gradient continua to address the material strong heterogeneity (see, e.g., [50–54]).

Furthermore, concrete can be treated as a porous material due to voids formed during the curing process and microcracks [55, 56]. These microcracks, in particular, affect concrete behavior by introducing asymmetry in its mechanical response due to compressive or tensile loads, and generating internal friction under cyclic compressive loads.

Modeling the dissipation in concrete presents a significant challenge. While viscous models are commonly used, they often offer a simplistic linearization of dissipative actions. Alternatively, Coulomb-type friction between microcrack surfaces is proposed as a more appropriate mechanism for dissipative behavior, which remains nearly independent of frequency. Rheological models and thermodynamic frameworks with diffusive internal variables are also employed to address dissipation in solid materials [57–59].

Finally, while this paper primarily focuses on dissipative effects in concrete under small deformations, it is important to acknowledge ongoing research efforts related to plasticity and damage evolution (see, e.g., [60–63]). Variational formulations are favored for their logical consistency and ability to minimize unnecessary assumptions (see, e.g., applications to damage formulation [64–66], buckling [67], internal friction in solid materials [68, 69], and thermoelastic theory [70]). Recent studies explored the use of material particles akin to swarms of robots, offering promising computational efficiency [71].

In summary, this work aims to explore the Coulomb nature of dissipative effects in concrete due to the mechanics of microcracks through numerical simulations obtained for a 1D generalized model, which is an enhanced version of the Timoshenko beam, built upon a previously introduced 3D model [72]. The proposed Timoshenko-like beam is a very efficient and powerful tool for quickly assessing material behavior. This novel beam model shows an improved capability to analyze the behavior of materials under certain circumstances, subsequently providing significant advantages over traditional beam models. In comparison with traditional beam models, this Timoshenko-like beam is more effective in predicting the dissipation in materials that are subjected to cyclic loads, and, as in the standard case, it is capable of more accurately predicting the effects of shear deformation. As a result of these improvements, the Timoshenko-like beam model can provide engineers and researchers with greater insight into the behavior of materials and allow them to make more informed decisions when designing structures and mechanical components.

2. The micromorphic beam model

The present section concerns a planar 1D model of a cement-based beam that can be described primarily by a reference curve $\mathscr{C}^*$ in the plane xy, which lies on the x-axis in its undeformed configuration and whose length is L. The current configuration of the beam, $\mathscr{C}$, is represented by the map $\boldsymbol{\chi}$, which depends on a generic S-abscissa, as illustrated in Figure 1. To this end, we propose to enlarge the standard kinematical description used in the Timoshenko model with a further descriptor that is able to take into account, to some extent, the sliding effect of the opposite faces of microcracks within the cement matrix [38, 72, 73]. Since we consider the small displacement and small deformation regime, we assume that the density of microcracks remains the same throughout the tests; thus, no damage evolution occurs. The fundamental kinematic assumption in the Timoshenko model is that, although the conservation of plane cross-sections and their rigidity apply, the orthogonality between the axial beam line and the cross-section is not retained. This refers to the hypothesis in which the influence of shear distortion on the beam deformation is not neglected [74]. The complete kinematical description of the system configuration is specified by means of the kinematic variables: u, v, φ, and γ. Expressly, these kinematical descriptors represent the longitudinal and transverse displacement of the beam axis, the cross-section rotation, and an average inner relative sliding between the opposite faces of microcracks, respectively. The first three variables are characteristic of the classical Timoshenko model accounting for extension, while the novel-introduced variable is assumed to be a scalar field since, as a first approximation, we can postulate that no preferential direction characterizes the microcracks and a random distribution of their orientation is in place [72, 75]. Thus, we define the map $\boldsymbol{\chi}$ as:

$$\boldsymbol{\chi} := \begin{cases} \boldsymbol{r} = \begin{cases} x = S + u(S) \\ y = v(S) \end{cases} \\ \hat{\varphi} = \varphi(S) \\ \hat{\gamma} = \gamma(S), \end{cases} \tag{2.1}$$

where the vector $\boldsymbol{r}$ specifies the position of the material particles lying on the axial line of the beam, and $\hat{\varphi}$ and $\hat{\gamma}$ are the characteristic features that describe the essential properties of the microstructure, i.e., the orientation of the cross-section and the sliding in the microcracks.

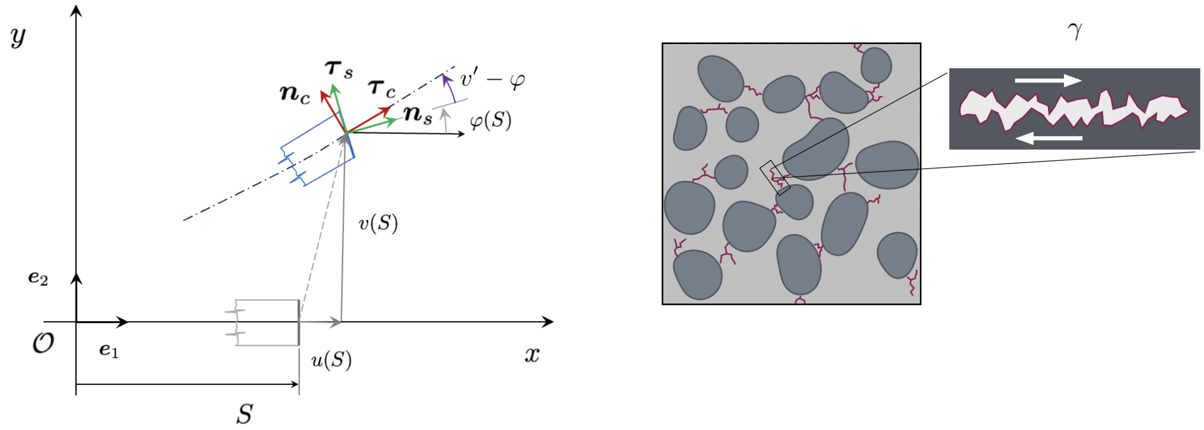

Figure 1. Kinematic descriptors of the beam (on the left); scheme of the microcrack microstructure of the beam material (on the right). $\boldsymbol{\tau}_c$ and $\boldsymbol{n}_c$ are the tangent and normal unit vectors to the axial curve of the beam, while $\boldsymbol{\tau}_s$ and $\boldsymbol{n}_s$ are the tangent and normal unit vectors to the beam cross-section. The red lines on the concrete section represent the microcracks; thus, γ can be interpreted as a descriptor of micro-slip accumulation within the material.

In order to characterize the behavior of the considered system, we employ an expanded version of the principle of virtual work (PVW). This principle states that, at equilibrium, the virtual work exerted by the external forces applied to the system, denoted by $\delta\mathcal{W}^{ext}$, must balance the virtual work performed by the internal contact forces, namely, $\delta\mathcal{W}^{el}$ for the conservative part associated with the elastic deformation, as well as any virtual work dissipated within the system, $\tilde{\delta}\mathcal{D}$, for the same virtual displacements; therefore, we consider the extended principle of virtual work as follows:

$$\delta\mathcal{W}^{el} + \tilde{\delta}\mathcal{D} = \delta\mathcal{W}^{ext}, \tag{2.2}$$

neglecting the inertial effects since we consider low-frequency applications of the materials. In this extended version of the variational principle, it is important to note that the dissipative contribution is not calculated as the first variation of $\mathcal{D}$. As a result, we use a different symbol, $\tilde{\delta}$, to account for the Rayleigh extension of Lagrangian formalism for dissipation.

The inner virtual work related to the elastic deformation is evaluated starting from a plausible expression of an elastic deformation energy based on the abovementioned kinematic variables:

$$\begin{aligned}\mathcal{W}^{el} = &\int_0^L \frac{1}{2}\mathrm{k}_b\,(\varphi')^2\,\mathrm{d}S + \int_0^L \frac{1}{2}\mathrm{k}_s\,(v'-\varphi)^2\,\mathrm{d}S + \int_0^L \frac{1}{2}\mathrm{k}_e\,(u')^2\,\mathrm{d}S +\\ &+ \int_0^L \frac{1}{2}\mathrm{k}_{m2}\,\gamma^2\mathrm{d}S + \int_0^L \frac{1}{4}\mathrm{k}_{m4}\,\gamma^4\mathrm{d}S +\\ &- \int_0^L \alpha_b\,\gamma\,\varphi'\mathrm{d}S - \int_0^L \alpha_s\,\gamma\,(v'-\varphi)\,\mathrm{d}S - \int_0^L \alpha_e\,\gamma u'\mathrm{d}S,\end{aligned} \tag{2.3}$$

where the material parameters k_b, k_s, k_e, k_{m2}, and k_{m4} are stiffnesses, while α_b, α_s, and α_e are coupling coefficients; all these parameters have to be determined by a micro-macro identification and validated with experimental tests. This elastic energy represents the energy stored in a material due to deformation, therefore, it must be inherently positive because it represents the ability of the material to do work when it returns to its original shape. To ensure that the postulated energy $\mathcal{W}^{el}$ is positive definite, then, we can assume that the coefficients satisfy the following inequalities:

$$\mathrm{k}_b > 0, \quad \mathrm{k}_s > 0, \quad \mathrm{k}_e > 0, \quad \mathrm{k}_b\mathrm{k}_e\mathrm{k}_s\mathrm{k}_{m2} - \alpha_s^2\mathrm{k}_b\mathrm{k}_e - \alpha_e^2\mathrm{k}_b\mathrm{k}_s - \alpha_b^2\mathrm{k}_e\mathrm{k}_s > 0, \quad \mathrm{k}_{m4} > 0. \tag{2.4}$$

The first three contributions of the energy (2.3) represent the classical constitutive behavior of the extensible Timoshenko model. They are representative of the bending, the shear, and the elongation energy that can be stored in the beam. The other contributions newly introduced in (2.3), are linked to the energy associated with the microcracks. In particular, the terms quadratic and quartic in γ are the amount of elastic energy that can be stored in the microcracks. The idea behind that is related to the specific morphology of the microcracks. From a geometric perspective, ideally, a microcrack can be visualized as a coin-shaped empty space. The microcrack consists of two faces or lips on opposite sides, which delimit the crack. Each lip of the microcrack exhibits asperities that may interact when the two lips on the opposite side of a crack come into contact (see Figure 1). When this occurs, these asperities can bend and, therefore, store a certain amount of elastic energy. We postulate a material nonlinearity with the quartic term on the ground that many experimental observations show a macroscopic nonlinear behavior in cement-based materials even at the small displacement and deformation regime [76]. The last three contributions of Eq (2.3) stand for the coupling energy exchanged between the macroscopic bending deformation and the microscopic asperity deformation within the microcracks, between the macroscopic shear distortion of the beam and the asperity deformation, as well as between the macroscopic elongation of the beam and the asperity deformation. Naturally, we can assume that a bending, a shear, or a change-of-length deformation of the beam could be responsible for the sliding of the microcrack lips. We have to remark, though, that the effect of such a sliding is noticeable only if the opposite faces of the microcracks are pushed against each other. This means that this effect becomes significant only in the case of compression. When bending and shear deformation are activated, only the part of the cross-section interested in compression is affected by such a phenomenon. On the contrary, the tensile part is free from this type of energy exchange. However, since the model is mono-dimensional, we cannot distinguish between the compressed and stretched parts of the cross-section, and thus, we have only to consider whether or not a compressed region exists. Consequently, whenever the beam bends, it produces a compressed region, and, hence, we can imagine that this phenomenon can be activated in this simple 1D context. The virtual work exerted by the inner forces is straightforwardly computed by the first variation of the elastic energy (2.3) as:

$$\begin{aligned}\delta\mathcal{W}^{el} = &\int_0^L \mathrm{k}_b\,\varphi'\,\delta\varphi'\,\mathrm{d}S + \int_0^L \mathrm{k}_s\,(v'-\varphi)\,\delta\,(v'-\varphi)\,\mathrm{d}S + \int_0^L \mathrm{k}_e\,u'\,\delta u'\,\mathrm{d}S + \\ &+ \int_0^L \mathrm{k}_{m2}\gamma\,\delta\gamma\,\mathrm{d}S + \int_0^L \mathrm{k}_{m4}\gamma^3\,\delta\gamma\,\mathrm{d}S - \int_0^L \alpha_b\,(\varphi'\,\delta\gamma + \gamma\,\delta\varphi')\,\mathrm{d}S + \\ &- \int_0^L \alpha_s\,[(v'-\varphi)\,\delta\gamma + \gamma\,\delta\,(v'-\varphi)]\,\mathrm{d}S - \int_0^L \alpha_e\,(u'\,\delta\gamma + \gamma\,\delta u')\,\mathrm{d}S,\end{aligned} \tag{2.5}$$

and, by performing an integration by parts, we can rearrange the contributions of the internal elastic energy as follows:

$$
\begin{aligned}
\delta\mathcal{W}^{el} = &-\int_0^L \Big[(\mathrm{k}_b\varphi')' + \mathrm{k}_s\,(v'-\varphi) - (\alpha_b\gamma)' - \alpha_s\gamma\Big]\,\delta\varphi\,\mathrm{d}S \;+\; (\mathrm{k}_b\varphi' - \alpha_b\gamma)\;\delta\varphi\Big|_0^L +\\
&-\int_0^L \Big[(\mathrm{k}_e u')' - (\alpha_e\gamma)'\Big]\,\delta u\,\mathrm{d}S \;+\; (\mathrm{k}_e u' - \alpha_e\gamma)\;\delta u\Big|_0^L +\\
&+\int_0^L \Big[\mathrm{k}_{m2}\gamma + \mathrm{k}_{m4}\gamma^3 - \alpha_b\,\varphi' - \alpha_s\,(v'-\varphi) - \alpha_e\,u'\Big]\,\delta\gamma\,\mathrm{d}S +\\
&-\int_0^L \Big\{[\mathrm{k}_s\,(v'-\varphi)]' - (\alpha_s\,\gamma)'\Big\}\,\delta v\,\mathrm{d}S \;+\; [\mathrm{k}_s\,(v'-\varphi) - \alpha_s\gamma]\,\delta v\Big|_0^L. \qquad (2.6)
\end{aligned}
$$

In order to model the process of dissipation, we take into account the virtual work carried out by the friction force applied at the microcrack face level, as follows:

$$
\tilde{\delta\mathcal{D}} = \int_0^L \zeta_b\,|\varphi'|\tanh(\eta\dot{\gamma})\,\delta\gamma\,\mathrm{d}S \;+\; \int_0^L \zeta_c\,\varsigma_C|u'|\tanh(\eta\dot{\gamma})\,\delta\gamma\,\mathrm{d}S. \qquad (2.7)
$$

The parameters ζ_b and ζ_c are related to the friction coefficient for the bending deformation and the compression, respectively. The appearance of the absolute value of the derivative of the angle of rotation $|\varphi'|$ in the first contribution of Eq (2.7) is due to the fact that when a cross-section undergoes a change in rotation, this can lead to a compression that closes the microcracks, at least in some parts of the cross-section. On the other hand, in the second integral, we consider the term $|u'|$, which represents a uniform compression within the cross-section that allows the microcracks to be closed. We have to remark that if the term $|u'|$ is originated by a tensile case, the dissipated energy associated with the second contribution must be erased from the model because there is no interaction between the microcrack asperities. For this reason, we introduce the boolean variable ς_C that assumes the value 1 for compression and 0 for traction. The concept of friction force could be accurately modeled with a Coulomb behavior. However, due to the non-Lipschitz continuity of the forcing term (a sign function), we lose the uniqueness of the solution. To overcome this challenge, a smoother version of the sign function, namely, the ‘tanh’-term has been developed to mimic the Coulomb behavior while avoiding the issue mentioned above. This approach has proven to be effective in ensuring the accuracy of simulations and models in a variety of contexts. Moreover, it introduces a viscous behavior for small velocity $\dot{\gamma}$ which could be beneficial in some context, without mentioning that with the slope η, we can control the feature tuning of the mechanical response on the basis of experimental observations. Here, for the sake of simplicity, we consider the same value of η for both contributions in Eq (2.7). For a comprehensive understanding of the formulation of the dissipative term, refer to [77–79].

The virtual work of external forces and torques can be expressed as:

$$
\delta\mathcal{W}^{ext} = \int_0^L b_x(S)\,\delta u\,\mathrm{d}S \;+\; F_x\delta u|_0^L + \int_0^L b_y(S)\,\delta v\,\mathrm{d}S \;+\; F_y\delta v\Big|_0^L + \int_0^L \mu(S)\,\delta\varphi\,\mathrm{d}S \;+\; W\delta\varphi|_0^L\,, \qquad (2.8)
$$

where we admit distributed forces b_x and b_y in the x-direction and y-direction as well as torques μ per unit length, point forces F_x and F_y in the x-direction and y-direction, as well as torques W applied at both ends, compatible with the energy (2.3).

By substituting the expressions (2.6)–(2.8) in the principle (2.2), the bulk equations are deduced as below:

$$\begin{cases} -\left[\mathrm{k}_e u'\right]' + (\alpha_e\,\gamma)' = b_x \\ -\left[\mathrm{k}_s\,(v' - \varphi)\right]' + (\alpha_s\,\gamma)' = b_y \\ -\left[(\mathrm{k}_b\varphi')' + \mathrm{k}_s\,(v' - \varphi) - (\alpha_b\gamma)' - \alpha_s\gamma\right] = \mu \\ \quad \mathrm{k}_{m2}\gamma + \mathrm{k}_{m4}\gamma^3 - \alpha_b\,\varphi' - \alpha_s\,(v' - \varphi) - \alpha_e\,u' = -\zeta_b\,|\varphi'|\tanh(\eta\dot{\gamma}) - \zeta_c\,\varsigma_C|u'|\tanh(\eta\dot{\gamma}), \end{cases} \tag{2.9}$$

alongside the essential boundary conditions related to the values of u, v, and φ and the natural boundary conditions associated with the axial force, the shear force, and the bending moment:

$$N = \mathrm{k}_e u' - \alpha_e\gamma, \qquad T = \mathrm{k}_s\,(v' - \varphi) - \alpha_s\gamma, \qquad M = \mathrm{k}_b\varphi' - \alpha_b\gamma, \tag{2.10}$$

respectively. We remark that from the deduction of the PVW, no boundary condition is provided for the variable γ since, in the energy, this quantity does not appear with the spatial derivative. Naturally, in the actual concrete sample, we do not have access to the microcracks, so we cannot give any boundary conditions on that level.

3. Numerical simulations

To evaluate the mechanical properties of cement-based materials, three-point flexural tests and compression tests are performed through numerical simulations to assess the predictive properties of the proposed model. The main advantage of these tests is the ease of specimen preparation and testing as well as widely available testing equipment. In the bending tests, a sample (in the shape of a parallelepiped of side $d \times d \times L$, namely, 25 × 25 × 87.5 cm) is placed on two supports positioned at a distance of $\ell = 75$ cm from each other, and a force is applied at the center on the top. These setups create a scenario where the material is subjected to both tension and compression, allowing for the measurement of various mechanical properties. The compression tests are instead performed on a cylindrical sample with a diameter ϕ of 11.28 cm and a height L of 22 cm. In particular, hereby, we are interested in evaluating the dissipative behavior of the specimen.

Table 1. Values of the coefficients used as a reference in the three-point flexural tests for the prism specimen.

k_b	k_s	k_e	k_{m2}	k_{m4}
1.023×10^7 N m^2	7.121×10^8 N	1.544×10^9 N	7.5×10^8 N/m^2	1.0×10^8 N/m^4
α_b	α_s	α_e	ζ_b	ζ_c
2.764×10^7 N	2.5×10^6 N/m	1.25×10^8 N/m	3.68×10^8 N	2.212×10^8 N/m

Table 2. Values of the coefficients used as a reference in the compression tests for the cylindrical specimen.

k_b	k_s	k_e	k_{m2}	k_{m4}
2.499×10^5 N m^2	1.366×10^8 N	3.143×10^8 N	7.5×10^8 N/m^2	1.0×10^8 N/m^4
α_b	α_s	α_e	ζ_b	ζ_c
9.48×10^6 N	2.5×10^6 N/m	1.25×10^8 N/m	3.68×10^6 N	2.212×10^8 N/m

The numerical computations are carried out using the commercial software COMSOL Multiphysics®, which enabled the direct use of Eq (2.2) with the weak form partial differential equation (PDE) package. Since a generalized continuum model of the first gradient in the kinematical descriptors is employed, we opted for the standard Lagrangian quadratic polynomials as the shape functions for the finite element interpolation. It is worth noting that said shape functions are particularly suited for such a formulation involving, at most, only the first derivative of the kinematical descriptors. For further details regarding the numerical implementation of similar problems, we refer the interested reader to [80, 81] for the isogeometric analysis and [82–85] for lumped models.

Specifically, we assumed for the considered material a Young modulus, $Y_c = 31.45$ GPa, and a Poisson ratio $\nu = 0.15$. Using the isotropic material symmetry the shear modulus is, thus, $G_c = Y_c/[2\,(1+\nu)]$. This information can be used to evaluate the classical stiffnesses for the bending $k_b = Y_c\,J$, being J the second moment of area of the beam cross-section and for the shear stiffness $k_s = 5/6\,G_c\,d^2$ for the three-point bending test, while $k_s = G_c\,\pi\,(\phi/2)^2$ is the expression considered in the cylinder specimen. The stiffness due to the stretching/compression deformation $k_e = Y_c\,A_c$, where A_c is the area of the cross-section. The slope characterizing the dissipative behavior in Eq (2.7) is set to be $\eta = 225$ s/m. To summarize, all values needed for the simulations are reported in Tables 1 and 2 for the bending and compression tests, respectively. The process of identifying all the necessary parameters that characterize the model can pose a significant challenge due to the complex mechanical responses that must be considered. However, it is pertinent to note that specific techniques commonly used for complex generalized materials, such as digital image correlation (DIC), energy methods, and neural networks, can also be applied in this context. These methods have proven to be effective tools in similar situations, as evidenced by their successful application in previous studies (see, for instance, references [86–95]). To analyze the dissipation, an external cyclic force with a sinusoidal trend is applied to the sample, as follows:

$$f(t) = \begin{cases} \frac{F_p}{2}\left[1-\cos\left(\pi f_q\,t\right)\right] & \forall t < t_s = 1/f_q \\ F_p + \frac{F_0}{2}\left[1-\cos\left(2\pi f_q\,t\right)\right] & \forall t \geq t_s, \end{cases} \tag{3.1}$$

where the amplitude of oscillation is F_0, and F_p is a small force set to ensure the adhesion and the closure of the microcracks with a pre-compression originated by the specific test (in the compression test, it is uniform, while in the bending test, it is related only to half part of the cross-section, where actually the dissipation occurs); in the numerical simulations, we set its value to $F_p = 0.1\,F_0$. The time $t_s = 0.1$ s defines the interval of application of the initial ramp of amplitude F_p (see Figure 2). The value of F_0 has been meticulously selected to mitigate any potential growth of microcracks. The force magnitude applied during the two tests was appropriately small to ensure reliable and accurate results. Specifically, $F_0 = 100$ kN for the compression tests and $F_0 = 15$ kN for the three point bending tests. The frequency f_q of the sinusoidally varying contribution is set to 10 Hz.

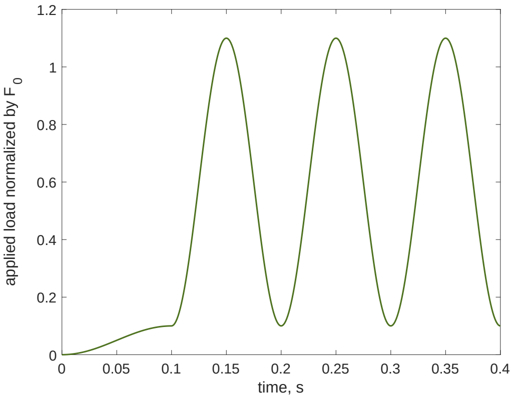

Figure 2. Normalized force applied to the samples for the cyclic tests.

4. Results and Discussion

The mechanical responses obtained performing finite-element-method-based numerical simulations are collected and discussed in this section. To begin, we consider two tests, the three-point and the compression one, with assumed reference parameters (see Tables 1 and 2) that allow us to mimic with reasonable accuracy the known experimental behavior of a building beam made of plain concrete. In addition to these reference cases, here we explore the influence of some crucial parameters, especially concerning the dissipative behavior of the material.

Figure 3 shows a cycle of loading and unloading for the two tests, namely, the three-point bending test and the compression test. Therefore, we can compare the two cases. The pictures display the external load versus the displacement of the loading point. The cycle area has been computed using a numerical approximated integral exploiting the trapezoidal rule. For the three-point bending test, we get a dissipated energy of 0.0074 J, and for the compression test, we evaluate a dissipated energy of 0.1699 J.

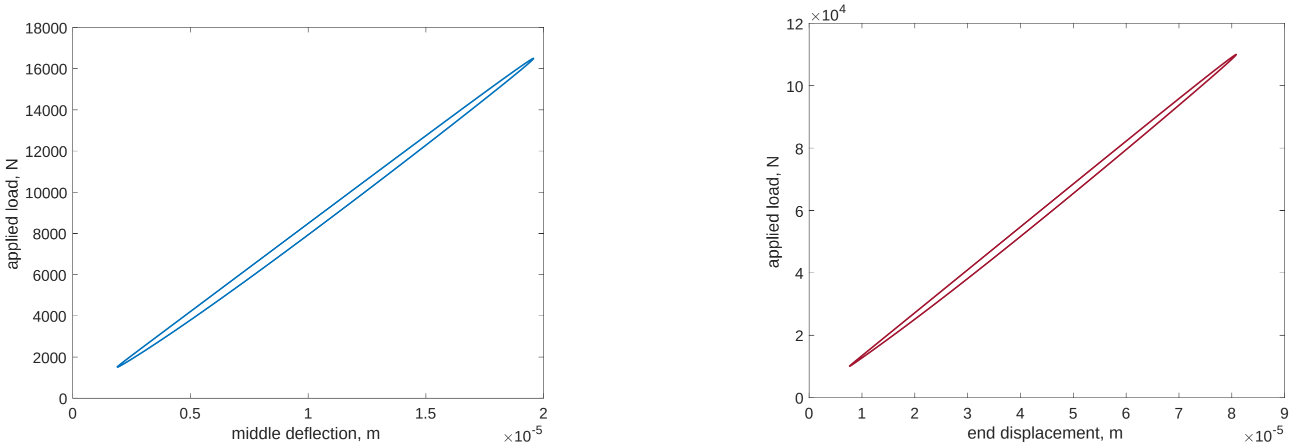

(a) **(b)**

Figure 3. Dissipative cycles for the three-point flexural test (a), and the compression test (b).

In order to provide a comprehensive understanding of the analyzed phenomenon, Figures 4 and 5 depict the time histories of the relative slip variable γ and the friction forces, $\zeta_b|\varphi'|\tanh(\eta\dot{\gamma})$ and $\zeta_c\,\varsigma_C|u'|\tanh(\eta\dot{\gamma})$, at the points of maximum load, respectively. These observations were made in the center of the beam during the three-point bending test and at the point where the load was applied in the compression test. It is worth noting that the behavior of these variables related to the mechanics of the microcracks is nonlinear; thus, we might expect nonlinear behavior even at the microscopic level.

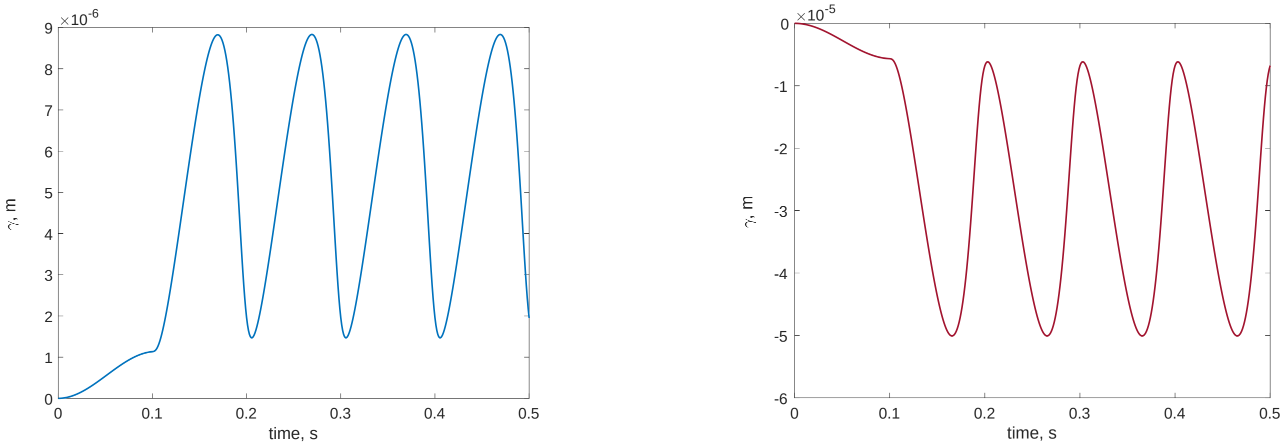

(a) **(b)**

Figure 4. Time history of the relative sliding, γ for the three-point flexural test at the middle point (a), and for the compression test at the loading point (b).

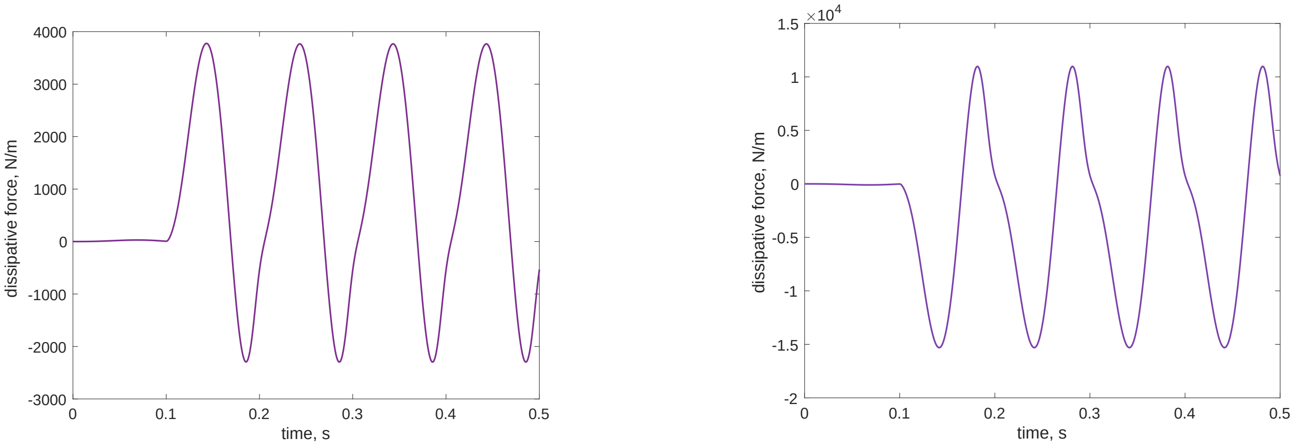

(a) **(b)**

Figure 5. Time history of the friction force, $\zeta_b|\varphi'|\tanh(\eta\dot{\gamma})$, for the three-point flexural test at the middle point (a), and $\zeta_c\,\varsigma_C|u'|\tanh(\eta\dot{\gamma})$ for the compression test at the loading point (b).

The relative sliding at the level of microcracks, γ are depicted in Figure 6 at the time instant of about 0.15 s corresponding to a maximum in the load amplitude. For the three-point flexural test, the new variable γ has significant values only in the portion of the beam where there is a flexural deformation, which, in turn, is directly related to compression in half of the cross-section, where the microcracks close and, due to some distortions in the shape of the beam, we can experience some sliding at that level of observation. For the compression test, instead, we observe that γ is constant since the compression is as such.

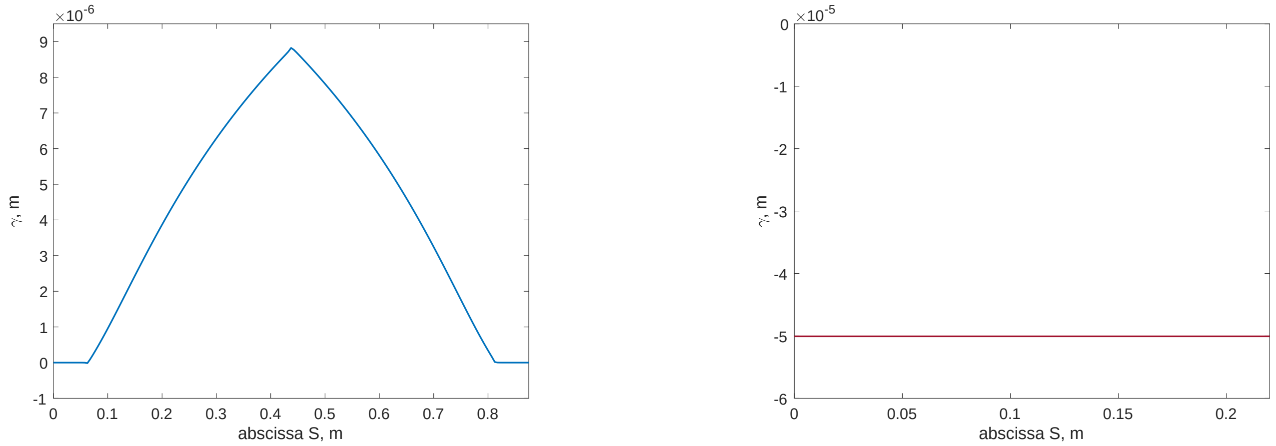

(a)

Figure 6. The relative sliding at the level of microcracks γ at one maximum value of the force at about 0.15 s, for the three-point flexural test (a) and for the compression test (b).

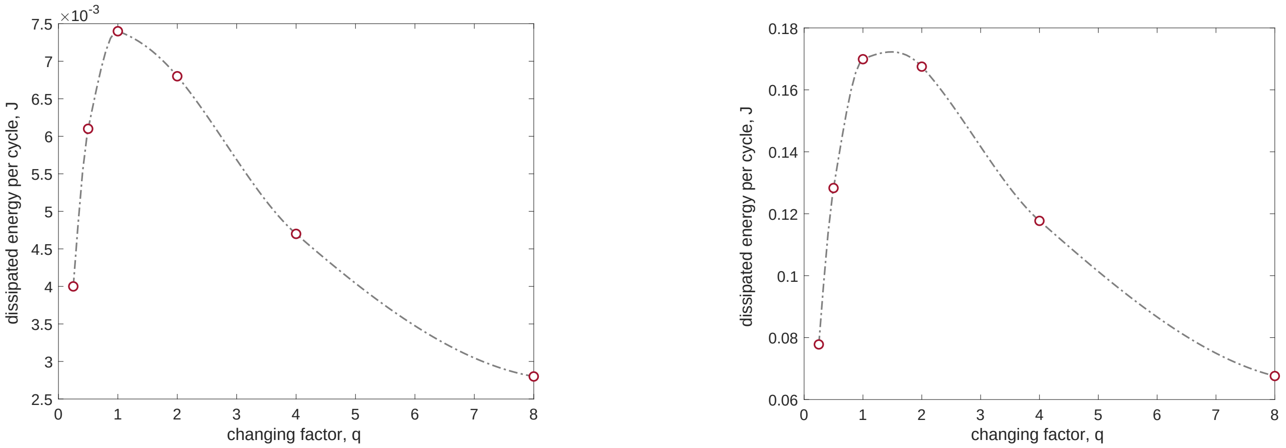

(a) **(b)**

Figure 7. Influence of the parameters ζ_b and ζ_c on the dissipative cycles for the three-point flexural test (a), and the compression test (b), respectively.

In order to obtain a more comprehensive understanding of the model outcomes, a parametric study is conducted. Specifically, we vary the amplitude of the friction force, denoted by ζ_b and ζ_c, by employing a scale factor, q. This approach allows us to investigate the effects of altering the frictional force on the model performance and overall behavior. Through this study, we are able to draw meaningful conclusions that can inform future research and improve our understanding of the mechanisms underlying the model. Figure 7 shows the results of such a parametric study. In fact, for different multiplying factors q, specifically $\{0.25, 0.5, 2, 4, 8\}$, we compute the loading-unloading cycles for the two categories of tests and evaluate the area of the cycles, i.e., the lost energy of the system. We get the dissipated energy $\{0.0040, 0.0061, 0.0074, 0.0068, 0.0047, 0.0028\}$ J for the three-point bending tests and larger values $\{0.0778, 0.1283, 0.1699, 0.1675, 0.1177, 0.0676\}$ J for the compression tests. These results are summarized in a plot in Figure 7. The dotted lines are regressed curves made from each series of six simulations made for the considered tests. The simulations of both tests show the same trend, highlighting the presence of a maximum of dissipated energy. This behavior is typical of phenomena with two competitive aspects. In this case, we have that with low friction forces, the energy dissipated is little; in this range, if the friction coefficient is increased, more energy is dissipated. On the other hand, when the friction force is too large, the relative motion of the microcrack faces becomes increasingly smaller as the friction force increases, and, therefore, the dissipated energy inevitably decreases. Consequently, it is possible to determine a friction coefficient such as to have the maximum dissipated energy in this framework. From the perspective of engineering the cementitious material, this aspect is crucial since acting only on increasing the friction coefficient within the microcracks can even be counterproductive if the friction effect is exaggerated.

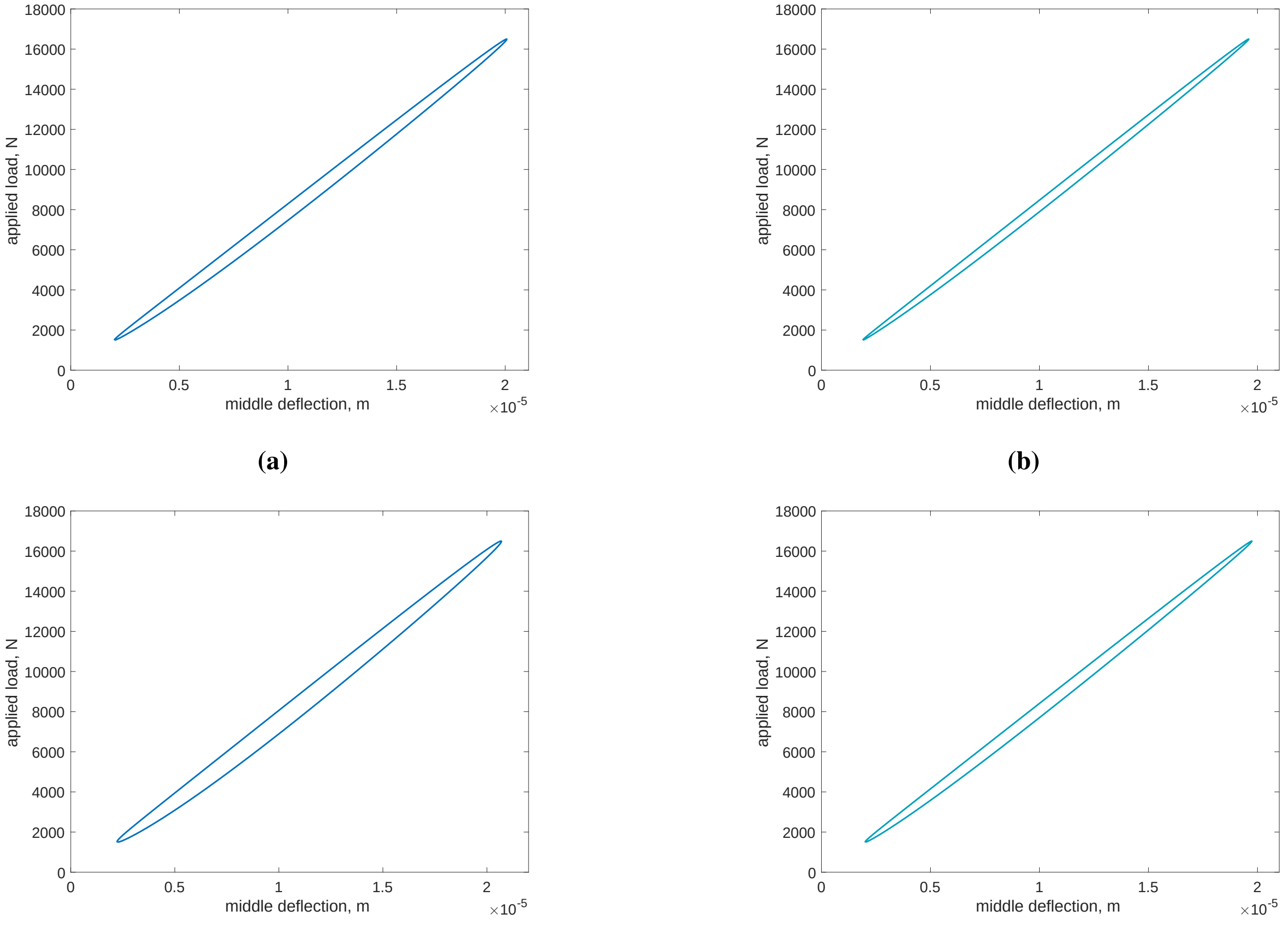

(a) **(b)**

(c) **(d)**

Figure 8. Influence of the parameter α_b on the dissipative cycles for the three-point flexural test with an amplifier factor of 1.2 (a) and 1.4 (c), and of α_s with 2 amplification (b), and 4 amplification (d).

Turning our focus to the coupling parameters, we analyze the effect of the coefficient α_b increasing its value by 20 and 40% with respect to the reference value. Figure 8 presents the dissipative cycles obtained via simulations conducted for the previously considered tests. The plots depicted in the figure show that increasing the coupling α_b results in a more considerable dissipation. For the three-point flexural test, we evaluate a dissipated energy of 0.0114 and 0.0167 J, respectively, when the coupling increases by 20 and 40%. The same analysis has been conducted for the coupling coefficient α_s. However, since this coefficient is less significant in the overall behavior, it is observed that with the same changes with respect to the reference case, the dissipation is almost the same. Therefore, the shear coupling has been increased by 100 and 200%, in the case of the three-point flexural test, resulting in a dissipation of energy of 0.0078 and 0.0097 J, respectively (see Figure 8). Overall, the general trend is the same but less effective.

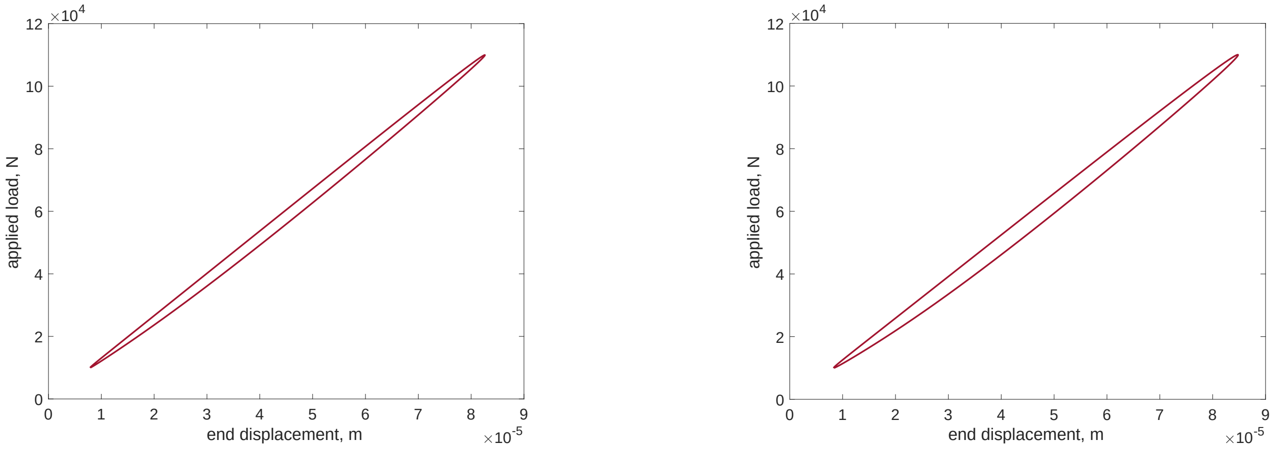

(a)

(b)

Figure 9. Influence of the parameter α_e on the dissipative cycles for the compressive test with an amplifier factor of 1.2 (a) and 1.4 (b).

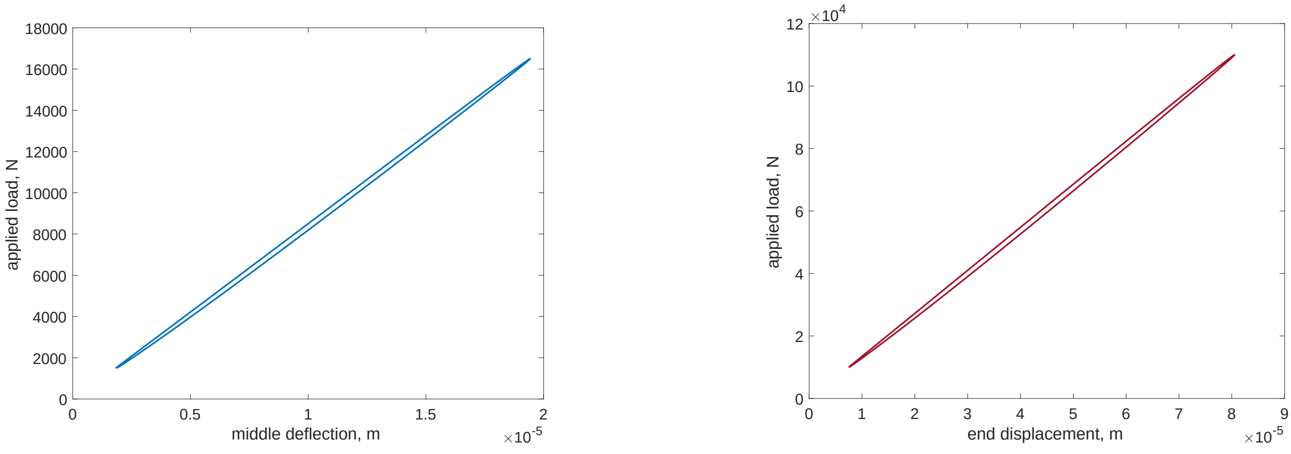

(a)

(b)

Figure 10. Influence of the parameter k_{m4} on the dissipative cycles for the three-point flexural test (a), and the compression test (b).

Similarly, in the compression test, we obtain 0.2554 J and 0.36589 J of dissipated energy for a 20 and 40% increase in the the coupling α_e, respectively (see Figure 9).

Therefore, in designing a building material to be earthquake-proof, i.e., capable of dissipating as much energy as possible, it seems very promising to concentrate our attention on those additives that increase these coupling coefficients without jeopardizing the mechanical strength and pursuing the optimal friction coefficient that provides the maximum level of dissipation simultaneously.

Finally, regarding the nonlinear stiffness k_{m4}, we carry out simulations to explore the influence of such a parameter. Figure 10 shows the dissipative cycles obtained by setting high values of k_{m4}. The dissipated energy obtained is 0.0043 J for the three-point flexural test with $k_{m4} = 1 \times 10^{19}$ N/m^4. Meanwhile, for the compression test, 0.1210 J of energy is dissipated in the loading-unloading cycle with $k_{m4} = 1 \times 10^{17}$ N/m^4. Thus, a greater stiffening of the asperities leads to a decrease in the energy dissipated.

5. Conclusions

In this paper, we propose a Timoshenko beam model augmented with a microcrack sliding descriptor that provides a promising framework for describing the mechanical behavior of cement-based materials. It is a very effective and efficient modeling tool that provides a beneficial computational advantage in evaluating both the strength of the material and also its dissipative behavior. Indeed, by introducing the variable γ to represent the relative sliding of microcracks within the material, the model captures additional dissipative mechanisms that contribute to energy loss during loading-unloading cycles.

Finite element method-based numerical simulations conducted using COMSOL Multiphysics demonstrated the effectiveness of the model in replicating experimental tests. The simulations revealed the influence of various parameters on the mechanical response of the material, including the dissipated energy and the behavior of kinematic descriptors such as longitudinal and transverse displacement, cross-section orientation, and relative sliding at microcracks.

A parametric study investigating the effects of altering the frictional force parameters provided insights into the relationship between frictional forces and energy dissipation. The study revealed a nonlinear relationship between these parameters and dissipated energy, with an optimal frictional force value maximizing energy dissipation.

The model predictions align well with known experimental behavior observed in flexural and compression tests of cement-based materials. This validation underscores the model ability to capture the complex mechanical response of such materials under loading and unloading conditions.

The insights gained from this study can inform the design and optimization of cement-based structures, particularly in applications where energy dissipation and mechanical resistance are critical factors, for example, in the case of earthquakes. By accurately modeling the dissipation mechanisms within the material, engineers can develop more resilient and durable structures.

Further research could focus on refining the model by incorporating additional complexities, such as heterogeneities in material properties and multi-axial loading conditions. Additionally, experimental validation of the model predictions using a wider range of test configurations and material compositions would enhance its applicability and robustness.

Overall, the study underscores the importance of considering microstructural phenomena, such as microcrack sliding, in developing accurate models for predicting the mechanical behavior of cement-based materials. By integrating such phenomena into computational models, researchers can advance our understanding of material behavior and contribute to the development of more resilient and sustainable infrastructure solutions.

Author contributions

G.A., C.C., L.M.T. and E.B.: Conceptualization, Idealization, Methodology, Formal Analysis, Numerical Simulation, Writing. E.B.: Supervision, Revising.

Use of AI tools declaration

The authors declare they have not used Artificial Intelligence (AI) tools in the creation of this article.

Conflict of interest

The authors declare that they have no conflict of interest.

References

1. A. Misra, Stabilization characteristics of clays using class C fly ash, *Transp. Res. Rec.*, **1611** (1998), 46–54. https://doi.org/10.3141/1611-06
2. D. A. S. Sclofani, L. Contrafatto, Experimental behaviour of polyvinyl-alcohol modified concrete, *Adv. Mater. Res.*, **687** (2013), 155–160. https://doi.org/10.4028/www.scientific.net/AMR.687.155
3. L. Contrafatto, 8-Volcanic ash, in *Sustainable Concrete Made with Ashes and Dust from Different Sources*, (eds. R. Siddique and R. Belarbi), Elsevier, (2022), 331–418. https://doi.org/10.1016/B978-0-12-824050-2.00011-5
4. L. Contrafatto, R. Cosenza, R. Barbagallo, S. Ognibene, Use of recycled aggregates in road sub-base construction and concrete manufacturing, *Ann. Geophys.*, **61** (2018), SE223. https://doi.org/10.4401/ag-7785
5. G. Goel, P. Sachdeva, A. K. Chaudhary, Y. Singh, The use of nanomaterials in concrete: A review, *Mater. Today Proc.*, **69** (2022), 365–371. https://doi.org/10.1016/j.matpr.2022.09.051
6. P. Franciosi, M. Spagnuolo, O. U. Salman, Mean Green operators of deformable fiber networks embedded in a compliant matrix and property estimates, *Continuum Mech. Thermodyn.*, **31** (2019), 101–132. https://doi.org/10.1007/s00161-018-0668-0
7. M. Spagnuolo, Symmetrization of mechanical response in fibrous metamaterials through micro-shear deformability, *Symmetry*, **14** (2022), 2660. https://doi.org/10.3390/sym14122660
8. M. Spagnuolo, P. Franciosi, F. Dell'Isola, A Green operator-based elastic modeling for two-phase pantographic-inspired bi-continuous materials, *Int. J. Solids Struct.*, **188** (2020), 282–308. https://doi.org/10.1016/j.ijsolstr.2019.10.018
9. I. Giorgio, N. L. Rizzi, E. Turco, Continuum modelling of pantographic sheets for out-of-plane bifurcation and vibrational analysis, *Proc. R. Soc. A*, **473** (2017), 1–21. https://doi.org/10.1098/rspa.2017.0636

10. E. Turco, M. Golaszewski, I. Giorgio, F. D'Annibale, Pantographic lattices with non-orthogonal fibres: Experiments and their numerical simulations, *Composites, Part B*, **118** (2017), 1–14. https://doi.org/10.1016/j.compositesb.2017.02.039

11. E. Turco, I. Giorgio, A. Misra, F. Dell'Isola, King post truss as a motif for internal structure of (meta) material with controlled elastic properties, *R. Soc. Open Sci.*, **4** (2017), 171153. https://doi.org/10.1098/rsos.171153

12. P. P. Abhilash, D. K. Nayak, B. Sangoju, R. Kumar, V. Kumar, Effect of nano-silica in concrete; a review, *Constr. Build. Mater.*, **278** (2021), 122347. https://doi.org/10.1016/j.conbuildmat.2021.122347

13. N. De Belie, E. Gruyaert, A. Al-Tabbaa, P. Antonaci, C. Baera, D. Bajare, et al., A review of self-healing concrete for damage management of structures, *Adv. Mater. Interfaces*, **5** (2018), 1800074. https://doi.org/10.1002/admi.201800074

14. S. Sangadji, E. Schlangen, Mimicking bone healing process to self repair concrete structure novel approach using porous network concrete, *Procedia Eng.*, **54** (2013), 315–326. https://doi.org/10.1016/j.proeng.2013.03.029

15. A. Casalotti, F. D'annibale, G. Rosi, Multi-scale design of an architected composite structure with optimized graded properties, *Composite Structures*, **252** (2020), 112608. https://doi.org/10.1016/j.compstruct.2020.112608

16. T. Lekszycki, F. Dell'Isola, A mixture model with evolving mass densities for describing synthesis and resorption phenomena in bones reconstructed with bio-resorbable materials, *ZAMM Z. Angew. Math. Mech.*, **92** (2012), 426–444. https://doi.org/10.1002/zamm.201100082

17. E. I. Bednarczyk, T. Lekszycki, W. Glinkowski, Effect of micro-cracks on the angiogenesis and osteophyte development during degenerative joint disease, *Comput. Assisted Methods Eng. Sci.*, **24** (2018), 149–156. http://doi.org/10.24423/cames.191

18. I. Giorgio, F. Dell'Isola, U. Andreaus, F. Alzahrani, T. Hayat, T. Lekszycki, On mechanically driven biological stimulus for bone remodeling as a diffusive phenomenon, *Biomech. Model. Mechanobiol.*, **18** (2019), 1639–1663. https://doi.org/10.1007/s10237-019-01166-w

19. I. Giorgio, F. Dell'Isola, U. Andreaus, A. Misra, An orthotropic continuum model with substructure evolution for describing bone remodeling: an interpretation of the primary mechanism behind Wolff's law, *Biomech. Model. Mechanobiol.*, **22** (2023), 2135–2152. https://doi.org/10.1007/s10237-023-01755-w

20. M. Rajczakowska, K. Habermehl-Cwirzen, H. Hedlund, A. Cwirzen, Autogenous self-healing: A better solution for concrete, *J. Mater. Civ. Eng.*, **31** (2019), 03119001. https://doi.org/10.1061/(ASCE)MT.1943-5533.0002764

21. M. E. Espitia-Nery, D. E. Corredor-Pulido, P. A. Castaño-Oliveros, J. A. Rodríguez-Medina, Q. Y. Ordoñez-Bello, M. S. Pérez-Fuentes, Mechanisms of encapsulation of bacteria in self-healing concrete, *Dyna*, **86** (2019), 17–22. https://doi.org/10.15446/dyna.v86n210.75343

22. J. Xue, B. Briseghella, F. Huang, C. Nuti, H. Tabatabai, B. Chen, Review of ultra-high performance concrete and its application in bridge engineering, *Constr. Build. Mater.*, **260** (2020), 119844. https://doi.org/10.1016/j.conbuildmat.2020.119844

23. L. Placidi, F. Dell'Isola, A. Kandalaft, R. Luciano, C. Majorana, A. Misra, A granular micromechanic-based model for Ultra High Performance Fiber-Reinforced Concrete (UHP FRC), *Int. J. Solids Struct.*, **297** (2024), 112844. https://doi.org/10.1016/j.ijsolstr.2024.112844
24. V. Nguyen-Van, B. Panda, G. Zhang, H. Nguyen-Xuan, P. Tran, Digital design computing and modelling for 3-D concrete printing, *Autom. Constr.*, **123** (2021), 103529. https://doi.org/10.1016/j.autcon.2020.103529
25. A. Kezmane, B. Chiaia, O. Kumpyak, V. Maksimov, L. Placidi, 3D modelling of reinforced concrete slab with yielding supports subject to impact load, *Eur. J. Environ. Civ. Eng.*, **21** (2017), 988–1025. https://doi.org/10.1080/19648189.2016.1194330
26. A. Casalotti, F. D'Annibale, G. Rosi, Optimization of an architected composite with tailored graded properties, *Z. Angew. Math. Phys.*, **75** (2014), 126. https://doi.org/10.1007/s00033-024-02255-2
27. I. Giorgio, A. Ciallella, D. Scerrato, A study about the impact of the topological arrangement of fibers on fiber-reinforced composites: Some guidelines aiming at the development of new ultra-stiff and ultra-soft metamaterials, *Int. J. Solids Struct.*, **203** (2020), 73–83. https://doi.org/10.1016/j.ijsolstr.2020.07.016
28. A. Ciallella, F. D'Annibale, D. Del Vescovo, I. Giorgio, Deformation patterns in a second-gradient lattice annular plate composed of "spira mirabilis" fibers, *Continuum Mech. Thermodyn.*, **35** (2023), 1561–1580. https://doi.org/10.1007/s00161-022-01169-6
29. T. Wangler, N. Roussel, F. P. Bos, T. A. M. Salet, R. J. Flatt, Digital concrete: A review, *Cem. Concr. Res.*, **123** (2019), 105780. https://doi.org/10.1016/j.cemconres.2019.105780
30. N. Rezaei, E. Barchiesi, D. Timofeev, C. A. Tran, A. Misra, L. Placidi, Solution of a paradox related to the rigid bar pull-out problem in standard elasticity, *Mech. Res. Commun.*, **126** (2022), 104015. https://doi.org/10.1016/j.mechrescom.2022.104015
31. M. F. Funari, S. Spadea, F. Fabbrocino, R. Luciano, A moving interface finite element formulation to predict dynamic edge debonding in FRP-strengthened concrete beams in service conditions, *Fibers*, **8** (2020), 42. https://doi.org/10.3390/fib8060042
32. W. Pietraszkiewicz, V. A. Eremeyev, On vectorially parameterized natural strain measures of the non-linear Cosserat continuum, *Int. J. Solids Struct.*, **46** (2009), 2477–2480. https://doi.org/10.1016/j.ijsolstr.2009.01.030
33. G. La Valle, A new deformation measure for the nonlinear micropolar continuum, *Z. Angew. Math. Phys.*, **73** (2022), 78. https://doi.org/10.1007/s00033-022-01715-x
34. I. Giorgio, A. Misra, L. Placidi, Geometrically nonlinear Cosserat elasticity with chiral effects based upon granular micromechanics, in *Sixty Shades of Generalized Continua*, (eds. H. Altenbach, A. Berezovski, F. Dell'Isola and A. Porubov), Springer, **170** (2023), 273–292. https://doi.org/10.1007/978-3-031-26186-2_17
35. I. Giorgio, M. De Angelo, E. Turco, A. Misra, A Biot–Cosserat two-dimensional elastic nonlinear model for a micromorphic medium, *Continuum Mech. Thermodyn.*, **32** (2020), 1357–1369. https://doi.org/10.1007/s00161-019-00848-1

36. E. Turco, F. Dell'Isola, A. Misra, A nonlinear Lagrangian particle model for grains assemblies including grain relative rotations, *Int. J. Numer. Anal. Methods Geomech.*, **43** (2019), 1051–1079. https://doi.org/10.1002/nag.2915

37. E. Turco, Forecasting nonlinear vibrations of patches of granular materials by elastic interactions between spheres, *Mech. Res. Commun.*, **122** (2022), 103879. https://doi.org/10.1016/j.mechrescom.2022.103879

38. D. Scerrato, I. Giorgio, A. Della Corte, A. Madeo, N. E. Dowling, F. Darve, Towards the design of an enriched concrete with enhanced dissipation performances, *Cem. Concr. Res.*, **84** (2016), 48–61. https://doi.org/10.1016/j.cemconres.2016.03.002

39. A. Scrofani, E. Barchiesi, B. Chiaia, A. Misra, L. Placidi, Fluid diffusion related aging effect in a concrete dam modeled as a Timoshenko beam, *Math. Mech. Complex Syst.*, **11** (2023), 313–334. https://doi.org/10.2140/memocs.2023.11.313

40. I. Giorgio, D. Scerrato, Multi-scale concrete model with rate-dependent internal friction, *Eur. J. Environ. Civ. Eng.*, **21** (2017), 821–839. https://doi.org/10.1080/19648189.2016.1144539

41. G. Jouan, P. Kotronis, F. Collin, Using a second gradient model to simulate the behaviour of concrete structural elements, *Finite Elem. Anal. Des.*, **90** (2014), 50–60. https://doi.org/10.1016/j.finel.2014.06.002

42. P. Germain, The method of virtual power in the mechanics of continuous media, I: Second-gradient theory, *Math. Mech. Complex Syst.*, **8** (2020), 153–190. https://doi.org/10.2140/memocs.2020.8.153

43. G. La Valle, B. E. Abali, G. Falsone, C. Soize, Sensitivity of a homogeneous and isotropic second-gradient continuum model for particle-based materials with respect to uncertainties, *ZAMM Z. Angew. Math. Mech.*, **103** (2023), e202300068. https://doi.org/10.1002/zamm.202300068

44. F. Dell'Isola, S. R. Eugster, R. Fedele, P. Seppecher, Second-gradient continua: From Lagrangian to Eulerian and back, *Math. Mech. Solids*, **27** (2022), 2715–2750. https://doi.org/10.1177/10812865221078822

45. F. Dell'Isola, U. Andreaus, L. Placidi, At the origins and in the vanguard of peridynamics, non-local and higher-gradient continuum mechanics: an underestimated and still topical contribution of Gabrio Piola, *Math. Mech. Solids*, **20** (2015), 887–928. https://doi.org/10.1177/1081286513509811

46. A. Berezovski, I. Giorgio, A. D. Corte, Interfaces in micromorphic materials: Wave transmission and reflection with numerical simulations, *Math. Mech. Solids*, **21** (2016), 37–51. https://doi.org/10.1177/1081286515572244

47. M. Golaszewski, R. Grygoruk, I. Giorgio, M. Laudato, F. D. Cosmo, Metamaterials with relative displacements in their microstructure: Technological challenges in 3D printing, experiments and numerical predictions, *Continuum Mech. Thermodyn.*, **31** (2019), 1015–1034. https://doi.org/10.1007/s00161-018-0692-0

48. A. Ciallella, I. Giorgio, S. R. Eugster, N. L. Rizzi, F. Dell'Isola, Generalized beam model for the analysis of wave propagation with a symmetric pattern of deformation in planar pantographic sheets, *Wave Motion*, **113** (2022), 102986. https://doi.org/10.1016/j.wavemoti.2022.102986

49. O. Szlachetka, I. Giorgio, Heat conduction in multi-component step-wise FGMs, *Continuum Mech. Thermodyn.*, (2024), 1–19. https://doi.org/10.1007/s00161-024-01296-2

50. V. A. Eremeyev, W. Pietraszkiewicz, Material symmetry group and constitutive equations of micropolar anisotropic elastic solids, *Math. Mech. Solids*, **21** (2016), 210–221. https://doi.org/10.1177/1081286515582862
51. G. La Valle, S. Massoumi, A new deformation measure for micropolar plates subjected to in-plane loads, *Continuum Mech. Thermodyn.*, **34** (2022), 243–257. https://doi.org/10.1007/s00161-021-01055-7
52. I. Giorgio, F. Dell'Isola, A. Misrav, Chirality in 2D Cosserat media related to stretch-micro-rotation coupling with links to granular micromechanics, *Int. J. Solids Struct.*, **202** (2020), 28–38. https://doi.org/10.1016/j.ijsolstr.2020.06.005
53. I. Giorgio, F. Hild, E. Gerami, F. Dell'Isola, A. Misra, Experimental verification of 2D Cosserat chirality with stretch-micro-rotation coupling in orthotropic metamaterials with granular motif, *Mech. Res. Commun.*, **126** (2022), 104020. https://doi.org/10.1016/j.mechrescom.2022.104020
54. G. La Valle, C. Soize, A higher-order nonlocal elasticity continuum model for deterministic and stochastic particle-based materials, *Z. Angew. Math. Phys.*, **75** (2024). https://doi.org/10.1007/s00033-024-02196-w
55. A. Madeo, F. Dell'Isola, F. Darve, A continuum model for deformable, second gradient porous media partially saturated with compressible fluids, *J. Mech. Phys. Solids*, **61** (2013), 2196–2211. https://doi.org/10.1016/j.jmps.2013.06.009
56. F. Dell'Isola, A. Madeo, P. Seppecher, Boundary conditions at fluid-permeable interfaces in porous media: A variational approach, *Int. J. Solids Struct.*, **46** (2009), 3150–3164. https://doi.org/10.1016/j.ijsolstr.2009.04.008
57. I. Giorgio, A variational formulation for one-dimensional linear thermoviscoelasticity, *Math. Mech. Complex Syst.*, **9** (2022), 397–412. https://doi.org/10.2140/memocs.2021.9.397
58. E. Barchiesi, N. Hamila, Maximum mechano-damage power release-based phase-field modeling of mass diffusion in damaging deformable solids, *Z. Angew. Math. Phys.*, **73** (2022). https://doi.org/10.1007/s00033-021-01668-7
59. A. Ramírez-Torres, R. Penta, A. Grillo, Effective properties of fractional viscoelastic composites via two-scale asymptotic homogenization, *Math. Methods Appl. Sci.*, **46** (2023), 16500–16520. https://doi.org/10.1002/mma.9457
60. L. Placidi, E. Barchiesi, Energy approach to brittle fracture in strain-gradient modelling, *Proc. R. Soc. A*, **474** (2018), 20170878. https://doi.org/10.1098/rspa.2017.0878
61. F. Fabbrocino, M. F. Funari, F. Greco, P. Lonetti, R. Luciano, R. Penna, Dynamic crack growth based on moving mesh method, *Composites, Part B*, **174** (2019), 107053. https://doi.org/10.1016/j.compositesb.2019.107053
62. C. Comi, R. Fedele, U. Perego, A chemo-thermo-damage model for the analysis of concrete dams affected by alkali-silica reaction, *Mech. Mater.*, **41** (2009), 210–230. https://doi.org/10.1016/j.mechmat.2008.10.010

63. A. Bilotta, A. Morassi, E. Turco, Simple convolutional neural networks for the damage identification in composite steel-concrete beams, in *International Conference on Experimental Vibration Analysis for Civil Engineering Structures*, Springer, **433** (2023), 422–431. https://doi.org/10.1007/978-3-031-39117-0_43

64. L. Placidi, A variational approach for a nonlinear one-dimensional damage-elasto-plastic second-gradient continuum model, *Continuum Mech. Thermodyn.*, **28** (2016), 119–137. https://doi.org/10.1007/s00161-014-0405-2

65. L. Placidi, E. Barchiesi, A. Misra, A strain gradient variational approach to damage: A comparison with damage gradient models and numerical results, *Math. Mech. Complex Syst.*, **6** (2018), 77–100. https://doi.org/10.2140/memocs.2018.6.77

66. L. Placidi, A. Misra, E. Barchiesi, Simulation results for damage with evolving microstructure and growing strain gradient moduli, *Continuum Mech. Thermodyn.*, **31** (2019), 1143–1163. https://doi.org/10.1007/s00161-018-0693-z

67. R. Luciano, A. Caporale, H. Darban, C. Bartolomeo, Variational approaches for bending and buckling of non-local stress-driven Timoshenko nano-beams for smart materials, *Mech. Res. Commun.*, **103** (2020), 103470. https://doi.org/10.1016/j.mechrescom.2019.103470

68. Ciallella, A and Pasquali, D and Gołaszewski, M and D'Annibale, F and Giorgio, I, A rate-independent internal friction to describe the hysteretic behavior of pantographic structures under cyclic loads, *Mech. Res. Commun.*, **116** (2021), 103761.

69. A. Ciallella, D. Pasquali, M. Gołaszewski, F. D'Annibale, I. Giorgio, Shear rupture mechanism and dissipation phenomena in bias-extension test of pantographic sheets: Numerical modeling and experiments, *Math. Mech. Solids*, **27** (2022), 2170–2188. https://doi.org/10.1016/j.mechrescom.2021.103761

70. I. Giorgio, L. Placidi, A variational formulation for three-dimensional linear thermoelasticity with 'thermal inertia', *Meccanica*, (2024). https://doi.org/10.1007/s11012-024-01796-0

71. A. Battista, L. Rosa, R. Dell'Erba, L. Greco, Numerical investigation of a particle system compared with first and second gradient continua: Deformation and fracture phenomena, *Math. Mech. Solids*, **22** (2017), 2120–2134. https://doi.org/10.1177/1081286516657889

72. D. Scerrato, I. Giorgio, A. Madeo, A. Limam, F. Darve, A simple non-linear model for internal friction in modified concrete, *Int. J. Eng. Sci.*, **80** (2014), 136–152. https://doi.org/10.1016/j.ijengsci.2014.02.021

73. D. Scerrato, I. Giorgio, A. Della Corte, A. Madeo, A. Limam, A micro-structural model for dissipation phenomena in the concrete, *Int. J. Numer. Anal. Methods Geomech.*, **39** (2015), 2037–2052. https://doi.org/10.1002/nag.2394

74. I. Giorgio, M. Spagnuolo, L. Greco, F. D'Annibale, A. Cazzani, A variational approach to address the problem of planar nonlinear beams, in *Comprehensive Mechanics of Materials*, (eds. V. Silberschmidt), Elsevier, **1** (2024), 67–97. https://doi.org/10.1016/B978-0-323-90646-3.00027-7

75. V. Pensée, D. Kondo, L. Dormieux, Micromechanical analysis of anisotropic damage in brittle materials, *J. Eng. Mech.*, **128** (2002), 889–897. https://doi.org/10.1061/(ASCE)0733-9399(2002)128:8(889)

76. B. R. Raveendra, G. S. Benipal, A. K. Singh, Constitutive modelling of concrete: An overview, *Asian J. Civ. Eng.*, **6** (2005), 211–214.
77. A. M. Bersani, P. Caressa, F. Dell'Isola, Approximation of dissipative systems by elastic chains: Numerical evidence, *Math. Mech. Solids*, **28** (2023), 501–520. https://doi.org/10.1177/10812865221081851
78. A. M. Bersani, P. Caressa, A. Ciallella, Numerical evidence for the approximation of dissipative systems by gyroscopically coupled oscillator chains, *Math. Mech. Complex Syst.*, **10** (2022), 265–278. https://doi.org/10.2140/memocs.2022.10.265
79. A. Ciallella, D. Scerrato, M. Spagnuolo, I. Giorgio, A continuum model based on Rayleigh dissipation functions to describe a Coulomb-type constitutive law for internal friction in woven fabrics, *Z. Angew. Math. Phys.*, **73** (2022). https://doi.org/10.1007/s00033-022-01845-2
80. L. Greco, M. Cuomo, L. Contrafatto, Two new triangular G1-conforming finite elements with cubic edge rotation for the analysis of Kirchhoff plates, *Comput. Methods Appl. Mech. Eng.*, **356** (2019), 354–386. https://doi.org/10.1016/j.cma.2019.07.026
81. L. Greco, D. Castello, M. Cuomo, An objective and accurate G1-conforming mixed Bézier FE-formulation for Kirchhoff–Love rods, *Math. Mech. Solids*, **29** (2024), 645–685. https://doi.org/10.1177/10812865231204972
82. I. Giorgio, A discrete formulation of Kirchhoff rods in large-motion dynamics, *Math. Mech. Solids*, **25** (2020), 1081–1100. https://doi.org/10.1177/1081286519900902
83. I. Giorgio, D. Del Vescovo, Energy-based trajectory tracking and vibration control for multilink highly flexible manipulators, *Math. Mecha. Complex Syst.*, **7** (2019), 159–174. https://doi.org/10.2140/memocs.2019.7.159
84. D. Baroudi, I. Giorgio, A. Battista, E. Turco, L. A. Igumnov, Nonlinear dynamics of uniformly loaded elastica: Experimental and numerical evidence of motion around curled stable equilibrium configurations, *ZAMM Z. Angew. Math. Mech.*, **99** (2019), e201800121. https://doi.org/10.1002/zamm.201800121
85. E. Turco, Discrete is it enough? The revival of Piola–Hencky keynotes to analyze three-dimensional Elastica, *Continuum Mech. Thermodyn.*, **30** (2018), 1039–1057. https://doi.org/10.1007/s00161-018-0656-4
86. R. Fedele, G. Maier, B. Miller, Identification of elastic stiffness and local stresses in concrete dams by in situ tests and neural networks, *Struct. Infrastruct. Eng.*, **1** (2005), 165–180. https://doi.org/10.1080/15732470500030513
87. R. Fedele, G. Maier, B. Miller, Image correlation-based identification of fracture parameters for structural adhesives, *Tech. Mech. Eur. J. Eng. Mech.*, **32** (2012), 195–204.
88. B. E. Abali, C. C. Wu, W. H. Müller, An energy-based method to determine material constants in nonlinear rheology with applications, *Continuum Mech. Thermodyn.*, **28** (2016), 1221–1246. https://doi.org/10.1007/s00161-015-0472-z
89. M. De Angelo, L. Placidi, N. Nejadsadeghi, A. Misra, Non-standard Timoshenko beam model for chiral metamaterial: Identification of stiffness parameters, *Mech. Res. Commun.*, **103** (2020), 103462. https://doi.org/10.1016/j.mechrescom.2019.103462

90. A. Ciallella, G. La Valle, A. Vintache, B. Smaniotto, F. Hild, Deformation mode in 3-point flexure on pantographic block, *Int. J. Solids Struct.*, **265** (2023), 112129. https://doi.org/10.1016/j.ijsolstr.2023.112129

91. M. De Angelo, E. Barchiesi, I. Giorgio, B. E. Abali, Numerical identification of constitutive parameters in reduced-order bi-dimensional models for pantographic structures: Application to out-of-plane buckling, *Arch. Appl. Mech.*, **89** (2019), 1333–1358. https://doi.org/10.1007/s00419-018-01506-9

92. N. Shekarchizadeh, B. E. Abali, E. Barchiesi, A. M. Bersani, Inverse analysis of metamaterials and parameter determination by means of an automatized optimization problem, *ZAMM Z. Angew. Math. Mech.*, **101** (2021), e202000277. https://doi.org/10.1002/zamm.202000277

93. I. Giorgio, P. Harrison, F. Dell'Isola, J. Alsayednoor, E. Turco, Wrinkling in engineering fabrics: A comparison between two different comprehensive modelling approaches, *Proc. R. Soc. A*, **474** (2018), 20180063. https://doi.org/10.1098/rspa.2018.0063

94. R. Fedele, A. Ciani, L. Galantucci, V. Casalegno, A. Ventrella, M. Ferraris, Characterization of innovative CFC/Cu joints by full-field measurements and finite elements, *Mater. Sci. Eng. A*, **595** (2014), 306–317. https://doi.org/10.1016/j.msea.2013.12.015

95. N. Cefis, R. Fedele, M. G. Beghi, An integrated methodology to estimate the effective elastic parameters of amorphous TiO2 nanostructured films, combining SEM images, finite element simulations and homogenization techniques, *Mech. Res. Commun.*, **131** (2023), 104153. https://doi.org/10.1016/j.mechrescom.2023.104153

AIMS Press

Chapter 4

An enhanced beam model incorporating a hysteresis-based solid friction damping mechanism for cementitious materials

Chapter abstract

This chapter explores the cyclic internal energy dissipation in cement-based materials utilizing a one-dimensional enhanced micromorphic beam model that incorporates a dynamic friction term. Energy dissipation is primarily attributed to microcracks, which result from relative sliding under cyclic loads without causing any significant macroscopic damage. The friction model adopted is grounded in P. R. Dahl's dry friction law and demonstrates time-dependent elastoplastic characteristics. The model efficiently represents the energy transfer among bending, shear distortion, and microcrack sliding, as well as the energy storage and dissipation from asperity interactions. Kinematic descriptors and dissipative cycles are assessed through finite element simulations conducted in COMSOL Multiphysics.

Continuum Mech. Thermodyn.
https://doi.org/10.1007/s00161-024-01335-y

ORIGINAL ARTICLE

Larry Murcia Terranova · Christian Cardillo · Giuliano Aretusi

An enhanced beam model incorporating a hysteresis-based solid friction damping mechanism for cementitious materials

Received: 14 July 2024 / Accepted: 24 September 2024

Abstract In this work, we investigate a dynamic internal dissipation mechanism in the context of cement-based materials by introducing a 1D-enhanced micromorphic beam model with a dynamic internal friction term. Here, we consider an inherent feature in concrete-like materials arising from the multi-scale structure, namely, microcracks. Thus, we assume that the internal dissipation of the energy depends on the overall relative sliding displacement of the opposite faces in the microcracks under the effects of an applied cyclic load whenever no significant phenomena related to damage occur at the macroscopic level. The dynamic friction term is based on a well-known model for dry friction in solids due to P. R. Dahl, where the friction force depends only on the sliding displacement and evolves in time, reproducing an elastoplastic behavior. The model proposed in this paper takes into account a mechanical energy interchange between both bending and shear distortion in the beam with the sliding occurring at the microcracks, a storage of mechanical energy because of the asperities inside the faces of the microcracks, and the dissipation of the energy that follows from the interaction between the bending and the microcracks. Numerical simulations of the kinematic descriptors and the dissipative cycles are also provided by using the Finite Element Method and the commercial software COMSOL Multiphysics®.

Keywords Timoshenko beam model · Concrete · Dahl-type friction force model · Energy dissipation · 1D continuum micromorphic model · Microcracks · Hysteretic damping

1 Introduction

Concrete is ubiquitous in the development of building environments in human societies [1]. Notwithstanding this, a rigorous understanding of all features and potential applications of cement-based materials like concrete itself, has not been achieved yet. In fact, many features of concrete and novel procedures to improve its performance are topics under current investigation. Moreover, since resources required to produce this type of materials, for instance, water and heat energy, are considerable and its recycling is not a straightforward

---

Christian Cardillo and Giuliano Aretusi have contributed equally to this work.

L. Murcia Terranova ( )
Department of Information Engineering, Computer Science and Mathematics, Università dell'Aquila, 67100 Coppito, L'Aquila, Italy
e-mail: larry.murciaterranova@graduate.univaq.it

C. Cardillo
Department of Civil Engineering and Architecture, Università di Catania, Piazza Università, 95100 Catania, Italy
e-mail: christian.cardillo@phd.unict.it

G. Aretusi
Department of Civil, Construction-Architectural and Environmental Engineering, Università dell'Aquila, Monteluco di Roio, 67100 L'Aquila, Italy
e-mail: giuliano.aretusi@graduate.univaq.it

process [2], concrete-like materials pose an environmental, social and economic efficiency problem of major interest to the scientific community. For instance, current research topics in this regard are: *supplementary cementitious materials* aimed primarily to mitigate carbon emission in manufacturing but also to enhance concrete features [3,4], *nanotechnology improvements* to advance properties like durability, particle packing and reduce the porosity [5–7], *self-healing technology* in concrete allowing the material to repair its own cracks by autogenous or encapsulated healing [8–12], and the development of *ultrahigh performance concrete* with outstanding properties [13].

Cement-based materials like concrete are widely acknowledged as heterogeneous materials that consist of a distribution of different types and quantities of microcracks, pores and solid phases. Furthermore, important properties of concrete, like strength, depend on factors such as the water-to-cement ratio and the incorporation of aggregates into the cement paste that mechanically or chemically modify its natural behavior. In this way, concrete could be conceived as a multi-scale engineered material with a complex microstructure that can be tailored to improve its macroscopic responses [3,14–16]. Therefore, inspired by the richness of applications in multiple contexts of this type of materials, in this paper, we are interested in the dissipation of energy for earthquake-proof applications of cement-based materials arising from the incorporation of supplements and aggregates in the mixture. It is worth noting that supplementary materials and aggregates are actively being investigated [17–21]. In fact, this research framework opens the gates to possibilities such as an improved dissipation from mechanical to internal energy. However, the dissipation that we study in the current work is due to internal friction tightly linked to reversible changes, a behavior observed experimentally in dissipative cycles that could have a substantial effect in practice: enhanced concrete-like materials that can dissipate as much energy as possible (because of an increasing of the internal friction) while preserving their strength (for further information on the study of dissipative systems, the reader can refer to, e.g., [22–24]).

From this point of view, it is possible to consider concrete as a mechanical metamaterial by incorporating micro-fillers that aim at enhancing its performance, particularly in dynamic applications. Indeed, mechanical metamaterials are engineered materials designed to have properties not found in naturally occurring materials, often through the use of specific microstructures or micro-fillers that impart unique mechanical characteristics [25–28]. By introducing microfillers, the microstructure of concrete can be tailored to achieve improved mechanical properties, such as increased strength, toughness, and dynamic performance. Possible types of microfillers are: *i*) nanoparticles, namely, materials like carbon nanotubes, graphene, or nano-silica can significantly enhance the mechanical properties of concrete; *ii*) fibers, e.g., steel, glass, polypropylene that can improve tensile strength, ductility, and crack resistance; *iii*) phase change materials (PCMs) that can enhance thermal properties and provide additional energy dissipation under dynamic loading; *iv*) magnetic or electro-responsive particles that can be used to create smart concrete with adaptive properties. This approach leverages the principles of metamaterial design to create concrete composites with tailored properties that meet specific engineering requirements, opening up new possibilities for advanced structural applications with superior dynamic performance.

Recent works in the literature follow different approaches to model, from a mathematical perspective, concrete's behavior, e.g., by means of tools like the classical Cauchy model, generalized continua models where aggregates can be added to the mixture [29], higher order continua descriptions that account for the material heterogeneity [30–36], and multi-scale models that describe phenomena in the macro, meso and microscale. Additionally, in the last few years, multiple works have tackled the modeling of energy dissipation in concrete through approaches ranging from experimental to analytical formulations, and with the objective of introducing mathematical tools for the study of advanced concrete in the context of earthquake-proof designs [2,37–42]. More precisely, inspired by experimental evidence, recent works like [37–39] describe friction phenomena and dissipation in modified concrete obtained by adding selected micro-particles/fillers in concrete pores to increase the internal dissipation under the effect of uniaxial dynamic cyclic loading in 3D concrete. In fact, in works like [2,39–42] micromorphic multi-scale models are introduced to explain dissipative loops arising from cyclic uniaxial loads for small strains in 3D concrete, and enhanced Timoshenko-like beam models with static friction, i.e., a stationary constitutive equation relating the friction force considered to a micro/macro-descriptor, to study dissipation mechanisms in cement-based materials whenever cyclic loads are considered.

On the other hand, it is worth mentioning that one of the inherent phenomena occurring in concrete-like materials due to the multi-scale structure is microcracks. Microcracks can be modeled from a geometrical point of view as empty coin-shaped spaces that can open and close, and consist of two delimiting opposite faces with asperities that can interact whenever the microcracks are closed. This kind of microstructure could be of particular interest in comprehending a source of damage evolution in the material body as well as internal energy dissipation. In fact, recent works like [43–48] consider damage-related phenomena in the presence of microstructures such as microcracks. Concretely, in [43], the authors aim to explain, in a general framework, the development of new microstructures due to damage with a monotonic evolution rule and employing a strain gradient regularization of continuum damage mechanics. Then, in [44] and [45], the damage and deformation within a concrete dam due to diffusion of an aging fluid is described through a Timoshenko beam model, and a novel model for cohesive interfaces based on thermodynamic principles and compatible with continuum damage mechanics is introduced. In the last case, the model employs friction that degrades with damage and allows for the description of the opening and reclosing at the interface level, even when permanent relative displacements occur. We remark that microcracks in cement-based materials can be generated by relative motions between cement paste and other aggregates added to the mixture and that these motions could be induced, for example, during the drying or cooling processes. Thus, microcracks can be found in concrete even when no load has been applied [1].

In this paper, we aim to investigate the internal dissipation mechanisms observed in the context of cement-based materials under the hypothesis that at the macroscopic level, no significant phenomena related to damage occur, and hence, the internal dissipation is assumed to rely upon the relative motion in the microcracks. Therefore, a first scalar term describing the average sliding displacement between opposite faces of the microcracks within the material is introduced. This path has been explored in works mentioned before with outstanding results that reveal an agreement between the model and experimental measurements. In particular, the authors in [37–40] introduced a friction force term arising from a mix between a Coulomb-type friction model and a viscous term, due to the different kinds of allowed deformations and associated with the internal dissipation because of the relative motion of opposite faces of microcracks. This approach has extended to other configurations like in [49], where the dissipation properties are analytically and experimentally investigated in the context of Pantographic fabrics (see [50,51] for a comprehensive discussion about Pantographic metamaterials) by means of a second-gradient continuum model enriched with a Dahl-type friction term [52] for the dissipative effects at the interconnecting pivots, and in [53] where the response and effects of friction phenomena between fibers in woven fabric are modeled by a Rayleigh dissipative potential based on a Coulomb-type friction.

Even though in multiple works regarding energy dissipation it can be observed a tendency for introducing a Coulomb-type friction term based on a constitutive relation describing the evolution of the sliding and its coupling [54–58], there exist some efforts to generalize this approach through a second step where an additional kinematical descriptor is introduced, more precisely, a term modeling the relative motion of the microstructure asperities. For instance, in [2], the authors employ an adapted version of the LuGre-type model built upon the Coulomb-type friction force and a description of the “Stribeck effect” for the relative motion of both the faces of the microcracks and the asperities inside them. Following this approach, in the current work where a dynamic point of view is considered, i.e., the friction force evolves in accordance with a differential equation relating different internal variables in the framework of the Timoshenko beam model. More precisely, we consider a solid friction model introduced by P. R. Dahl in [52,59] (Dahl-type friction force) that reproduces a nonlinear elastoplastic behavior where the response is almost linearly elastic for small deformations and plastic for large deformations. In Dahl’s formulation, the friction force, henceforth denoted by F, is assumed to depend only on the sliding displacement γ in such a way that $\frac{dF}{d\gamma} > 0$ at all times, even if $\dot{\gamma}$ changes its sign. Additionally, if F_c denotes the magnitude of the Coulomb friction force, then $F \to F_c$ monotonically as long as $\dot{\gamma} > 0$, and $F \to -F_c$ monotonically as long as $\dot{\gamma} < 0$ (see Sect. 2 for more details).

Modeling microcracks’ behavior is not an easy task, and from a mechanical point of view, it seems that simplified models are frequently employed to predict phenomena in specific regimes. Moreover, because of the microcracks considered here, in addition to the dissipation of the energy, a nonlinear elastic behavior is expected. This approach arises as an alternative path to describe the internal dissipation experimentally observed and lies in the field of micromorphic continuum models, which are highly suitable when describing complex phenomena similar to those explained by higher gradient models [60–64].

This work is organized as follows. In Sect. 2, we provide a more detailed discussion about our approach and introduce the enhanced micromorphic beam model. Later, in Sect. 3, numerical results and examples are given to corroborate that a proper adjustment to the parameters associated with the evolution of the friction term could allow for the model to explain mechanical responses with different ranges of energy dissipation. Finally, concluding remarks about the results are reported in Sect. 4.

2 Enhanced beam model

In this section, we introduce the framework of our study and the improved 1D micromorphic continuum beam model for cementitious metamaterials [65–73]. The exploited approach is built upon an extended version of the Principle of Virtual Work to take into account the internal elastic contributions in the material, the external contributions due to three-point flexural tests, which is carried out through cyclic loads, as well as a dissipative contribution due to the presence of microcracks. First, let us emphasize that here we are mainly interested in the effect of this last contribution, i.e., in studying dissipation of mechanical energy due to micro–macro interactions and under the assumption of a small deformation regime (no damage growth under fatigue tests).

Thus, in the light of the previous premise, let us consider a planar xy reference framework and a simple 1D characterization of the beam such that, in the reference configuration, it is described by a curve of length L lying on the x-axis, and in the current configuration it is described by a map $\mathcal{X}$ that depends on the abscissa X (x-axis coordinate). Here, we consider the effects of bending and shear distortions on the beam and neglect the effects of stretching. In addition to that, we improve the classical Timoshenko beam model by including an additional scalar kinematical descriptor which accounts for the relative micro-sliding accumulation within the material due to the sliding between opposite faces of the microcracks in the beam. For that purpose, we assume that the microcracks are randomly distributed along the beam, and hence, no further consideration about their orientation is required.

Following on from those considerations, the map $\mathcal{X}(X)$ describing the current configuration consists of the following kinematical descriptors: the transverse displacement of the beam axis material particles in the y direction, denoted by $v(X)$, the angle of the cross-section $\varphi(X)$, and the overall relative microsliding $\gamma(X)$. Here, the model aims to consider a mechanical energy interchange between both bending and shear distortion with the sliding occurring at the micro level (microcracks), a storage of mechanical energy because of the asperities inside the faces of the microcracks which are deformed when they are in contact, and a subsequent dissipation of the energy that follows from the interaction between the bending (change of orientation of the cross-sections) and the microcracks. This last interaction potentially induces compression in some parts of the cross-section that is assumed to activate the dissipation mechanism. More precisely, we assume that there is a compression-caused effect along cross-sections, which consists of a closing of the microcracks so that the opposite faces are forced to get in contact. It is worth mentioning at this point that because of our assumption about the stretching contribution, uniform compression in the x-axial direction is not considered here. Nevertheless, an analysis including this last contribution may be carry on by following the ideas in [42].

Next, we introduce an extension of the Principle of Virtual Work (PVW) that allows us to include any virtual work dissipated in a system (see, for example, the discussion in [2,41]). This extended PVW asserts that, at equilibrium, the virtual work exerted by the external forces applied to the beam, $\delta\mathcal{W}^{ext}$, must balance both the virtual work done by the elastic inner forces, $\delta\mathcal{W}^{el}$, and the virtual work dissipated $\delta\mathcal{D}$. Thus, at the equilibrium configuration of the beam model, we have that

$$\delta\mathcal{W}^{ext} + \delta\mathcal{W}^{el} + \delta\mathcal{D} = 0. \tag{1}$$

Henceforth, for the sake of simplicity, let us assume that our kinematical descriptors lie in the proper space of functions in such a way that the following expression is a viable internal elastic energy $\mathcal{E}^{el} = -\mathcal{W}^{el}$:

$$\begin{aligned}\mathcal{E}^{el} = &\int_0^L \frac{1}{2}K_b(\varphi')^2 dX + \int_0^L \frac{1}{2}K_s(v'-\varphi)^2 dX + \int_0^L \frac{1}{2}K_2\gamma^2 dX \\ &+ \int_0^L \frac{1}{4}K_4\gamma^4 dX - \int_0^L \alpha_b\varphi'\gamma dX - \int_0^L \alpha_s(v'-\varphi)\gamma dX,\end{aligned} \tag{2}$$

where K_b, K_s, K_2 an K_4 denote material parameters corresponding to stiffness coefficients for the bending, the shear distortion, and the nonlinear internal restoring force induced at the microcracks level, and α_b, α_s denote coupling coefficients between the macro-descriptors (macroscopic bending and macroscopic shear distortion) and the micro-descriptor (microcrack sliding).

We remark that tests carried out with cyclic loads in this context (see, for instance, [2]) reveal that even for small strains, the stress–strain constitutive equation seems to be nonlinear. Thus, it is possible to assume that this nonlinear behavior, whenever a cyclic load is applied, is induced by internal factors like microcracks and that it poses an elastic nature. Here, we consider an elastic contribution in γ given by a fourth order and even polynomial that vanishes at $\gamma \equiv 0$. This postulate follows from the geometry of the microcracks and the interaction of the faces due to bending (the asperities in the opposite faces of microcracks can bend and store elastic energy), and it is motivated by experimental observations for cement-based materials [74]. It is worth emphasizing once again that we remain in the small deflection regime and that our assumptions in this regard are motivated by the fact that, during the micro–macro interactions, small contributions, likely arising due to higher order terms as the one associated with K_4, should be taken into account. We also observe that the proposed elastic energy is non-objective for large deformations. Therefore, the expression (2) should be appropriately modified for such a regime.

Moreover, due to the coupling terms in the internal elastic energy (2), sufficient conditions over the control parameters are required in order to have a valid expression for the energy. In fact, if $K_4 > 0$, then the expression obtained collecting the remaining terms in (2) arises from a quadratic form which is positive definite whenever the next conditions hold nontrivially: $i)$ $K_b > 0$; $ii)$ $K_s > 0$ and $iii)$ $K_b K_s K_2 > \alpha_s^2 K_b + \alpha_b^2 K_s$.

On the other hand, it is worth noting that in the study of the friction phenomena in solids, we can distinguish between static and dynamic friction models (see for instance [75,76]). In the first case, a constitutive equation describes the relation between the friction force and a micro/macro level variable, and in the second case, the friction force evolves in accordance with a differential equation relating different internal variables [75,77–79]. Here, we proposed a model based on the ideas in works like [41,42], nevertheless, contrary to the static analysis reported there, where a Coulomb-type friction force model was considered, in this work, a dissipation micromechanism given by a Dahl-type friction force is introduced throughout the faces of the microcracks in the material. This implies a new contribution is taken into account because of the coupling between the evolution of γ and the Dahl-type friction force.

Additionally, in the modeling of internal dissipation in solids, we can distinguish between dissipated energy associated with damage and plastic phenomena (which could increase the density of microcracks or enlarge those already existing), and the dissipated energy associated with the friction phenomena that induces a reversible internal motion (no damage occur at the macroscopic level). Some works in this line are [80,81], where the number of microcracks and their mechanical and geometrical properties are invariant when dynamic loads are applied.

Now, with a view to considering mechanical energy dissipation, we introduce a mechanism of solid friction [59], more precisely, a shear stress between the contact area of opposite faces of a microcrack that is induced by dry sliding friction. In general, solid friction has been considered a quasi-static phenomenon mainly caused by contact stress and a subsequent process of creation and rupture of bonds between the surface elements of the material bodies in contact (quasi-static properties of materials). This last process is entirely dynamic and can be described by the motion of the bodies due to external or inertial forces [59]. In this way, the friction function F, considered as a function of the relative displacement γ (in our case, the overall relative micro-sliding), can evolve in time. Thus, the time rate of change of the friction function introduces a constitutive equation for F such that

$$\dot{F}(\gamma) = \frac{dF}{d\gamma}(\gamma)\dot{\gamma}. \tag{3}$$

In fact, as in many problems in engineering, we can expect hysteretic behavior of the friction force for this case, i.e., a lagging effect from the change of the friction in response to a reversing in the direction of the motion. This behavior is resembled by the assumption that F depends only on γ [52], and it can be generated by a friction slope of the form

$$\frac{dF}{d\gamma}(\gamma) = \sigma_0 \left| 1 - \frac{F(\gamma)}{F_c}\,\mathrm{sgn}(\dot{\gamma}) \right|^{\beta} \mathrm{sgn}\left(1 - \frac{F(\gamma)}{F_c}\,\mathrm{sgn}(\dot{\gamma}) \right), \tag{4}$$

where β and σ_0 are parameters associated with the basic shape of the friction law at hand and the rest stiffness at $F = 0$ (slope of the stress/force–deflection curve), respectively. In fact, the parameter β induces a type of friction force for which the material is ductile whenever $\beta \geq 1$ and brittle whenever $0 \leq \beta < 1$. In practice, these parameters should be properly estimated by studying the stress/force–deflection test data.

Dahl's friction model is based on a Coulomb-type friction mechanism, where the last one can be thought of as a yield force for which the "unloading" path, in a friction force–deflection context (see [59]), exhibits plastic behavior. More precisely, the friction slope (4) shows that for small displacements, the friction force F, seems to be linear and elastic (in general, it resembles a nonlinear but soft spring), and after a certain threshold for the displacement, F is required to change its sign to reach small displacements again, this is the plastic nature for large deflections.

At this point, we remark that for this kind of dynamic friction model, the dissipative cycles do not depend on the frequency of the applied load [2]. Nevertheless, it is worth noting, as it was done in [59], that there is a stochastic nature behind the friction curve caused by the random distribution of the contact area, matter that we have overcome by defining γ as the overall sliding of the opposite faces of a uniform distribution of penny-shaped microcracks.

Hence, we model the dissipated work in terms of the sliding γ by considering the Dahl-type friction model with a friction force per unit line of magnitude $\mathcal{F}(\gamma)$ that evolves in time in accordance with (3)-(4), and such that

$$\delta\mathcal{D} = -\int_0^L \mathcal{F}(\gamma)\delta\gamma dX, \tag{5}$$

We remark that in the overall friction term considered in (5), there exists an implicit coupling between the bending (a change in the cross-section orientation) and a subsequent compression that potentially closes microcracks along some part of the cross-section. In other words, the dissipative effect of the sliding is activated when compression pushes the microcrack faces together.

Now, because of the modeling approach followed in this work and the expression for the elastic energy (2), it is straightforward to conclude that the possible external forces, namely, vertical direction forces on the bulk, b_y, concentrated forces in the vertical direction, $\bar{b}$, torques per unit line, μ, and torques acting on edges, $\bar{\mu}$, induce the following virtual work contribution $\delta\mathcal{W}^{ext}$

$$\delta\mathcal{W}^{ext} = \int_0^L \mu(X)\delta\varphi dX + \int_0^L b_y(X)\delta v dX + \bar{\mu}(X)\delta\varphi|_0^L + \bar{b}(X)\delta v|_0^L. \tag{6}$$

Moreover, it is not difficult to check through a direct computation and integrating by parts that the first variation of the internal elastic contribution is given by

$$\begin{aligned}\delta\mathcal{E}^{el} = &-\int_0^L [(K_b\varphi')' + K_s(v'-\varphi) - (\alpha_b\gamma)' - \alpha_s\gamma]\delta\varphi dX\\ &-\int_0^L [K_s(v'-\varphi)' - (\alpha_s\gamma)']\delta v dX\\ &+\int_0^L [K_2\gamma + K_4\gamma^3 - \alpha_s\varphi' - \alpha_s(v'-\varphi)]\delta\gamma dX\\ &+ (K_b\varphi - \alpha_b\gamma)\delta\varphi|_0^L + (K_s(v'-\varphi) - \alpha_s\gamma)\delta v|_0^L.\end{aligned} \tag{7}$$

In this sense, we can define the bending moment M, the shear force T and Γ as follows:

$$M{:=}K_b\varphi' - \alpha_b\gamma, \quad ,T{:=}K_s(v'-\varphi) - \alpha_s\gamma, \quad \Gamma{:=}K_2\gamma + K_4\gamma^3 - \alpha_b\varphi' - \alpha_s(v'-\varphi),$$

so that the PVW implies that the bulk equations, along with the corresponding boundary conditions for the system considered here, are given by

$$\begin{cases}-(M'+T) - \mu = 0,\\ -T' - b_y = 0,\\ \Gamma + \mathcal{F}(\gamma) = 0,\\ (M - \bar{\mu})|_{0,L}{=}\,0,\\ (T - \bar{b})|_{0,L}{=}\,0.\end{cases} \tag{8}$$

It is worth noting that, as mentioned in [41,42], the PVW employed to deduce the boundary value problem describing the equilibrium of the beam does not provide nor impose any boundary condition over the bulk for γ.

Table 1 Values of the parameters for the numerical simulations

Parameters	Values
d	150.0 mm
L	600.0 mm
ℓ	450.0 mm
K_b	$1.330 \times 10^6\,\mathrm{N\,m^2}$
K_s	$2.560 \times 10^8\,\mathrm{N}$
K_2	$7.500 \times 10^8\,\mathrm{N\,m^{-2}}$
K_4	$1.000 \times 10^8\,\mathrm{N/m^4}$
α_b	$8.050 \times 10^6\,\mathrm{N}$
α_s	$0.5000 \times 10^7\,\mathrm{N\,m^{-1}}$

3 Numerical simulations and results

In this section, we provide numerical evidence about the dissipation mechanism and the mechanical properties of cement-based metamaterials described by the improved beam model introduced in the previous section. For that purpose, we consider a three-point bending test (3PB) and a concrete specimen as in [41]. Thus, the study consists of a sample with the geometry of a parallelepiped of dimensions $d \times d \times L$, which is placed over two fixed supports located at a distance ℓ from each other, and a cyclic load that is applied on the top center of the sample. It is worth recalling that here, we neglect uniform tension/compression of the beam in the x-axis direction, but we are interested in bending deformations of the specimen along with the subsequent shear distortions perceived when the concentrated cyclic load is applied.

Table 1 contains the values of geometry parameters, material parameters and coupling coefficients employed in the numerical simulations. We point out that sufficient conditions $i) - iii)$ given in page 7 for the positive definiteness of the postulated elastic energy are verified for these values of the parameters. More precisely, we assume a material with a Young modulus $Y_0 = 31.450 \times 10^9$Pa and a Poisson ration $\nu = 015$. Following on from this assumption, we can compute the stiffness coefficients for both the bending and shear distortion in a classical way by using the second moment of area of the beam cross-section J and the shear modulus $G_0 = {}^{Y_0}\!/_{2(1+\nu)}$, so that $K_b = Y_0 J$ and $K_s = {}^5\!/_6 G_0 d^2$. The remaining coefficients K_2 and K_4, associated with the internal restoring force due to the deformation of microcracks' asperities, and the coupling coefficients α_b and α_s, are estimated through a delicate adjustment to produce the desired response. Furthermore, the cyclic load leading to the external contribution in our system is assumed to be applied in the transverse direction to the beam axis, over the middle point of this last one, and with a time dependent magnitude given by

$$f_y(t) = \frac{A_0}{2}(1 - \cos(2\pi\omega t)), \tag{9}$$

where A_0=4.500 kN is the maximum load and $\omega = 10.00$ Hz is the frequency.

Henceforth, with a view to understanding the effects of a long-term cyclic load on our descriptors, we consider a 10-cycle test, which does not deviate from what it is reported to be in agreement with a seismic activity [39]. Additionally, as mentioned in [39], the maximum load has to be chosen in such a way that an unsafe level of stress in the material is avoided, whilst the minimum level of compressible stress is enough to guarantee that some interactions between opposite faces of microcracks occur.

The numerical results in this section are obtained by means of the commercial software COMSOL Multiphysics®, which allows us to employ the improved model proposed here in its extended PVW formulation (1) with the Weak Form PDE module. Since only first order derivatives of the kinematical descriptors are considered, our micromorphic model belongs to the class of first gradient continuum models, and thus, standard Lagrangian quadratic polynomials can be utilized as shape functions for the Finite Element interpolation (for more efficient numerical methods, the reader can refer to [82–87]). At this point, it is worth addressing that, in general, identifying the proper set of parameters that characterizes this kind of model is not an easy problem because of the complex mechanical responses that can eventually take place. Besides, when considering multi-scale phenomena such as those in the present work, a delicate micro–macro identification process is required to achieve a satisfactory correspondence between experimental data and numerical simulations. For instance, in [39], a parameter identification for a micromorphic model describing the effect of micro-particle addition on the internal dissipation in concrete is performed to show that the model is suitable to forecast dissipative behavior. This is a cornerstone matter because, in practice, the additives/fillers could either decrease or

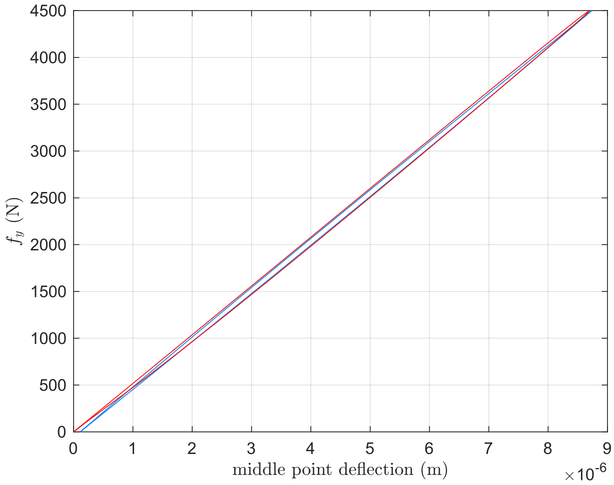

Fig. 1 Comparison between dissipative cycles obtained for two improved Timoshenko beam models, one with a Dahl-type friction force (blue) and the other with a Coulomb-type friction term (red), for the loading and unloading during the 10th-cycle for the 3PB test (color figure online)

increase the internal friction and even degrade the mechanical strength (see also discussions in [39,88]), and therefore, an optimal percentage of their amount is required. In this context, there exist different techniques, such as digital image correlation (DIC), energy methods, and neural networks that can be employed when studying complex generalized materials. To see different applications of these techniques in recent works, the reader is referred to [88–94].

Figure 1 shows a comparison between dissipative cycles obtained under a 3PB test for the improved Timoshenko beam model with the Dahl-like friction term here considered (blue) and a static friction term based on a smoother version of the Coulomb model (red) [37]. More precisely, in the first case, a friction term per unit line of magnitude $\mathcal{F}$ based on a Dahl-type friction force F verifying the evolution law (3)-(4) is employed with $\beta = 6.689 \times 10^5$ and $\sigma_0 = 4.691 \times 10^{11}\,\mathrm{N\,m^{-1}}$. The exponent β is selected from the range of values for which the model describes solid friction in ductile materials since asperities in the microcracks can be deformed without damage, at least in the small deflection regime. In the second case, a friction force term per unit line of magnitude $\zeta\,|\varphi'|\tanh(\eta\dot{\gamma})$ is employed for $\zeta = 2.950 \times 10^8$N and $\eta = 225.0\,\mathrm{s\,m^{-1}}$. This last concept of friction force has been recently included in works like [41,42] to accurately describe the experimental observations of a beam made of concrete in the context of energy dissipation, and it represents a Coulomb-type viscous friction that depends on the sliding velocity, $\dot{\gamma}$, with a friction coefficient (dissipation) due to microscopic sliding displacements induced by bending deformations, ζ, and the characteristic slope of the sliding velocity, η (inverse of the reference velocity, employed to modulate the extension of the viscous range whenever tanh is introduced).

On the other hand, the dissipated energy associated with the numerical results can be measured, for instance, by computing the areas of the corresponding dissipative cycles that originate from each branch of loading and unloading. Here, the areas of dissipative cycles depicted in Fig. 1 are numerically estimated by using the trapezoidal rule so that for the improved Timoshenko beam model with a dynamic friction term, we obtain an approximate dissipated energy of 4.170×10^{-4} J whilst for the model with a static Coulomb-type friction term we obtain an approximate dissipated energy of 6.183×10^{-4} J. We emphasize that a proper adjustment to the exponent β and the coefficient σ_0 can be done to achieve higher dissipated energy, possibly greater than the one illustrated here (Fig. 8, presented at the end of this section, illustrates how the dissipated energy changes when β is small and big enough).

A careful inspection of Fig. 1 reveals that there is a slight displacement of the starting point (strain) of the cycle in blue with respect to the starting point of the cycle in red. This discrepancy is explained by the long-term cyclic load that was considered for the simulations. In fact, for the initial cycles, we observed a relatively small discrepancy between the starting point when loading and the ending point when unloading for the dynamic friction term, and as the test progressed, this gap was considerably mitigated. Moreover, as mentioned in [39], the behavior of the cycles is convergent towards a conservative limit cycle, and thus, we expect our numerical simulations to be reliable when compared with experimental measurements.

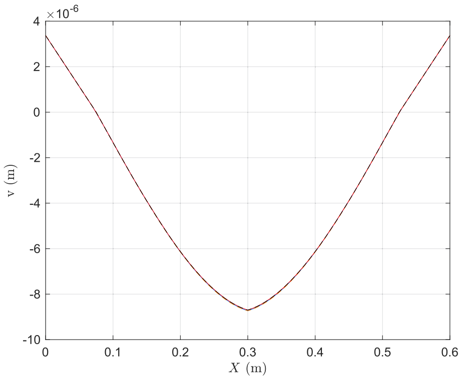

(a) Comparison between the vertical displacements.

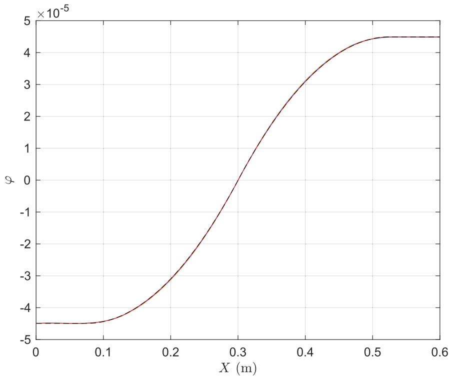

(b) Comparison between the cross-section rotations.

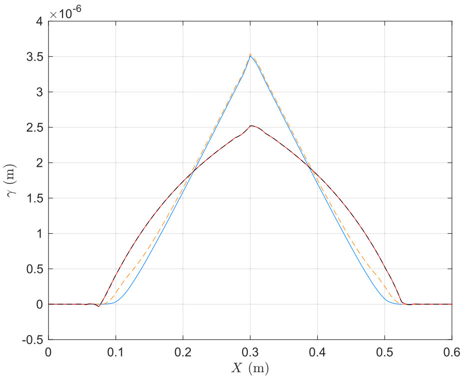

(c) Comparison between inner relative sliding displacements.

Fig. 2 Comparison between the descriptors of the improved Timoshenko-like beam models employing an internal dynamic friction term (Dahl-type friction; solid blue and dashed orange) and the Coulomb-type friction (solid red and dashed black), for two instants of maximum applied load in the 3PB test of 10-cycles and load magnitude f_y, at the middle point of the sample (color figure online)

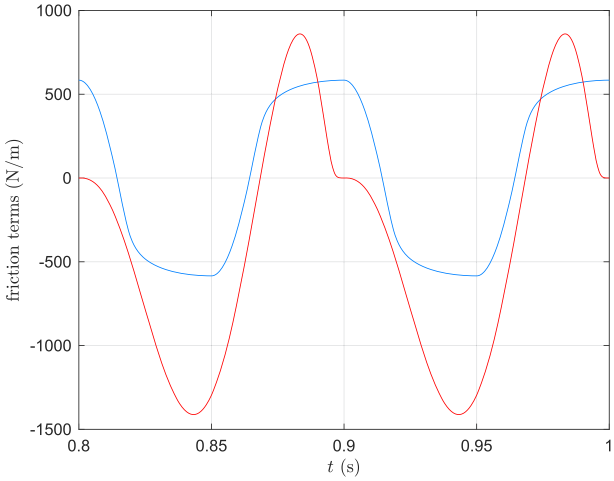

Fig. 3 Comparison between the friction forces per unit line at the middle point of the sample based on Dahl's model (blue) and Coulomb's model (red) during the last two cycles (color figure online)

Now, regarding the kinematical descriptors taken into account in our formulation, Fig. 2 shows a comparison between the vertical displacements 2a, the orientations of the cross-sections 2b, and the relative sliding displacement 2c, at the maximum applied load of magnitude f_y for the model proposed in the current work (solid blue line at $t = 0.05$s; dashed orange line at $t = 0.95$s), and for the model with a Coulomb-type friction force (solid red line at $t = 0.05$s; dashed black line at $t = 0.95$s). A thorough observation reveals that, for the values of the parameters considered in this case, no major deviation regarding the shape of both vertical displacements and orientations of the cross-sections is perceived. Hence, besides small quantitative differences, the mechanical responses at the macroscopic level provided by the dynamic and static approaches are in agreement. The response at the microscopic level is slightly different between the two models, where a greater relative sliding displacement γ at the middle point of the beam is perceived under the same conditions of loading for the model introduced in this work.

A comparison between the evolution in time of the friction forces per unit line is presented in Fig. 3. More precisely, the curve in blue portrays the Dahl-type friction force and the curve in red portrays the Coulomb-type friction force, in both cases for the last two cycles of the applied load. Figure 4 shows the expected hysteretic behavior of the magnitude $\mathcal{F}$ (hysteretic damping) that evolves in accordance with (3)-(4). It is worth mentioning at this point that, even though the dynamic friction in blue approaches the static one in red near the times for which the maximum load is applied (see Fig. 3), the overall behavior is rather different. This last remark is supported by the nature of the friction terms at hand, i.e., in addition to the explicit evolution in time of the dynamic term here introduced, we have a different measurement of similar phenomena since for the dynamic term it is assumed a dependence only on the relative displacement instead of the corresponding velocity.

Figure 5 shows the evolution in time for the complete 3PB test of the relative sliding γ at the middle point for both models, one with the dynamic friction term (blue) and the other one with the static friction term (red). The sliding responses are quite similar regarding their amplitude; nevertheless, it seems that the sliding corresponding to the dynamic term is shifted some tenths of micrometers over the common baseline from which both curves start.

Figure 6 shows a comparison between shear forces and between bending moments at the maximum applied load in the last cycle. More precisely, the shear stresses and bending moments are portrayed, respectively, in Fig. 6a and b, for the improved Timoshenko-beam model here considered (solid blue) and the model with a static friction term, both at time $t = 0.95$s. A careful inspection reveals that no significant changes in the behavior of the shear force T and the bending moment M occur when the dynamic friction term and the static friction term are considered. This observation is in agreement with the behavior described in [41] where it is stated that the stresses are not significantly influenced by the mechanics at the microcracks level.

Figure 7 shows the dissipated power given by the model considered in this work. Figure 7a illustrates the evolution of the dissipated power throughout the complete 3PB test, whilst Fig. 7b shows a close-up of the same quantity in an interval of time where it may reach positive values. In fact, a visual inspection of Fig. 7a

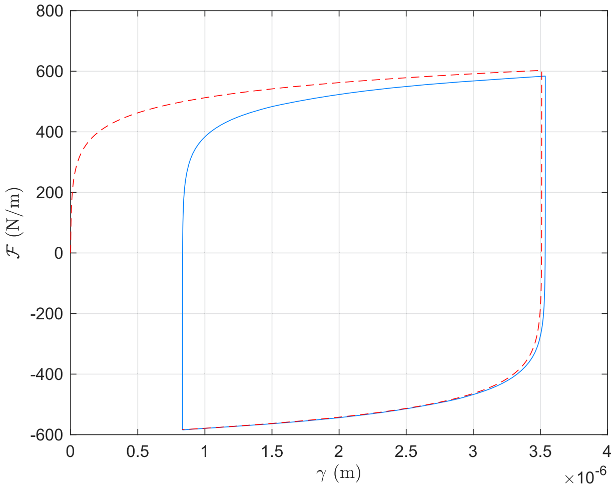

Fig. 4 Dahl-type friction term magnitude $\mathcal{F}$ at the middle point of the sample for the first (red) and last (blue) cycles in the 3PB test (color figure online)

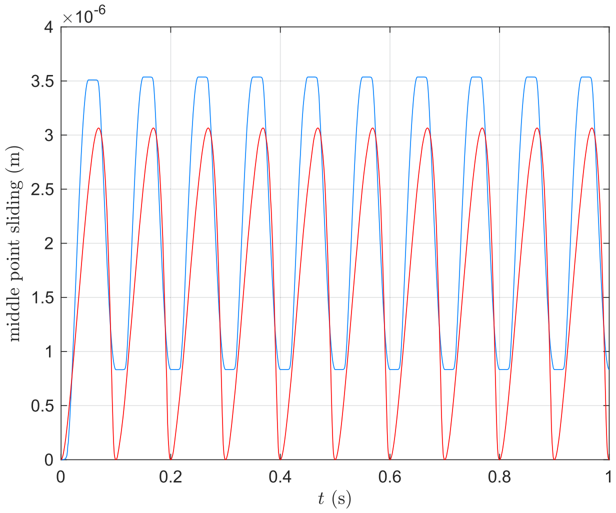

Fig. 5 Evolution in time of the relative sliding γ at the middle point of the sample for the 3PB test

reveals that the overall dissipated power leads to a passive operator ensuring dissipation of the energy for a system with a dynamic friction term (see [2] and the references therein for more details).

Some dissipative cycles obtained under a 3PB test using different values of the control parameters σ_0 and β are provided in Fig. 8. The cycle in Fig. 8a was obtained for $\sigma_0 = 1.425 \times 10^9\,\mathrm{N\,m^{-1}}$ and $\beta = 25$, and the corresponding dissipated energy in this case is 2.867×10^{-7}J: a rather small variation of the macro-descriptors υ (concentrated around the middle point) and φ (near the boundary of the sample) is perceived while the amplitude of the micro-descriptor γ decreases and remains always under the response provided by the model employing Coulomb-type friction. A higher value of the dissipated energy can be obtained if β is increased. Figure 8b shows the dissipative cycle for $\sigma_0 = 8.867 \times 10^{10}\,\mathrm{N\,m^{-1}}$ and $\beta = 5.500 \times 10^5$: in this case, the dissipated energy is 4.090×10^{-4}J.

4 Concluding remarks

In this work, we introduced a Timoshenko-like beam model employing a dynamic friction term with a view to improving the understanding of energy dissipation in the context of concrete-based materials and metamaterials. Our approach assumes that microcracks are inhere in the material's inner structure, leading to both an elastic mechanical contribution and a dissipation micromechanism under the effect of cyclic loads applied on the

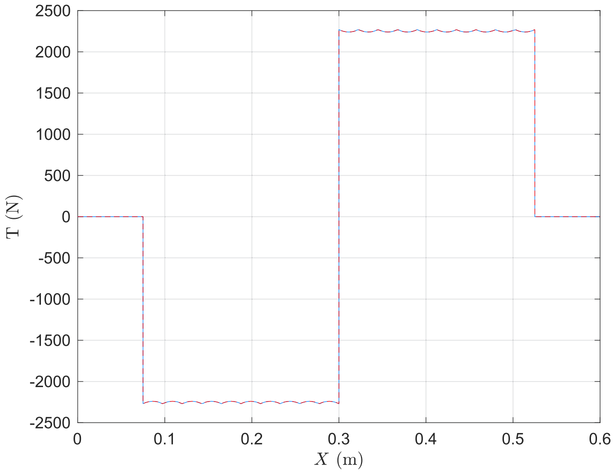

(a) Shear forces T.

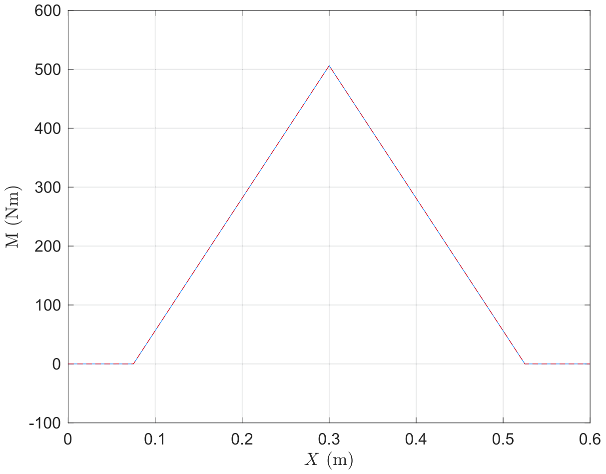

(b) Bending moments M.

Fig. 6 Comparison between internal stresses at the maximum applied load for the last cycle employing Dahl's model (solid blue) and Coulomb's model (dashed red) (3PB) (color figure online)

middle point of the beam. The novel contribution of this paper consists in the fact that the dynamic friction term is built upon the quasi-static description proposed by P. R. Dahl for dry friction in solids [59], in our case, a friction force arising due to some (partial) compression in some part of the cross-section caused by a bending deformation as the flexural test is carried out. This compression leads to the closing of the microcracks so that the opposite faces are forced to get in contact from where a sliding displacement between opposite faces of a microcrack occurs. Thus, the friction term considered here evolves in time and describes an elastoplastic response enriching the scope of phenomena that can be perceived in the system through a 1D micromorphic continuum model. In fact, some characteristics of a plastic behavior are illustrated numerically in the simulations reported in this work, whilst those descriptors not directly affected by the inner friction contribution seem to concur with predictions previously reported in works like [41].

The model and the analysis provided in this paper could be of interest, for example, to researchers in the field of dissipation mechanisms for cementitious materials since a suitable adjustment to the control parameters, in particular those associated with the evolution law of the friction force (3)-(4), namely σ_0 and β, could provide a grasp in quantifying, after a careful identification process, the amount of aggregates/fillers required in the mixture to obtain a material with the desired mechanical features. Thus, the approach in this work could be

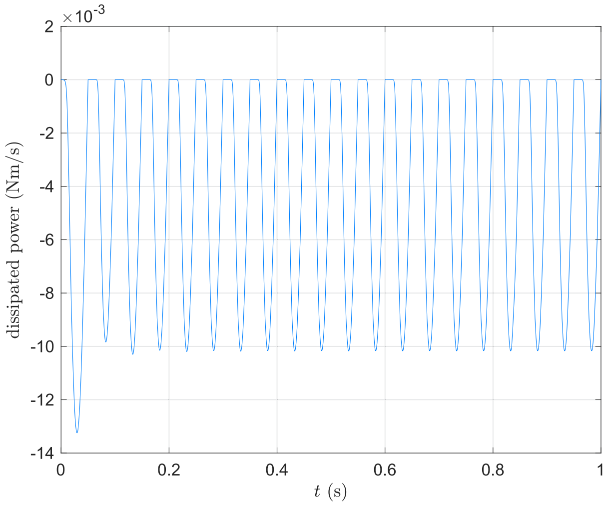

(a) Dissipated power.

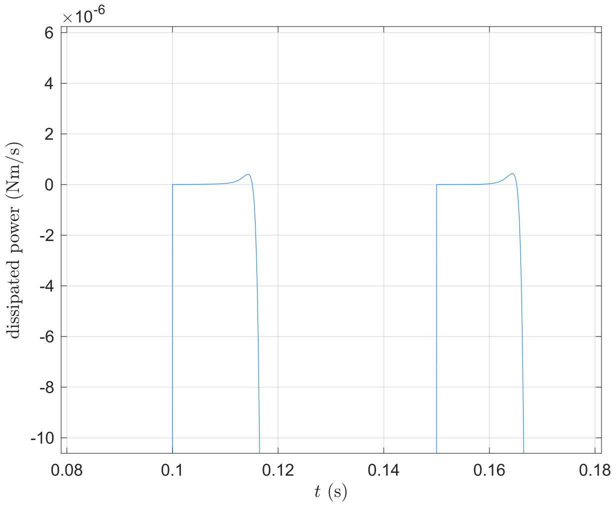

(b) Close-up of the dissipated power

Fig. 7 Dissipated power for the complete 3PB test

potentially considered as a simplified tool in the first stage of assessing major aspects like energy dissipation and the mechanical response reliability for earthquake-proof concrete. Nevertheless, we note that, in order to provide insights leading to further levels of assessment, an experimental campaign to validate the scope of the proposed model is required. In fact, similar experimental campaigns were reported in works like [38,39]. Perhaps the approach in the aforementioned papers could lead to devising an experimental testing procedure, considering different additives, to assess the connection between friction and the mechanical properties of cementitious materials in our context.

We emphasize that some efforts to accomplish the modeling of advanced features and phenomena in concrete-like metamaterials can be made. For instance, in [41], the authors suggest a different approach where the first scalar descriptor γ could be instead considered as a microstructural parameter so that a dependence on γ' of the energy is introduced. Furthermore, in recent works like [95], [96] and [97], the authors consider the underlying connection between Mohr's circles and the definition of Cauchy stress, the strain problem associated with the inclusion of a particular incompressible liquid in an infinite anisotropic elastic matrix subjected to uniform loading at infinite, and the possibility of expressing a three-dimension state of stress by

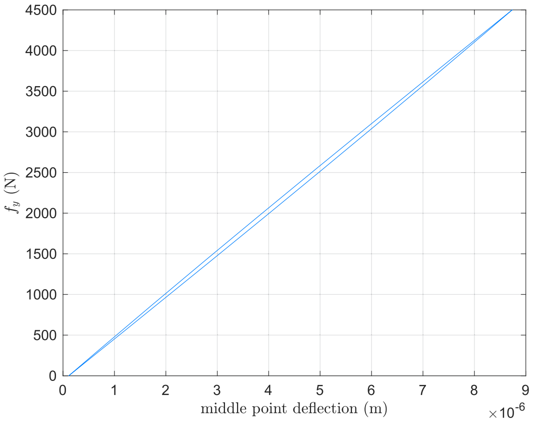

(a) Dissipative cycle obtained for $\sigma_0 = 1.425 \times 10^9\,\mathrm{N\,m^{-1}}$ and $\beta = 25$.

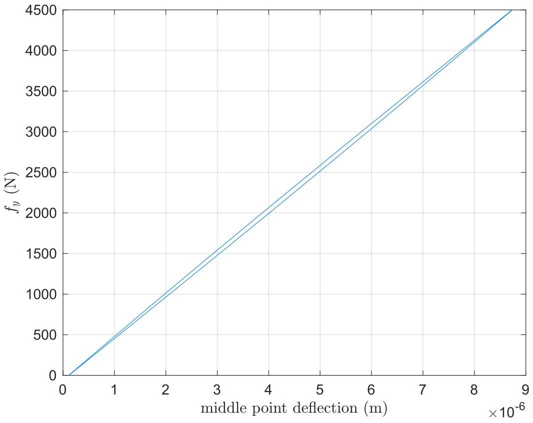

(b) Dissipative cycle obtained for $\sigma_0 = 8.867 \times 10^{10}\,\mathrm{N\,m^{-1}}$ and $\beta = 5.500 \times 10^5$.

Fig. 8 Dissipative cycles for the improved Timoshenko beam model with a Dahl-type friction term for different values of the parameters σ_0 and β

means of a single scalar function, respectively. Perhaps a suitable adaptation of the treatments and notions in the aforementioned works could allow us to, for example, better characterize the stress in cement-based materials, leading to significant improvements in determining if microstructures, such as the microcracks, are open, to describe phenomena like water inclusion in concrete-like metamaterials, and to obtain particular solutions of the governing equations in this regard by considering a lower dimension approach. These results open the gates to further insights into concrete-like materials and may be considered to improve our model in future works.

Furthermore, dissipation is always connected with the transformation of mechanical energy into heat. In specific applications, an increase in temperature can significantly affect the mechanical response of the material. Therefore, introducing thermal effects will contribute to developing a comprehensive topic formulation (see for an efficient formulation of the thermoelastic problem [98,99]).

Funding None.

References

1. Monteiro, P., Mehta, P.: Concrete: Microstructure, Properties and Materials (2006)
2. Giorgio, I., Scerrato, D.: Multi-scale concrete model with rate-dependent internal friction. Eur. J. Environ. Civ. Eng. **21**(7–8), 821–839 (2016). https://doi.org/10.1080/19648189.2016.1144539
3. Misra, A.: Stabilization characteristics of clays using class C fly ash. Transp. Res. Rec. J. Transp. Res. Board **1611**(1), 46–54 (1998). https://doi.org/10.3141/1611-06
4. Contrafatto, L., Lazzaro Danzuso, C., Gazzo, S., Greco, L.: Physical, mechanical and thermal properties of lightweight insulating mortar with recycled Etna volcanic aggregates. Constr. Build. Mater. **240**, 117917 (2020). https://doi.org/10.1016/j.conbuildmat.2019.117917
5. Goel, G., Sachdeva, P., Chaudhary, A.K., Singh, Y.: The use of nanomaterials in concrete: a review. Mater. Today Proc. **69**, 365–371 (2022). https://doi.org/10.1016/j.matpr.2022.09.051
6. P. P., A., Nayak, D.K., Sangoju, B., Kumar, R., Kumar, V.: Effect of nano-silica in concrete; a review. Constr. Build. Mater. **278**, 122347 (2021). https://doi.org/10.1016/j.conbuildmat.2021.122347
7. Alasfar, R.H., Ahzi, S., Barth, N., Kochkodan, V., Koç, M.: Modeling and experimental validation of the elastic modulus of polysulfone membranes reinforced with cellulose nanofibers. Math. Mech. Complex Syst. **10**(4), 413–429 (2023). https://doi.org/10.2140/memocs.2022.10.413
8. De Belie, N., Gruyaert, E., Al-Tabbaa, A., Antonaci, P., Baera, C., Bajare, D., Darquennes, A., Davies, R., Ferrara, L., Jefferson, T., Litina, C., Miljevic, B., Otlewska, A., Ranogajec, J., Roig-Flores, M., Paine, K., Lukowski, P., Serna, P., Tulliani, J., Vucetic, S., Wang, J., Jonkers, H.M.: A review of self-healing concrete for damage management of structures. Adv. Mater. Interfaces (2018). https://doi.org/10.1002/admi.201800074
9. Rajczakowska, M., Habermehl-Cwirzen, K., Hedlund, H., Cwirzen, A.: Autogenous self-healing: a better solution for concrete. J. Mater. Civ. Eng. (2019). https://doi.org/10.1061/(asce)mt.1943-5533.0002764
10. Espitia Nery, M.E., Corredor Pulido, D.E., Castaño Oliveros, P.A., Rodriguez Medina, J.A., Ordoñez Bello, Q.Y., Perez Fuentes, M.S.: Mechanisms of encapsulation of bacteria in self-healing concrete: review. DYNA **86**(210), 17–22 (2019). https://doi.org/10.15446/dyna.v86n210.75343
11. Giorgio, I., Spagnuolo, M., Andreaus, U., Scerrato, D., Bersani, A.M.: In-depth gaze at the astonishing mechanical behavior of bone: a review for designing bio-inspired hierarchical metamaterials. Math. Mech. Solids **26**(7), 1074–1103 (2021). https://doi.org/10.1177/10812865209785
12. Scerrato, D., Bersani, A.M., Giorgio, I.: Bio-inspired design of a porous resorbable scaffold for bone reconstruction: a preliminary study. Biomimetics **6**(1), 18 (2021). https://doi.org/10.3390/biomimetics6010018
13. Xue, J., Briseghella, B., Huang, F., Nuti, C., Tabatabai, H., Chen, B.: Review of ultra-high performance concrete and its application in bridge engineering. Constr. Build. Mater. **260**, 119844 (2020). https://doi.org/10.1016/j.conbuildmat.2020.119844
14. Turco, E., Golaszewski, M., Giorgio, I., D'Annibale, F.: Pantographic lattices with non-orthogonal fibres: experiments and their numerical simulations. Compos. Part B Eng. **118**, 1–14 (2017). https://doi.org/10.1016/j.compositesb.2017.02.039
15. Ciallella, A., D'Annibale, F., Del Vescovo, D., Giorgio, I.: Deformation patterns in a second-gradient lattice annular plate composed of "spira mirabilis" fibers. Contin. Mech. Thermodyn. **35**(4), 1561–1580 (2023). https://doi.org/10.1007/s00161-022-01169-6
16. Eremeyev, V.A., Turco, E.: Enriched buckling for beam-lattice metamaterials. Mech. Res. Commun. **103**, 103458 (2020). https://doi.org/10.1016/j.mechrescom.2019.103458
17. Dobiszewska, M., Beycioğlu, A.: Physical properties and microstructure of concrete with waste basalt powder addition. Materials **13**(16), 3503 (2020). https://doi.org/10.3390/ma13163503
18. Sucharda, O., Marcalikova, Z., Gandel, R.: Microstructure, shrinkage, and mechanical properties of concrete with fibers and experiments of reinforced concrete beams without shear reinforcement. Materials **15**(16), 5707 (2022). https://doi.org/10.3390/ma15165707
19. Xu, F., Li, Z., Li, T., Wang, S.: The mechanical properties and microstructure of tailing recycled aggregate concrete. Materials **17**(5), 1058 (2024). https://doi.org/10.3390/ma17051058
20. Ahmad Wani, T., Ganesh, S.: Study on fresh properties, mechanical properties and microstructure behavior of fiber reinforced self compacting concrete: A review. Mater. Today Proc. **62**, 6663–6670 (2022). https://doi.org/10.1016/j.matpr.2022.04.666
21. Guo, N., Guo, J.: Mechanical properties and crack detection method of nano concrete. Int. J. Microstruct. Mater. Prop. **16**(1), 90 (2022). https://doi.org/10.1504/ijmmp.2022.123331
22. Bersani, A.M., Caressa, P.: Lagrangian descriptions of dissipative systems: a review. Math. Mech. Solids **26**(6), 785–803 (2021). https://doi.org/10.1177/1081286520971
23. Bersani, A.M., Caressa, P., dell'Isola, F.: Approximation of dissipative systems by elastic chains: numerical evidence. Math. Mech. Solids **28**(2), 501–520 (2023). https://doi.org/10.1177/10812865221081851
24. Bersani, A.M., Caressa, P., Ciallella, A.: Numerical evidence for the approximation of dissipative systems by gyroscopically coupled oscillator chains. Math. Mech. Complex Syst. **10**(3), 265–278 (2022). https://doi.org/10.2140/memocs.2022.10.265
25. Dell'Isola, F., Lekszycki, T., Pawlikowski, M., Grygoruk, R., Greco, L.: Designing a light fabric metamaterial being highly macroscopically tough under directional extension: first experimental evidence. Zeitschrift für angewandte Mathematik und Physik **66**, 3473–3498 (2015). https://doi.org/10.1007/s00033-015-0556-4
26. Barchiesi, E., dell'Isola, F., Hild, F.: On the validation of homogenized modeling for bi-pantographic metamaterials via digital image correlation. Int. J. Solids Struct. **208**, 49–62 (2021). https://doi.org/10.1016/j.ijsolstr.2020.09.036
27. Yildizdag, M.E., Tran, C.A., Barchiesi, E., Spagnuolo, M., Dell'Isola, F., Hild, F.: A multi-disciplinary approach for mechanical metamaterial synthesis: a hierarchical modular multiscale cellular structure paradigm. State of the art and future trends in material modeling, 485–505 (2019) https://doi.org/10.1007/978-3-030-30355-6_20
28. Misra, A., Lekszycki, T., Giorgio, I., Ganzosch, G., Müller, W.H., Dell'Isola, F.: Pantographic metamaterials show atypical Poynting effect reversal. Mech. Res. Commun. **89**, 6–10 (2018). https://doi.org/10.1016/j.mechrescom.2018.02.003

29. Bongué Boma, M., Brocato, M.: A continuum model of micro-cracks in concrete. Contin. Mech. Thermodyn. **22**(2), 137–161 (2009). https://doi.org/10.1007/s00161-009-0130-4
30. Carcaterra, A., dell'Isola, F., Esposito, R., Pulvirenti, M.: Macroscopic description of microscopically strongly inhomogenous systems: a mathematical basis for the synthesis of higher gradients metamaterials. Arch. Ration. Mech. Anal. **218**(3), 1239–1262 (2015). https://doi.org/10.1007/s00205-015-0879-5
31. Jouan, G., Kotronis, P., Collin, F.: Using a second gradient model to simulate the behaviour of concrete structural elements. Finite Elem. Anal. Des. **90**, 50–60 (2014). https://doi.org/10.1016/j.finel.2014.06.002
32. Germain, P.: The method of virtual power in the mechanics of continuous media, I: second-gradient theory. Math. Mech. Complex Syst. **8**(2), 153–190 (2020). https://doi.org/10.2140/memocs.2020.8.153
33. dell'Isola, F., Andreaus, U., Placidi, L.: At the origins and in the vanguard of peridynamics, non-local and higher-gradient continuum mechanics: an underestimated and still topical contribution of Gabrio Piola. Math. Mech. Solids **20**(8), 887–928 (2015). https://doi.org/10.1177/10812865135098
34. Placidi, L., dell'Isola, F., Kandalaft, A., Luciano, R., Majorana, C., Misra, A.: A granular micromechanic-based model for Ultra High Performance Fiber-Reinforced Concrete (UHP FRC). Int. J. Solids Struct. **297**, 112844 (2024). https://doi.org/10.1016/j.ijsolstr.2024.112844
35. Eremeyev, V.A., Reccia, E.: Nonlinear strain gradient and micromorphic one-dimensional elastic continua: comparison through strong ellipticity conditions. Mech. Res. Commun. **124**, 103909 (2022). https://doi.org/10.1016/j.mechrescom.2022.103909
36. dell'Isola, F., Eugster, S.R., Fedele, R., Seppecher, P.: Second-gradient continua: from lagrangian to eulerian and back. Math. Mech. Solids **27**(12), 2715–2750 (2022). https://doi.org/10.1177/1081286522107882
37. Scerrato, D., Giorgio, I., Madeo, A., Limam, A., Darve, F.: A simple non-linear model for internal friction in modified concrete. Int. J. Eng. Sci. **80**, 136–152 (2014). https://doi.org/10.1016/j.ijengsci.2014.02.021
38. Scerrato, D., Giorgio, I., Della Corte, A., Madeo, A., Limam, A.: A micro-structural model for dissipation phenomena in the concrete. Int. J. Numer. Anal. Methods Geomech. **39**(18), 2037–2052 (2015). https://doi.org/10.1002/nag.2394
39. Scerrato, D., Giorgio, I., Della Corte, A., Madeo, A., Dowling, N.E., Darve, F.: Towards the design of an enriched concrete with enhanced dissipation performances. Cem. Concr. Res. **84**, 48–61 (2016). https://doi.org/10.1016/j.cemconres.2016.03.002
40. Aretusi, G., Ciallella, A.: An Application of Coulomb-Friction Model to Predict Internal Dissipation in Concrete, pp. 73–86. Springer (2021). https://doi.org/10.1007/978-3-030-42707-8_5
41. Aretusi, G., Cardillo, C., Salvatori, A., Bednarczyk, E., Fedele, R.: A simple extension of Timoshenko beam model to describe dissipation in cementitious elements. Zeitschrift für angewandte Mathematik und Physik (2024). https://doi.org/10.1007/s00033-024-02304-w
42. Aretusi, G., Cardillo, C., Murcia Terranova, L., Bednarczyk, E.: A dissipation model for concrete based on an enhanced Timoshenko beam. Netw. Heterog. Media **19**, 700–723 (2024). https://doi.org/10.3934/nhm.2024031
43. Placidi, L., Misra, A., Barchiesi, E.: Simulation results for damage with evolving microstructure and growing strain gradient moduli. Contin. Mech. Thermodyn. **31**(4), 1143–1163 (2018). https://doi.org/10.1007/s00161-018-0693-z
44. Scrofani, A., Barchiesi, E., Chiaia, B., Misra, A., Placidi, L.: Fluid diffusion related aging effect in a concrete dam modeled as a Timoshenko beam. Math. Mech. Complex Syst. **11**(2), 313–334 (2023). https://doi.org/10.2140/memocs.2023.11.313
45. Cuomo, M., Contrafatto, L., Greco, L.: A cohesive interface model with degrading friction coefficient. Math. Mech. Complex Syst. **12**(2), 113–133 (2024). https://doi.org/10.2140/memocs.2024.12.113
46. Yilmaz, N., Yildizdag, M.E., Fabbrocino, F., Placidi, L., Misra, A.: Emergence of critical state in granular materials using a variationally-based damage-elasto-plastic micromechanical continuum model. Int. J. Numer. Anal. Methods Geomech. (2024). https://doi.org/10.1002/nag.3795
47. Funari, M.F., Spadea, S., Fabbrocino, F., Luciano, R.: A moving interface finite element formulation to predict dynamic edge debonding in FRP-strengthened concrete beams in service conditions. Fibers **8**(6), 42 (2020). https://doi.org/10.3390/fib8060042
48. Comi, C., Fedele, R., Perego, U.: A chemo-thermo-damage model for the analysis of concrete dams affected by alkali-silica reaction. Mech. Mater. **41**(3), 210–230 (2009). https://doi.org/10.1016/j.mechmat.2008.10.010
49. Ciallella, A., Pasquali, D., Gołaszewski, M., D'Annibale, F., Giorgio, I.: A rate-independent internal friction to describe the hysteretic behavior of pantographic structures under cyclic loads. Mech. Res. Commun. **116**, 103761 (2021). https://doi.org/10.1016/j.mechrescom.2021.103761
50. dell'Isola, F., Seppecher, P., Alibert, J.J., Lekszycki, T., Grygoruk, R., Pawlikowski, M., Steigmann, D., Giorgio, I., Andreaus, U., Turco, E., Gołaszewski, M., Rizzi, N., Boutin, C., Eremeyev, V.A., Misra, A., Placidi, L., Barchiesi, E., Greco, L., Cuomo, M., Cazzani, A., Corte, A.D., Battista, A., Scerrato, D., Eremeeva, I.Z., Rahali, Y., Ganghoffer, J.-F., Müller, W., Ganzosch, G., Spagnuolo, M., Pfaff, A., Barcz, K., Hoschke, K., Neggers, J., Hild, F.: Pantographic metamaterials: an example of mathematically driven design and of its technological challenges. Contin. Mech. Thermodyn. **31**(4), 851–884 (2019). https://doi.org/10.1007/s00161-018-0689-8
51. dell'Isola, F., Seppecher, P., Spagnuolo, M., Barchiesi, E., Hild, F., Lekszycki, T., Giorgio, I., Placidi, L., Andreaus, U., Cuomo, M., Eugster, S.R., Pfaff, A., Hoschke, K., Langkemper, R., Turco, E., Sarikaya, R., Misra, A., De Angelo, M., D'Annibale, F., Bouterf, A., Pinelli, X., Misra, A., Desmorat, B., Pawlikowski, M., Dupuy, C., Scerrato, D., Peyre, P., Laudato, M., Manzari, L., Göransson, P., Hesch, C., Hesch, S., Franciosi, P., Dirrenberger, J., Maurin, F., Vangelatos, Z., Grigoropoulos, C., Melissinaki, V., Farsari, M., Muller, W., Abali, B.E., Liebold, C., Ganzosch, G., Harrison, P., Drobnicki, R., Igumnov, L., Alzahrani, F., Hayat, T.: Advances in pantographic structures: design, manufacturing, models, experiments and image analyses. Contin. Mech. Thermodyn. **31**(4), 1231–1282 (2019). https://doi.org/10.1007/s00161-019-00806-x
52. Dahl, P.R.: Solid friction damping of mechanical vibrations. AIAA J. **14**(12), 1675–1682 (1976). https://doi.org/10.2514/3.61511
53. Ciallella, A., Scerrato, D., Spagnuolo, M., Giorgio, I.: A continuum model based on Rayleigh dissipation functions to describe a Coulomb-type constitutive law for internal friction in woven fabrics. Zeitschrift für angewandte Mathematik und Physik (2022). https://doi.org/10.1007/s00033-022-01845-2

54. Kachanov, M.L.: A microcrack model of rock inelasticity part I: frictional sliding on microcracks. Mech. Mater. **1**(1), 19–27 (1982). https://doi.org/10.1016/0167-6636(82)90021-7
55. Hernández-Olivares, F., Barluenga, G., Bollati, M., Witoszek, B.: Static and dynamic behaviour of recycled tyre rubber-filled concrete. Cem. Concr. Res. **32**(10), 1587–1596 (2002). https://doi.org/10.1016/s0008-8846(02)00833-5
56. Pensée, V., Kondo, D., Dormieux, L.: Micromechanical analysis of anisotropic damage in brittle materials. J. Eng. Mech. **128**(8), 889–897 (2002). https://doi.org/10.1061/(asce)0733-9399(2002)128:8(889)
57. El Shamy, U., Denissen, C.: Microscale energy dissipation mechanisms in cyclically-loaded granular soils. Geotech. Geol. Eng. **30**(2), 343–361 (2011). https://doi.org/10.1007/s10706-011-9472-3
58. Zhu, Q., Kondo, D., Shao, J., Pensee, V.: Micromechanical modelling of anisotropic damage in brittle rocks and application. Int. J. Rock Mech. Min. Sci. **45**(4), 467–477 (2008). https://doi.org/10.1016/j.ijrmms.2007.07.014
59. Dahl, P.R.: A Solid Friction Model (1968). https://doi.org/10.21236/ada041920
60. dell'Isola, F., Seppecher, P., Della Corte, A.: The postulations á la D'Alembert and á la Cauchy for higher gradient continuum theories are equivalent: a review of existing results. Proc. R. Soc. A Math. Phys. Eng. Sci. **471**(2183), 20150415 (2015). https://doi.org/10.1098/rspa.2015.0415
61. Abali, B.E., Müller, W.H., dell'Isola, F.: Theory and computation of higher gradient elasticity theories based on action principles. Arch. Appl. Mech. **87**(9), 1495–1510 (2017). https://doi.org/10.1007/s00419-017-1266-5
62. Alibert, J.-J., Seppecher, P., dell'Isola, F.: Truss modular beams with deformation energy depending on higher displacement gradients. Math. Mech. Solids **8**(1), 51–73 (2003). https://doi.org/10.1177/1081286503008001
63. La Valle, G., Soize, C.: Identifying second-gradient continuum models in particle-based materials with pairwise interactions using acoustic tensor methodology. J. Elast. (2024). https://doi.org/10.1007/s10659-024-10067-8
64. Eremeyev, V.A., Elishakoff, I.: On rotary inertia of microstuctured beams and variations thereof. Mech. Res. Commun. **135**, 104239 (2024). https://doi.org/10.1016/j.mechrescom.2023.104239
65. Del Vescovo, D., Giorgio, I.: Dynamic problems for metamaterials: review of existing models and ideas for further research. Int. J. Eng. Sci. **80**, 153–172 (2014). https://doi.org/10.1016/j.ijengsci.2014.02.022
66. dell'Isola, F., Bucci, S., Battista, A.: Against the Fragmentation of Knowledge: The Power of Multidisciplinary Research for the Design of Metamaterials, pp. 523–545. Springer (2016). https://doi.org/10.1007/978-981-10-0959-4_28
67. Eugster, S., dell'Isola, F., Steigmann, D.: Continuum theory for mechanical metamaterials with a cubic lattice substructure. Math. Mech. Complex Syst. **7**(1), 75–98 (2019). https://doi.org/10.2140/memocs.2019.7.75
68. Turco, E., Barchiesi, E., Giorgio, I., dell'Isola, F.: A Lagrangian Hencky-type non-linear model suitable for metamaterials design of shearable and extensible slender deformable bodies alternative to timoshenko theory. Int. J. Non-Linear Mech. **123**, 103481 (2020). https://doi.org/10.1016/j.ijnonlinmec.2020.103481
69. Turco, E., Barchiesi, E., dell'Isola, F.: Nonlinear dynamics of origami metamaterials: energetic discrete approach accounting for bending and in-plane deformation of facets. Zeitschrift für angewandte Mathematik und Physik (2022). https://doi.org/10.1007/s00033-022-01917-3
70. Turco, E., Barchiesi, E., Causin, A., dell'Isola, F., Solci, M.: Kresling tube metamaterial exhibits extreme large-displacement buckling behavior. Mech. Res. Commun. **134**, 104202 (2023). https://doi.org/10.1016/j.mechrescom.2023.104202
71. Barchiesi, E., dell'Isola, F., Seppecher, P., Turco, E.: A beam model for duoskelion structures derived by asymptotic homogenization and its application to axial loading problems. Eur. J. Mech. A/Solids **98**, 104848 (2023). https://doi.org/10.1016/j.euromechsol.2022.104848
72. Ciallella, A., Giorgio, I., Barchiesi, E., Alaimo, G., Cattenone, A., Smaniotto, B., Vintache, A., D'Annibale, F., dell'Isola, F., Hild, F., Auricchio, F.: A 3D pantographic metamaterial behaving as a mechanical shield: experimental and numerical evidence. Mater. Des. **237**, 112554 (2024). https://doi.org/10.1016/j.matdes.2023.112554
73. Turco, E., Barchiesi, E., Causin, A., dell'Isola, F., Solci, M.: Harnessing unconventional buckling of tube origami metamaterials based on Kresling pattern. Int. J. Solids Struct. **300**, 112925 (2024). https://doi.org/10.1016/j.ijsolstr.2024.112925
74. Babu, R., Benipal, G., Singh, A.: Constitutive modeling of concrete: an overview. Asian J. Civ. Eng. (Build. Hous.) **6**, 211–246 (2005)
75. Olsson, H., Åström, K.J., Wit, C., Gäfvert, M., Lischinsky, P.: Friction models and friction compensation. Eur. J. Control **4**(3), 176–195 (1998). https://doi.org/10.1016/s0947-3580(98)70113-x
76. Savkoor, A.R.: Section 8.3 - models of friction. In: Lemaitre, J. (ed.) Handbook of Materials Behavior Models, pp. 700–759. Academic Press, Burlington (2001). https://doi.org/10.1016/B978-012443341-0/50075-2 . https://www.sciencedirect.com/science/article/pii/B9780124433410500752
77. Wit, C., Olsson, H., Astrom, K.J., Lischinsky, P.: A new model for control of systems with friction. IEEE Trans. Autom. Control **40**(3), 419–425 (1995). https://doi.org/10.1109/9.376053
78. Dankowicz, H.: On the modeling of dynamic friction phenomena. ZAMM **79**(6), 399–409 (1999). DOI: https://doi.org/10.1002/(sici)1521-4001(199906)79:6<399::aid-zamm399>3.0.co;2-k
79. Swevers, J., Al-Bender, F., Ganseman, C.G., Projogo, T.: An integrated friction model structure with improved presliding behavior for accurate friction compensation. IEEE Trans. Autom. Control **45**(4), 675–686 (2000). https://doi.org/10.1109/9.847103
80. Bhattacharjee, S.S., Léger, P.: Seismic cracking and energy dissipation in concrete gravity dams. Earthq. Eng. Struct. Dyn. **22**(11), 991–1007 (1993). https://doi.org/10.1002/eqe.4290221106
81. Adelaide, L., Richard, B., Ragueneau, F., Cremona, C.: Thermodynamical admissibility of a set of constitutive equations coupling elasticity, isotropic damage and internal sliding. C. R. Méc. **338**(3), 158–163 (2010). https://doi.org/10.1016/j.crme.2010.03.005
82. Niiranen, J., Khakalo, S., Balobanov, V., Niemi, A.H.: Variational formulation and isogeometric analysis for fourth-order boundary value problems of gradient-elastic bar and plane strain/stress problems. Comput. Methods Appl. Mech. Eng. **308**, 182–211 (2016). https://doi.org/10.1016/j.cma.2016.05.008
83. Baroudi, D., Giorgio, I., Battista, A., Turco, E., Igumnov, L.A.: Nonlinear dynamics of uniformly loaded elastica: experimental and numerical evidence of motion around curled stable equilibrium configurations. ZAMM-Zeitschrift für Angewandte Mathematik und Mechanik **99**(7), 201800121 (2019). https://doi.org/10.1002/zamm.201800121

84. Giorgio, I., Del Vescovo, D.: Energy-based trajectory tracking and vibration control for multilink highly flexible manipulators. Math. Mech. Complex Syst. **7**(2), 159–174 (2019)
85. Giorgio, I.: A discrete formulation of Kirchhoff rods in large-motion dynamics. Math. Mech. Solids **25**(5), 1081–1100 (2020). https://doi.org/10.1177/1081286519900902
86. Greco, L.: An iso-parametric G^1-conforming finite element for the nonlinear analysis of Kirchhoff rod. Part I: the 2D case. Contin. Mech. Thermodyn. **32**(5), 1473–1496 (2020). https://doi.org/10.1007/s00161-020-00861-9
87. Greco, L., Cammarata, A., Castello, D., Cuomo, M.: An objective FE-formulation for Cosserat rods based on the spherical Bézier interpolation. Comput. Methods Appl. Mech. Eng. **425**, 116947 (2024). https://doi.org/10.1016/j.cma.2024.116947
88. Angelo, M.D., Placidi, L., Nejadsadeghi, N., Misra, A.: Non-standard Timoshenko beam model for chiral metamaterial: identification of stiffness parameters. Mech. Res. Commun. **103**, 103462 (2020). https://doi.org/10.1016/j.mechrescom.2019.103462
89. Fedele, R., Maier, G., Miller, B.: Identification of elastic stiffness and local stresses in concrete dams by in situ tests and neural networks. Struct. Infrastruct. Eng. **1**(3), 165–180 (2005). https://doi.org/10.1080/15732470500030513
90. Fedele, R.: Simultaneous assessment of mechanical properties and boundary conditions based on Digital Image Correlation. Exp. Mech. **55**, 139–153 (2015). https://doi.org/10.1007/s11340-014-9931-x
91. Abali, B.E., Wu, C.-C., Müller, W.H.: An energy-based method to determine material constants in nonlinear rheology with applications. Contin. Mech. Thermodyn. **28**(5), 1221–1246 (2015). https://doi.org/10.1007/s00161-015-0472-z
92. De Angelo, M., Barchiesi, E., Giorgio, I., Abali, B.E.: Numerical identification of constitutive parameters in reduced-order bi-dimensional models for pantographic structures: application to out-of-plane buckling. Arch. Appl. Mech. **89**(7), 1333–1358 (2019). https://doi.org/10.1007/s00419-018-01506-9
93. Shekarchizadeh, N., Abali, B.E., Barchiesi, E., Bersani, A.M.: Inverse analysis of metamaterials and parameter determination by means of an automatized optimization problem. ZAMM - Journal of Applied Mathematics and Mechanics / Zeitschrift für Angewandte Mathematik und Mechanik **101**(8) (2021) https://doi.org/10.1002/zamm.202000277
94. Ciallella, A., La Valle, G., Vintache, A., Smaniotto, B., Hild, F.: Deformation mode in 3-point flexure on pantographic block. Int. J. Solids Struct. **265–266**, 112129 (2023). https://doi.org/10.1016/j.ijsolstr.2023.112129
95. Heiduschke, K.: On tensor projections, stress or stretch vectors and their relations to Mohr's three circles. Math. Mech. Complex Syst. **12**(2), 173–216 (2024). https://doi.org/10.2140/memocs.2024.12.173
96. Wang, X., Schiavone, P.: An elliptical incompressible liquid inclusion in an infinite anisotropic elastic space. Math. Mech. Complex Syst. **12**(2), 217–232 (2024). https://doi.org/10.2140/memocs.2024.12.217
97. Federico, S., Alhasadi, M.F., Imatani, S., Epstein, M.: A three-dimensional Airy stress function. Math. Mech. Complex Syst. **11**(3), 429–449 (2023). https://doi.org/10.2140/memocs.2023.11.429
98. Giorgio, I.: A variational formulation for one-dimensional linear thermoviscoelasticity. Math. Mech. Complex Syst. **9**(4), 397–412 (2022). https://doi.org/10.2140/memocs.2021.9.397
99. Giorgio, I., Placidi, L.: A variational formulation for three-dimensional linear thermoelasticity with 'thermal inertia'. Meccanica (2024). https://doi.org/10.1007/s11012-024-01796-0

Chapter 5

Evaluating corneal biomechanics using shear wave elastography and finite element modeling

Chapter abstract

This investigation delivers an in-depth examination of corneal biomechanics utilizing shear wave elastography, employing finite element modeling to explore the mechanical characteristics of corneal tissue. A three-dimensional axis-symmetric corneal model was crafted and tested under various simulated scenarios, including intraocular pressure (IOP) alterations, boundary conditions, excitation pressure, and corneal curvature changes. The model features hyper-viscoelastic material properties, providing a precise depiction of the cornea's nonlinear behavior within physiological pressure limits. Parametric analyses were performed to evaluate how shear wave velocity responds to alterations in corneal biomechanical parameters. Findings indicated that intrinsic material attributes, especially viscoelastic constants, significantly affect shear wave propagation, whereas external elements such as IOP and boundary conditions exert minimal effect. The study also utilized the Taguchi method for optimizing parameters, identifying the first relaxation time as a crucial factor affecting shear wave velocity. This work provides essential insights into corneal biomechanics, suggesting enhancements in diagnostic technology and a deeper understanding of corneal dynamics under various physiological situations. The research supports the potential use of shear wave elastography as a non-invasive technique for determining corneal stiffness, thus advancing clinical practices in ophthalmology.

Continuum Mech. Thermodyn. (2025) 37:12
https://doi.org/10.1007/s00161-024-01340-1

ORIGINAL ARTICLE

Pouria Mazinani · Christian Cardillo · Peiman Mosaddegh

Evaluating corneal biomechanics using shear wave elastography and finite element modeling: sensitivity analysis and parametric optimization

Received: 19 October 2024 / Accepted: 6 November 2024 /

Abstract This study presents a comprehensive analysis of corneal biomechanics using shear wave elastography, leveraging finite element modeling to investigate the mechanical properties of corneal tissue. A 3D axis-symmetric corneal model was developed and subjected to various simulated conditions, including changes in intraocular pressure (IOP), boundary conditions, excitation pressure, and corneal curvature. The model incorporates hyper-viscoelastic material properties, allowing for an accurate representation of the cornea nonlinear behavior within physiological pressure ranges. Parametric studies were conducted to assess the sensitivity of shear wave velocity to variations in corneal biomechanical parameters. The results revealed that intrinsic material properties, particularly viscoelastic constants, significantly influence shear wave propagation, while external factors such as IOP and boundary conditions have minimal impact. The study also employed the Taguchi method for parametric optimization, identifying the first relaxation time as a critical factor affecting shear wave velocity. This work offers valuable insights into corneal biomechanics, with implications for improving diagnostic techniques and enhancing our understanding of corneal behavior under different physiological conditions. The findings support the potential application of shear wave elastography as a non-invasive tool for assessing corneal stiffness and advancing clinical practice in ophthalmology.

Keywords Corneal biomechanics · Shear wave elastography (SWE) · Hyper-viscoelastic materials · Taguchi method · Non-invasive assessment

1 Introduction

Over the last decade, there has been significant research interest in ultrasound-based elastography within the medical ultrasound community. Scholars have hypothesized that incorporating data on tissue mechanical properties could offer valuable enhancements to conventional B-mode ultrasound or magnetic resonance imaging (MRI). Various ultrasound-based techniques have been explored to evaluate the viscoelastic properties of tissues, with potential diagnostic applications in areas such as breast cancer diagnosis [1,2], staging liver fibrosis [3–5], assessing arterial wall characteristics [6,7], and imaging cardiac muscle elasticity [8,9].

P. Mazinani ( ) · P. Mosaddegh
Department of Mechanical Engineering, Isfahan University of Technology, Isfahan, Iran
e-mail: pouria.mazinani789@gmail.com

P. Mosaddegh
e-mail: mosadegh@iut.ac.ir

C. Cardillo ( )
Department of Civil Engineering and Architecture, University of Catania, Catania, Italy
e-mail: christian.cardillo@phd.unict.it

Hamilton et al. [10] measured Young's modulus of cornea in young healthy eyes and found it to be 0.29 ± 0.06 MPa. The Variations of Young's modulus can lead to clinically significant errors in IOP measurements using applanation tonometry.

To find the shear wave velocity on the cornea, Tanter et al. [11] used ultrasonic systems and the supersonic shear imaging (SSI) technique on ex vivo porcine corneas, real-time and high-resolution maps of corneal elasticity. After the SSI technique, the elastic cornea has been modeled. the shear wave velocity has been reported as 7.96 m/s for the healthy Young's modulus 190 ± 32 kPa. shows potential for in vivo investigations, with significant increases in Young's modulus observed after photodynamic Riboflavin/UVA-induced corneal cross-linking.

By using the reflected shear waves in noninvasive stiffness imaging techniques, Deffieux et al. [12] introduce a directional filter to address artifacts. This filter improves elastography methods in high-stiffness contrast situations by propagating the forward- and backward-waves separately.

For assessing the cornea elastic anisotropy in vivo and ex vivo, Supersonic Shear Imaging (SSI) elastography is used on porcine eyes, showing higher shear wave speed along the horizontal meridian, consistent with collagen fiber orientation. This method is a recent development, and its findings aid in predicting corneal response to surgery and preventing complications in ophthalmology [13].

Researchers used SSI to assess corneal stiffening in rabbits undergoing iontophoresis-assisted transepithelial corneal collagen cross-linking (I-CXL). The behavior of the cornea showed that with the increase of the IOP, the stiffness of the cornea will increase and become less deformed. As a result, the shear wave velocity increases with the increase of stiffness of the cornea. Ex vivo inflation tests with SSI successfully evaluated the CXL process under physiological conditions [14].

Han et al. [15] used a modified Rayleigh-Lamb frequency equation and non-contact optical coherence elastography to measure corneal viscoelastic properties. By using this technique, Young's modulus at approximately 60 kPa and shear viscosity at 0.33 Pa are estimated for porcine corneas.

Nguyen et al. [16] used shear wave elastography (SWE) based on optical coherence tomography to investigate the elasticity of eye tissue. A pulse compression approach is proposed to minimize ultrasound (US) pressure for safety in ophthalmology. Successful measurements of SWE in tissue simulator phantoms at low US pressures were demonstrated.

Corneal elasticity is essential for human vision and can be affected by eye pathology and surgical procedures. Ultrasound-based elastography has become a promising and efficient method for evaluating the mechanical properties of tissues, such as the cornea. Conventional methods, such as tonometry and ocular response analyzer (ORA), present limited information on corneal elasticity [17].

For measuring the soft tissue mechanical properties, Elastography techniques are used, utilizing both ultrasonic and optical approaches. for high spatial resolution, Optical Coherence Elastography (OCE) is offered, but some methods may introduce errors. Ophir proposed Ultrasound-based elastography; this method measures strain distribution in soft tissues but requires high-frequency ultrasound for accurate measurements [18–20].

"Remote palpation" using acoustic radiation force (ARF) has been developed to evaluate corneal biomechanics noninvasively. The base of ARF is imaging modalities, including vibroacoustic imaging, harmonic imaging, ARFI imaging, and shear wave elasticity imaging, which have been used to assess soft tissue mechanical properties [21,22].

Ultrasound shear imaging (SSI) provides a few elastic images but has limited image resolution. By using a common frequency range for ophthalmic applications to assess corneal elasticity, a new high-resolution shear wave imaging (HR-SWI) method has been developed. Overall, for quantitative measurement of corneal elasticity, which may be useful in diagnosing corneal pathology and evaluating treatment efficacy, the development of advanced elastography techniques such as HR-SWI provides valuable tools [11,23].

Chen et al. [24] introduced a high-resolution shear wave imaging (HR-SWI) method for estimating corneal elasticity. A dual-mode high-resolution shear wave imaging system was used to measure corneal elasticity in a human cornea model. In this experiment, the time-of-flight algorithm was used to calculate the group velocity of shear waves in different positions. As a result, Lamb's theory and the group velocity of shear waves were used to calculate Young's modulus of the cornea.

OCE, by using the AirPuff, measured shear modulus in human corneas (72 ± 14 kPa) noninvasively. No wave speed correlation with IOP at 13–18 mmHg was found; this method, by using low-energy elastic waves, was safely stimulated on the cornea in the range of 10 kHz. By calculating the shear wave speed, in [25] the shear modulus was evaluated.

Clinical measurement of corneal biomechanics is crucial for diagnosing, tracking, and treating ocular diseases. Interdisciplinary collaborations have advanced our understanding of corneal biomechanics, leading

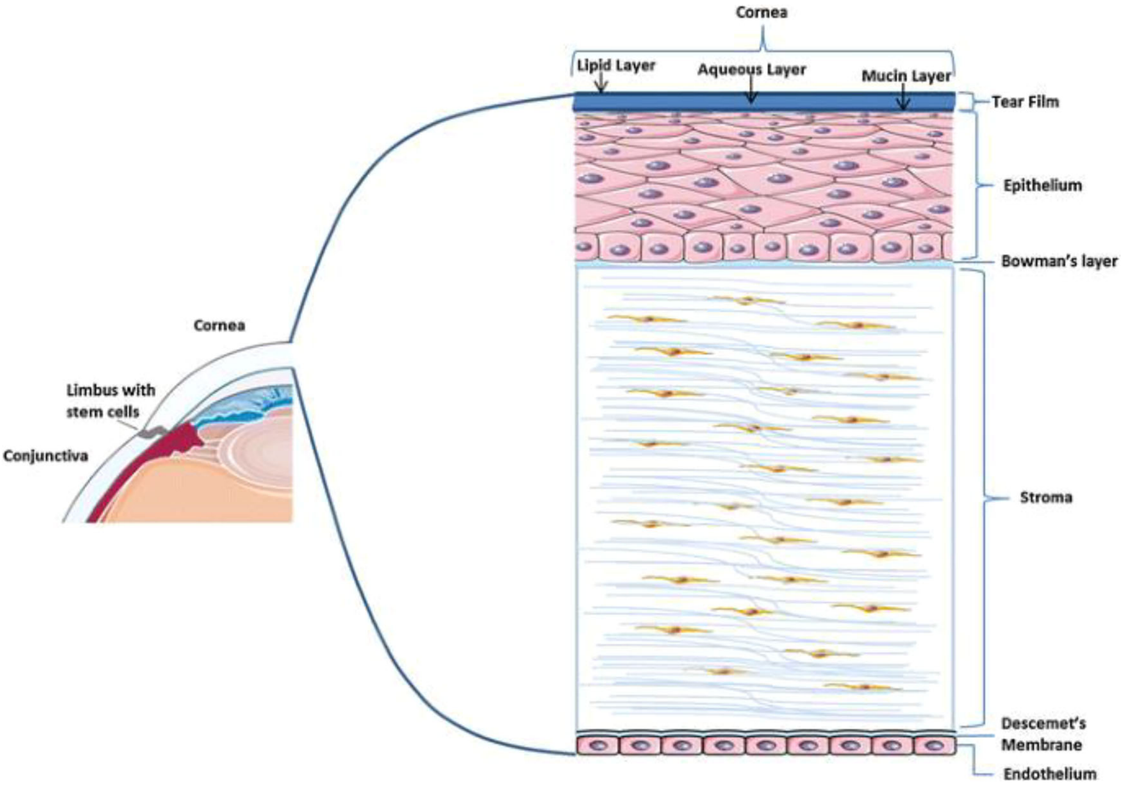

Fig. 1 Structure of the cornea

to innovations in testing methods both in lab settings and in vivo. However, assessing corneal biomechanics in living tissue remains challenging, and ongoing research aims to refine existing techniques for better diagnosis and management of ocular conditions [26]. Therefore, the objective of the current study is to develop a robust finite element model combined with SWE to investigate the biomechanical properties of the cornea.

Different elastography methods for finding the mechanical properties were evaluated in the literature as above mentioned. In this paper, the excitation pressure for propagating the shear wave on the cornea is used by using the incident wave module in Abaqus with a particular amplitude. This method helps to find the shear wave velocity of a specific point of the cornea and, after that, obtain Young's modulus of the hyper-viscoelastic cornea.

The cornea has a highly organized microstructure that is critical to its transparency, strength, and refractive properties (see Fig. 1). The key components of the corneal microstructure include [27]: (1) Epithelium; (2) Bowman's layer; (3) Stroma; (4) Descemet's membrane; (5) Endothelium.

The epithelium is the outermost layer of the cornea, consisting of multiple layers of tightly packed epithelial cells. These cells are crucial for providing a barrier against dust, debris, and microorganisms, and they help maintain corneal hydration through tear film interactions. Bowman's layer is a thin, acellular layer located just beneath the epithelium. It is composed mainly of randomly arranged collagen fibers. Although thin, it provides some degree of strength and acts as a protective barrier for the underlying stroma. This last is the thickest layer of the cornea, making up about 90% of its thickness. The stroma consists of regularly arranged collagen fibrils (primarily Type I collagen) that are organized into parallel lamellae. This precise arrangement is essential for corneal transparency, as it minimizes light scattering. The stroma also contains keratocytes (specialized fibroblasts) that maintain the extracellular matrix, which includes proteoglycans that regulate the spacing of collagen fibrils. Descemet's membrane is a thin but strong layer that serves as the basement membrane for the endothelium. It is composed of a network of collagen (primarily Type IV collagen) and other extracellular matrix proteins, providing elasticity and contributing to the overall structural integrity of the cornea. The endothelium is the innermost layer of the cornea, composed of a single layer of hexagonal endothelial cells. These cells are responsible for maintaining corneal transparency by regulating fluid balance within the stroma, preventing it from swelling and becoming opaque. They pump excess fluid out of the stroma, which is crucial for keeping the cornea clear. Then, we must also mention nerve fibers. In fact, the cornea is densely innervated, with nerve fibers primarily originating from the ophthalmic branch of the trigeminal nerve. These nerves penetrate the corneal stroma and form a network that extends into the epithelium, making the cornea one of the most sensitive tissues in the body. Although not part of the central cornea, there is also the limbal region at the periphery of the cornea where corneal epithelial stem cells reside. These stem cells are vital for the regeneration of the corneal epithelium. This highly organized and specialized microstructure is essential for the cornea role in focusing light onto the retina and maintaining clear vision. The precise arrangement of collagen fibers in the stroma and the health of the endothelial layer are particularly crucial for maintaining corneal transparency and overall ocular health.

Because of such a complex structure, it is possible to model the cornea tissue with different levels of complexity and accuracy. Generally speaking, the cornea is a complex biological tissue with heterogeneous and anisotropic properties, and it exhibits nonlinear, viscoelastic, and time-dependent behaviours. The simplest way to describe the mechanical behavior of the cornea is by using some standard continuum models where material parameters are considered in an effective fashion. This is the first level of complexity that fits a preliminary study to assess the main essential aspects to be considered in successive phases. Herein, we refrain from considering more complex models since we want to explore how simple models accounting for factors such as viscoelasticity, boundary conditions, and intraocular pressure can be fruitfully used in clinical applications.

In future developments, we can conceive more complex ways to model the cornea that can be used to describe better the macroscopic behavior inherited by the microstructure. Generalized continuum mechanics, which includes advanced models like micropolar, micromorphic, nonlocal, and second or higher gradient theories can provide a more accurate description of the cornea mechanical behaviour by incorporating these complexities (see, e.g., [28–31]).

Micropolar theories account for the rotational effects of particles within the material and are useful for modelling materials with microstructures, such as the collagen fibrils in the corneal stroma. By incorporating rotational degrees of freedom, micropolar theories can capture the behaviour of the cornea more accurately, especially in situations where the microstructure plays a significant role, such as in response to shear deformations or in areas near the limbus where structural properties change (see, for more details, [32–35]).

Micromorphic theories are an extension of micropolar theories and include additional micro-deformations beyond simple rotations. They can describe the deformation of the cornea at different scales, considering the influence of the microstructure on the overall mechanical response. For example, they can describe the responses due to the fibre network within the tissue (see, e.g., [36–41], which models these scenarios).

Nonlocal and second gradient theories incorporate the influence of the material microstructure by allowing the stress at a point to depend on the strain at distant points. This is particularly relevant for the cornea, where the interaction between collagen fibrils and the extracellular matrix can affect mechanical behaviour at scales larger than the fibril spacing. Nonlocal theories can help model the cornea response to external forces more accurately by accounting for long-range interactions within its microstructure (see, e.g., [42–45]). Indeed, collagen fibrils and the extracellular matrix are critical to the microstructure of the cornea and play a key role in maintaining its transparency and mechanical strength. The cornea needs to be transparent to allow light to pass through and reach the retina. Therefore, collagen fibrils in the cornea are arranged in a very regular, parallel pattern within the extracellular matrix. This specific organization minimizes light scattering, which is crucial for transparency. This arrangement, however, affects also the mechanical properties of the corneal tissue, since they behave like fibre-reinforcement in a surrounding matrix and the long-range interactions. The extracellular matrix, hence, provides structural support to the cornea, while collagen fibrils give it tensile strength and flexibility. This combination allows the cornea to maintain its shape, which is important for focusing light properly onto the retina. In summary, collagen fibrils and the extracellular matrix create the organized microstructure of the cornea, which is essential for both its transparency and its structural integrity.

By extending beyond traditional continuum mechanics, these advanced models can capture the nuanced behaviour of the cornea more effectively, providing valuable insights for both diagnostic and therapeutic applications in ophthalmology. Moreover, since these advanced models are often based on variational formulations, they can be easily and efficiently implemented in finite element models to simulate the cornea behaviour under various conditions. These models can include complex boundary conditions, variable material properties, and interactions between different layers of the cornea, leading to more accurate predictions of its mechanical response in clinical scenarios. Of particular interest could be the perspective to exploit this powerful formulation to describe complex dissipative phenomena [46–50], damage accumulation (such as in keratoconus, where the cornea gets thinner and gradually bulges outward into a cone shape) [51–55], as well as regeneration and growth [56–58]. In addition, the complex microstructure can significantly impact the mechanical response and, specifically, wave propagation [59–63]. Since this dynamical behaviour is used to identify some crucial characteristics of the cornea, a more accurate description of this phenomenon could help shed more light on the knowledge of the cornea.

In the application of generalized continuum mechanics to model the mechanical behaviour of the cornea, parameter identification is a critical process. In this context, it involves determining the specific values of material properties and model parameters that accurately describe the cornea complex mechanical behaviour (see [64–68] for some application examples). It is crucial for ensuring that models accurately reflect the true mechanical behaviour of the cornea. It underpins the reliability of simulations, the effectiveness of personalized medical treatments, and the accuracy of diagnostic tools. In the context of generalized continuum mechanics, precise identification of parameters is essential for capturing the cornea complex biomechanical properties, leading to better patient outcomes and advancements in ophthalmic research and practice.

2 Method

Corneal tissue shows a highly nonlinear behavior [6]; however, within the range of intraocular pressures (IOP) for healthy cornea between 10 and 25 mmHg, the response of tissue can be approximated as quasi-linear, which is helpful for a simplification in modeling. For this specific range, a hyper-viscoelastic model of the Stroma (Stroma represents 80% of the cornea) can be employed [69]. Furthermore, the Stroma can be treated as incompressible due to its high-water content [70]. The cornea has two significant properties: hyper-elastic and viscoelastic [71].

The cornea is modeled using a hyperelastic Neo-Hookean model, which is described by two unknown material parameters. The dissipative behavior is characterized by the modified Maxwell viscoelastic model, expressed in terms of the generalized Prony series.

The hyperelastic material is defined by a potential function which gives the strain energy density $W = W(\boldsymbol{C}) = W(I_1, I_2, I_3)$, where:

1. $\boldsymbol{C}$ is the right Cauchy–Green deformation tensor;
2. I_1, I_2, I_3 are the three principal invariants of the deformation tensor $\boldsymbol{C}$;

In this context, the second Piola-Kirchhoff stress tensor, $\boldsymbol{S}$, can be evaluated as follows:

$$\boldsymbol{S} = 2\frac{\partial W(I_1, I_2, I_3)}{\partial \boldsymbol{C}} \tag{1}$$

The invariants I_1, I_2 and I_3 of the right Cauchy–Green deformation tensor $\boldsymbol{C}$ are given by:

$$I_1 = \mathrm{tr}(\boldsymbol{C}) \tag{2}$$

$$I_2 = \frac{1}{2}\left[(\mathrm{tr}(\boldsymbol{C}))^2 - \mathrm{tr}(\boldsymbol{C}^2)\right] \tag{3}$$

$$I_3 = \det(\boldsymbol{C}) \tag{4}$$

Therefore, the Piola-Kirchhoff stress tensor can be specified as:

$$\boldsymbol{S} = 2\left(\frac{\partial W}{\partial I_1}\frac{\partial I_1}{\partial \boldsymbol{C}} + \frac{\partial W}{\partial I_2}\frac{\partial I_2}{\partial \boldsymbol{C}} + \frac{\partial W}{\partial I_3}\frac{\partial I_3}{\partial \boldsymbol{C}}\right) \tag{5}$$

The stored energy density W can be further divided into two parts [72]:

1. The isochoric part, $\bar{W}$
2. The hydrostatic part, W_h

As a result, the stored energy can be expressed in the form:

$$W = \bar{W} + W_h = f\left(\bar{I}_1 - 3, \bar{I}_2 - 3\right) + P(J - 1) \tag{6}$$

This decomposition separates the energy associated with volume-preserving (isochoric) deformations, expressed by the function f, from the energy associated with changes in volume (hydrostatic deformations) given by the function P. This partition is beneficial for accurately modeling the complex behavior of hyperelastic materials, such as the cornea.

Besides, $\bar{I}_1 = J^{-2/3}I_1$ and $\bar{I}_2 = J^{-4/3}I_2$ define the first and second invariants of the isochoric part $\bar{\boldsymbol{C}} = \det(\boldsymbol{C})^{-1/3}\boldsymbol{C}$ of the right Cauchy–Green tensor. Additionally, $J = \det(\boldsymbol{C})^{1/2}$ represents the volumetric change ratio.

The stored energy density due to the hydrostatic pressure can be defined as:

$$P\,(J-1) = \sum_{m=1}^{M} \frac{1}{D_m}\,(J-1)^{2m} \tag{7}$$

where D_m represent compressibility constants of the material and M is the upper limit for m. Therefore, the complete strain energy density function is described by the expression:

$$W = \sum_{i,j=0}^{N_i,N_j} C_{ij}\left(\bar{I}_1, -3\right)^i \left(\bar{I}_2 - 3\right)^j + \sum_{m=1}^{M} \frac{1}{D_m}\,(J-1)^{2m} \tag{8}$$

where C_{ij} are constant material coefficients and the bulk modulus, while N_i and N_j are the upper limits for i and j, respectively. Equation 8 describes a common hyperelastic model used for the cornea [72]. The chosen hyperelastic model is one that balances simplicity and the ability to accurately represent the experimental data. This ensures that the model is not overly complex while still providing a precise fit to the observed behavior of the corneal tissue. This approach minimizes computational effort and avoids overfitting, ensuring that the results are both reliable and reproducible. Therefore, in this study, we set the upper limits as follows:

$$N_i = 1 \tag{9}$$

$$N_j = 0 \tag{10}$$

$$M = 1 \tag{11}$$

By substituting the settings 9, 10, and 11 into Eq. 8, the neo-Hookean strain energy function assumed is:

$$W = C_{10}\left(\bar{I}_1 - 3\right) + \frac{1}{D_1}\,(J-1)^2 \tag{12}$$

The constants of the stored energy function W are determined based on experimental imaging [73–75]. In laboratory experiments, various methods are available to determine these constants [76,77]. In the current study, the constants were obtained using images from shear wave elastography.

Additionally, the constants of the Neo-Hookean model for small strains exhibit the following relationship with the bulk modulus, K, and shear modulus, G:

$$C_{10} = \frac{\mathrm{G}}{2} = \frac{\mathrm{E}}{4\,(1+\nu)} \tag{13}$$

$$D_1 = \frac{2}{\mathrm{K}} = \frac{6\,(1-2\nu)}{\mathrm{E}} \tag{14}$$

where E is the elastic modulus and ν is the Poisson ratio, set to .49.

To describe the dissipative effect in the cornea tissue, the generalized Maxwell model, also known as the Maxwell–Wiechert model, is employed [75]. It is one of the most general forms of the linear model for viscoelasticity. In particular, it represents an extension of the traditional Maxwell model, which consists of a spring and a dashpot connected in series. In the generalized Maxwell model, multiple Maxwell elements are assembled in parallel, allowing for a more accurate representation of the viscoelastic material.

To describe the viscoelastic behavior of materials by means of their relaxation modulus as a function of time, the mathematical representation employing the Prony series is used to express the relaxation modulus $G\,(t)$ of the corneal material. The Prony series is explicitly given by:

$$G\,(t) = \sum_{i=1}^{n} G_i e^{-t/\tau_i} + G_0 \tag{15}$$

Table 1 Prony coefficients ($g_i = G_i/G_0$) normalized by $G_0 = 0.14$ MPa and the relaxation times for the porcine cornea

g_1 (…)	g_2 (…)	g_3 (…)	τ_1 (second)	τ_2 (second)	τ_3 (second)
0.1105	0.1114	0.1888	0.5866	7.35	42.58

where G_i and τ_i are parameters of the model, the shear modulus of the single ith element of the parallel in the generalized Maxwell model (the Prony coefficients) and the corresponding relaxation time, respectively. The constant n is the number of Prony series and G_0 is the static modulus. In formula:

$$G_0 = \frac{\sigma_0}{\varepsilon_0} \tag{16}$$

where the symbol σ_0 represents the residual stress, while ε_0 denotes the constant strain.

This formulation allows for capturing both the elastic and viscous responses of materials over time.

The steps to perform using the Prony series in studying the viscoelastic material of the cornea are: (1) *Data collection*: perform Dynamic Mechanical Analysis (DMA) or similar tests to obtain stress-strain data under varying conditions (e.g., creep and relaxation tests). This data provides insights into how the material behaves under different rates of loading and unloading; (2) *Data regression*: fit the collected data to a Prony series model using nonlinear regression techniques, such as the Marquardt-Levenberg algorithm. This involves minimizing the difference between experimental data and model predictions to determine optimal values for G_i and τ_i; (3) *Implementation in Software*: utilize Computer-Aided Engineering (CAE) software, in our case Abaqus, to implement the Prony series. In Abaqus, we input the calculated Prony coefficients and relaxation times into a designated table, allowing for accurate simulation of viscoelastic behavior in structural analyses; (4) *Validation*: validate the model by comparing simulated results with experimental data. This will ensure that the model accurately predicts material behavior across a range of frequencies and strain rates; (5) *Iterative Refinement*: adjust the model based on validation results, possibly increasing the number of terms in the Prony series if necessary to improve accuracy. This iterative process helps refine predictions and enhances understanding of material properties under different loading scenarios.

The hyper-viscoelastic model of the cornea is developed accordingly. The hyperelastic property deals with deformation-recovery, while the viscoelastic property involves time-dependence, both of which need to be considered simultaneously under loading conditions.

A finite element model with a three-dimensional axis-symmetric geometry was used to study corneal shear wave velocity. To replicate the experimental conditions accurately, the pressure characteristics generated by the in vivo Air Puff system of Kling et al. [78] are adopted. FEM techniques were then employed to identify the biomechanical parameter set that best represented the various experimental conditions. Subsequently, Sensitivity analysis was performed to determine the parameters most strongly correlated with the corneal shear wave velocity response following stimulation pressure.

An innovative approach for examining the viscoelastic properties of soft tissue involves elastography based on shear wave propagation. This method entails the generation and analysis of transient shear waves within tissue, enabling the assessment of its temporal behavior and shear characteristics.

Shear wave-based elastography employs transient vibration, facilitating the examination of deeper tissues. This motion allows for the gradual propagation of shear waves through the tissue, which can be detected using ultrasound waves. The velocity of shear wave propagation is contingent upon the tissue stiffness.

Through the utilization of Equation $G = 3\rho c^2$ to calculate shear wave velocity, an approximate determination of the tissue elasticity modulus can be achieved. This method of shear wave-based elastography offers the capacity to generate quantitative outcomes and temporal diagrams, thereby furnishing localized insights into tissue properties. The implementation of this approach, commonly known as shear wave elastography, necessitates not only advancements in imaging techniques but also developments in the realm of medical imaging employing ultrasound waves.

The rationale behind employing this method lies in its capability to discern images with an approximate resolution of one millimeter and its imaging rate, which can be determined by the time necessary to scan the entire desired volume. The efficacy of shear wave elastography systems can be assessed through the utilization of calibrated phantoms featuring specific elasticity coefficients [72].

In this paper, the data, such as the Prony series for viscoelastic material and hyper-elastic coefficient used in the simulation, were derived from the previous [79].

Table 2 Hyper-elastic value of Neo Hookean model for the porcine cornea

IOP (mmHg)	C_{10} (MPa)	D_1 (MPa^{-1})
16	0.316	0.185

To estimate $\boldsymbol{C}_{10}$ and $\boldsymbol{D}_1$ using experimental data or computational simulations, you would typically fit the neo-Hookean model to your data. This often involves minimizing the difference between the experimental or simulated strain energy density.

In the present study, shear wave elastography images were utilized to obtain the constants $\boldsymbol{C}_{10}$ and $\boldsymbol{D}_1$. Initially, an approximate guess for these two constants was made. Subsequently, the Levenberg-Marquardt optimization algorithm, implemented in MATLAB software, was employed to iteratively refine these estimates until they converged to their correct values (see Table 2).

Shear wave velocity characteristics The elastography setup used acoustic radiation force to excite the cornea and propagate the shear wave in it. After the experiment, while the experiment is done, the viscoelastic property (Prony series and elastic modulus) and the hyper-elastic coefficient (Neo-Hookean model) appear. Elastography systems are founded upon the propagation of shear waves to ascertain shear wave velocity, enabling the derivation of Young's modulus in soft tissues. Consequently, the initiation of the simulation process in Abaqus hinges upon acquiring the properties of the cornea and its shear wave velocity.

The purpose of this study was to simulate the shear wave elastography experiments by using ABAQUS and performing sensitive analyses for several terms of the corneal properties.

3 Structural finite element simulation

Geometry A 3-D axis-symmetric Corneal model was defined for the corneal conditions and boundaries. The external thickness of the cornea, assumed to be 0.65 mm, has been modeled with 13 nodes with quadratic displacement behavior. Initial corneal curvatures were adjusted to match the experimental values after the IOP (16 mmHg) application. The limbus was defined as a spring and damper that connects the cornea and sclera.

Material models The corneal tissue was modeled by a Hyper-Viscoelastic material as previously specified. Initially, the hyper-elastic Neo-Hookean model of the cornea, based on the stored energy function, can be simplified as a linear equation with two unknown parameters. Then, the modified Maxwell viscoelastic model of the cornea, which has analytical form extended with the Prony series model, is proposed from a materials mechanics perspective. In general, it can be attributed to the non-linear hyper-viscoelastic problem. It is a complex problem in the field of mechanics because the relationship between the deformation rate and time rate is a series of energy conversion behaviors.

FEM settings In the FEM implementation, the cornea is considered as a two-dimensional axisymmetric geometry. A convergence analysis was performed on a range of element sizes in this simulation, with a focus on the displacement of the corneal apex. The specific displacement of this point was calculated at the moment the pressure stimulus affected it, and all displacements were reported at a specified time point. The selected element type is C3D8R in Abaqus, and its maximum size is 0.05 mm. This particular element utilizes a reduced integration method, which is favored in simulations of shear wave propagation in the cornea because of its computational efficiency, ability to prevent shear locking, and suitability for modeling soft tissue mechanics. It enables accurate simulation of complex, nonlinear behaviors while maintaining manageable computational requirements.

The solution method used in Abaqus software is "Dynamic Explicit". This choice is made because it is an adequate algorithm for simulating wave propagation and reduces the solution time compared to other methods. Following a Courant–Friedrich–Levy condition, we set the time step at 0.7 s.

Boundary conditions and loads For the simulation of the ex vivo whole globe, the sclera was fixed, mimicking the fixation of the cornea in the eye-holder in the experiments. For the in vivo condition, the corneal was damped along the vertical symmetry axis representing the ocular muscles and other surrounding fatty tissue. It was posited that the external damping factors could be consolidated into a singular vertical damping component, with horizontal damping influences being disregarded. The vertical damping was incorporated through a massless longitudinal spring-damper system, represented by a uniaxial tension-compression element characterized by a spring constant (5×10^6N/m) and a damping coefficient of 1. In the model, intraocular

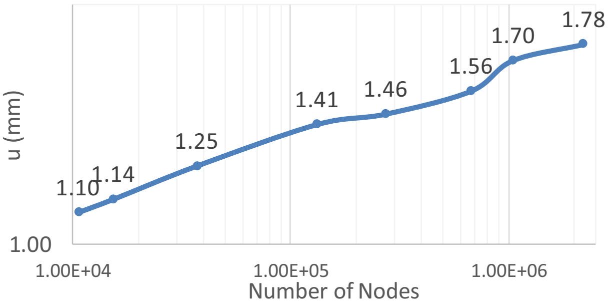

Fig. 2 Convergence analysis: top displacement vs number of elements

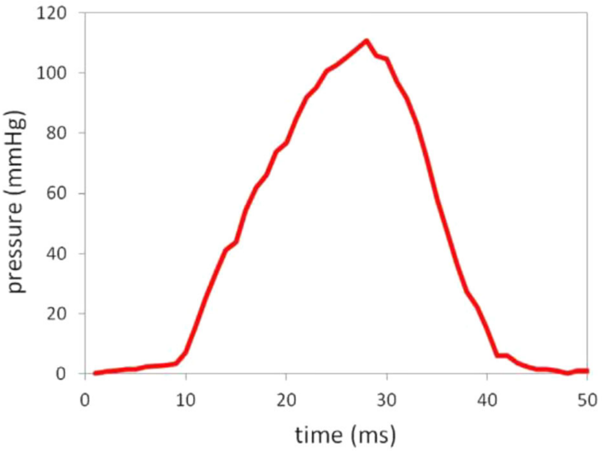

Fig. 3 Experimentally measured temporal air-puff profile [78]

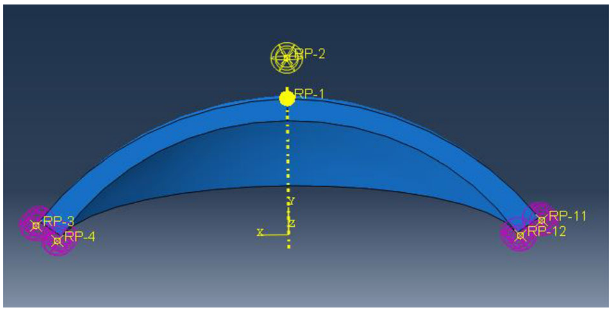

Fig. 4 Excitation force for propagation of the shear wave in ABAQUS

pressure was applied to the internal surfaces of the cornea, limbus, and sclera based on experimental data points of 10, 15, 20, 30, and 50 mmHg.

Excitation pressure A pressure load was exerted on the edges of the anterior corneal surface elements, corresponding to the spatial pressure distribution resulting from the incident wave at varying indentation depths. This measure was deemed essential due to the notable alterations in fluid dynamics characteristics as the cornea undergoes deformation and shear wave propagation. Furthermore, the incident wave and pressure variation with time (measured experimentally with the pressure tensor with the specific amplitude) was considered by multiplying the current pressure with the normalized temporal pressure profile.

Load steps During the initial load step, the intraocular pressure (IOP) was applied to the model. Subsequently, in the subsequent step, the excitation pressure, modeled as an incident wave, was applied as the load.

Shear wave velocity calculation in ABAQUS 2023 Three points were delineated on the surface of the cornea, with the first positioned at 1.65 mm from the apex point, the second at 3.15 mm from the apex point,

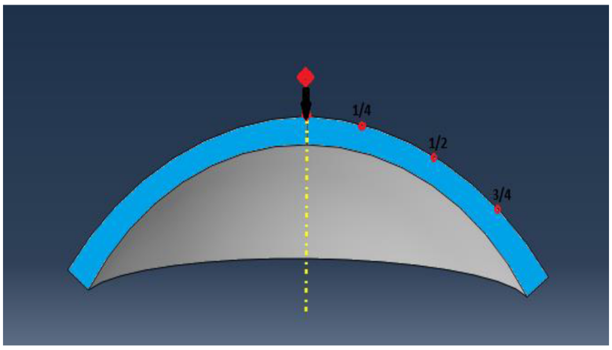

Fig. 5 Three points were delineated on the surface of the cornea in ABAQUS

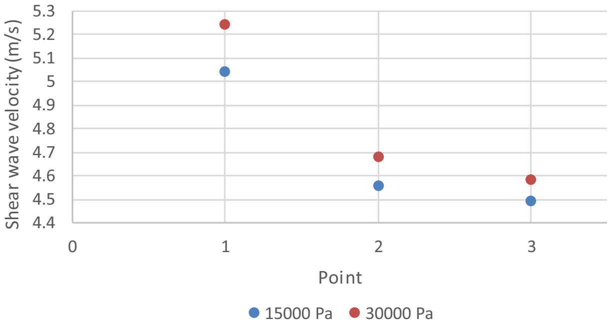

Fig. 6 Decreasing the shear wave velocity during the cornea

and the third at 4.65 mm from the apex point. These points are shown in Figure 5. For each node, we analyze the displacement time-history curves. The time when the shear wave first arrives at the node is typically characterized by: (1) a sharp rise in the simulated signal; we used the time of the first peak or a significant change in the signal as the wave arrival time.

Utilizing the time increments of these points obtained from the history output of ABAQUS, the shear wave velocity can be computed using the formula.

$$V_S = \frac{Distance + deformation}{time} \tag{17}$$

The result is that shown in Fig. 6 as the wave gets closer to the third point, the velocity of the shear wave decreases.

3.1 Finding Young's modulus by using the shear wave velocity

In hyper-viscoelastic material such as the cornea, the shear modulus could be expressed in the frequency domain, and the Fourier transform of the time-dependent stress-strain behavior is often used to separate the material elastic (storage) and viscous (loss) components.

The mechanical behavior is not purely elastic but has time-dependent, dissipative characteristics. The complex representation of the shear modulus G^* can be expressed as:

$$G^* (\omega) = G^{'} (\omega) + iG^{''} (\omega) \tag{18}$$

where $G^{'}$is the storage modulus, which represents the elastic or energy-storing behavior of the material. It corresponds to the stiffness or elasticity that stores energy during deformation; $G^{''}$ is the loss modulus, which represents the viscous or energy-dissipating behavior. It quantifies the energy lost during deformation [80–82].

To analyze the complex shear modulus, a common approach is to apply dynamic mechanical analysis (DMA) or oscillatory testing. A sinusoidal strain is applied to the material, and the resulting stress is measured.

The applied strain is given by:

$$\varepsilon(t) = \varepsilon_0 \sin(\omega t)$$

where $\varepsilon_0$is the strain amplitude, ω is the angular frequency.

The resulting stress is out of phase with the strain, due to the viscoelastic nature of the material. The stress response is typically expressed as:

$$\sigma(t) = \sigma_0 \sin(\omega t + \delta)$$

where δ is the phase lag between the stress and strain, indicating the material viscoelasticity.

Taking the Fourier transform of the time history of stress and strain provides information in the frequency domain, allowing the extraction of the storage $G^{'}$ and loss modulus$G^{''}$. The storage modulus $G^{'}$is related to the in-phase component of the stress, while the loss modulus $G^{''}$ is related to the out-of-phase component:

$$G^{'} = \frac{\sigma_0}{\varepsilon_0}\cos(\delta)$$

$$G^{''} = \frac{\sigma_0}{\varepsilon_0}\sin(\delta)$$

The loss tangent tan (δ) is the ratio of energy dissipated to energy stored in one cycle of loading:

$$\tan(\delta) = \frac{G^{''}}{G^{'}}$$

The Prony series (15) can be transformed into the frequency domain using a Laplace transform or Fourier transform to obtain the real and imaginary component of the shear modulus, respectively, $G^{'}$ and $G^{''}$, at different frequencies.

Considering the relationship between the shear modulus and the shear wave velocity ($|G^*| = 3\rho V_s^2$), the shear modulus can be converted to Young's modulus. For isotropic materials, the conversion is given by Equation: $E = 2G(1+\nu)$, where ν is the Poisson's ratio. Similarly, the complex Young's modulus can be defined using the complex shear modulus through Equation: $E^* = 2G^*(1+\nu)$.

Given the relationship between the shear modulus and shear wave velocity, Young's modulus can be calculated using:

$$\left|E^*\right| = 2\left(3\rho V_s^2\right)(1+\nu) \tag{19}$$

In this study, we simulated the propagation of shear waves in a hyper-viscoelastic cornea, and the simulation was validated with experimental testing conducted by Kling et al. [78] and Tanter et al. [11]. The shear wave speed is almost equal to what we have obtained. Besides, if the calculated shear wave speed is used in the formula, Young's modulus obtained is consistent with Young's modulus of a healthy cornea.

4 Sensitivity analysis

This sensitivity analysis represents a crucial step toward comprehending the intricate influences of various factors on corneal shear wave velocity, particularly in the realm of clinical diagnostics. Through the systematic manipulation of parameters across physiological or pathological ranges and the subsequent observation of their effects on corneal shear wave velocity, researchers can discern the factors exerting the most substantial influence. This insight, in turn, holds promise for refining diagnostic techniques and deepening our understanding of the underlying biomechanics governing corneal behavior.

The selection of parameters, encompassing corneal thickness, boundary conditions, excitation pressure, curvature, intraocular pressure (IOP), hyper-elastic coefficients, and viscoelastic constants (by using Taguchi method), underscores the multifaceted nature of corneal response to external stimuli such as an excitation pressure.

By scrutinizing alterations in parameters such as maximal corneal indentation and peak distance, researchers stand to uncover nuanced insights into the impact of various conditions on corneal dynamics. Such findings may bear significance in the diagnosis and monitoring of conditions like keratoconus, where corneal shape and stiffness serve as pivotal indicators.

In sum, this sensitivity analysis augments the corpus of knowledge within the realm of corneal biomechanics and holds the potential to advance clinical practice by furnishing more nuanced diagnostic tools.

Table 3 The comparison of the vertical distance from the apex (mm) between the two simulations

This simulation	Sabine's simulation
1.2 mm	≈ 1.1 mm

4.1 Computing techniques

For the mechanical simulation of the cornea, ABAQUS Standard/Explicit (version: 2023) was employed. This process comprised two steps: the first step aimed to evaluate the influence of intraocular pressure (IOP), while the second step focused on simulating shear wave propagation by employing an incident wave to excite the cornea.

4.2 Comparison with other simulations and their results

Kling et al. [78] used a non-destructive method involving an air puff to the cornea to extract its viscoelastic properties. Their simulation was in a two-dimensional space for cornea using these properties and following the deformations by applying air puff at the apex of the cornea to study its deformations under various conditions. In this simulation, Kling used air puffs with pressures ranging from 15,000 to 30,000 Pa for boundary conditions between the corneal space and the limbus were applied using a spring with a constant of (5×10^6N/m) and a damper with a constant of 1.0. In this study, by applying Kling's conditions for boundary conditions and the viscoelastic properties in a three-dimensional space, similar results with minimal error were obtained. The comparison of the vertical distance from the apex (mm) between the two simulations is shown in the Table 3

On the other hand, if the shear wave velocity obtained in this study (5.040 m/s) is used in the formula 22, the calculated Young's modulus is equal to that extracted in the Tanter elastography test that is equal to the 190 ± 32 kPa [11]. In this study, the calculated Young modulus is equal to 227 kPa. The error obtained is 2%, providing evidence of the correctness of the simulation of this research.

5 Results

5.1 Exciting pressure modeling

Figure 3 illustrates the experimentally measured temporal pressure profile at the center of the air-puff, revealing a maximal air pressure of 120 mmHg at the corneal surface. The geometry-dependent spatial pressure profile was derived from a distinct computational simulation [78].

5.2 Corneal response simulation under different conditions

The finite element model enabled the reproduction of average experimental data pertaining to corneas under varying levels of intraocular pressure (IOPs), incorporating boundary conditions, excitation pressure, and biomechanical parameters.

Corneal response of the shear wave velocity for different intraocular pressures (IOPs)- porcine eye model In the simulations conducted to analyze the sensitivity of internal pressure on the effect of shear wave velocity in the cornea, the central thickness of the cornea, the radius of curvature of the external corneal surface, the radius of curvature of the internal corneal surface, and the external stimulus pressure (15000 Pa) remained constant. Internal pressures ranging from 10 to 50 mmHg were examined. Our findings revealed that the maximum shear wave velocity was 5.0388 m/s for the lowest intraocular pressure (IOP) and 5.03864 m/s for the highest IOP. The alteration in shear wave velocity resulting from fluctuations in corneal internal pressure exhibited a decrease of 0.0032%, a change deemed negligible.

Corneal response of the shear wave velocity for the different boundary conditions-porcine corneal model One potential factor influencing shear wave velocity in the cornea is the boundary conditions applied between the cornea and the limbus. As described, the space between these structures is typically filled with layers of fat, serving as a shock absorber in instances such as external impacts on the eye. However, the quantity and efficacy

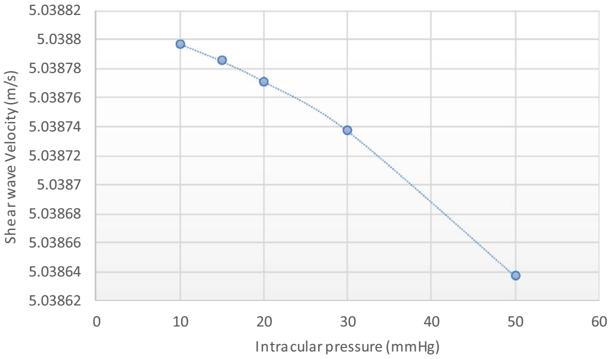

Fig. 7 Corneal response of the shear wave velocity for different intraocular pressures (IOPs)- porcine eye model

of this fatty tissue can vary with age and among individuals, potentially introducing error into experimental studies.

In our investigation, boundary conditions were scrutinized through two approaches:

1. Complete constraint of motion in three coordinate directions within the space between the cornea and the limbus.

2. Additional constraint of rotation in three directions within the space between the cornea and the limbus, in addition to motion constraint.

Furthermore, two additional methods were explored:

3. Filling the space between the cornea and the limbus using 8 spring and dashpot elements.

4. Filling the space between the cornea and the limbus using 16 spring and dashpot elements.

Despite these constraints, the inherent variability in the quantity and functionality of fatty and connective tissue among individuals and age groups necessitates acknowledgment. Consequently, modeling such tissue is inherently prone to errors. Considering the utilization of Hyper-Viscoelastic models in this study, errors arising from the modeling of complex linear viscoelastic tissue are deemed inevitable.

In the simulations aimed at investigating and analyzing the sensitivity of boundary conditions, the material properties, external stimulation pressure, internal pressure, and inner and outer curvature radii of the cornea remained constant. Under both boundary conditions, the propagation speed of the wave was reported to be consistent.

However, it was observed that when employing 8 springs and dampers, the wave speed decreased by 1.7%. Conversely, the velocity observed reached 5.04076 m/s. When utilizing 16 springs and dampers, this reduction diminished to 1.2%. Thus, the velocity observed reached 5.065548 m/s. Furthermore, increasing the number of springs and dampers from 8 to 16 led to a rise in wave speed, with the increment measuring 0.4%.

Corneal response of the shear wave velocity for the different excitation pressure- porcine corneal model In the simulations conducted within this research to probe and analyze the sensitivity of external stimulation pressure on the shear wave speed within the cornea, certain constants such as central corneal thickness, radius of curvature of the corneal surface, internal and external curvature radii of the cornea, internal pressure, and material constants were held constant. The external stimulation pressure was scrutinized across two values: 15,000 Pa and 30,000 Pa. An escalation in stimulation pressure corresponds to an increase in the propagation speed of the shear wave within the cornea. The augmentation of excitation pressure from 15,000 Pa to 30,000 Pa leads to a rise in wave speed, with the increment amounting to 3.4%.

Corneal response of the shear wave velocity for the different curvatures- porcine corneal model The radius of curvature of the corneal surface holds pivotal importance in the transmission and focusing of incoming light rays onto the retina, a factor subject to variation among individuals due to lifestyle and environmental influences. Accordingly, the external corneal radius spans from 7.4 mm to 8.4 mm, with a variance of 0.5. Notably, the magnitude of changes in shear wave speed resulting from alterations in corneal curvature radius amounts to a 0.09% increase.

In this study, uniformity of material properties, external stimulation pressure, internal pressure, and boundary conditions in simulations are assumed to remain constant. By varying the corneal curvature radius, the propagation speed of shear waves is scrutinized. It is observed that an increase in curvature radius correlates with heightened magnitude and impact of internal pressure.

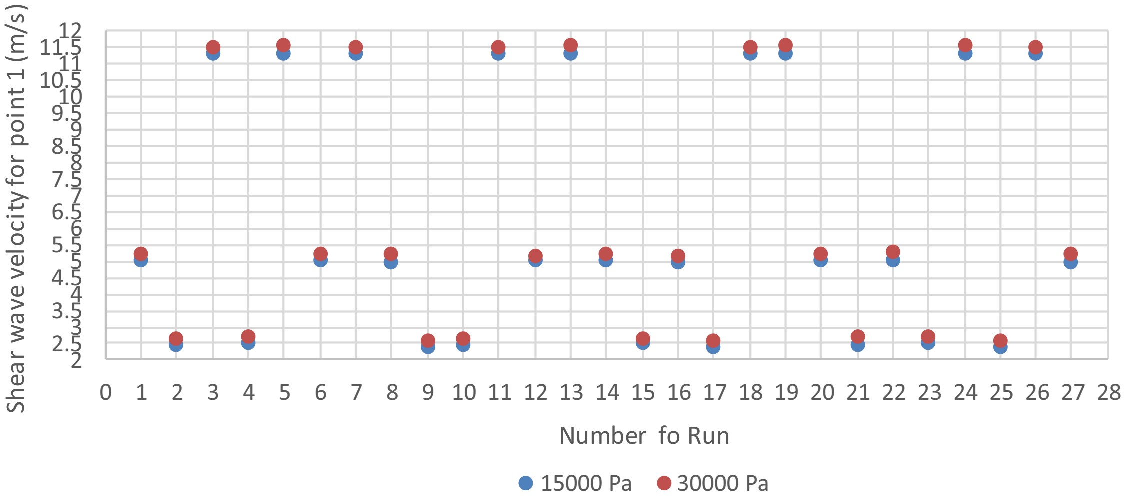

Fig. 8 Corneal response of the shear wave velocity for the biomechanical parameters

Corneal response of the shear wave velocity for the biomechanical parameters In Fig. 5, the dispersion of results is evident, showcasing variations in material properties achieved through the Taguchi method. Taguchi designs employ orthogonal arrays to systematically assess the impact of factors on mean response and variability estimation. An orthogonal array represents a balanced design wherein factor levels are equally distributed across different levels. As a result, each factor can be evaluated independently of others, mitigating the risk of one factor confounding the effect of another. This approach streamlines experimentation time and cost, particularly when utilizing fractional factorial designs. By optimizing resource allocation and reducing experimental redundancy, Taguchi designs support robust experimentation and optimization across diverse industries [83]. The general symbol for a Taguchi design is $L(number)$, denoting the number of runs in the experimental setup. For instance, in the present study, employing the Taguchi method catalog for 11 inputs, each with 3 levels (3^{11}), the symbol L (27) has been selected. Consequently, the number of simulations has been reduced to 27. This dispersion arises from alterations in material coefficients, which encompass hyperelastic and viscoelastic properties. Subsequently, a thorough analysis of the most significant effects of these parameters will be undertaken. In this study, a total of 54 runs were done. Specifically, 27 runs were dedicated to analyzing the impact of biomechanical properties by using the excitation pressure of 15,000 Pa; similarly, 27 runs were done by using the excitation pressure of 30000 Pa.

As evident from Fig. 8, there is considerable dispersion in the results regarding the speed of the shear wave in the cornea using the Taguchi method, rendering it impractical to analyze these results in a single graph. Consequently, the results have been segmented into three groups based on rest time and simulation time for analysis in Figures 9a–c.

Figure 9a corresponds to a simulation time of 0.3 s, Fig. 9b to a simulation time of 0.7 s, and Fig. 9c to a simulation time of 1.5 s. Notably, it is evident that the variations in speed exhibit variability depending on the simulation time.

By increasing the simulation time, attributed to the augmentation of the first rest time per the variable change algorithm employed in the Taguchi method, the speed of shear wave propagation decreases. Specifically, in Fig. 9b, where a simulation time of 0.7 s is utilized, determined in accordance with the first rest time of the porcine cornea, the resulting shear wave speed closely approximates real-world conditions.

In Table 3, a summary of the sensitivity analysis results with the parameter gradients was presented. This table likely includes information about how variations in different parameters, such as material properties or boundary conditions, affect the model outcomes, as quantified by their gradients. These gradients indicate the rate of change in the model response with respect to changes in each parameter.

6 Discussion

The results of this study provide a detailed examination of corneal biomechanics through the innovative application of shear wave elastography (SWE) and advanced finite element modeling. By simulating various

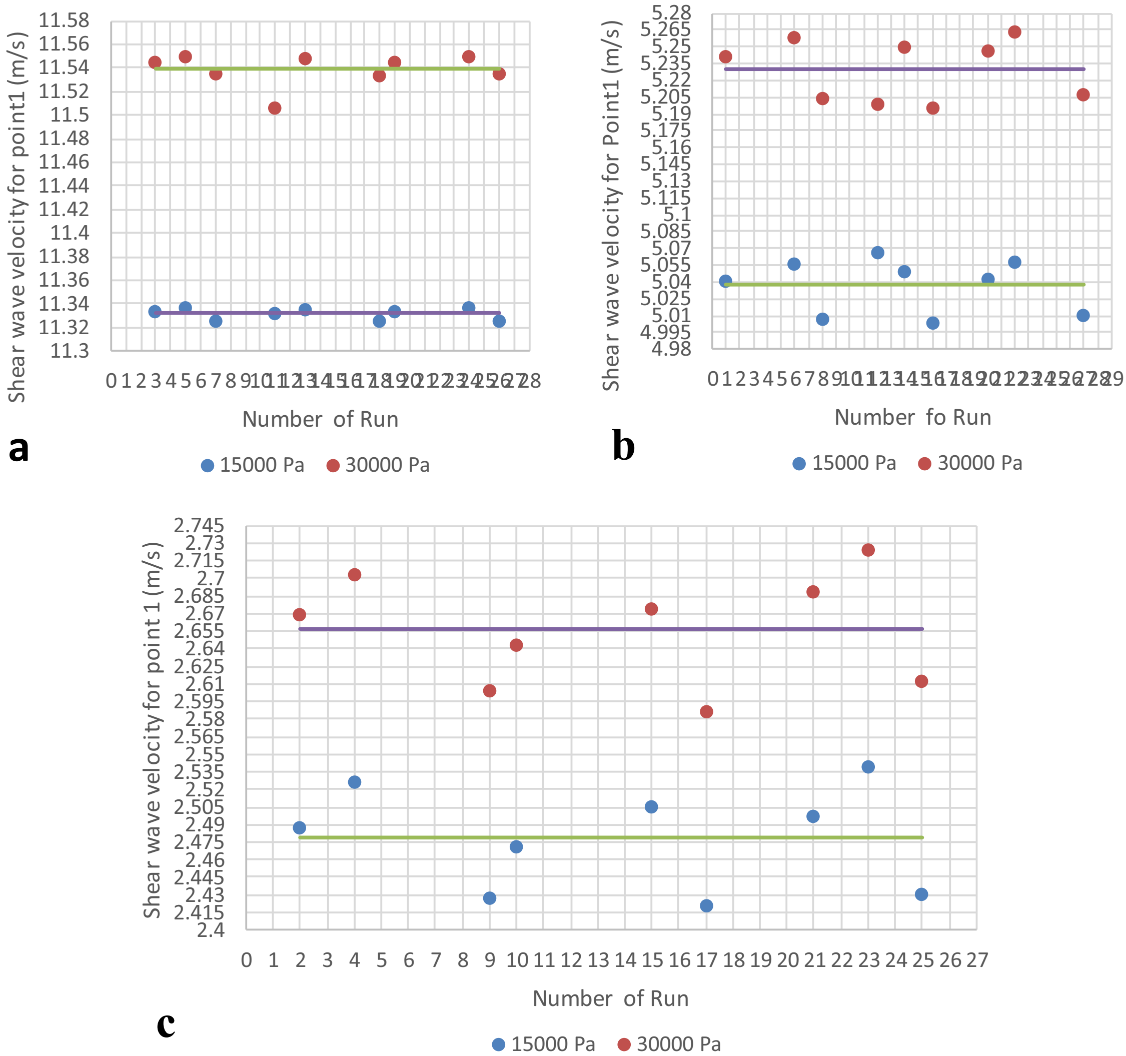

Fig. 9 Time of simulation 0.3 s (**a**), time of simulation 0.7 s (**b**), and time of simulation 1.5 s (**c**)

Table 4 Sensitive analysis results with the parameter gradients

Geometrical/biomechanical parameters	Variance	Percent of change %
Excitation pressure	Δ15000	3.4↑
Curvature	Δ0.5	0.09↑
IOP	Δ40	0.0032↓
Boundary condition 1	Fix and free rotation	0
Boundary condition 2	8 spring and dashpot	1.7↓
Boundary condition 3	16 spring and dashpot	1.2↓
C10	Δ0.474	0.04↓
D1	Δ0.2775	0.01↑
First relaxation time	Δ0.88	76↑

conditions, including intraocular pressure (IOP) variations, boundary conditions, excitation pressures, and corneal curvatures, we explored the multifaceted interactions that influence shear wave propagation and corneal stiffness.

One of the most significant findings of this study is the clear influence of the cornea intrinsic material properties, particularly its viscoelastic behavior, on shear wave velocity. Our analysis demonstrated that the first relaxation time—a key viscoelastic parameter—has a pronounced effect on the mechanical response of the cornea. This insight highlights the importance of accurately characterizing these intrinsic properties in order to predict corneal behavior more effectively. In contrast, external factors such as IOP and boundary conditions were found to have relatively minimal effects on shear wave speed, suggesting that the cornea material properties dominate its mechanical response under physiological conditions.

The implementation of the Taguchi method for sensitivity analysis and parametric optimization provided a rigorous approach to evaluating the impact of various biomechanical parameters. This method allowed us to systematically identify the most influential factors, enhancing the precision and efficiency of the modeling process. The robustness of the model was further validated by its ability to replicate experimental findings with minimal error, demonstrating its potential utility in clinical applications. As a result, by using the Taguchi method as an optimization method, the biomechanical parameters were analyzed, for the cornea, the effect of the Neo-Hookean coefficients is negligible. The most effective factor on the shear wave velocity on the cornea is the First Relaxation Time of the cornea that it is the intrinsic property of the cornea (Viscoelastic part of the biomechanical property of the cornea). The simulation was done until the third relaxation time, and the result was that the shear wave velocity decreased, and after passing the third relaxation time, the shear wave velocity dropped to zero. The reason for this major is because the cornea has completely relaxed.

Our study also revealed that while boundary conditions and excitation pressures do affect corneal shear wave propagation, their impact is comparatively small. This finding is particularly relevant in the context of in vivo assessments, where variations in external conditions are inevitable. The minimal sensitivity of shear wave velocity to these external factors suggests that SWE could provide consistent and reliable measurements of corneal stiffness, even in the face of such variations.

Furthermore, the exploration of corneal curvature variations shed light on the complex relationship between corneal geometry and its mechanical behavior. Although changes in curvature did not significantly alter shear wave velocity, the subtle effects observed underscore the importance of considering individual corneal geometries in clinical assessments.

The shear wave speed in the cornea is more influenced by its inherent material properties rather than by external factors like IOP, excitation pressure, boundary conditions, and radius of curvature. These external factors have a minimal effect because they do not significantly alter the intrinsic mechanical properties that govern shear wave propagation.

In summary, this study advances our understanding of corneal biomechanics by pinpointing the critical role of viscoelastic properties and demonstrating the effectiveness of SWE in evaluating these properties non-invasively. The findings have important implications for improving diagnostic techniques, particularly in the early detection and management of corneal disorders such as keratoconus. Additionally, the insights gained from this research could inform the development of more sophisticated models that account for patient-specific variations, ultimately leading to better outcomes in corneal surgery and treatment.

7 Conclusions

This study successfully applied shear wave elastography (SWE) combined with finite element modeling to analyze the complex biomechanical behavior of the cornea. By developing a 3D axis-symmetric model that simulates corneal response under varying intraocular pressures, boundary conditions, excitation pressures, and curvatures, we gained significant insights into the factors that most strongly influence shear wave propagation and corneal stiffness.

Our findings underscore the dominance of intrinsic corneal material properties, particularly viscoelastic constants, in determining shear wave velocity. External factors such as intraocular pressure and boundary conditions, though relevant, exhibited minimal impact on shear wave propagation. The sensitivity analysis highlighted the first relaxation time as a critical parameter, demonstrating its substantial effect on the cornea mechanical response.

Moreover, the application of the Taguchi method for parametric optimization provided a robust framework for identifying and prioritizing the factors that most significantly affect corneal biomechanical behavior. The minimal error between our model predictions and experimental data further validates the model accuracy and potential for real-world application.

These insights have important implications for ophthalmological diagnostics, particularly in non-invasive assessments of corneal stiffness, which is critical in the detection and monitoring of conditions such as keratoconus and in evaluating the biomechanical effects of surgical interventions. Future research should focus on extending this model to incorporate additional complexities, such as patient-specific corneal geometries and multi-axial loading conditions, to enhance its applicability and accuracy in clinical settings. Additionally, expanding the experimental validation of these models across a broader range of clinical scenarios will be essential in ensuring their accuracy and applicability in diverse patient populations.

Author Contribution All authors contribute equally to the manuscript.

Data availability No datasets were generated or analysed during the current study.

Declarations

Competing interests The authors declare no competing interests.

References

1. Garra, B.S., Cespedes, I., Ophir, J., Pratt, S., Zuubier, R., Magnat, C.M., Pennanen, M.F.: Elastography of breast lesions: initial clinical results, breast imaging. Radiology **202**, 79–86 (2002)
2. Tanter, M., Bercoff, J., Athanasiou, A., Deffieux, T., Gennisson, J.L., Montaldo, G., Muller, M., Tardivon, A., Fink, M.: Quantitative assessment of breast lesion viscoelasticity: initial clinical results using supersonic shear imaging. Ultrasound Med. Biol. **34**(9), 1373–1386 (2008)
3. Sandrin, L., Fourquet, B., Hasquenoph, J.M., Yon, S., Fournier, C., Mal, F., Christidis, C., Ziol, M., Poulet, B., Kazemi, F., Beaugrand, M., Palau, R.: Transient elastography: a new non-invasive method for assessment of hepatic fibrosis. Ultrasound Med. Biol. **29**, 1705–1713 (2003)
4. Ziol, M., Handra-Luca, A., Kettaneh, A., Christidis, C., Mal, F., Kazemi, F., de Lédinghen, V., Marcellin, P., Dhumeaux, D., Trinchet, J.C., Beaugrand, M.: Noninvasive assessment of liver fibrosis by measurement of stiffness in patients with chronic hepatitis C. Hepatology **41**, 48–54 (2005)
5. Friedrich-Rust, M., Ong, M.F., Herrman, E., Dries, V., Samaras, P., Zeuzem, S., Sarrazin, C.: Real-time elastography for noninvasive assessment of liver fibrosis in chronic viral hepatitis. Am. J. Roentgenol. **188**, 758–764 (2007)
6. De Korte, C.L., Pasterkamp, G., van der Steen, A.F.W., Woutman, H.A., Bom, N.: Characterization of plaque components with intravascular ultrasound elastography in human femoral and coronary arteries in vitro. Circulation **102**(6), 617–623 (2000)
7. De Korte, C.L., van der Steen, A.F.W., Cespedes, E.I., Pasterkamp, P.: Intravascular ultrasound elastography in human arteries: initial experience in vitro. Ultrasound Med. Biol. **24**(3), 401–408 (1998)
8. Kowalski, M., Kukulski, T., Jamal, F., D’Hooge, J., Weidemann, F., Rademakers, F., Bijnens, B., Hatle, L., Sutherland, G.R.: Can natural strain and strain rate quantify regional myocardial deformation? A study in healthy subjects. Ultrasound Med. Biol. **27**(8), 1087–1097 (2001)
9. Konofagou, E.E., D’Hooge, J., Ophir, J.: Myocardial elastography–A feasibility study in vivo. Ultrasound Med. Biol. **28**(4), 475–482 (2002)
10. Hamilton, K.E., Pye, D.C.: Young’s modulus in normal corneas and the effect on applanation tonometry. Opt. Vis. Sci. **85**(6), 445 (2008)
11. Tanter, M., Touboul, D., Gennisson, J.-L., Bercoff, J., Fink, M.: High-resolution quantitative imaging of cornea elasticity using supersonic shear imaging. IEEE Trans. Med. Imag. **28**(12), 1881 (2009). https://doi.org/10.1109/TMI.2009.2021471
12. Deffieux, T., Gennisson, J.-L., Bercoff, J., Tanter, M.: On the effects of reflected waves in transient shear wave elastography. IEEE Trans. Ultrason. Ferroelectr. Fr 2032 Equ. Control **58**(10), 2032 (2011)
13. Nguyen, T., Boyce, B.: An inverse finite element method for determining the anisotropic properties of the cornea. Biomech. Model. Mechanobiol. **10**, 323–337 (2011)
14. Touboul, D., Gennisson, J.-L., Nguyen, T.-M., et al.: Supersonic shear wave elastography for the in vivo evaluation of transepithelial corneal collagen cross linking. Invest. Ophthalmol. Vis. Sci. **55**, 1976–1984 (2014). https://doi.org/10.1167/iovs.13-13445
15. Han, Z., Aglyamov, S.R., Li, J., Singh, M., Wang, S., Vantipalli, S., Wu, C., Liu, C.H., Twa, M.D., Larin, K.V.: Quantitative assessment of corneal viscoelasticity using optical coherence elastography and a modified Rayleigh-Lamb equation. J. Biomed. Opt. **20**, 020501 (2015)
16. Nguyen, T.M., Arnal, B., Song, S., Huang, Z., Wang, R.K., O’Donnell, M.: Shear wave elastography using amplitude-modulated acoustic radiation force and phase-sensitive optical coherence tomography. J. Biomed. Opt. **20**(1), 016001 (2015)
17. Luce, D.A.: Determining in vivo biomechanical properties of the cornea with an ocular response analyzer. J. Cataract Refract. Surg. **31**, 156–162 (2005)
18. Han, Z., Li, J., Singh, M., Wu, C., Liu, C.H., Raghunathan, R., Aglyamov, S.R., Vantipalli, S., Twa, M.D., Larin, K.V.: Optical coherence elastography assessment of corneal viscoelasticity with a modified Rayleigh-Lamb wave model. J. Mech. Behav. Biomed. Mater. **66**, 87–94 (2017)

19. Han, Z., Li, J., Singh, M., Wu, C., Liu, C.H., Wang, S., Idugboe, R., Raghunathan, R., Sudheendran, N., Aglyamov, S.R., et al.: Quantitative methods for reconstructing tissue biomechanical properties in optical coherence elastography: a comparison study. Phys. Med. Biol. **60**, 3531–3547 (2015)
20. Qian, X., Ma, T., Shih, C.C., Heur, M., Jun, Z., Shung, K.K., Varma, R., Humayun, M., Zhou, Q.: Ultrasonic microelastography to assess biomechanical properties of the cornea. IEEE Trans. Biomed. Eng. **66**, 647 (2018)
21. Nightingale, K.R., Palmeri, M.L., Nightingale, R.W., Trahey, G.E.: On the feasibility of remote palpation using acoustic radiation force. J. Acoust. Soc. Am. **110**, 625–634 (2001)
22. Sarvazyan, A.P., Rudenko, O.V., Swanson, S.D., Fowlkes, J.B., Emelianov, S.Y.: Shear wave elasticity imaging: a new ultrasonic technology of medical diagnostics. Ultrasound Med. Biol. **24**, 1419–1435 (1998)
23. Silverman, R.H.: High-resolution ultrasound imaging of the eye-a review. Clin. Exp. Ophthalmol. **37**, 54–67 (2009)
24. Chen, P.Y., Shih, C.C., Lin, W.C., Ma, T., Zhou, Q., Shung, K.K., Huang, C.C.: High-resolution shear wave imaging of the human cornea using a dual-element transducer. Sensors **18**(12), 4244 (2018). https://doi.org/10.3390/s18124244
25. Ramier, A., Eltony, A.M., Chen, Y., Clouser, F., Birkenfeld, J.S., Watts, A., Yun, S.H.: In vivo measurement of shear modulus of the human cornea using optical coherence elastography. Sci. Rep. **10**(1), 17366 (2020). https://doi.org/10.1038/s41598-020-74383-4
26. Lan, G., Twa, M.D., Song, C., Feng, J., Huang, Y., Xu, J., Qin, J., An, L., Wei, X.: In vivo corneal elastography: a topical review of challenges and opportunities.' Published by Elsevier B.V. on behalf of Research Network of Computational and Structural Biotechnology. https://doi.org/10.1016/j.csbj.2023.04.009
27. Fatt, I., Weissman, B.A.: Physiology of the Eye: An Introduction to the Vegetative Functions. Butterworth-Heinemann, Oxford (2013)
28. dell'Isola, F., Andreaus, U., Placidi, L.: At the origins and in the vanguard of peridynamics, non-local and higher-gradient continuum mechanics: an underestimated and still topical contribution of Gabrio Piola. Math. Mech. Solids **20**(8), 887–928 (2015)
29. Alibert, J.-J., Seppecher, P., dell'Isola, F.: Truss modular beams with deformation energy depending on higher displacement gradients. Math. Mech. Solids **8**(1), 51–73 (2003)
30. Turco, E., Giorgio, I., Misra, A., dell'Isola, F.: King post truss as a motif for internal structure of (meta) material with controlled elastic properties. R. Soc. Open Sci. **4**(10), 171153 (2017)
31. Tepedino, M.: The mechanical role of the periodontal ligament for developing mathematical models in orthodontics. Math. Mech. Complex Syst. **11**(4), 525–539 (2023)
32. Altenbach, H., Eremeyev, V.A.: On the linear theory of micropolar plates. ZAMM J. Appl. Math. Mech. Z. Angew. Math. Mech. **89**(4), 242–256 (2009)
33. Eremeyev, V.A., Pietraszkiewicz, W.: Material symmetry group and constitutive equations of micropolar anisotropic elastic solids. Math. Mech. Solids **21**(2), 210–221 (2016)
34. La Valle, G.: A new deformation measure for the nonlinear micropolar continuum. Z. Angew. Math. Phys. **73**(2), 78 (2022)
35. La Valle, G., Massoumi, S.: A new deformation measure for micropolar plates subjected to in-plane loads. Contin. Mech. Thermodyn. **34**, 1–15 (2022)
36. Spagnuolo, M., Franciosi, P., dell'Isola, F.: A Green operator-based elastic modeling for two-phase pantographic-inspired bi-continuous materials. Int. J. Solids Struct. **188**, 282–308 (2020)
37. Schulte, J., Dittmann, M., Eugster, S.R., Hesch, S., Reinicke, T., dell'Isola, F., Hesch, C.: Isogeometric analysis of fiber reinforced composites using Kirchhoff-Love shell elements. Comput. Methods Appl. Mech. Eng. **362**, 112845 (2020)
38. Turco, E., Golaszewski, M., Giorgio, I., D'Annibale, F.: Pantographic lattices with non-orthogonal fibres: experiments and their numerical simulations. Compos. B Eng. **118**, 1–14 (2017)
39. Ciallella, A., D'Annibale, F., Del Vescovo, D., Giorgio, I.: Deformation patterns in a second-gradient lattice annular plate composed of spira mirabilis fibers. Contin. Mech. Thermodyn. **35**(4), 1561–1580 (2023)
40. Giorgio, I., Harrison, P., dell'Isola, F., Alsayednoor, J., Turco, E.: Wrinkling in engineering fabrics: a comparison between two different comprehensive modelling approaches. Proc. R. Soc. A Math. Phys. Eng. Sci. **474**(2216), 20180063 (2018)
41. Giorgio, I., Ciallella, A., Scerrato, D.: A study about the impact of the topological arrangement of fibers on fiber-reinforced composites: some guidelines aiming at the development of new ultra-stiff and ultra-soft metamaterials. Int. J. Solids Struct. **203**, 73–83 (2020)
42. Auffray, N., dell'Isola, F., Eremeyev, V.A., Madeo, A., Rosi, G.: Analytical continuum mechanics à la Hamilton–Piola least action principle for second gradient continua and capillary fluids. Math. Mech. Solids **20**(4), 375–417 (2015)
43. dell'Isola, F., Eugster, S.R., Fedele, R., Seppecher, P.: Second-gradient continua: from Lagrangian to Eulerian and back. Math. Mech. Solids **27**(12), 2715–2750 (2022)
44. Madeo, A., dell'Isola, F., Darve, F.: A continuum model for deformable, second gradient porous media partially saturated with compressible fluids. J. Mech. Phys. Solids **61**(11), 2196–2211 (2013)
45. La Valle, G., Abali, B.E., Falsone, G., Soize, C.: Sensitivity of a homogeneous and isotropic second-gradient continuum model for particle-based materials with respect to uncertainties. ZAMM Z. Angew. Math. Mech. **103**(10), e202300068 (2023)
46. Ciallella, A., Scerrato, D., Spagnuolo, M., Giorgio, I.: A continuum model based on Rayleigh dissipation functions to describe a Coulomb-type constitutive law for internal friction in woven fabrics. Z. Angew. Math. Phys. **73**(5), 209 (2022)
47. Giorgio, I., Andreaus, U., Scerrato, D., dell'Isola, F.: A visco-poroelastic model of functional adaptation in bones reconstructed with bio-resorbable materials. Biomech. Model. Mechanobiol. **15**, 1325–1343 (2016)
48. Bersani, A.M., Caressa, P., dell'Isola, F.: Approximation of dissipative systems by elastic chains: numerical evidence. Math. Mech. Solids **28**(2), 501–520 (2023)
49. Bersani, A.M., Caressa, P.: Lagrangian descriptions of dissipative systems: a review. Math. Mech. Solids **26**(6), 785–803 (2021)
50. Bersani, A.M., Caressa, P., Ciallella, A.: Numerical evidence for the approximation of dissipative systems by gyroscopically coupled oscillator chains. Math. Mech. Complex Syst. **10**(3), 265–278 (2022)

51. Abali, B.E., Klunker, A., Barchiesi, E., Placidi, L.: A novel phase-field approach to brittle damage mechanics of gradient metamaterials combining action formalism and history variable. ZAMM J. Appl. Math. Mech. Z. Angew. Math. Mech. **101**(9), e202000289 (2021)
52. Timofeev, D., Barchiesi, E., Misra, A., Placidi, L.: Hemivariational continuum approach for granular solids with damage-induced anisotropy evolution. Math. Mech. Solids **26**(5), 738–770 (2021)
53. Placidi, L., Barchiesi, E., dell'Isola, F., Maksimov, V., Misra, A., Rezaei, N., Scrofani, A., Timofeev, D.: On a hemi-variational formulation for a 2D elasto-plastic-damage strain gradient solid with granular microstructure. Math. Eng. **5**, 1–24 (2022)
54. Placidi, L., Barchiesi, E., Misra, A.: A strain gradient variational approach to damage: a comparison with damage gradient models and numerical results. Math. Mech. Complex Syst. **6**(2), 77–100 (2018)
55. Addessi, D., D'Annibale, F., Placidi, L., Giorgio, I.: A bone remodeling approach encoding the effect of damage and a diffusive bio-mechanical stimulus. Contin. Mech. Thermodyn. **36**, 1–20 (2024)
56. Grillo, Alfio, Di Stefano, Salvatore: An a posteriori approach to the mechanics of volumetric growth. Math. Mech. Complex Syst. **11**(1), 57–86 (2023)
57. Grillo, Alfio, Di Stefano, Salvatore: Comparison between different viewpoints on bulk growth mechanics. Math. Mech. Complex Syst. **11**(2), 287–311 (2023)
58. Giorgio, I., dell'Isola, F., Andreaus, U., Misra, A.: An orthotropic continuum model with substructure evolution for describing bone remodeling: an interpretation of the primary mechanism behind Wolff's law. Biomech. Model. Mechanobiol. **22**(6), 2135–2152 (2023)
59. Ciallella, A., Giorgio, I., Eugster, S.R., Rizzi, N.L., dell'Isola, F.: Generalized beam model for the analysis of wave propagation with a symmetric pattern of deformation in planar pantographic sheets. Wave Motion **113**, 102986 (2022)
60. Placidi, L., Rosi, G., Giorgio, I., Madeo, A.: Reflection and transmission of plane waves at surfaces carrying material properties and embedded in second-gradient materials. Math. Mech. Solids **19**(5), 555–578 (2014)
61. Turco, E., Barchiesi, E., Ciallella, A., dell'Isola, F.: Nonlinear waves in pantographic beams induced by transverse impulses. Wave Motion **115**, 103064 (2022)
62. Berezovski, A., Yildizdag, M.E., Scerrato, D.: On the wave dispersion in microstructured solids. Contin. Mech. Thermodyn. **32**, 569–588 (2020)
63. Berezovski, A., Giorgio, I., Della Corte, A.: Interfaces in micromorphic materials: wave transmission and reflection with numerical simulations. Math. Mech. Solids **21**(1), 37–51 (2016)
64. Fedele, R., Placidi, L., Fabbrocino, F.: A review of inverse problems for generalized elastic media: formulations, experiments, synthesis. Contin. Mech. Thermodyn. **1–41**, 1413 (2024)
65. Valoroso, N., Fedele, R.: Characterization of a cohesive-zone model describing damage and de-cohesion at bonded interfaces. Sensitivity analysis and mode-I parameter identification. Int. J. Solids Struct. **47**(13), 1666–1677 (2010)
66. De Angelo, M., Barchiesi, E., Giorgio, I., Abali, B.E.: Numerical identification of constitutive parameters in reduced-order bi-dimensional models for pantographic structures: application to out-of-plane buckling. Arch. Appl. Mech. **89**(7), 1333–1358 (2019)
67. Shekarchizadeh, N., Laudato, M., Manzari, L., Abali, B.E., Giorgio, I., Bersani, A.M.: Parameter identification of a second-gradient model for the description of pantographic structures in dynamic regime. Z. Angew. Math. Phys. **72**(6), 190 (2021)
68. Yang, H., Abali, B.E., Timofeev, D., Müller, W.H.: Determination of metamaterial parameters by means of a homogenization approach based on asymptotic analysis. Contin. Mech. Thermodyn. **32**, 1251–1270 (2020)
69. Elsheikh, A., Alhasso, D., Rama, P.: Biomechanical properties of human and porcine corneas. Exp. Eye Res. **86**(5), 783–790 (2008)
70. Ethier, C.R., Johnson, M., Ruberti, J.: Ocular biomechanics and biotransport. Annu. Rev. Biomed. Eng. **6**, 249–273 (2004)
71. Su, P., Yang, Y., Song, Y.: Corneal hyper-viscoelastic model: derivations, experiments, and simulations. Acta Bioeng. Biomech. (2015). https://doi.org/10.5277/ABB-00142-2014-03
72. Friedrich, M.: Liver fibrosis in viral Hepatits: noninvasive assessment with acoustic radiation force impulse imaging verus transient elastography. Ultrasonography **252**, 595 (2009)
73. Kampmeier, J., Radt, B., Birngruber, R., Brinkmann, R.: Thermal and biomechanical parameters of porcine cornea. Cornea **19**(3), 355–363 (2000)
74. Palmeri, M.L., et al.: Acoustic radiation force impulse (ARFI) imaging of the gastrointestinal tract. Ultrason Imaging **27**, 75–88 (2005)
75. Bryant, M.R., Mcdonnell, P.J.: Constitutive laws for biomechanical modeling of refractive surgery. J. Biomech. Eng. TASME **118**(4), 473–481 (1996)
76. Abali, B.E.: Inverse analysis of cellulose by using the energy-based method and a rotational rheometer. Appl. Sci. **8**(8), 1354 (2018)
77. Yang, H., Ganzosch, G., Giorgio, I., Abali, B.E.: Material characterization and computations of a polymeric metamaterial with a pantographic substructure. Z. Angew. Math. Phys. **69**, 1–16 (2018)
78. Kling, S., Bekesi, N., Dorronsoro, C., Pascual, D., Marcos, S.: Corneal viscoelastic properties from finite-element analysis of in vivo air-puff deformation. PLoS ONE **9**(8), e104904 (2014). https://doi.org/10.1371/journal.pone.0104904
79. Jannesari, M., Kadkhodaei, M., Mosaddegh, P., Kasprzak, H., Behrouz, M.J.: Assessment of corneal and fatty tissues biomechanical response in dynamic tonometry tests by using inverse models. Acta Bioeng. Biomech. (2017). https://doi.org/10.5277/ABB-00969-2017-02
80. Ferry, J.D.: Viscoelastic Properties of Polymers. John Wiley & Sons, Hoboken (1980)
81. Findley, W.N., Lai, J.S., Onaran, K.: Creep and Relaxation of Nonlinear Viscoelastic Materials. Dover Publications, Mineola (1976)
82. Lakes, R.S.: Viscoelastic measurement techniques. Rev. Sci. Instrum. **75**(4), 797–810 (2004). https://doi.org/10.1063/1.1687973
83. https://support.minitab.com/en-us/minitab/21/help-and-how-to/statisticalmodeling/doe/supporting-topics/taguchi-designs/taguchi-designs/

Chapter 6

Shear wave velocity and finite element modeling for understanding keratoconus biomechanics

Chapter abstract

Keratoconus is a progressive eye condition involving the thinning and steepening of the cornea peak, resulting in critical biomechanical changes that affect its structural stability and vision. This investigation combines shear wave elastography (SWE) with finite element modeling (FEM) to explore the biomechanical changes in keratoconus-afflicted corneas versus healthy ones. The study examined shear wave velocity and apex deformation under different material characteristics, corneal thickness, and intraocular pressure (IOP). The findings indicated that keratoconus significantly decreases shear wave velocity at the apex, signaling reduced stiffness, while increased apex deformation correlated with the disease progression. These results suggest that SWE and FEM could serve as valuable diagnostic techniques for the early detection and monitoring of keratoconus. The framework also facilitates the enhancement of treatment options, like corneal cross-linking, by employing patient-specific biomechanical models. The study emphasizes the necessity of incorporating advanced diagnostic methods to enhance the management of keratoconus.

Article

MMS

Mathematics and Mechanics of Solids
1–15

DOI: 10.1177/10812865251347512
journals.sagepub.com/home/mms
Sage

Shear wave velocity and finite element modeling for understanding keratoconus biomechanics: Comparison with healthy cornea

Pouria Mazinani
Department of Civil, Construction-Architectural and Environmental Engineering, University of L'Aquila, L'Aquila, Italy

Christian Cardillo
Department of Civil, Construction-Architectural and Environmental Engineering, University of L'Aquila, L'Aquila, Italy; Department of Civil Engineering and Architecture, Università di Catania, Catania, Italy

Received 24 January 2025; accepted 20 May 2025

Abstract

Keratoconus is a progressive corneal disorder characterized by localized thinning and steepening at the apex, leading to significant biomechanical changes that compromise structural integrity and vision. This study integrates shear wave elastography (SWE) and finite element modeling (FEM) to investigate the biomechanical alterations in keratoconus corneas compared to healthy ones. Shear wave velocity and apex deformation were analyzed under varying material properties, corneal thickness, and intraocular pressure (IOP). Results revealed that keratoconus significantly reduces shear wave velocity at the apex, reflecting a loss of stiffness, while apex deformation increased, correlating with disease severity. These findings highlight the potential of SWE and FEM as complementary diagnostic tools for early detection and monitoring of keratoconus progression. The proposed framework also supports the optimization of therapeutic interventions, such as corneal cross-linking, through patient-specific biomechanical modeling. This study underscores the importance of integrating advanced diagnostic techniques to improve outcomes in keratoconus management.

Keywords

Corneal biomechanics, shear wave elastography, hyperviscoelastic materials, non-invasive assessment, keratoconus

---

Corresponding authors:
Christian Cardillo, Department of Civil Engineering and Architecture, Università di Catania, Via Santa Sofia 64, Catania 95123, Italy.
Email: christian.cardillo@phd.unict.it

Pouria Mazinani, Department of Civil, Construction-Architectural and Environmental Engineering, University of L'Aquila, P.zza Ernesto Pontieri 1, Monteluco di Roio 67100 L'Aquila, Italy.
Email: pouria.mazinani@student.univaq.it

1. Introduction

Keratoconus is a progressive degenerative disorder of the cornea, characterized by localized thinning and steepening, particularly at the apex. These structural changes result in significant biomechanical alterations that compromise the cornea ability to maintain its shape and optical properties, ultimately affecting vision. Despite advances in diagnostic and therapeutic techniques, a comprehensive understanding of the biomechanical mechanisms underlying keratoconus remains essential for early detection, disease monitoring, and effective treatment planning.

Shear wave elastography (SWE) has emerged as a non-invasive imaging modality capable of quantifying corneal stiffness by measuring the propagation speed of induced mechanical waves. In healthy corneas, shear wave velocity correlates with structural integrity and is influenced by factors such as thickness, hydration, and regional stiffness. However, in keratoconus, the localized thinning and weakening of the apex result in significantly reduced shear wave velocity, making it a valuable biomarker for disease progression [1]. Regional variations in shear wave velocity further underscore the importance of apex-focused assessments for accurate diagnostics.

Finite element modeling (FEM) complements SWE by simulating the corneal biomechanical response under physiological and pathological conditions. FEM allows for the analysis of complex interactions between material properties, intraocular pressure (IOP), and geometric variations, providing insights into stress distribution and deformation patterns. Previous studies have demonstrated the utility of FEM in replicating apex deformation observed in keratoconus, revealing its potential for evaluating treatment outcomes, such as corneal cross-linking (CXL). Figure 1 shows the cornea before and after keratoconus. This disease usually occurs due to the local reduction of collagen fibers, and this decrease in fiber reduces the rigidity of the corneal stroma, and as a result, it becomes spindly. Keratoconus disease is not hereditary, and factors such as air pollution, eye rubbing, and corneal surgeries can provide the conditions for its occurrence.

Dupps and Wilson [3] used FEM to simulate corneal deformation in keratoconus and demonstrated that the apical deformation was significantly higher than in normal corneas. This increase in deformation is closely associated with disease severity. Kling et al. [4] used FEM to simulate the progression of keratoconus, showing that the apex is the region of maximum deformation and the most significant reduction in stiffness. Vellara and Patel [5] showed that post-CXL simulations indicated reduced deformation and increased stiffness at the apex, confirming the treatment effectiveness in halting keratoconus progression.

The degree of deformation at the apex is strongly influenced by corneal thinning, which is one of the hallmark features of keratoconus. Thinner corneal regions, particularly the apex, deform more under the same intraocular pressure compared to thicker, healthier regions. Mahmoud et al. [6] used optical coherence elastography to measure apex deformation and confirmed that the highest displacements occurred at the thinnest points.

In order to understand the mechanical behavior of the corneal tissue, different modeling approaches can be conceived based on its particular inner structure. The cornea is a highly complex biological

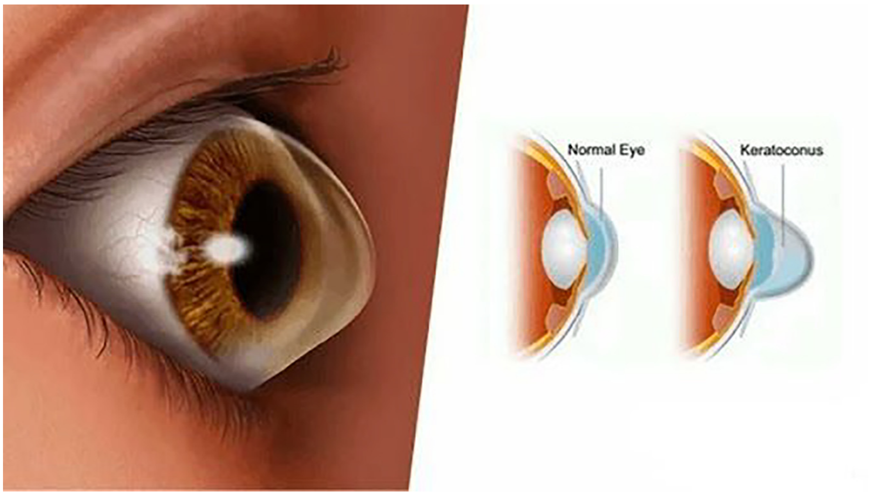

Figure 1. Difference between the shape of healthy cornea and keratoconus [2].

structure with unique mechanical characteristics, such as heterogeneity, anisotropy, and behaviors that are nonlinear, viscoelastic, and time-dependent. Simplified continuum models are often used to represent these features, offering an effective starting point for exploring essential mechanical behaviors in clinical contexts. These models prioritize simplicity, incorporating viscoelasticity, boundary conditions, and intraocular pressure, without delving into more advanced approaches.

To consider future developments in corneal modeling, advanced methodologies, grounded in generalized continuum mechanics, are being developed to capture the macroscopic mechanical behaviors derived from the cornea's complex microstructure. Models such as micropolar, micromorphic, nonlocal, and higher-order gradient theories are gaining prominence. These approaches enhance the representation of complex tissue mechanics, improving our understanding of phenomena like deformation, stress distribution, and microstructural interactions [7–12].

Micropolar theories focus on rotational effects within the material, ideal for capturing the behavior of the corneal stroma collagen fibrils, especially near the limbus [13–16]. Micromorphic theories extending micropolar models incorporate additional micro-deformations, enabling a multiscale representation of corneal mechanics [17–23]. Nonlocal, second or higher gradient theories account for long-range interactions within the microstructure, crucial for modeling the impact of collagen fibril networks on the cornea's response to external forces [24–29].

By leveraging variational formulations, these advanced models integrate seamlessly with finite element methods, allowing for simulations that include complex boundary conditions, variable material properties, and layer interactions. As practical Applications of these advanced models, they facilitate: (1) Precise predictions of corneal behavior under clinical scenarios [30,31]; (2) Insights into dissipative phenomena [32–38], tissue damage (e.g., keratoconus) [39–44], regeneration, and growth [45–47]; and (3) Improved characterization of dynamic behaviors, such as wave propagation, which can reveal critical corneal properties [48–53].

The accuracy of these models relies heavily on precise parameter identification, ensuring that simulations faithfully replicate the cornea biomechanical behavior [54–58]. This process is critical for (1) Reliable simulations [59–62]; (2) Personalized medical treatments; and (3) Development of diagnostic tools [63].

Such advancements contribute to better patient outcomes and drive innovation in ophthalmic research and applications.

This study aims to integrate SWE and FEM to investigate the interplay between shear wave velocity and apex deformation in keratoconus corneas compared to healthy controls. By combining experimental measurements and computational simulations, this approach provides a comprehensive framework for understanding the biomechanical alterations associated with keratoconus. The findings offer critical insights into the potential of SWE and FEM as complementary tools for early diagnosis, personalized treatment planning, and monitoring disease progression. Furthermore, this work underscores the importance of patient-specific modeling in advancing the field of ophthalmic biomechanics and improving clinical outcomes.

2. Method

Corneal tissue exhibits a highly nonlinear mechanical behavior [64]. However, within the intraocular pressure (IOP) range of 10–25 mmHg for a healthy cornea, the tissue response can be approximated as quasi-linear, facilitating simplification in modeling. In this specific pressure range, a hyper-viscoelastic model can be applied to the stroma, which constitutes approximately 80% of the corneal structure [65]. Due to its high-water content, the stroma can also be treated as incompressible [66]. The cornea is characterized by two key mechanical properties: hyperelasticity and viscoelasticity [67].

The cornea is modeled using a hyperelastic Neo-Hookean framework, defined by two unknown material parameters. Its dissipative behavior is represented by a modified Maxwell viscoelastic model, which is expressed through the generalized Prony series.

In this study, the model employed for the cornea is hyper-viscoelastic, similar to the hyper-viscoelastic model utilized in the previous study [68].

The hyperelastic material is defined by a potential function that gives the strain energy density $W = W(C) = W(I_1, I_2, I_3)$, where:

1. C is the right Cauchy-Green deformation tensor;
2. I_1, I_2, I_3 are the three principal invariants of the deformation tensor C.

In this context, the second Piola-Kirchhoff stress tensor, S, can be evaluated as follows:

$$S = 2\frac{\partial W(I_1, I_2, I_3)}{\partial C}. \tag{1}$$

Denoting the principal stretches as $\lambda_i(\mathrm{i} = 1, 2, 3)$.The principal strains ε_i can be evaluated as:

$$\varepsilon_i = \lambda_i - 1 \tag{2}$$

The invariants I_1, I_2 and I_3 of the right Cauchy-Green deformation tensor C is given by:

$$I_1 = \lambda_1^2 + \lambda_2^2 + \lambda_3^2 \tag{3}$$

$$I_2 = \lambda_1^2\lambda_2^2 + \lambda_2^2\lambda_3^2 + \lambda_3^2\lambda_1^2 \tag{4}$$

$$I_3 = \lambda_1^2\lambda_2^2\lambda_3^2 \tag{5}$$

Therefore, the Piola-Kirchhoff stress tensor can be specified as:

$$S = 2\left(\frac{\partial W}{\partial I_1}\frac{\partial I_1}{\partial C} + \frac{\partial W}{\partial I_2}\frac{\partial I_2}{\partial C} + \frac{\partial W}{\partial I_3}\frac{\partial I_3}{\partial C}\right) \tag{6}$$

The stored energy density W can be further divided into two parts [7]:

1. The isochoric part, $\bar{W}$
2. The hydrostatic part, W_h

As a result, the stored energy density can be expressed in the form:

$$W = \bar{W} + W_h = f(\bar{I}_1 - 3, \bar{I}_2 - 3) + P(J - 1). \tag{7}$$

This decomposition separates the energy associated with volume-preserving (isochoric) deformations resulting only in a change of shape, expressed by the function f, from the energy associated with changes in volume (hydrostatic deformations) given by the function P. This partition is beneficial for accurately modeling the complex behavior of hyperelastic materials, such as the cornea.

Besides, $\bar{I}_1 = J^{-2/3}I_1$ and $\bar{I}_2 = J^{-4/3}I_2$ define the first and second invariants of the isochoric part $\bar{C} = \det(C)^{-1/3}C$ of the right Cauchy–Green deformation tensor.

Additionally, $J = \det(C)^{1/2}$ represents the volumetric change ratio.

The hydrostatic pressure can be defined as:

$$P(J - 1) = \sum_{i=1}\frac{1}{Di}(J - 1)^2. \tag{8}$$

Therefore, the complete strain energy density function is described by the expression:

$$W = \sum_{i,j=0}^{N_i, N_j} C_{ij}(\bar{I}_1 - 3)^i(\bar{I}_2 - 3)^j + \sum_{m=1}^{M}\frac{1}{D_m}(J - 1)^{2m}. \tag{9}$$

Here C_{ij} are constant material coefficients, as well as the modulus D_m that represents the compressibility of the material.

Equation (9) outlines a widely used hyperelastic model for the cornea [69]. The selected hyperelastic model achieves a balance between simplicity and the ability to accurately capture experimental data. Hyperelastic models can range from simple (e.g., Neo-Hookean) to very complex (e.g., Ogden, Mooney-Rivlin, or Holzapfel-Gasser-Ogden models). A simpler model may not capture all details of the material behavior, but it is easier to calibrate and use. Consequently, the selected model strikes a good compromise between accuracy and practicality, being sufficiently intricate to ensure precision without exceeding the level of complexity that would render it impractical for use with the available corneal data. More complex models often require more computational resources, such as memory and simulation time, especially in finite element analysis. By selecting a model of moderate complexity, one can ensure fast simulations while maintaining sufficient accuracy to properly represent the nonlinear behavior of corneal tissue, which is subject to large deformations and exhibits nonlinear elasticity. Thus, by avoiding excessive complexity, the model minimizes computational effort and reduces the risk of overfitting, ensuring that the results are both reliable and reproducible. Overfitting happens when a model is too complex for the available data—it may fit experimental noise rather than the true behavior. With simpler models, fewer parameters are needed, which helps avoid overfitting and makes the results more generalizable and easier to reproduce across different datasets or patient-specific simulations. Also, less complex models are more transparent, making them easier for others to validate or replicate the findings. In this study, we set:

$$i = 1 \tag{10}$$

$$j = 0 \tag{11}$$

$$k = 1. \tag{12}$$

These choices are made to accomplish the above-mentioned reduction of excessive complexity. By substituting these settings 10, 11, and 12 into equation (9), the neo-Hookean strain energy density function assumed is:

$$W = C_{10}(\bar{I}_1 - 3) + \frac{1}{D_1}(J - 1)^2. \tag{13}$$

The constants appearing in the stored energy density W can be determined based on experimental imaging techniques [70–72] applied to various laboratory experiments [73,74]. Furthermore, the constants of the Neo-Hookean model for small strains exhibit the following relationship with the bulk modulus (K) and the shear modulus (G):

$$C_{10} = \frac{G}{2} = \frac{E}{4(1+\nu)} \tag{14}$$

$$D_1 = \frac{2}{K} = \frac{6(1-2\nu)}{E} \tag{15}$$

where E is the elastic modulus and ν is Poisson's ratio, which is set to 0.49. These equations are based on standard relationships between hyperelastic and linear elastic material parameters in the small-strain limit. The value $\nu = 0.49$ was chosen to approximate near-incompressibility, which is a well-established mechanical behavior of soft biological tissues such as the cornea.

To describe the dissipative effect in the cornea tissue, the generalized Maxwell model, also known as the Maxwell-Wiechert model, is employed [72]. It is one of the most general forms of the linear model for viscoelasticity. In particular, it represents an extension of the traditional Maxwell model, which consists of a spring and a dashpot connected in series. In the generalized Maxwell model, multiple Maxwell elements are assembled in parallel, allowing for a more accurate representation of the viscoelastic material.

The viscoelastic model of the cornea can be defined in terms of the overall modulus:

$$E(t) = \sum_{i=1}^{n} E_i e^{-t/\tau_i} + E_\infty. \tag{16}$$

The analytical form in equation (16) is consistent with the generalized Prony series model, where E_i and τ_i are parameters of the model, the modulus of the single ith element of the parallel, and the corresponding relaxation time, respectively. The constant n is the number of Prony series and E_∞ is the static elastic modulus. In formulas:

$$E_\infty = \frac{\sigma_\infty}{\varepsilon_0} \tag{17}$$

where the symbol σ_∞ represents the residual stress, while ε_0 denotes the constant strain.

For a given applied force F_i, the strain ε_i, the cross-sectional area in the specimen A, and the number of tests k, the ith elastic modulus can be calculated as:

$$E_i = \frac{1}{kA}\sum\nolimits_{i=1}^{k}\frac{F_i}{\varepsilon_i}. \tag{18}$$

Assuming an initial load force F_0 and an initial elastic modulus E_0 The constant strain can be calculated as follows:

$$\varepsilon_0 = \frac{F_0}{AE_0} \tag{19}$$

The hyper-viscoelastic model of the cornea is developed accordingly. The hyperelastic property deals with deformation-recovery, while the viscoelastic property involves time-dependence, both of which need to be considered simultaneously under loading conditions.

In this study, the data, including the Prony series for viscoelastic materials and the hyperelastic coefficients used in the simulation, were derived from previous studies [75,76], (see Tables 1 and 2).

The study of corneal shear wave velocity using a finite element model with three-dimensional axis-symmetric geometry represents a significant advancement in understanding the biomechanical properties of the cornea. By adopting the pressure characteristics from the in vivo Air Puff system as described by Kling S. et al., the model aims to closely replicate experimental conditions, enhancing the accuracy of the findings.

The application of finite element methods (FEM) allows for the identification of biomechanical parameters that best correlate with experimental observations. Sensitivity analysis further refines this understanding by pinpointing which parameters most significantly influence the corneal shear wave velocity in response to applied pressure.

The relationship between shear wave velocity and tissue stiffness is critical, as it enables the calculation of the tissue elasticity modulus using the equation $G = 3\rho c^2$, where G is the shear modulus, ρ is the tissue density, and c is the shear wave velocity.

1. Prony Coefficients: The Prony series is often used to model the time-dependent viscoelastic behavior of materials. For the cornea, studies have reported Prony coefficients that can vary widely. Generally, the coefficients are determined experimentally and can depend on factors such as age, hydration, and the severity of keratoconus. Specific values may not be universally available, but literature suggests that the Prony coefficients for the cornea can range from approximately 0.1 to 0.5 for the relaxation times.
2. Neo Hookean Coefficient: The Neo Hookean model is a common hyperelastic model used to describe the mechanical behavior of soft biological tissues, including the cornea. The shear modulus is a key parameter in this model. For the cornea, values for the shear modulus can range

Table 1. Prony coefficients ($g_i = G_i/G_0$) normalized by $G_0 = 0.14$ MPa and the relaxation times for the porcine cornea.

g_1 (...)	g_2 (...)	g_3 (...)	τ_1 (s)	τ_2 (s)	τ_3 (s)
0.1105	0.1114	0.1888	0.5866	7.35	42.58

Table 2. Hyper-elastic value of Neo Neo-Hookean model for the porcine cornea.

IOP (mmHg)	C_{10} (MPa)	D_1 (MPa^{-1})
16	0.316	0.185

Table 3. The mechanical properties of the porcine cornea.

	Unit	Healthy case	Keratoconus case
g_1	…	0.1115	0.37
τ_1	s	0.5866	1.173
k_1	…	0.140	0.07
C_{10}	MPa	0.316	0.158
D_1	MPa^{-1}	0.185	0.0925
IOP	mmHg	16	16

> from about 0.5 to 1.5 MPa in healthy corneas, while in keratoconus, the values may be lower due to the structural changes associated with the disease.

For the healthy cornea of the porcine, the Prony coefficients and the Neo Hookean coefficients were obtained from the previous paper [68].

In this paper, the first relation time was so important that the mechanical properties that have been used in this research were mentioned in Table 3.

Table 3 has clarified differences in mechanical properties between healthy and keratoconus corneas, emphasizing how these differences relate to changes in corneal stiffness, deformation behavior, and shear wave speed, as mentioned in the section results.

According to the previous studies, the Young modulus of the keratoconus is mentioned smaller than the healthy cornea and also, the shear modulus and the relaxation time of the keratoconus are mentioned greater than the healthy cornea [77–80], in this study, the data that used in the simulation mentioned in Table 3 that shown the selected values have been selected and used correctly using previous research data [68].

Shear wave velocity characteristics were investigated in this study. The elastography setup employed acoustic radiation force to excite the cornea and facilitate the propagation of shear waves within it. Upon completion of the experiment, the viscoelastic properties, including the Prony series and elastic modulus, as well as the hyper-elastic coefficient derived from the Neo-Hookean model, were determined. Elastography systems are based on the propagation of shear waves to measure shear wave velocity, which allows for the calculation of Young's modulus in soft tissues. Therefore, the initiation of the simulation process in Abaqus is contingent upon obtaining the properties of the cornea and its shear wave velocity. The objective of this study was to simulate the shear wave elastography experiments using ABAQUS and to conduct sensitivity analyses on various parameters related to corneal properties. The structure of the simulation for the shear wave propagation is shown in Figure 2.

2.1. Structural finite element simulation

2.1.1. Geometry. A three-dimensional corneal model was established to represent the corneal conditions and boundaries. The external thickness of the cornea, assumed to be 0.50 mm, was modeled using 10 nodes exhibiting quadratic displacement behavior, and the internal thickness of the cornea, assumed to be 0.30 mm (less than 0.4 mm [75]). The initial corneal curvatures were modified to align with the experimental values following the application of intraocular pressure (IOP) at 16 mmHg, and the internal and external curvatures of the keratoconus were assumed to be 5 mm and 6 mm [81,82]. The limbus was characterized as a spring-damper system that connects the cornea and sclera. Figure 3 shows the geometry of the cornea that was simulated by Abaqus.

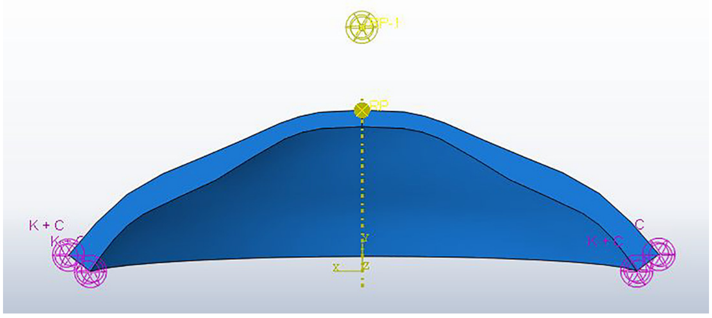

Figure 2. Scheme of the excitation for shear wave propagation with the boundary condition in Abaqus.

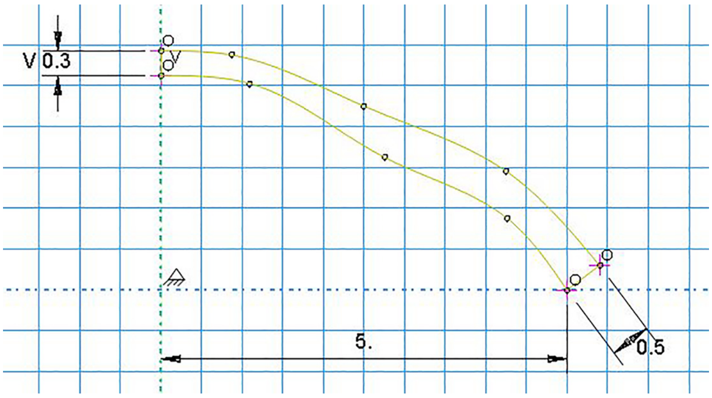

Figure 3. The structure of the keratoconus cornea simulated in Abaqus.

2.1.2. Material model. The modeling of corneal tissue as a hyper-viscoelastic material presents a sophisticated approach to understanding its mechanical behavior. The initial use of the hyper-elastic Neo-Hookean model allows for a simplified representation of the cornea's stored energy function, which can be expressed as a linear equation involving two unknown parameters. This simplification is beneficial for initial analyses and provides a foundational understanding of the corneal mechanics.

However, to capture the more complex viscoelastic behavior of the cornea, the modified Maxwell viscoelastic model is introduced. This model incorporates the Prony series, which allows for a more detailed representation of the time-dependent response of the material. The transition from a hyper-elastic to a hyper-viscoelastic framework acknowledges the intricate relationship between deformation rates and time, highlighting the energy conversion processes that occur within the corneal tissue.

2.1.3. The other parts of the structural finite element simulation. The remaining components, including the finite element method (FEM) settings, boundary conditions, loads, and excitation pressure, are identical to those utilized in the previous study, as summarized in Table 4.

For the simulation of the ex vivo whole globe, the sclera was fixed to replicate the fixation of the cornea within the eye holder during the experiments. In the in vivo condition, the cornea was damped along the vertical symmetry axis to represent the ocular muscles and surrounding adipose tissue. It was proposed that the external damping factors could be consolidated into a singular vertical damping component, while horizontal damping influences were considered negligible. The vertical damping was implemented through a massless longitudinal spring-damper system, represented by a uniaxial tension-compression element characterized by a spring constant of 5×10^6N/m and a damping coefficient of 1.0 [76].

The element size in the mesh modulus of Abaqus is shown in Figure 4.

Table 4. Details of the simulation.

Structure	Definition
Solution method	Dynamic explicit
Excitation pressure	15,000 Pa
Boundary condition	8 springs and 8 dashpots
IOP	16 mmHg
Mesh size	0.05 mm

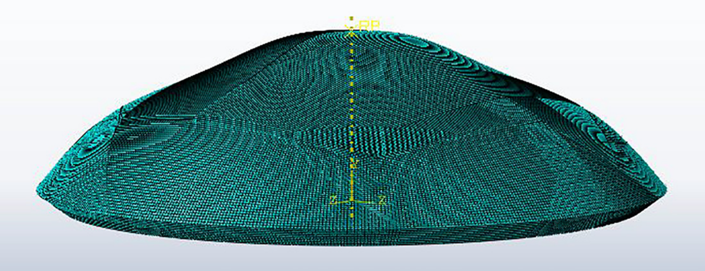

Figure 4. The element size in the Abaqus mesh.

In this study, as in the previous study [68], we have conducted a mesh refinement study to assess the influence of element size on the FEM results, particularly on the deformation at the corneal apex and wave speed estimation. This analysis shows that further mesh refinement beyond a certain level had a negligible impact on the key outcome parameters, thereby confirming the adequacy of the chosen mesh density.

2.2. Computing techniques

For the mechanical simulation of the cornea, ABAQUS Standard/Explicit (version: 2023) was utilized. This process consisted of two phases: the initial phase aimed to assess the impact of intraocular pressure (IOP), while the subsequent phase concentrated on simulating shear wave propagation through the application of an incident wave to stimulate the cornea.

Upon the completion of shear wave propagation, Young's modulus can be determined from the shear wave velocity using equation (20) [68].

$$|E^*| = 2\left(3\rho V_s^2\right)(1+\nu) \tag{20}$$

3. Discussion

The findings of this study highlight the significant biomechanical alterations associated with keratoconus, emphasizing the potential of shear wave elastography (SWE) and finite element modeling (FEM) as complementary tools for diagnosis and treatment planning. The observed reduction in shear wave velocity and increased apex deformation in keratoconus corneas align with previous research, corroborating the link between structural thinning, stiffness loss, and disease progression.

3.1. Shear wave velocity as a biomarker

The shear wave velocity in the cornea depends on some factors, and the most important factor is the first relaxation time of the part of viscoelastic property of the cornea [68]. In this study, the shear wave velocity was calculated in two parts in a predetermined point set at 1.65 mm from the apex point:

Table 5. The shear wave velocity in keratoconus.

Shear wave velocity (m/s)		
Type	15,000 Pa	30,000 Pa
Material	2.49	2.69

Table 6. The deformation in the apex point for keratoconus.

Deformation (mm)	
15,000 Pa	30,000 Pa
3.43	3.40

Table 7. The deformation in the apex point for the healthy cornea.

Deformation (mm)	
15,000 Pa	30,000 Pa
3.29	3.21

- Change the material property,
- Change the material property + changing thickness.

According to the material used for keratoconus in Table 3, and the thickness of keratoconus the shear wave speed obtained is in Table 5.

The reduced shear wave velocity at the apex of keratoconus corneas underscores its role as a sensitive biomarker for early detection and monitoring of disease severity. The findings suggest that shear wave velocity is inversely correlated with the degree of corneal thinning and stiffness loss. This parameter's sensitivity to changes in material properties and intraocular pressure (IOP) highlights its diagnostic potential, particularly in detecting subclinical keratoconus, where traditional diagnostic methods may fall short.

3.2. Apex deformation and biomechanical integrity

The apex point deformation was calculated after applying the excitation pressure to the keratoconus. In this study, the apex point deformation was calculated for two excitation pressures in Table 6.

As shown in Table 6, the deformation in the apex point decreased by increasing the excitation pressure. Changes were around 0.8%, which was noticeable in engineering issues.

The deformation of the apex point was calculated after applying the excitation pressure to the healthy cornea. In this study, the apex point deformation was determined for two excitation pressures, as presented in Table 7.

As shown in Table 7, the deformation at the apex point decreased with an increase in excitation pressure. The observed changes were approximately 2.4%, which is significant in the context of engineering applications.

The increased apex deformation observed in keratoconus corneas further demonstrates the mechanical consequences of structural weakening. FEM simulations provided valuable insights into how material properties, geometric factors, and IOP influence corneal deformation. These results validate FEM capability to replicate in vivo conditions and predict biomechanical behavior, making it an essential tool for understanding keratoconus mechanics and assessing therapeutic interventions.

Table 8. Comparison between the healthy cornea and keratoconus.

	Shear wave velocity (m/s)		Deformation in apex	
	15,000 Pa	30,000 Pa	15,000 Pa	30,000 Pa
Healthy cornea	5.04	5.21	3.29	3.21
Keratoconus (material change)	2.49	2.69	3.43	3.40

3.3. Comparison between the healthy and keratoconus cornea results

The summary of the results of the comparison between the healthy cornea and keratoconus was shown in Table 8.

Based on the obtained results, it is observed that in keratoconus, due to the decreased stiffness, the shear wave velocity is smaller compared to the healthy cornea. Consequently, the deformation at the apex point in the vertical direction is greater in the keratoconus than in the healthy cornea.

According to the findings of a previous study [68] and the simulations conducted in this research, as well as changes in excitation pressure, thickness variations, and the intrinsic material properties of both healthy cornea and keratoconus, it is evident that the most significant impact on the shear wave velocity is associated with the first relaxation time.

The deformation of the apex point in the healthy cornea was less than the deformation of the apex points in Keratoconus. So, this decrease can be attributed to a reduction in corneal thickness and alterations in the mechanical properties of the cornea; however, these changes are minimal, approximately 2%, and can therefore be considered negligible in engineering discussions.

Based on these results, we can assert that the integration of SWE and FEM offers a robust framework for a comprehensive analysis of corneal biomechanics. By combining experimental data with computational modeling, this approach enables precise characterization of mechanical properties and deformation patterns. This synergy not only enhances diagnostic accuracy but also facilitates the development of patient-specific treatment strategies, such as optimizing parameters for corneal cross-linking (CXL).

The study findings have important clinical implications. Reduced shear wave velocity and increased apex deformation can serve as reliable indicators for identifying keratoconus at its early stages, potentially enabling timely intervention to halt disease progression. Moreover, the patient-specific insights gained from FEM simulations can guide customized therapeutic approaches, improving the efficacy of treatments like CXL and mitigating the risk of over- or under-treatment.

4. Conclusion

This study highlights the critical role of shear wave velocity and apex deformation in understanding the biomechanical alterations associated with keratoconus. The integration of shear wave elastography and finite element modeling offers a robust and non-invasive approach to quantify these changes, enabling a deeper insight into disease progression and treatment outcomes. The results confirm that keratoconus corneas exhibit reduced shear wave velocity and increased deformation at the apex due to thinning and loss of stiffness, making these parameters reliable biomarkers for early detection and monitoring.

The findings also emphasize the importance of patient-specific modeling, which can incorporate variations in corneal geometry, material properties, and intraocular pressure. Such an approach not only enhances the accuracy of simulations but also facilitates the development of tailored therapeutic strategies, including corneal cross-linking and other biomechanical interventions.

While the study demonstrates the potential of SWE and FEM, certain limitations should be addressed in future research. The reliance on previously published material parameters and simplified assumptions in FEM models, such as isotropy and homogeneity, may limit the accuracy of simulations. Incorporating anisotropic and heterogeneous properties into FEM models could provide a more realistic representation of corneal biomechanics [83]. In addition, expanding the study to include in vivo measurements and longitudinal data would enhance the clinical applicability of the findings.

Future work could explore the integration of real-time SWE with advanced FEM techniques to enable dynamic monitoring of corneal behavior. Investigating the impact of different therapeutic interventions on shear wave velocity and deformation patterns would further refine treatment protocols. Ultimately, the continued development of SWE and FEM methodologies has the potential to revolutionize the diagnosis and management of keratoconus, paving the way for personalized medicine in ophthalmology.

One of the main limitations of the present study lies in the assumption of corneal isotropy and homogeneity. While these simplifications facilitate the computational modeling process, they do not fully capture the complex biomechanical behavior of the cornea, which is known to exhibit anisotropic and depth-dependent properties due to its collagen fiber architecture. Future studies will focus on incorporating anisotropic hyperelastic models, such as fiber-reinforced formulations, to better represent the structural heterogeneity of the cornea, particularly in keratoconus eyes. In addition, while the current work demonstrates the feasibility of using SWE combined with FEM for estimating corneal stiffness, further research is needed to apply this framework dynamically in vivo. Developing a real-time monitoring system could enable clinicians to track corneal biomechanical changes over time or in response to therapeutic interventions, offering significant potential for personalized diagnostics and treatment planning.

Declaration of conflicting interests

The author(s) declared no potential conflicts of interest with respect to the research, authorship, and/or publication of this article.

Funding

The author(s) received no financial support for the research, authorship, and/or publication of this article.

ORCID iD

Christian Cardillo https://orcid.org/0009-0005-2169-7630

References

[1] Scarcelli, G, Pineda, R, and Yun, SH. Brillouin optical microscopy for corneal biomechanics. *Invest Ophthalmol Vis Sci* 2015; 56(1): 13–22.

[2] Keratoconus. https://vijayanethralaya.com/can-you-reverse-keratoconus-treatment-options/cornea-2/keratoconus/

[3] Dupps, WJ, and Wilson, SE. Biomechanics and wound healing in the cornea. *Exp Eye Res* 2006; 83(4): 709–720.

[4] Kling, S, Hafezi, F, and Richoz, O. Corneal biomechanics after collagen cross-linking: a finite element analysis. *Invest Ophthalmol Vis Sci* 2015; 56(5): 2973–2981.

[5] Vellara, HR, and Patel, DV. Biomechanical properties of the keratoconus cornea: a review. *Clin Exp Optom* 2015; 98(1): 31–38.

[6] Mahmoud, AM, Elsheikh, A, and Anderson, DA. Optical coherence elastography for measuring corneal biomechanical properties. *Exp Eye Res* 2016; 151: 76–82.

[7] dell'Isola, F, Andreaus, U, and Placidi, L. At the origins and in the vanguard of peridynamics, non-local and higher-gradient continuum mechanics: an underestimated and still topical contribution of Gabrio Piola. *Math Mech Solids* 2015; 20(8): 887–928.

[8] Alibert, J-J, Seppecher, P, and dell'Isola, F. Truss modular beams with deformation energy depending on higher displacement gradients. *Math Mech Solids* 2003; 8(1): 51–73.

[9] Turco, E, Giorgio, I, Misra, A, et al. King post truss as a motif for internal structure of (meta) material with controlled elastic properties. *R Soc Open Sci* 2017; 4(10): 171153.

[10] Fedele, R, and Luciano, R. A recursive formula to compute Lagrangian actions corresponding to an Eulerian edge H-force in elastic materials with a sufficiently high grade. *Math Mech Complex Syst* 2024; 12(4): 389–410.

[11] Tepedino, M. The mechanical role of the periodontal ligament for developing mathematical models in orthodontics. *Math Mech Complex Syst* 2023; 11(4): 525–539.

[12] Wang, X, and Schiavone, P. An elliptical incompressible liquid inclusion in an infinite anisotropic elastic space. *Math Mech Complex Syst* 2024; 12(2): 217–232.

[13] Altenbach, H, and Eremeyev, VA. On the linear theory of micropolar plates. *ZAMM J Appl Math Mech/ Z Fur Angew Math* 2009; 89(4): 242–256.

[14] Eremeyev, VA, and Pietraszkiewicz, W. Material symmetry group and constitutive equations of micropolar anisotropic elastic solids. *Math Mech Solids* 2016; 21(2): 210–221.

[15] La Valle, G. A new deformation measure for the nonlinear micropolar continuum. *Z Fur Angew Math Phys* 2022; 73(2): 78.

[16] La Valle, G, and Massoumi, S. A new deformation measure for micropolar plates subjected to in-plane loads. *Contin Mech Thermodyn* 2022; 34: 243–257.

[17] Spagnuolo, M, Franciosi, P, and dell'Isola, FF. A Green operator-based elastic modeling for two-phase pantographic-inspired bi-continuous materials. *Int J Solids Struct* 2020; 188: 282–308.

[18] Schulte, J, Dittmann, M, Eugster, SR, et al. Isogeometric analysis of fiber reinforced composites using Kirchhoff–Love shell elements. *Comput Methods Appl Mech Eng* 2020; 362: 112845.

[19] Turco, E, Golaszewski, M, Giorgio, I, et al. Pantographic lattices with non-orthogonal fibres: experiments and their numerical simulations. *Compos B: Eng* 2017; 118: 1–14.

[20] Ciallella, A, D'Annibale, F, Del Vescovo, D, et al. Deformation patterns in a second-gradient lattice annular plate composed of spira mirabilis fibers. *Contin Mech Thermodyn* 2023; 35(4): 1561–1580.

[21] Giorgio, I, Harrison, P, dell'Isola, F, et al. Wrinkling in engineering fabrics: a comparison between two different comprehensive modelling approaches. *Proc R Soc A: Math Phys Eng Sci* 2018; 474(2216): 20180063.

[22] Giorgio, I, Ciallella, A, and Scerrato, D. A study about the impact of the topological arrangement of fibers on fiber-reinforced composites: some guidelines aiming at the development of new ultra-stiff and ultra-soft metamaterials. *Int J Solids Struct* 2020; 203: 73–83.

[23] Barchiesi, E. Equilibria of axial-transversely loaded homogenized duoskelion beams. *Math Mech Complex Syst* 2024; 12(3): 283–309.

[24] Auffray, N, dell'Isola, F, Eremeyev, VA, et al. Analytical continuum mechanics à la Hamilton–Piola least action principle for second gradient continua and capillary fluids. *Math Mech Solids* 2015; 20(4): 375–417.

[25] dell'Isola, F, Eugster, SR, Fedele, R, et al. Second-gradient continua: from Lagrangian to Eulerian and back. *Math Mech Solids* 2022; 27(12): 2715–2750.

[26] Madeo, A, dell'Isola, F, and Darve, F. A continuum model for deformable, second gradient porous media partially saturated with compressible fluids. *J Mech Phys Solids* 2013; 61(11): 2196–2211.

[27] La Valle, G, Abali, BE, Falsone, G, et al. Sensitivity of a homogeneous and isotropic second-gradient continuum model for particle-based materials with respect to uncertainties. *ZAMM Z Fur Angew Math* 2023; 103(10): e202300068.

[28] Giorgio, I. Lattice shells composed of two families of curved Kirchhoff rods: an archetypal example, topology optimization of a cycloidal metamaterial. *Contin Mech Thermodyn* 2021; 33(4): 1063–1082.

[29] dell'Isola, F, Moschini, S, and Turco, E. Towards the synthesis of planar beams whose deformation energy depends on the third gradient of displacement. *Math Mech Complex Syst* 2024; 12(4): 573–597.

[30] Ratsaby, J. On system complexity, stability and performance: application to prediction. *Math Mech Complex Syst* 2024; 12(4): 411–470.

[31] Giorgio, I. A variational formulation for one-dimensional linear thermoviscoelasticity. *Math Mech Complex Syst* 2022; 9(4): 397–412.

[32] Ciallella, A, Scerrato, D, Spagnuolo, M, et al. A continuum model based on Rayleigh dissipation functions to describe a Coulomb-type constitutive law for internal friction in woven fabrics. *Z Fur Angew Math Phys* 2022; 73(5): 209.

[33] Giorgio, I, Andreaus, U, Scerrato, D, et al. A visco-poroelastic model of functional adaptation in bones reconstructed with bio-resorbable materials. *Biomech Model Mechanobiol* 2016; 15: 1325–1343.

[34] Bersani, AM, Caressa, P, and dell'Isola, F. Approximation of dissipative systems by elastic chains: numerical evidence. *Math Mech Solids* 2023; 28(2): 501–520.

[35] Bersani, AM, and Caressa, P. Lagrangian descriptions of dissipative systems: a review. *Math Mech Solids* 2021; 26(6): 785–803.

[36] Bersani, AM, Caressa, P, and Ciallella, A. Numerical evidence for the approximation of dissipative systems by gyroscopically coupled oscillator chains. *Math Mech Complex Syst* 2022; 10(3): 265–278.

[37] Cuomo, M, Contrafatto, L, and Greco, L. A cohesive interface model with degrading friction coefficient. *Math Mech Complex Syst* 2024; 12(2): 113–133.

[38] Ponomarev, D. A generalised time-evolution model for contact problems with wear and its analysis. *Math Mech Complex Syst* 2022; 10(3): 279–319.

[39] Abali, BE, Klunker, A, Barchiesi, E, et al. A novel phase-field approach to brittle damage mechanics of gradient metamaterials combining action formalism and history variable. *ZAMM J Appl Math Mech/ Z Fur Angew Math* 2021; 101(9): e202000289.

[40] Timofeev, D, Barchiesi, E, Misra, A, et al. Hemivariational continuum approach for granular solids with damage-induced anisotropy evolution. *Math Mech Solids* 2021; 26(5): 738–770.

[41] Placidi, L, Barchiesi, E, dell'Isola, F, et al. On a hemi-variational formulation for a 2D elasto-plastic-damage strain gradient solid with granular microstructure. *Math Eng* 2022; 5: 1–24.

[42] Placidi, L, Barchiesi, E, and Misra, A. A strain gradient variational approach to damage: a comparison with damage gradient models and numerical results. *Math Mech Complex Syst* 2018; 6(2): 77–100.

[43] Addessi, D, D'Annibale, F, Placidi, L, et al. A bone remodeling approach encoding the effect of damage and a diffusive bio-mechanical stimulus. *Contin Mech Thermodyn* 2024; 36: 993–1012.

[44] Heiduschke, K. On tensor projections, stress or stretch vectors and their relations to Mohr's three circles. *Math Mech Complex Syst* 2024; 12(2): 173–216.

[45] Grillo, A, and Di Stefano, S. An a posteriori approach to the mechanics of volumetric growth. *Math Mech Complex Syst* 2023; 11(1): 57–86.

[46] Grillo, A, and Di Stefano, S. Comparison between different viewpoints on bulk growth mechanics. *Math Mech Complex Syst* 2023; 11(2): 287–311.

[47] Giorgio, I, dell'Isola, F, Andreaus, U, et al. An orthotropic continuum model with substructure evolution for describing bone remodeling: an interpretation of the primary mechanism behind Wolff's law. *Biomech Model Mechanobiol* 2023; 22(6): 2135–2152.

[48] Ciallella, A, Giorgio, I, Eugster, SR, et al. Generalized beam model for the analysis of wave propagation with a symmetric pattern of deformation in planar pantographic sheets. *Wave Motion* 2022; 113: 102986.

[49] Placidi, L, Rosi, G, Giorgio, I, et al. Reflection and transmission of plane waves at surfaces carrying material properties and embedded in second-gradient materials. *Math Mech Solids* 2014; 19(5): 555–578.

[50] Turco, E, Barchiesi, E, Ciallella, A, et al. Nonlinear waves in pantographic beams induced by transverse impulses. *Wave Motion* 2022; 115: 103064.

[51] Berezovski, A, Yildizdag, ME, and Scerrato, D. On the wave dispersion in microstructured solids. *Contin Mech Thermodyn* 2020; 32: 569–588.

[52] Berezovski, A, Giorgio, I, and Della Corte, A. Interfaces in micromorphic materials: wave transmission and reflection with numerical simulations. *Math Mech Solids* 2016; 21(1): 37–51.

[53] Di Michele, F, Styahar, A, Pera, D, et al. Shape effects on wave propagation in a 2D domain using the finite element method. *Math Mech Complex Syst* 2024; 12(3): 311–331.

[54] Fedele, R, Placidi, L, and Fabbrocino, F. A review of inverse problems for generalized elastic media: formulations, experiments, synthesis. *Contin Mech Thermodyn* 2024; 36: 1413–1453.

[55] Valoroso, N, and Fedele, R. Characterization of a cohesive-zone model describing damage and de-cohesion at bonded interfaces. Sensitivity analysis and mode-I parameter identification. *Int J Solids Struct* 2010; 47(13): 1666–1677.

[56] De Angelo, M, Barchiesi, E, Giorgio, I, et al. Numerical identification of constitutive parameters in reduced-order bi-dimensional models for pantographic structures: application to out-of-plane buckling. *Arch Appl Mech* 2019; 89(7): 1333–1358.

[57] Shekarchizadeh, N, Laudato, M, Manzari, L, et al. Parameter identification of a second-gradient model for the description of pantographic structures in dynamic regime. *Z Fur Angew Math Phys* 2021; 72(6): 190.

[58] Yang, H, Abali, BE, Timofeev, D, et al. Determination of metamaterial parameters by means of a homogenization approach based on asymptotic analysis. *Contin Mech Thermodyn* 2020; 32: 1251–1270.

[59] Giorgio, I. A discrete formulation of Kirchhoff rods in large-motion dynamics. *Math Mech Solids* 2020; 25(5): 1081–1100.

[60] Greco, L, Scrofani, A, and Cuomo, M. A non-linear symmetric G1-conforming Bézier finite element formulation for the analysis of Kirchhoff beam assemblies. *Comput Methods Appl Mech Eng* 2021; 387: 114176.

[61] Greco, L, and Cuomo, M. An implicit G1-conforming bi-cubic interpolation for the analysis of smooth and folded Kirchhoff–Love shell assemblies. *Comput Methods Appl Mech Eng* 2021; 373: 113476.

[62] Ardic, IT, Yildizdag, ME, and Ergin, A. Hybrid isogeometric-based analysis and experimental investigation on the dynamic response characteristics of a clamped circular plate partially in contact with fluid. *Thin-Walled Struct* 2024; 203: 112171.

[63] Allen, AR, and Rémond, Y. Theramechanics: how acting on mechanics will help conceive new medical treatments. *Math Mech Complex Syst* 2023; 11(4): 541–566.

[64] De Korte, CL, Pasterkamp, G, van der Steen, AFW, et al. Characterization of plaque components with intravascular ultrasound elastography in human femoral and coronary arteries in vitro. *Circulation* 2000; 102(6): 617–623.

[65] Elsheikh, A, Alhasso, D, and Rama, P. Biomechanical properties of human and porcine corneas. *Exp Eye Res* 2008; 86(5): 783–790.

[66] Ethier, CR, Johnson, M, and Ruberti, J. Ocular biomechanics and biotransport. *Annu Rev Biomed Eng* 2004; 6: 249–273.

[67] Su, P, Yang, Y, Xiao, J, et al. Corneal hyper-viscoelastic model: derivations, experiments and simulations. *Acta Bioeng Biomech* 2015; 17: 73–84.

[68] Mazinani, P, Cardillo, C, and Mosaddegh, P. Evaluating corneal biomechanics using shear wave elastography and finite element modeling: sensitivity analysis and parametric optimization. *Contin Mech Thermodyn* 2024; 37: 12.

[69] Friedrich-Rust, M, Wunder, K, Kriener, S, et al. Liver fibrosis in viral hepatitis: noninvasive assessment with acoustic radiation force impulse imaging versus transient elastography. *Radiology* 2009; 252(2): 595-604.

[70] Kampmeier, J, Radt, B, Birngruber, R, et al. Thermal and biomechanical parameters of porcine cornea. *Cornea* 2000; 19(3): 355–363.

[71] Palmeri, MFK. Acoustic radiation force impulse (ARFI) imaging of the gastrointestinal tract. *Ultrason Imaging* 2005; 27: 75–88.

[72] Bryant, MR, and Mcdonnell, PJ. Constitutive laws for biomechanical modeling of refractive surgery. *J Biomech Eng-Tasme* 1996; 118(4): 473–481.
[73] Abali, BE. Inverse analysis of cellulose by using the energy-based method and a rotational rheometer. *Appl Sci* 2018; 8(8): 1354.
[74] Yang, H, Ganzosch, G, Giorgio, I, et al. Material characterization and computations of a polymeric metamaterial with a pantographic substructure. *Z Fur Angew Math Phys* 2018; 69: 1–16.
[75] Alio, JL, and Shabayek, MH. Keratoconus: a review of the literature. *Clin Exp Ophthalmol* 2006; 34(5): 487–493.
[76] Kling, S, Bekesi, N, Dorronsoro, C, et al. Corneal viscoelastic properties from finite-element analysis of In Vivo air-puff deformation. *PLoS ONE* 2014; 9(8): e104904.
[77] Kling, S, and Hafezi, F. Corneal biomechanics—a review. *Ophthalmic Physiol Opt* 2017; 37(3): 240–252.
[78] Ariza-Gracia, MÁ, Zurita, JF, Piñero, DP, et al. Coupled biomechanical response of the cornea assessed by non-contact tonometry. A simulation study. *PloS one* 2015; 10(3): e0121486.
[79] Elsheikh, A, Alhasso, D, and Rama, P. Biomechanical properties of human and porcine corneas. *Exp Eye Res* 2008; 86(5): 783–790.
[80] Nguyen TD. Biomechanics of the Cornea and Sclera. In: Kassab, G, and Sacks, M (eds) *Structure-Based Mechanics of Tissues and Organs*. Boston, MA: Springer, 2016.
[81] Meek, KM, and Knupp, C. Corneal structure and transparency. *Prog Retin Eye Res* 2015; 49: 1–16.
[82] Roy, AS, and Dupps, WJ. Patient-specific modeling of corneal refractive surgery outcomes and inverse estimation of elastic property changes. *J Biomech Eng* 2011; 133(1): 011002.
[83] dell'Isola, F, D'Annibale, F, Luciano, R, et al. A generalised plate with kinematically independent thickness for modelling shapes of corneas affected by keratoconus before and after penetrating keratoplasty. *Math Mech Solids* 2025. DOI: 10.1177/10812865251345814

Chapter 7

Experimental study of fluid displacement and viscous fingering in fractured porous media

Chapter abstract

Empirical studies have investigated the viscous fingering instability by examining the displacement of miscible fluids in fractured porous media. Despite extensive research on viscous fingering, there is a scarcity of data on its behavior within fractured porous frameworks. Experiments conducted in rectangular porous models with fractures at 0°, 45°, and 90° orientations sought to understand the influence of fracture orientation on fluid displacement, where both channeling and fingering are critical mechanisms. This chapter focuses on how the viscosity ratio, a crucial parameter, affects the complexity of fingering patterns. Using image processing techniques, quantitative factors like sweep efficiency, tip location, and breakthrough time were evaluated. The findings reveal that a higher viscosity ratio results in more intricate finger formations. Moreover, raising the injection rate slightly enlarges the finger patterns while diminishing the channeling effect. Importantly, 0°-aligned fractures had the greatest effect on sweep efficiency and tip location, enhancing the tip velocity of the fingers by as much as 90%.

Continuum Mech. Thermodyn. (2025) 37:29
https://doi.org/10.1007/s00161-025-01362-3

ORIGINAL ARTICLE

**Amirhosein Zadehkabir · Pouria Mazinani ·
Behrouz Zare Vamerzani · Christian Cardillo ·
Hamid Saffari · Seyed Mostafa Hosseinalipour**

Experimental study of fluid displacement and viscous fingering in fractured porous media: effect of viscosity ratio

Received: 8 December 2024 / Accepted: 13 January 2025 / Published online: 4 February 2025

Abstract Viscous fingering instability has been analyzed through empirical studies using miscible flow displacement in fractured porous media. While significant research has been conducted on viscous fingering, limited information is available regarding its behavior in fractured porous structures. The experiments were conducted in rectangular porous models with fractures oriented at 0°, 45°, and 90°, to investigate how fracture orientation influences fluid displacement, where both channeling and fingering mechanisms play significant roles. This paper, which is the second part of a previous study, places particular emphasis on the impact of the viscosity ratio, a crucial parameter in determining the complexity of the fingering patterns. Quantitative parameters such as sweep efficiency, tip location, and breakthrough time were evaluated and analyzed using image processing techniques. The results indicate that increasing the viscosity ratio leads to more complex finger formations. Additionally, as the injection rate increases, the size of the finger patterns slightly increases, while the channeling effect becomes less pronounced. Notably, fractures aligned at 0° had the most significant impact on the rate of sweep efficiency and tip location, increasing the tip velocity of the fingers by up to 90%.

Keywords Fractured porous media · Viscous fingering · Saffman-Taylor instability · Two-phase displacement flow · Flow channeling

1 Introduction

Displacement flow in porous media has been an important matter of interest in fluid mechanics since many studies have been conducted regarding multiphase flow in porous models. Viscous fingering is an interfacial instability that occurs when a fluid is driven by another less viscous one. The “fingering” phenomenon could appear as a result of the nonlinear instability of a moving contact line [1]. Viscous fingering or commonly known as Saffman-Taylor instability was first studied and described by Hill [2] and later by Saffman and Taylor [3]. It is a ubiquitous hydrodynamic instability that plays a key role in hydrology, filtration, underground water pollution [4], geothermal wells and, chromatography [5–7]. viscous fingering is mostly described as undesired phenomenon [8] and any process aimed toward eliminating this instability or controlling the growth rate of the viscous fingers is of technological importance. In other words, in many of these cases, the goal is to optimize and control displacement front and the amount of mixing that occurs between the two fluids. However, it can also

---

Communicated by Andreas Öchsner.

A. Zadehkabir ·B. Z. Vamerzani · H. Saffari · S. M. Hosseinalipour · P. Mazinani ( )
School of Mechanical Engineering, Iran University of Science and Technology, Tehran, Iran
E-mail: pouria.mazinani789@gmail.com

C. Cardillo ( )
Department of Civil Engineering and Architecture, University of Catania, Catania, Italy
E-mail: christian.cardillo@phd.unict.it

be controlled and used for shaping fluids in various applications including capillary pumps and microfluidics [9]. This phenomenon can be encountered in miscible and immiscible displacements as well as in Newtonian and non-Newtonian fluids [10–12]. Viscous fingering characteristics can be affected by several parameters such as injection rate [13], viscosity ratio [14] and, physical properties of the porous medium [15].

Since it is challenging to visualize the fluid interface in 3D models, the experiments of viscous fingering instability have primarily been carried out in planar porous mediums and Hele-Shaw cells which the flow in low Reynolds numbers is mathematically analogous to the flow through pores. 2D models have provided the opportunity to study the fluid displacement in radial [16], longitudinal [17] and, diagonal [18] directions. Christie et al. [19] and Zhang et al. [20] used packs of glass beads in order to simulate the flow inside the porous media. Other methods have also been developed to make 2D porous models. Optical Lithography [21], chemical etching [22,23], sandblasting [24] and CO_2 laser technology [25,26] are among these methods. Furthermore, in [27] a small-thickness two-dimensional model was fabricated based on thin sections of a real sandstone sample. In some research works fluid displacement and viscous fingering instability have been studied in 2D micromodels [18,28–30]. However, recently a number of experimental and numerical studies have also been conducted, investigating two phase fluid displacements such as Rayleigh-Taylor instability in 3D models [31,32].

Saffman and Taylor [2] studied this instability and observed that during the immiscible fluid displacement, the fingers eventually coalesce into a single finger. Tan and Homsy [33] studied the nonlinear viscous fingering instability in miscible displacement. They defined mobility ratio (M) and Péclet number (Pe) as the two parameters affecting the stability characteristics and observed that always a few dominant fingers spread and shield the growth of other fingers. In another research, Kopf-Sill and Homsy [34] studied the viscous fingering instability experimentally. They reported that there is a limit to the complexity of the fingers and studied the tip location parameter which increased linearly during the secondary fluid injection. Nijjer et al. [6] numerically studied the dynamics of viscous fingering instability. They studied the injection of fluid into a planar porous medium containing more viscous fluid. Also, the evolution of the fingers from linear instability to non-linear and late-time single finger regime was studied. According to this study, in early times viscous fingering instability started with series of fine fingers and in intermediate regime and reaching certain amplitude, fingers began to interact with each other resulting in non-linear instability which eventually evolved to single finger exchange flow.

Budek et al. [35] also modeled the initiation of fingering instability and the interactions between the fingers known as "loop formation regime". They determined a range of mobility contrast between primary and displacing fluid in which the most intense loop formation occurs. Out of the determined range, the fingers were small or distant enough to have less interaction in transverse direction. It was also confirmed that the finger formation is just a transient phenomenon which leads to single-finger state by periodic interactions and coalescing fingers into one another.

Underground rocks and geological layers where viscous fingering happens in practice, contain heterogeneities and fractures and are rarely homogenous. In addition to fingering instability, also channeling effect is observed due to the heterogeneities in porous medium. During the multiphase flow, the displacing fluid is mobilized through the fractures with permeability contrast. Excessive hydraulic conductivity and permeability within the fractures, contribute to fluid bypassing much of the porous matrix. In order to overcome this problem, many methods such as chemical [36], polymer [28,37], CO_2 and foam flooding [38,39] have been considered and utilized. Loggia et al. [40] found that the channeling effect in porous medium happens when the permeability ratio is higher than the viscosity ratio. Ahmadi et al. [41] investigated the impact of different injection sites on fluid displacement parameters during polymer flooding. They introduced the location of injection point as a significant factor affecting other parameters such as sweep efficiency and breakthrough time.

Fingering instability can be modeled utilizing second-gradient deterministic and stochastic frameworks. The model described in [42–45] is distinguished by a symmetric and positive definite acoustic tensor, rendering it advantageous for constitutive identification.

Another pertinent line of research investigates the integration and generalization of Darcy's law within models to more accurately represent fluid velocity in relation to permeability and pressure gradients in fractured porous media [46–49]. Furthermore, alteration of porosity within the microstructured matrix may provide enhanced insights into the interaction between fracture channels and bulk porous regions [50–53]. This advancement would aid in understanding how local pore-scale effects and heterogeneous porosity distributions influence the initiation and evolution of viscous fingering patterns. The incorporation of microstructural models that consider the variability of material properties [54–56] could facilitate a more precise prediction of complex displacement patterns [57–60], thereby offering practical implications for the improved management of multiphase flows in practical applications [61–65]. Emphasizing these elements could yield a more comprehensive understanding of the dynamics of porous media and suggest potential practical applications.

In this paper, horizontal flow of miscible viscous fingering instability has been studied in three 2D fractured porous mediums. In this regard, the effect of viscosity ratio by using different viscosities of glycerol-water solutions as displaced fluid has been investigated. The experiments are repeated in three different injection rates in order to determine the role of injection rate on altering the characteristics of viscous fingering instability in fractured porous mediums. Fingering patterns and mechanisms which have been introduced and described in other research works [6,8] are discussed in different temporal stages of fluid flow and the cycle of fingering mechanisms which contributed to evolution of fingers from onset to final regime. In addition, both fingering and channeling effects are compared and investigated in different conditions where they dominated over each other. Quantitative parameters of fluid displacement are measured and discussed including sweep efficiency, tip location and, breakthrough time. As it was confirmed in previous studies [26], the complexity of fingers increased in higher viscosity ratios and the role of fractures on flow channeling was more distinct. Moreover, the role of fracture orientation is clearly shown in tip location.

2 Materials and methods

To study the viscous fingering instability within fractured porous media, the displacing fluid was injected into the model at three different injection rates and viscosity ratios to analyze their effects on instability patterns. The flow regime in the model follows Darcy's law, which relates fluid velocity to the physical properties of the porous medium:

$$u = -\frac{k}{\mu}\nabla p \tag{1}$$

where u is fluid velocity, k is the permeability, μ is, viscosity, and$p$is pressure. The viscosity ratio, defined as the ratio of viscosities between the displaced and displacing fluids, is given by:

$$R = \frac{\mu_1}{\mu_2} \tag{2}$$

where μ_1 and μ_2 are the viscoties of the displaced and displacing fluids, respectively. Additionally, the injection rate, defined as the amount of fluid introduced into a system per unit of time, Q (ml/min), plays a crucial role in flow dynamics. Fractures within the porous media provide preferential pathways, channeling the displacing fluid and affecting the effective permeability and channeling capacity. The angle between the flow direction and fracture orientation also influences these effects [66]:

$$k_{fr} = k_f \cos^2\alpha \tag{3}$$

where $k_{fr}$is the effective permeability along the fracture, and k_f is permeability in the direction parallel to flow, and $\alpha$is the angle between flow and fracture directions. The perpendicular permeability is not considered.

2.1 Fluids: properties and composition of displacing and displaced fluids used in the experiment

The experiments were carried out at standard room temperature. Dyed methanol was injected as the displacing fluid into the porous medium saturated with a glycerol-water solution. Three glycerol-water solutions with different viscosities were prepared to be used as primary displaced fluids. According to the tests, minor changes were observed in the physical properties of methanol after the dye was added. Water and glycerol are miscible in all proportions, making it possible to prepare fluids with viscosities ranging from 1 to 1350 mPa·s [67]. Table 1 shows the properties of methanol as the displacing fluid and the glycerol-water solutions as displaced fluids. The values shown in Table 1 were measured using a rotational MCR300 rheometer.

2.2 Experimental setup

The experimental setup consists of a horizontally oriented acrylic porous model with dimensions of 33 cm in length and 20 cm in width. A 1 cm thick transparent acrylic plate is securely fastened on top of the engraved

Table 1 Fluid properties

Fluid	Viscosity (mPa·s)
methanol	0.6
Glycerol-water solution 1	7.4
Glycerol-water solution 2	26.5
Glycerol-water solution 3	47.1

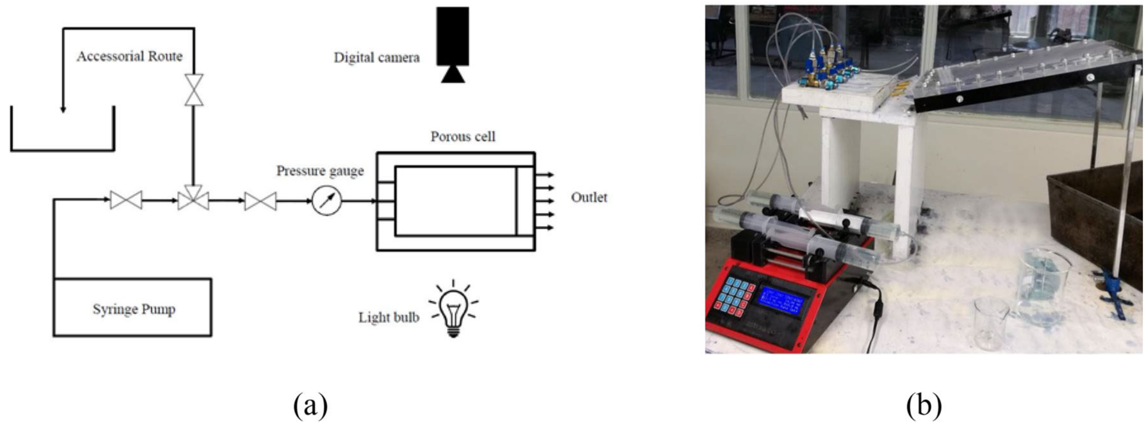

Fig. 1 **a** Schematic diagram and **b** photograph of the experimental setup [68]

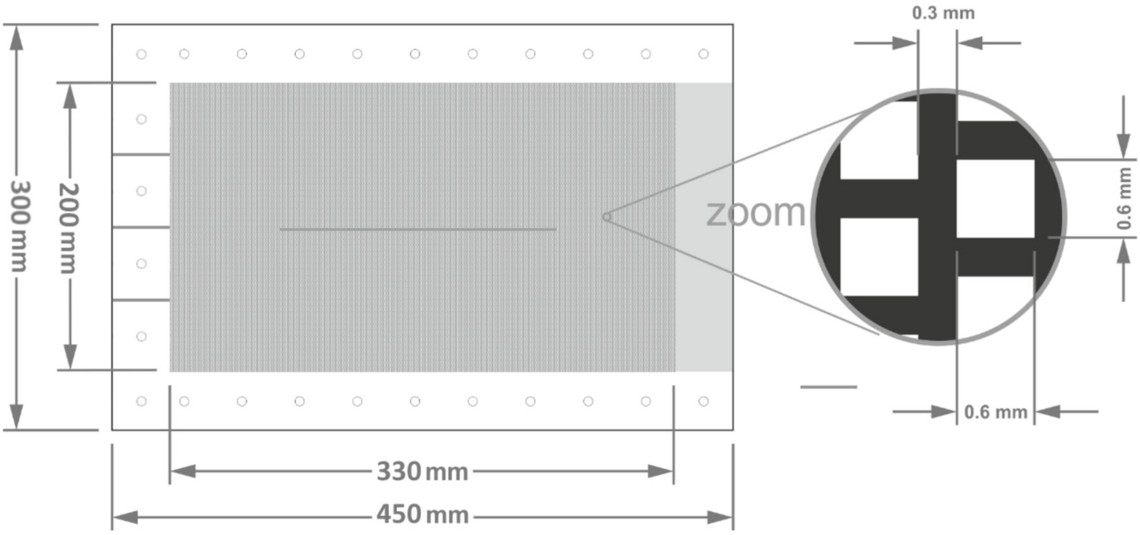

Fig. 2 Schematic diagram of the porous cell with a zero-degree fracture orientation and pore pattern [68]

plate to seal the porous cell. A schematic of the setup is shown in Fig. 1. Fluids are injected into the porous cell via a precise syringe pump. Three inlets, located on the left side of the cell, facilitate fluid injection, while an open outlet on the right side allows the fluid to exit, maintaining a zero relative pressure condition.

The porous pattern of the medium, as depicted in Fig. 2 was engraved onto the lower plate using a CO_2 laser to a depth of 3 mm, resulting in a model porosity of 0.52. Three distinct porous models with different fracture orientations were fabricated, each containing fractures with a width of 0.4 mm. Images of the porous models and fracture locations are shown in Figs. 2 and 3. The physical properties of the models are presented in Table 2. The porosity values in Table 2 reflect the matrix porosity, with the presence of fractures causing only minimal changes to the overall porosity of the cell. The permeability values measured correspond to the matrix alone, as the presence of fractures alters the cell's overall permeability.

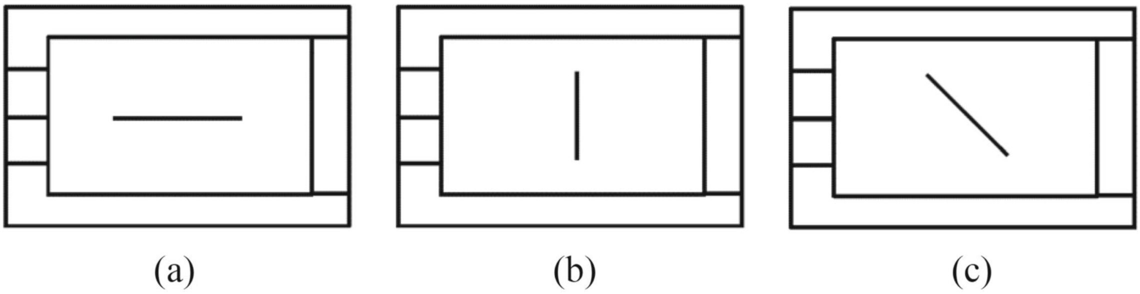

Fig. 3 Schematic sketch of porous media with different fracture orientations: **a** 0 degrees, **b** 45 degrees, **c** 90 degrees [68]

Table 2 Physical properties of the porous models

Width × Length	33× 20 cm
Porosity	0.52
Matrix permeability	2.1E-11 m^2
Fracture width	4E-4 m
Engraved depth	3E-3 m

A support structure with two degrees of freedom was installed above the cell and mounted to the ceiling. This setup supports the camera and allows for lens adjustments to capture the flow displacement and fingering patterns at the optimal angle. In the experiments, an accurate syringe pump manufactured by Zist Raah e Daanesh Co. was used to provide a precise and adjustable flow rate with an accuracy of 0.07 ml/min into the porous medium. In addition, a centrifugal pump was used for the cleaning process with distilled water.

2.3 Experimental procedure

Initially, the glycerol-water solution was injected into the porous model until complete saturation was achieved. The injection rate was kept low during this process to prevent air bubbles from becoming trapped within the cell. Once saturated, the cell was positioned horizontally, and the displacing fluid (dyed methanol) was injected into the porous medium through three inlets, while the excess fluid exited from the opposite side of the cell. The displacing fluid was injected at three different flow rates: $Q = 35.88$, 71.76, and 107.64 ml/min. These injection rates were selected to ensure a fluid velocity in which diffusion between the two fluids could be considered negligible. Throughout the experiment, the flow patterns were continuously monitored using the Nikon D300 camera.

2.4 Image processing and quantitative analysis

As previously mentioned, the displacement of the glycerol-water solution by methanol was monitored using the Nikon D300 camera, capable of capturing continuous, high-quality images. The images were taken at 1-second intervals and processed using custom image-processing code developed in MATLAB. First, the red channel was extracted from the raw images to maximize contrast between the two fluids. Then, the red channel images were converted into binary black-and-white images Fig. 4. Various quantitative parameters were calculated from the binary images. Examples of the processed images are shown in Fig. 5, where R is the viscosity ratio as defined in Eq. (2).

3 Results: influence of viscosity ratio

The miscible viscous fingering (MVF) phenomenon in fractured porous media is investigated experimentally. Three different porous models with fractures oriented at 0°, 45°, and 90° were used to explore the influence of fracture orientation and viscosity ratio on fluid displacement behavior. The results show that the fluid displacement is significantly affected by the fracture orientation, with the most noticeable effects observed in

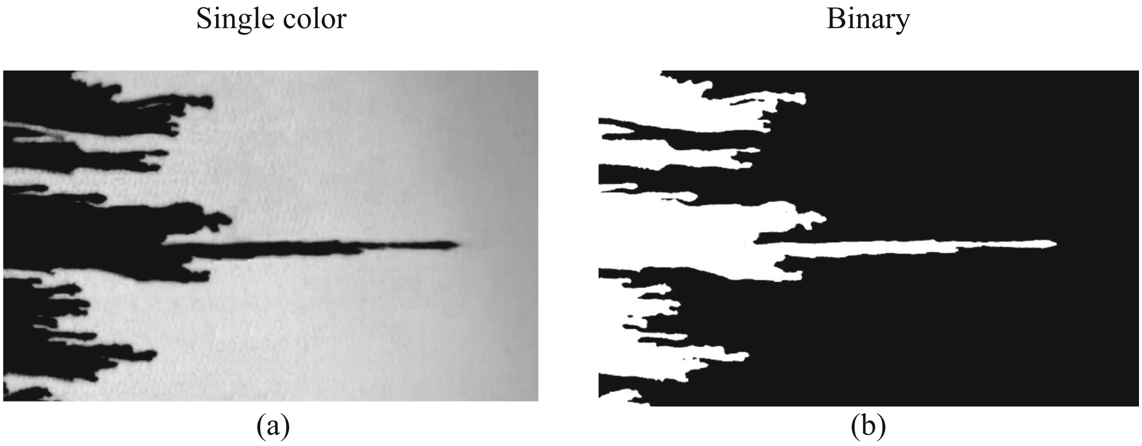

Fig. 4 **a** Single-color image and **b** binary image at $R = 78.5$

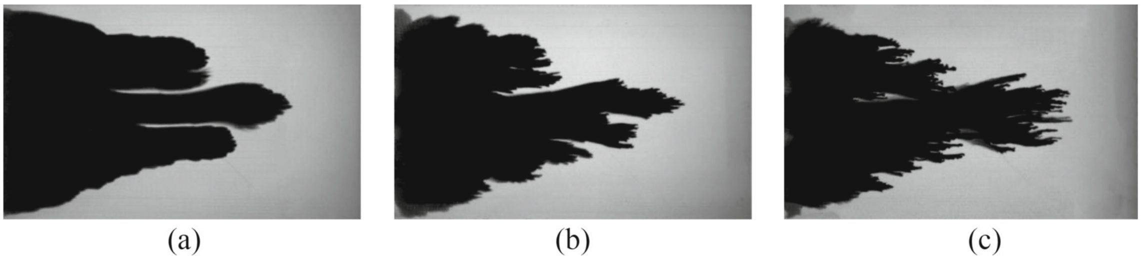

Fig. 5 Fluid displacement in a 45-degree fractured medium at Q = 35.88 ml/min, with **a** R = 12.3, **b** R = 44.2, and **c** R = 78.5

the 0° fracture model. As the fracture orientation is rotated to 90°, subtle changes in both quantitative and qualitative results are noted.

The formation of finger patterns can be described by several mechanisms, which have been defined and categorized in previous studies [6,8,26]. Initially, the displacing fluid enters the porous medium with a sharp interface, generating small finger-like structures. As the displacing fluid continues to advance, the interface smooths out, and larger fingers emerge. The most common fingering mechanisms observed in the experiments include: *shielding*, where a longer finger shields the growth of smaller fingers at its tip; *splitting*, where a finger splits into two smaller ones; *side branching*, where a new finger forms from the side of a larger one; *fading*, where a finger stops growing and diffuses into the surrounding medium; and *skewering*, where fingers flatten, and a new bump forms at the tip. The general fingering mechanism includes the *splitting* and *side-branching* of fingers into smaller ones, followed by coalescence, which leads to the formation of larger fingers. These interactions were also observed in our experiments.

3.1 Influence of viscosity ratio on fingering mechanisms

The viscosity ratio plays a crucial role in the dynamics of fingering instability. At lower viscosity ratios, the displacing fluid forms a soft front, resulting in relatively simple interface dynamics and low instability. Figure 5a illustrates this behavior with the formation of bulk fingers at low viscosity ratios, where the complexity of the fluid interface is minimal. As the viscosity ratio increases (see Fig. 5b), smaller fingers begin to emerge from the bulk, indicating a higher instability and greater interaction between the fingers. At high viscosity ratios (see Fig. 5c), fingers interact more intensely, and the fingering mechanisms become more pronounced, with increased splitting and side branching.

The dynamics of viscous fingering are particularly pronounced at high viscosity ratios, where a sequence of three phases is observed, as reported by previous studies [6]. These phases include: (1) the early-time phase with small, localized instabilities; (2) the intermediate-time phase, where fingers begin to interact with each other; and (3) the late-time phase, in which the displacing fluid evolves into a single bulk flow interface. During

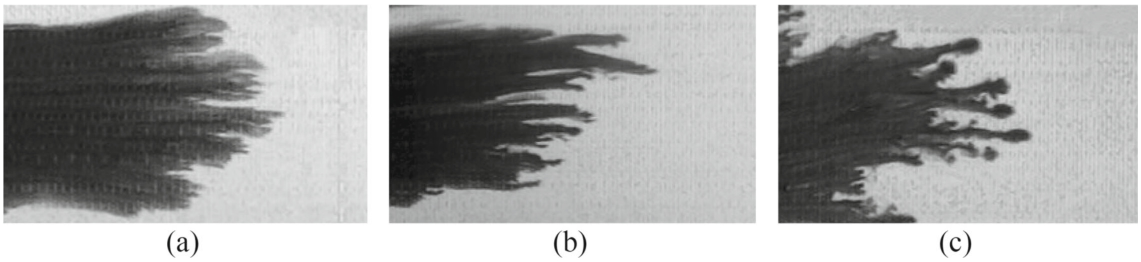
(a) (b) (c)

Fig. 6 Finger shapes at Q=107.64 ml/min for **a** R=12.3R, **b** R=44.2, and **c** R=78.5

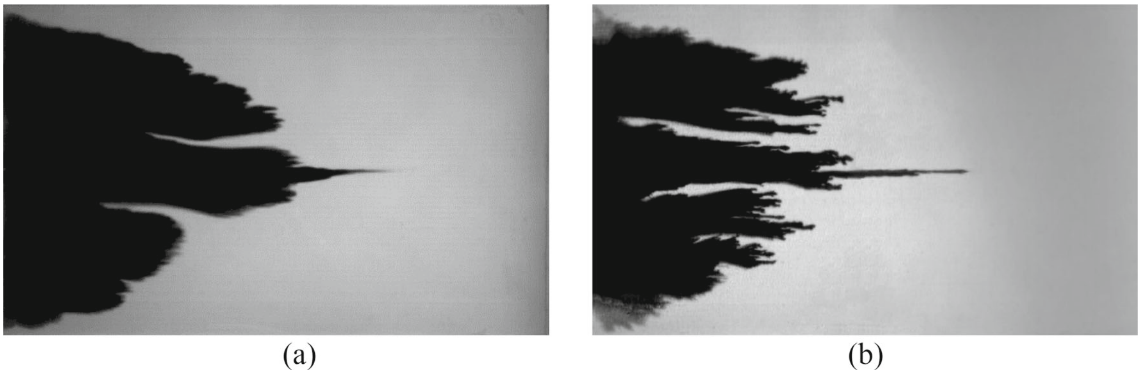
(a) (b)

Fig. 7 Fracture channeling in 0° fractured medium at Q=35.88 ml/min for **a** R=12.3 and **b** R=78.5

the experiments, the cycle of splitting and coalescing fingers repeated several times, resulting in progressively larger fingers as they coalesced until they reached the outlet.

It is also clearly shown that the number of fingers and the interaction between the fingers increase by R. As it is presented in Fig. 6, the fingers confront different mechanisms. According to Fig. 6a and Fig. 6b, splitting occurs by increasing R, and more fingers develop at small sizes. By further increasing R, the skewering mechanism becomes dominant, and the fingers widen at their tip. Since it is reported in [69] that the pressure gradient is lower in smaller fingers, the pressure difference between adjacent fingers of different sizes leads to the *shielding* mechanism.

3.2 Effect of viscosity ratio and fracture orientation on channeling and finger length

The influence of fracture orientation on flow channeling is especially noticeable in the 0° fracture model. The high permeability and pressure gradient along the fracture implies that the channeling effect is predominant through the fracture. As shown in Fig. 7, the channeling effect is most pronounced when the fracture is aligned with the flow direction, resulting in a rapid advancement of the displacing fluid. The channeling effect diminishes as the fracture orientation deviates from 0°.

The fracture's influence on fluid flow dynamics is particularly evident in the high viscosity ratio scenario (R=78.5). As seen in Figs. 5 and 7, finger length -defined as longitudinal extent of the fingered zone where the concentrations of the displacing fluid in both ends are 1 and 0 respectively [70]- generated in the 0° fractured model is significantly greater compared to the other orientations, indicating the dominance of the fracture in controlling the flow pattern

3.3 Effect of viscosity ratio and injection rate on finger length

Highlights the effect of injection rate on finger length in the 0° fracture model. At higher injection rates, the channeling effect becomes less pronounced, and the length of the fingers decreases. At low velocities and high viscosity ratios, the channeling effect remains dominant, resulting in a longer finger length. In contrast, at higher injection rates, the mixing length of the displacing fluid becomes slightly longer, and the channeling effect is overshadowed by the increased finger length (Fig. 8).

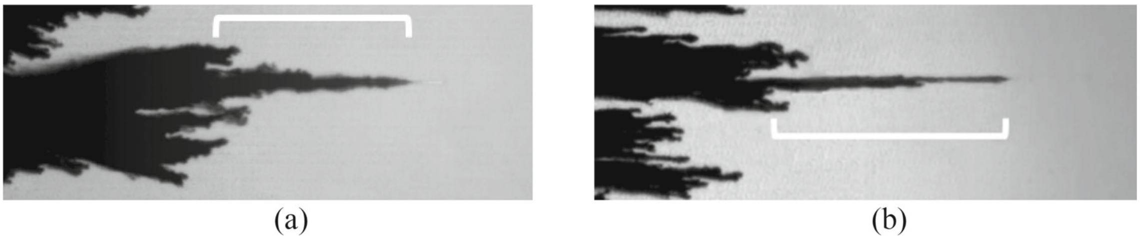

Fig. 8 Channeling effect and finger size in a 0° fracture at R=78.5, with **a** Q=107.64 **b** Q=35.88 ml/min at the same tip location

3.4 Effect of viscosity ratio, fractur orientation, and injection rate on tip location and breakthrough time

Tip location is defined as the longitudinal location of the most advanced finger in the porous medium. Figure 9 shows the tip locations for the three fracture orientations. The tip velocity increases with both the injection rate and viscosity ratio. In particular, Fig. 9c shows that the tip velocity increases significantly when the displacing fluid reaches the fracture, with a 90% increase in velocity once the fluid encounters the fracture.

The breakthrough time, defined as the moment when the most advanced finger exits the matrix, is influenced by fracture orientation and viscosity ratio. As shown in Fig. 10, the breakthrough time decreases with increasing injection rates and viscosity ratios, indicating that fracture orientation plays a key role in fluid displacement efficiency. The plot highlights the effect of fracture orientation: as the fracture rotates to a perpendicular position, the breakthrough time correspondingly increases. Additionally, the plot reveals that as the injection rate increases, the differences in breakthrough times decrease at higher velocities. This suggests that with higher injection rates, the influence of channeling becomes less significant across different fracture orientations. In other words, this parameter effectively illustrates the asymptotic nature of fluid displacement under more intense instabilities, which has been observed in other studies [6,34].

3.5 Effect of viscosity rati on sweep efficiency

Sweep efficiency, which measures the effectiveness of the fluid displacement, is influenced by both viscosity ratio and fracture orientation. As shown in Fig. 11, sweep efficiency decreases with increasing injection rate and viscosity ratio, consistent with findings from previous studies [26]. The decrease in the sweep efficiency becomes less pronounced at higher velocities, suggesting that the fracture's role in channeling diminishes at higher injection rates. Notably, the sweep efficiency is higher in the 0° fracture model at lower viscosity ratios compared to the 45° fracture model at higher viscosity ratios, indicating that fracture orientation and viscosity ratio interact to determine the overall displacement efficiency

Moreover, in the zero-degree fracture, the difference in sweep efficiencies between R=12.3 and R=78.5 decreases from 17% at Q=35.88 ml/min to 12% at Q=107.64 ml/min. Similar results have been observed in other research works investigating fluid displacement in fractured porous models [71]. According to the observations in Figs. 7 and 8, the channeling effect is more dominant at low velocities and high viscosity ratios. As shown in Fig. 11a, the channeling effect is dominant at high viscosity ratios, resulting in lower sweep efficiency. Similar to the interpretations regarding breakthrough time, as the injection rate increases, the sweep efficiencies become closer in value. This observation demonstrates the less distinctive feature of fractures at higher velocities.

4 Conclusions

In this study, a series of tests were conducted on rectangular porous models to investigate the role of fracture orientation and viscosity ratio in altering the fluid displacement process and fingering instability. The concluding points of the effects of fracture orientation and viscosity ratio are presented below:

- At low viscosity ratios, a smooth surface of bulk fingers was created; however, as the viscosity ratio increased, more complex fingers emerged at the interface between the two fluids. At R =44.2, simpler fingers were generated with slight interactions in the form of splitting and coalescing mechanisms. At R =78.5, the dynamics of instability became more complex, with fingers undergoing periodic changes in

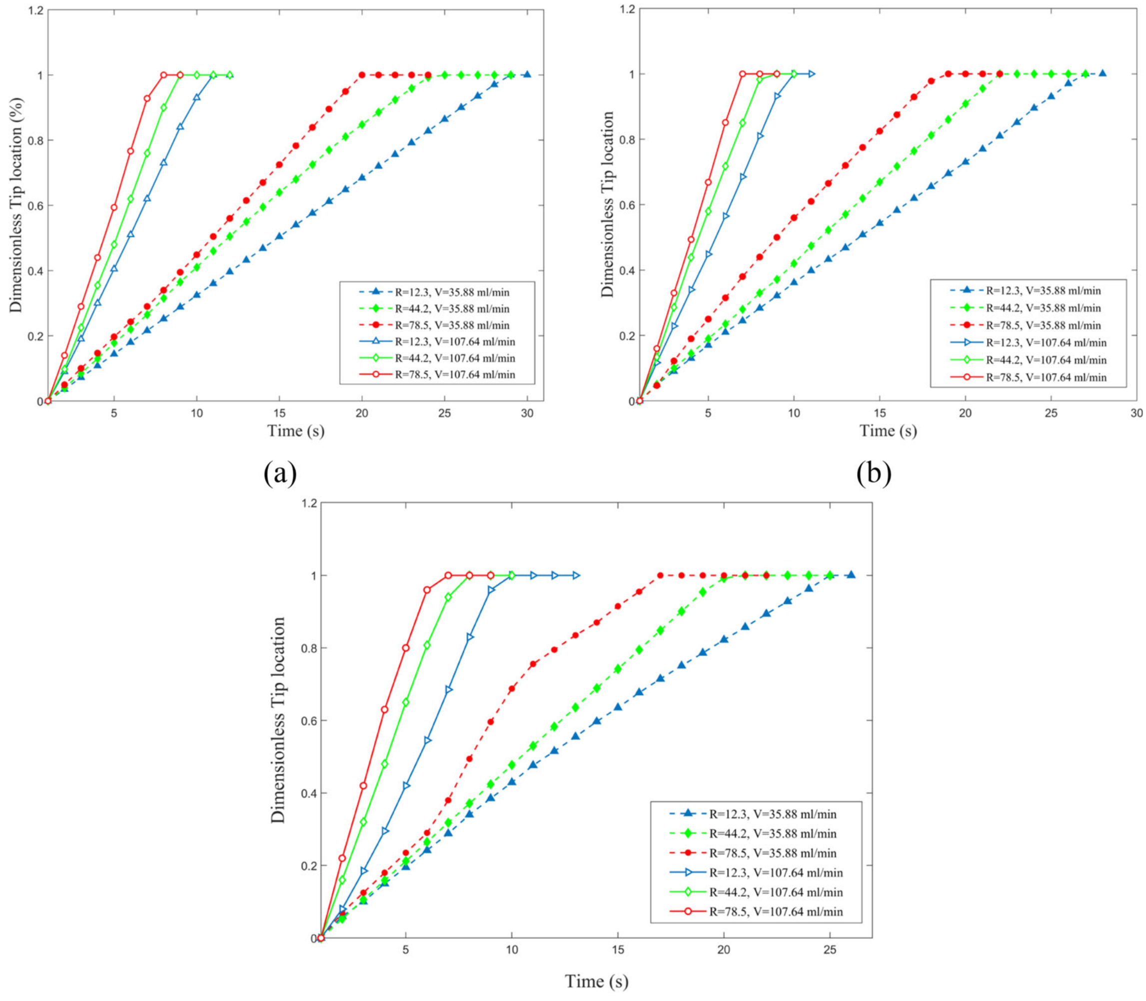

(a)

(b)

(c)

Fig. 9 Tip location in fractured porous cells with fracture orientations of **a** 90°, **b** 45°, and **c** 0°

shape and mechanisms. The fingers experienced a general cycle of mechanisms, including tip splitting, shielding, branching, and coalescing, eventually leading to the development of bulkier fingers. Mechanisms such as fading and skewering were observed only at R =78.5.

- The channeling effect of fractures was most dominant in the 0° fracture and at high viscosity ratios. The 45° and 90° fractures showed weaker effects on altering the flow patterns of displacement instability. Due to the high contrast in permeability, pressure drop, and fluid mobility, the channeled fluid front was most distinctive at low velocities and high viscosity ratios.
- The steepened slope of the tip location due to the channeling effect was most clearly observed in the 0° fracture as the fluid approached the fracture. Breakthrough time and sweep efficiency generally decreased with increasing injection rate and viscosity ratio, with an asymptotic trend predicted for breakthrough time at higher velocities and viscosity ratios. Sweep efficiency exhibited a similar decreasing trend, with differences in sweep efficiency diminishing at higher velocities. This observation suggests that the sensitivity of sweep efficiency to fracture orientation declines slightly as injection rate increases, showing the less pronounced role of flow channeling by fractures at higher injection rates.

The findings of this study have implications for several practical applications, including environmental remediation, enhanced oil recovery, and biological systems such as tissue engineering. Viscous fingering dynamics, characterized by the instability patterns observed during fluid displacement, play a critical role in fluid transport and distribution in porous media. In the context of biological systems, these flow dynamics could inspire novel approaches to engineering vascularized tissues. Specifically, manipulating flow patterns similar to viscous

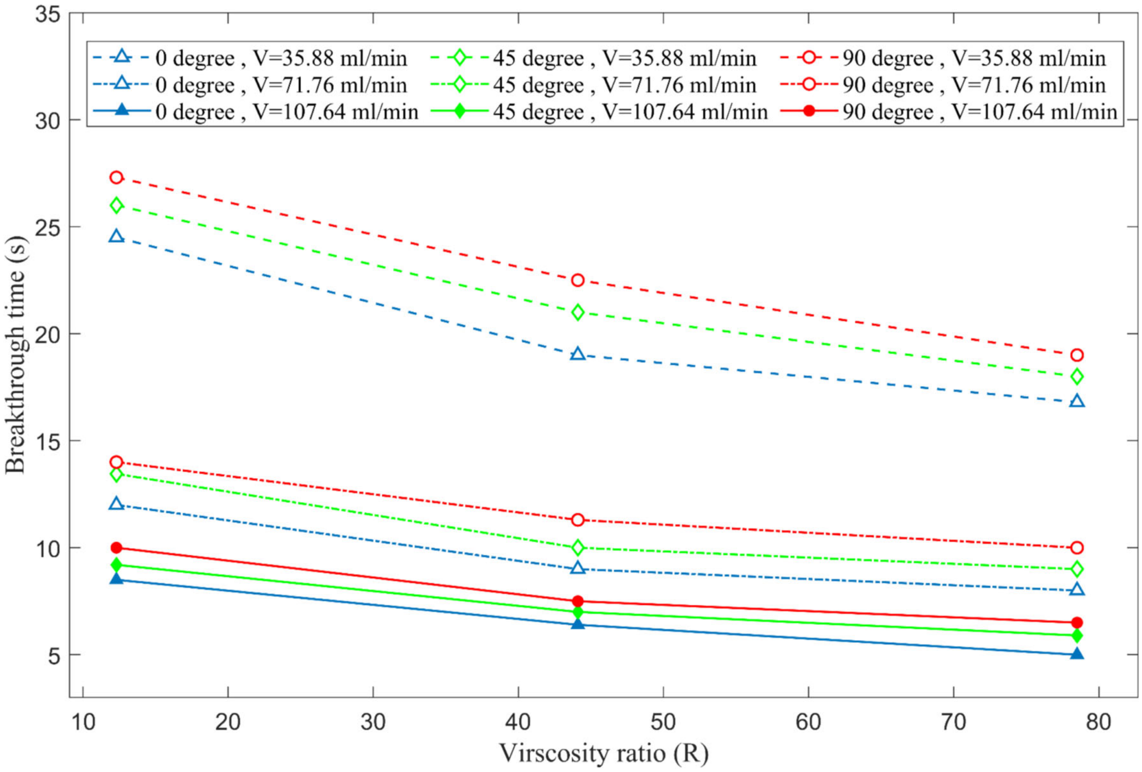

Fig. 10 Breakthrough time vs. viscosity ratio

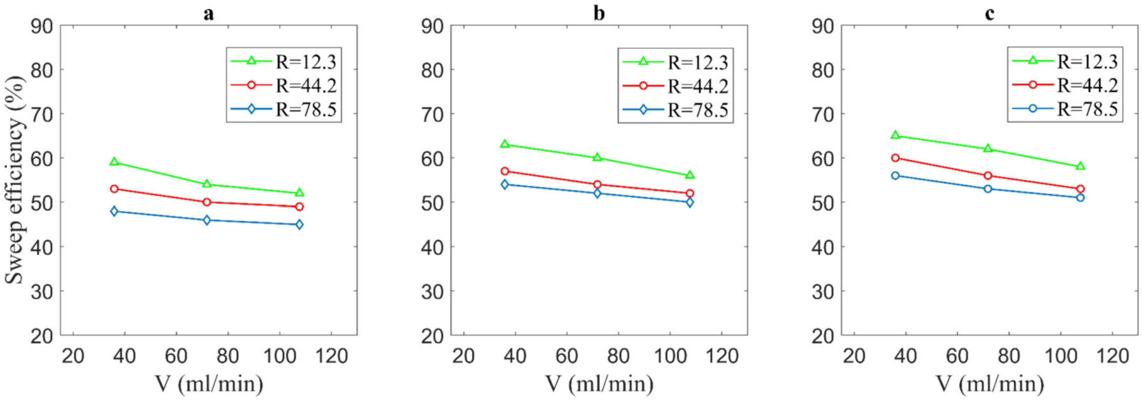

Fig. 11 Sweep efficiency vs. injection rate in **a** 0°, **b** 45°, and **c** 90° fractured porous medium

fingering could enable the creation of vascular networks within tissue constructs, enhancing nutrient delivery and improving tissue regeneration therapies. In [72,73], it is shown how viscoelastic properties influence structural adaptation of porous biological materials, drawing parallels with the mechanisms observed in viscous fingering. Additionally, [74] highlights the potential for integrating flow-induced dynamics into tissue engineering designs to optimize nutrient flow in bioengineered systems. These connections underline the broader applicability of our findings and provide a foundation for interdisciplinary research bridging fluid dynamics, bioengineering, and environmental science.

While conducting additional simulations is beyond the scope of the current study, we acknowledge the importance of integrating theoretical frameworks to validate our findings. Recent studies, such as those in [75,76], have developed numerical and experimental models to understand complex behaviors in porous materials, including multiscale dynamics and elastic properties. These approaches provide potential avenues for future validation of our experimental results. By referencing these frameworks, we aim to contextualize our findings within the broader scope of theoretical and numerical research, setting the stage for future work that bridges experimental observations with predictive modeling.

One limitation of the present study is the use of regular fracture geometries, which do not fully replicate the complexity of natural porous media with irregular and heterogeneous fracture networks. Fractures in natural systems often exhibit a high degree of variability, including differences in size, orientation, and connectivity, which significantly influence fluid displacement dynamics. Future studies should aim to address this limitation by incorporating more realistic fracture geometries into experimental setups. For instance, exploring fractures with varying aperture sizes, irregular patterns, and rough surfaces could provide deeper insights into the influence of structural heterogeneity on viscous fingering phenomena. Additionally, combining experimental results with numerical simulations of realistic geometries could further enhance our understanding of the interplay between structural complexity and fluid dynamics in fractured porous media.

Fracture orientation plays a pivotal role in governing fluid displacement, as demonstrated by experiments conducted with fractures oriented at 0°, 45°, and 90°. The results highlight the influence of fracture geometry on the balance between channeling and fingering mechanisms, with structural heterogeneity amplifying the complexity of fluid flow patterns. These findings are consistent with the theoretical perspectives offered in [77], who developed a variational formulation of pre-stressed solid–fluid mixture theory to address wave phenomena in heterogeneous porous systems. While our study focuses on empirical investigations, the parallels between our experimental findings and theoretical frameworks emphasize the need for interdisciplinary approaches to understanding fluid flow in fractured porous media.

Author Contributions All authors equally contributed to the manuscript.

Data availibility No datasets were generated or analysed during the current study.

Funding Open access funding provided by Università degli Studi di Catania within the CRUI-CARE Agreement.

Declarations

Competing interests The authors declare no competing interests.

References

1. Gavrilyuk, S., Gouin, H.: Dynamic boundary conditions for membranes whose surface energy depends on the mean and Gaussian curvatures. Math. Mech. Comp. Syst. **7**(2), 131–157 (2019)
2. Hill, S., Inst, F.: P, Channeling in packed columns. Chem. Eng. Sci. **1**, 247–253 (1952). https://doi.org/10.1016/0009-2509(52)87017-4
3. Saffman, P.G., Taylor, G.I.: The penetration of a fluid into a porous medium or Hele-Shaw cell containing a more viscous liquid. Proc. R. Soc. Lond. A Math. Phys. Sci. **245**, 312–329 (1958). https://doi.org/10.1098/rspa.1958.0085
4. Aramideh, S., Vlachos, P.P., Ardekani, A.M.: Unstable displacement of non-aqueous phase liquids with surfactant and polymer. Transp. Porous Media **126**, 455–474 (2019). https://doi.org/10.1007/s11242-018-1168-1
5. Manickam, O., Homsy, G.M.: Fingering instabilities in vertical miscible displacement flows in porous media. J. Fluid Mech. **288**, 75–102 (1995). https://doi.org/10.1017/S0022112095001078
6. Nijjer, J.S., Hewitt, D.R., Neufeld, J.A.: The dynamics of miscible viscous fingering from onset to shutdown. J. Fluid Mech. (2018). https://doi.org/10.1017/jfm.2017.829
7. Shoghi, M.R., Norouzi, M.: Linear stability analysis and nonlinear simulation of non-Newtonian viscous fingering instability in heterogeneous porous media. Rheol. Acta **54**, 973–991 (2015)
8. Homsy, G.M.: Viscous fingering in porous media. Annu. Rev. Fluid Mech. **19**, 271–311 (1987). https://doi.org/10.1146/annurev.fl.19.010187.001415
9. ul Islam, T., Gandhi, P.S.: Viscous fingering in multiport Hele Shaw cell for controlled shaping of fluids. Sci. Rep. **7**, 16602 (2017). https://doi.org/10.1038/s41598-017-16830-3
10. Chaudhuri, A., Vishnudas, R.: A systematic numerical modeling study of various polymer injection conditions on immiscible and miscible viscous fingering and oil recovery in a five-spot setup. Fuel **232**, 431–443 (2018). https://doi.org/10.1016/J.FUEL.2018.05.115

11. Li, H., Maini, B., Azaiez, J.: Experimental and numerical analysis of the viscous fingering instability of the shear-thinning fluids. Can. J. Chem. Eng. **84**, 52–62 (2006)
12. Eslami, A., Taghavi, S.M.: Viscous fingering regimes in elasto-visco-plastic fluids. J. Nonnewton. Fluid Mech. **243**, 79–94 (2017). https://doi.org/10.1016/j.jnnfm.2017.03.007
13. Kampitsis, A.E., Kostorz, W.J., Muggeridge, A.H., Jackson, M.D.: The life span and dynamics of immiscible viscous fingering in rectilinear displacements. Phys. Fluids **33**, 096608 (2021). https://doi.org/10.1063/5.0064955
14. Bouquet, S., Douarche, F., Roggero, F., Leray, S.: Characterization of viscous fingering and channeling for the assessment of polymer-based heavy oil displacements. Transp. Porous Media **131**, 873–906 (2020). https://doi.org/10.1007/s11242-019-01370-3
15. Jeon, M.-K., Kim, S., Hosseini Zadeh, A., Kwon, T.-H.: Study on viscous fluid flow in disordered-deformable porous media using hydro-mechanically coupled pore-network modeling. Transp. Porous Media **133**, 207–227 (2020). https://doi.org/10.1007/s11242-020-01419-8
16. Logvinov, O.A.: Radial viscous fingering in case of poorly miscible fluids. Transp. Porous Media **124**, 495–508 (2018). https://doi.org/10.1007/s11242-018-1081-7
17. Chung, C.A., Lin, H.-Y.: Enhancing immiscible fluid displacement in porous media by capillary pressure discontinuities. Transp. Porous Media **120**, 309–325 (2017). https://doi.org/10.1007/s11242-017-0922-0
18. YadaliJamaloei, B., Babolmorad, R., Kharrat, R.: Correlations of viscous fingering in heavy oil waterflooding. Fuel **179**, 97–102 (2016). https://doi.org/10.1016/J.FUEL.2016.03.064
19. Christie, M.A., Jones, A.D.W., Muggeridge, A.H.: Comparison between Laboratory Experiments and Detailed Simulations of Unstable Miscible Displacement Influenced by Gravity, North Sea Oil and Gas Reservoirs—II 245–250, (1990). https://doi.org/10.1007/978-94-009-0791-1_20
20. Zhang, H., Ramakrishnan, T.S., Nikolov, A., Wasan, D.: Enhanced oil displacement by nanofluid's structural disjoining pressure in model fractured porous media. J. Colloid Interface Sci. **511**, 48–56 (2018). https://doi.org/10.1016/j.jcis.2017.09.067
21. Cheng, J.-T., Giordano, N.: Fluid flow through nanometer-scale channels. Phys. Rev. E: Stat., Nonlin, Soft Matter Phys. **65**, 31206 (2002). https://doi.org/10.1103/PhysRevE.65.031206
22. Farzaneh, S.A., Ghazanfari, M.H., Kharrat, R., Vossoughi, S.: An experimental and numerical investigation of solvent injection to heavy oil in fractured five-spot micromodels. Pet. Sci. Technol. **28**, 1567–1585 (2010). https://doi.org/10.1080/10916460903160784
23. Farzaneh, S.A., Dehghan, A.A., Kharrat, R., Ghazanfari, M.H.: An experimental investigation of fracture physical properties on heavy oil displacement efficiency during solvent flooding. Energy Sources Part A Recovery Utiliz. Environ. Eff. **33**, 1993–2004 (2011). https://doi.org/10.1080/15567030903515039
24. Ferer, M., Ji, C., Bromhal, G.S., Cook, J., Ahmadi, G., Smith, D.H.: Crossover from capillary fingering to viscous fingering for immiscible unstable flow: experiment and modeling. Phys. Rev. E: Stat., Nonlin, Soft Matter Phys. **70**, 16303 (2004). https://doi.org/10.1103/PhysRevE.70.016303
25. Mohammadi, S., Maghzi, A., Ghazanfari, M.H., Masihi, M., Mohebbi, A., Kharrat, R.: On the control of glass micro-model characteristics developed by laser technology. Energy Sources Part A Recovery Utiliz. Environ. Eff. **35**, 193–201 (2013). https://doi.org/10.1080/15567036.2010.516325
26. Hosseinalipoor, Seyed Mostafa, Nemati, Arash, Zare Vamerzani, Behrooz, Saffari, Hamid: Experimental study of finger behavior due to miscible viscous and gravity contrast in a porous model. Energy Sources Part A Recovery Utiliz. Environ. Eff. **42**(19), 2434–2447 (2020). https://doi.org/10.1080/15567036.2019.1607943
27. Yadali Jamaloei, B., Babolmorad, R., Kharrat, R.: Visualization and analysis of viscous fingering in alcohol-assisted surfactant waterflooding of heavy oil in a two-dimensional sandstone micromodel. Fuel **184**, 169–179 (2016). https://doi.org/10.1016/J.FUEL.2016.07.016
28. Mejia, L., Tagavifar, M., Xu, K., Mejia, M., Du, Y., Balhoff, M.: Surfactant flooding in oil-wet micromodels with high permeability fractures. Fuel **241**, 1117–1128 (2019). https://doi.org/10.1016/j.fuel.2018.12.076
29. Kianinejad, A., Rashtchian, D., Ghazanfari, M.H., Kharrat, R.: A pore-level investigation of surfactant-crude oil displacements behavior in fractured porous media using one-quarter five spot micromodels. Energy Sources Part A Recovery Utiliz. Environ. Eff. **36**, 727–737 (2014). https://doi.org/10.1080/15567036.2010.540632
30. Saidian, M., Ghazanfari, M.H., Masihi, M., Kharrat, R.: Monitoring the role of fracture geometrical characteristics on fingering initiation/development during heavy oil miscible displacements in fractured porous media. Energy Sources Part A Recovery Utiliz. Environ. Eff. **35**, 1129–1139 (2013). https://doi.org/10.1080/15567036.2010.516321
31. Wilkinson, J.P., Jacobs, J.W.: Experimental study of the single-mode three-dimensional Rayleigh-Taylor instability. Phys. Fluids **19**, 124102 (2007). https://doi.org/10.1063/1.2813548
32. Morgan, R.V., Cabot, W.H., Greenough, J.A., Jacobs, J.W.: Rarefaction-driven Rayleigh-Taylor instability. Part 2. Experiments and simulations in the nonlinear regime. J Fluid Mech. **838**, 320–355 (2018). https://doi.org/10.1017/jfm.2017.893
33. Tan, C.T., Homsy, G.M.: Simulation of nonlinear viscous fingering in miscible displacement. Phys. Fluids **31**, 1330 (1988). https://doi.org/10.1063/1.866726
34. Kopf-Sill, Anne R.., Homsy, G.. M..: Nonlinear unstable viscous fingers in Hele–Shaw flows. i. experiments. Phys. Fluids **31**(2), 242–249 (1988). https://doi.org/10.1063/1.866854
35. Budek, Agnieszka, Kwiatkowski, Kamil, Szymczak, Piotr: Effect of mobility ratio on interaction between the fingers in unstable growth processes. Phys. Rev. E (2017). https://doi.org/10.1103/PhysRevE.96.042218
36. Shabani, Mohammad Hossein, Jafari, Arezou, Mousavi, Seyyed Mohammad, Abdi-Khanghah, Mahdi: Comparison of produced biosurfactants performance in in-situ and ex-situ MEOR: micromodel study. Energy Sources Part A Recovery Utiliz. Environ. Eff. **46**(1), 15286–15296 (2024). https://doi.org/10.1080/15567036.2020.1810826
37. Cheraghian, G.: An experimental study of surfactant polymer for enhanced heavy oil recovery using a glass micromodel by adding nanoclay. Pet. Sci. Technol. **33**, 1410–1417 (2015)
38. Zuta, J., Fjelde, I., Berenblyum, R.: Oil recovery during CO2-foam injection in fractured chalk rock at reservoir conditions, in: Int. Symp. Society of Core Analysts, Noordwijk, Netherlands, pp. 26–30 (2009)

39. Ma, K., Liontas, R., Conn, C.A., Hirasaki, G.J., Biswal, S.L.: Visualization of improved sweep with foam in heterogeneous porous media using microfluidics. Soft Matter **8**, 10669–10675 (2012). https://doi.org/10.1039/C2SM25833A
40. Loggia, D., Rakotomalala, N., Salin, D., Yortsos, Y.: Phase diagram of stable miscible displacement in layered porous media. EPL (Europhysics Letters) **36**, 105–110 (1996). https://doi.org/10.1209/epl/i1996-00194-y
41. Ahmadi, P., Shahsavani, B., Malayeri, M.R., Riazi, M.: Impact of different injection sites on the water and oil exchange in a fractured porous medium for different polymers: a visual study. J. Pet. Sci. Eng. **174**, 948–958 (2019). https://doi.org/10.1016/J.PETROL.2018.12.012
42. La Valle, G., Abali, B.E., Falsone, G., Soize, C.: Sensitivity of a homogeneous and isotropic second-gradient continuum model for particle-based materials with respect to uncertainties. ZAMM J. Appl. Math. Mech. **103**(10), e202300068 (2023)
43. La Valle, G., Soize, C.: A higher-order nonlocal elasticity continuum model for deterministic and stochastic particle-based materials. Z. Angew. Math. Phys. **75**(2), 49 (2024)
44. La Valle, G., Soize, C.: Stochastic second-gradient continuum theory for particle-based materials: part II. Z. Angew. Math. Phys. **75**(3), 93 (2024)
45. La Valle, Gabriele, Soize, Christian: Identifying second-gradient continuum models in particle-based materials with pairwise interactions using acoustic tensor methodology. J. Elast. **156**(2), 623–639 (2024). https://doi.org/10.1007/s10659-024-10067-8
46. dell'Isola, F., Madeo, A., Seppecher, P.: Boundary conditions at fluid-permeable interfaces in porous media: a variational approach. Int. J. Solids Struct. **46**(17), 3150–3164 (2009)
47. dell'Isola, F., Guarascio, M., Hutter, K.: A variational approach for the deformation of a saturated porous solid. A second-gradient theory extending Terzaghi's effective stress principle. Arch. Appl. Mech. **70**, 323–337 (2000)
48. Giorgio, I., Andreaus, U., Scerrato, D., dell'Isola, F.: A visco-poroelastic model of functional adaptation in bones reconstructed with bio-resorbable materials. Biomech. Model. Mechanobiol. **15**, 1325–1343 (2016)
49. Madeo, A., dell'Isola, F., Darve, F.: A continuum model for deformable, second gradient porous media partially saturated with compressible fluids. J. Mech. Phys. Solids **61**(11), 2196–2211 (2013)
50. Liu, Y., Abali, B.E., Müller, W.H.: Multiphysics simulation of two-phase viscous fluid flow steered by electric field for jetting of microdroplets. Int. J. Multiph. Flow **176**, 104843 (2024)
51. Abali, B.E., Müller, W.H., Georgievskii, D.V.: A discrete-mechanical approach for computation of three-dimensional flows. ZAMM-J. Appl. Math. Mech. **93**(12), 868–881 (2013)
52. Rosi, G., Placidi, L., dell'Isola, F.: "Fast" and "slow" pressure waves electrically induced by nonlinear coupling in Biot-type porous medium saturated by a nematic liquid crystal. Z. Angew. Math. Phys. **68**(2), 51 (2017)
53. Giorgio, I., De Angelo, M., Turco, E., Misra, A.: A Biot-Cosserat two-dimensional elastic nonlinear model for a micromorphic medium. Contin. Mech. Thermodyn. **32**(5), 1357–1369 (2020)
54. Giorgio, I., dell'Isola, F., Misra, A.: Chirality in 2D Cosserat media related to stretch-micro-rotation coupling with links to granular micromechanics. Int. J. Solids Struct. **202**, 28–38 (2020)
55. Giorgio, I., Hild, F., Gerami, E., dell'Isola, F., Misra, A.: Experimental verification of 2D Cosserat chirality with stretch-micro-rotation coupling in orthotropic metamaterials with granular motif. Mech. Res. Commun. **126**, 104020 (2022)
56. Grillo, A., Di Stefano, S.: An a posteriori approach to the mechanics of volumetric growth. Math. Mech. Comp. Syst. **11**(1), 57–86 (2023)
57. Scerrato, D., Giorgio, I., Bersani, A.M., Andreucci, D.: A proposal for a novel formulation based on the hyperbolic Cattaneo's equation to describe the mechano-transduction process occurring in bone remodeling. Symmetry **14**(11), 2436 (2022)
58. Giorgio, I., Scerrato, D.: Multi-scale concrete model with rate-dependent internal friction. Eur. J. Environ. Civ. Eng. **21**(7–8), 821–839 (2017)
59. Aretusi, G., Cardillo, C., Salvatori, A., Bednarczyk, E., Fedele, R.: A simple extension of Timoshenko beam model to describe dissipation in cementitious elements. Z. Angew. Math. Phys. **75**(5), 166 (2024)
60. Fedele, R., Maier, G., Miller, B.: Identification of elastic stiffness and local stresses in concrete dams by in situ tests and neural networks. Struct. Infrastruct. Eng. **1**(3), 165–180 (2005)
61. Barchiesi, E., Hamila, N.: Maximum mechano-damage power release-based phase-field modeling of mass diffusion in damaging deformable solids. Z. Angew. Math. Phys. **73**(1), 35 (2022)
62. Scrofani, A., Barchiesi, E., Chiaia, B., Misra, A., Placidi, L.: Fluid diffusion related aging effect in a concrete dam modeled as a Timoshenko beam. Math. Mech. Comp. Syst. **11**(2), 313–334 (2023)
63. Oka, T.: Corrector results for space-time homogenization of nonlinear diffusion. Math. Mech. Comp. Syst. **10**(2), 171–190 (2022)
64. Morozova, A.S., Vilchevskaya, E.N., Müller, W.H., Bessonov, N.M.: Models for drug release of gentamicin in a polylactic acid matrix. Math. Mech. Comp. Syst. **8**(4), 307–320 (2020)
65. Barchiesi, E.: Multi-scale and multi-physics: towards next-generation engineering materials. Contin. Mech. Thermodyn. **32**, 541–554 (2020)
66. Nelson, R.A.: Geologic Analysis of Naturally Fractured Reservoirs, 2nd edn. Gulf Professional Publishing, Woburn (2001)
67. Bischofberger, I., Ramachandran, R., Nagel, S.R.: Fingering versus stability in the limit of zero interfacial tension. Nat. Commun. **5**, 1–6 (2014). https://doi.org/10.1038/ncomms6265
68. Zare Vamerzani, B., Zadehkabir, A., Saffari, H., Hosseinalipoor, S.M., Mazinani, P., Honari, P.: Experimental analysis of fluid displacement and viscous fingering instability in fractured porous medium: effect of injection rate. J. Braz. Soc. Mech. Sci. Eng. **43**, 66 (2021). https://doi.org/10.1007/s40430-020-02790-9
69. Sherwood, J.D.: Island size distribution in stochastic simulations of the Saffman-Taylor instability. J. Phys. A Gen. Phys. **19**, L195 (1986). https://doi.org/10.1088/0305-4470/19/4/005
70. Manickam, O., Homsy, G.M.: Simulation of viscous fingering in miscible displacements with nonmonotonic viscosity profiles. Phys. Fluids **6**, 95–107 (1994). https://doi.org/10.1063/1.868049
71. Rokhforouz, M.R., Akhlaghi Amiri, H.A.: Pore-level influence of micro-fracture parameters on visco-capillary behavior of two-phase displacements in porous media. Adv. Water Resour. **113**, 260–271 (2018). https://doi.org/10.1016/j.advwatres.2018.01.030

72. Giorgio, I., Andreaus, U., Scerrato, D., Braidotti, P.: Modeling of a non-local stimulus for bone remodeling process under cyclic load: application to a dental implant using a bioresorbable porous material. Math. Mech. Solids **22**(9), 1790–1805 (2017). https://doi.org/10.1177/1081286517700567
73. Giorgio, I., dell'Isola, F., Andreaus, U., Misra, A.: An orthotropic continuum model with substructure evolution for describing bone remodeling: an interpretation of the primary mechanism behind Wolff's law. Biomech. Model. Mechanobiol. **22**(6), 2135–2152 (2023). https://doi.org/10.1007/s10237-023-01672-1
74. Tepedino, M.: The mechanical role of the periodontal ligament for developing mathematical models in orthodontics. Math. Mech. Comp. Syst. **11**(4), 525–539 (2023). https://doi.org/10.2140/memocs.2023.11.525
75. Burson, R., Enakoutsa, K.: Ductile void growing in micromorphic GLPD porous plastic solids containing two populations of cavities with different sizes. Math. Mech. Comp. Syst. **10**(4), 395–412 (2023). https://doi.org/10.2140/memocs.2023.10.395
76. Alasfar, R.H., Ahzi, S., Barth, N., Kochkodan, V., Koç, M.: Modeling and experimental validation of the elastic modulus of polysulfone membranes reinforced with cellulose nanofibers. Math. Mech. Comp. Syst. **10**(4), 413–429 (2023). https://doi.org/10.2140/memocs.2023.10.413
77. Placidi, L., dell'Isola, F., Ianiro, N., Sciarra, G.: Variational formulation of pre-stressed solid-fluid mixture theory, with an application to wave phenomena. Eur. J. Mech. A/Solids **27**(4), 582–606 (2008). https://doi.org/10.1016/j.euromechsol.2007.10.005

Chapter 8

Thermomechanical process modelling and simulation for additive manufacturing of nanoparticle dispersed Inconel 718 alloys

Chapter abstract

The study develops a finite element model to analyze the laser powder bed fusion (L-PBF) process for Inconel 718 (IN718) and ODS superalloys (ODS-IN718). It uses a linear isotropic elastic-perfectly plastic model for mechanical simulation, with temperature-dependent thermophysical properties. The model incorporates metal phases (powder, liquid, solid) in simulations and evaluates multilayered samples for thermomechanical behavior and interlayer residual stress. Initial benchmarks verify the model accuracy for transient temperatures and residual stress. It includes thermomechanical analysis of a single-track three-layer test for IN718 and ODS-IN718 under various laser powers and scan speeds. ODS-IN718 thermal characterization is validated with experiments, and mechanical analysis shows significant tensile residual stress at the track center. The study compares manufacturing quality focusing on stress distribution at different layers and scan speeds, identifying optimal speeds to reduce stress in ODS-IN718. ODS-IN718 shows lower residual stress than IN718, especially at reduced scan speeds, due to improved properties from dispersed particles.

Continuum Mech. Thermodyn. (2025) 37:11
https://doi.org/10.1007/s00161-024-01346-9

ORIGINAL ARTICLE

E. Yousefimiab · A. Kendibilir · Y. Yalcin · C. Cardillo · E. Aydogan · A. Kefal

Thermomechanical process modelling and simulation for additive manufacturing of nanoparticle dispersed Inconel 718 alloys

Received: 19 August 2024 / Accepted: 13 November 2024 / Published online: 6 December 2024

Abstract In this study, a coupled transient thermomechanical finite element model is developed to examine the laser powder bed fusion (L-PBF) process of the Inconel 718 (IN718) and Oxide Dispersion Strengthened (ODS) superalloys (ODS-IN718). The linear isotropic elastic perfectly plastic constitutive model is implemented for the mechanical part whereas all the thermophysical properties are defined as fully temperature dependent. This new model enables three states of the metal including powder, liquid, and solid phases in the continuum-based finite element simulations. Besides, it can meticulously simulate multi-layered samples to assess thermomechanical performance and residual stress between layers. First, benchmark problems are revisited to verify the high accuracy of the present model for predicting transient temperature profile and residual stress accumulation. Then, thermomechanical analysis of a single-track three-layer test case is performed to investigate the L-PBF process of IN718 and ODS-IN718 samples for various laser powers and scan speeds. Also, the thermal characterization of ODS-IN718 samples is experimentally conducted. It is demonstrated that the numerical melt pool dimensions provide good agreement with experiments with an average error of 17% for melt pool dimensions. Moreover, mechanical results reveal that high tensile residual stresses accumulate in the middle part of the track. The manufacturing quality of the IN718 and ODS-IN718 samples are comprehensively compared based on the variations of stress distribution at different layers for different laser scan speeds. Also, the optimal laser scan speed is achieved to minimize the residual stresses for the ODS-IN718 alloy. Overall, ODS-IN718 has a lower residual stress than IN718 especially at lower laser scan speeds due to the enhanced thermomechanical behavior attributed to the change in material properties due to the presence of dispersed particles.

E. Yousefimiab · A. Kendibilir · A. Kefal
Faculty of Engineering and Natural Sciences, Sabanci University, Tuzla, Istanbul 34956, Turkey

E. Yousefimiab · A. Kendibilir · A. Kefal
Integrated Manufacturing Technologies Research and Application Center, Sabanci University, Tuzla, Istanbul 34956, Turkey

E. Yousefimiab · A. Kendibilir · A. Kefal ( )
Composite Technologies Center of Excellence, Istanbul Technology Development Zone, Sabanci University-Kordsa, Pendik, Istanbul 34906, Turkey
E-mail: adnankefal@sabanciuniv.edu

Y. Yalcin · E. Aydogan ( )
Department of Metallurgical and Materials Engineering, Middle East Technical University, Ankara 06800, Turkey
E-mail: aydogane@metu.edu.tr

C. Cardillo ( )
Department of Civil Engineering and Architecture, Università di Catania, Catania 95100, Italy
E-mail: christian.cardillo@phd.unict.it

Keywords Thermomechanical analysis · Residual stress · Laser powder bed fusion · Process modelling · Nanoparticle dispersed Inconel

1 Introduction

Additive manufacturing (AM) is a vital technological advancement for producing complex 3D geometries layer-by-layer directly from a CAD file. Essentially, AM increases design flexibility and production efficiency as well as decreases material consumption rate compared to conventional methods [1]. Therefore, in the last decade, dozens of research efforts from a variety of research areas including biomedical, aerospace, automotive sciences have been dedicated to improving AM processes [2–5]. In addition, additive manufacturing is a cutting-edge field that enables the design and production of complex, customized inner structures in materials with unique properties that are difficult or impossible to achieve with traditional manufacturing methods. In fact, additive manufacturing, often referred to as 3D printing, allows for the creation of structures with complex geometries, which are not feasible with conventional manufacturing techniques. These structures usually have intricated internal structures, which can include repeating patterns, lattice structures, or intricate voids, designed to achieve specific physical properties.

With additive manufacturing, complex materials can be customized for specific applications, allowing for the optimization of properties such as strength, flexibility, thermal conductivity, and mechanical response [6–8]. The ability of additive manufacturing to produce highly complex and customizable materials with unique properties opens new possibilities for designing and producing innovative materials with outstanding performance unattainable with traditional manufacturing methods, such as so-called metamaterials [9–13]. Mechanical metamaterials are engineered materials with properties that are determined by their structure rather than their composition [14–20]. These materials often have complex geometries and internal architectures that give them unusual mechanical properties, such as negative Poisson's ratio, programmable deformation, relative displacements in their microstructure, atypical Poynting effect reversal, shield capabilities or exceptional strength-to-weight ratios [21–26]. To handle the greater complexity of the mechanical response, these metamaterials can be described by generalized continua models that are more complex than the traditional ones. This complexity results in a wide range of parameters that need to be identified using specific techniques developed for this purpose [27–30].

Laser powder bed fusion (L-PBF) is a subcategory of the AM and employs a high-energy laser beam as a moving heat source. In this process, moving heat source follows a specified pattern exported from a CAD file to heat, melt, and fuse the powder in each layer of the printed structure. During the process, the melt pool cools down and solidifies. Then, the built platform comes one powder layer thickness down, and the recoater spreads the powder on the powder bed. The procedure repeats layer by layer until the final product is printed entirely. Among the products produced using L-PBF, parts made of metal powder demonstrate advantages such as low porosity and high mechanical strength [31]. Especially, selective laser melted alloys have been reported to exhibit corrosion resistance, weldability, and fine-grain structure [32]. Inconel 718 (IN718) alloy has emerged as one of the most common metals in AM because of its outstanding properties such as high-temperature performance. L-PBF with IN 718 enables near-net-shape products with less material wastage, thus making the process very cost-effective (as such considering high expense of this material [33]) for aerospace and energy applications. Hence, more advanced research should be focused on the parts produced by L-PBF using IN 718, which constitutes one of the main motivations of the present study.

In fact, the L-PBF is a complex process that involves different phase transformations, including solid, liquid, and even gas phases, accompanied by various heat transfer mechanisms such as conduction, convection, and radiation. High-temperature gradients caused by the high-energy laser beam in the L-PBF process result in high residual stresses in the final product. The residual stresses might cause defects such as warpage [34,35], balling effect [36,37], mechanical strength reduction [38], distortions and layer delamination [39], pores, and cracks [40] in the final part, which makes it necessary to investigate the L-PBF manufacturing approach with greater caution. Hence, numerous studies have been conducted on the assessments of residual stresses and structural integrity of the products manufactured by L-PBF process.

Among the research scopes exploring the L-PBF process, computational thermomechanical modelling is of essential importance for studying the L-PBF process. This is because, without an accurate thermomechanical simulation, a costly trial and error experimenting procedure is required to correlate the thermomechanical properties of the final product with the residual stress accumulation within the part. To perform such an analysis, the finite element method (FEM) has received considerable attention from many researchers. Recent research papers use FEM simulations to find experimental/numerical methods for minimizing the residual stress of the final product. Some of these methods can be elaborated as implementing the proper laser scan strategy [41–51], heat treatment of the printed product [52–57], investigating the effect of process parameters such as laser scan speed, laser power, laser beam size, powder layer thickness, etc. on the residual stress, with the aim of having an understanding for the optimization of these parameters. Besides, FEM and variational methods are closely related in computational mechanics and engineering due to their common theoretical foundation and practical applications in solving complex physical problems. In fact, variational methods provide a systematic way to derive the governing equations for complex physical systems, making it easier to develop FEM models for a wide range of problems together with the proper boundary conditions that are, from a mathematical perspective, well-posed. All this, leaving aside the fact that the variational approach ensures that the FEM solutions are stable and converge to the proper solution as the mesh is refined. This is particularly important for providing accurate and reliable results in simulations. Furthermore, it is possible to develop specific elements for FE analysis that deal with complex problems such as those involved in the L-PBF process. For example, the literature contains some recent sources about the use of variational methods applied to phenomena such as thermomechanical effects [58,59], damage and its evolution [60-63], or dissipation [64–67], and even to solve inverse problems [68–70].

Specifically, many studies were conducted on the effect of process parameters such as laser power and scan speed on the thermomechanical response and quality of the final product. For example, Waqar et al. [71] developed a 3D FEM model to investigate the effects of process parameters on the thermomechanical response of a part produced by the L-PBF of 316 L stainless steel, which was also validated against experimental data. The results showed a noticeable direct effect of laser power and an inverse effect of scan speed on the maximum melt pool temperature. Also, they found that the increment in laser power and scan speed yield to higher residual stress and cooling rate. Furthermore, Xiao et al. [72] presented a 3D FEM model to analyze the impact of process parameters on the residual stress during the L-PBF process of Ti6Al4V. According to their results, a complex relationship was observed between the residual stresses and the process parameters since there is a complex pattern of residual stress evolution during the process. In addition, Besides, Tawfik et al. [73] simulated the deposition process of a single-track multilayer AISI 304 stainless steel using a 3D FEM model. They concluded that the effect of scan speed on the temperature distribution and vertical displacement in the depth direction of the part should be examined in more than one layer since it will increase the available heat transfer time. Shrivastava et al. [74] conducted a FEM thermomechanical study of Inconel 718 during the L-PBF process to provide insight into determining the optimum process parameters to decline stress and distortion. The results suggested that increasing the printing time for each layer has a different effect on the distortion depending on the geometry and printing pattern design. Hence, various optimized process parameters might be achieved to improve the final product's quality for diverse geometries and printing patterns.

Apart from the process parameter analysis/optimization, another method of improving the mechanical properties of the parts produced using L-PBF involves modifying the material properties using a second material phase. It has been found that adding strengthening particles could improve the mechanical properties of the metal parts produced by L-PBF. Particularly, oxide dispersion strengthened (ODS) superalloys have recently received attention from many researchers because mixing ODS particles with metal powders provides enhanced chemical stability and high-temperature strength [75], improved wear, corrosion, irradiation, creep, and oxidation resistance [76–78], and finer microstructure [79]. Most recently, it was proved that adding Y_2O_3 oxide particles can compensate for the low strength of IN718 in higher temperatures [75]. In another study, Yalcin et al. [76] designed a product produced by L-PBF with nano-oxide strengthened IN718 alloy with a composition of 0. 3 wt.% Y_2O_3, Such a careful selection of the mixture provided the best microstructure with low porosity and high strength and ductility.

The methods used for the optimization of the process parameters provide an efficient tool to achieve better quality additive manufacturing with less residual stress and improved mechanical properties. Yet, to the best of the authors' knowledge, these methods have not been explored for the alloys strengthened by a second phase. However, there is a significant need to perform and comprehensively understand the AM process simulation of alloys mixed with nano-oxide particles since thermomechanical modelling can potentially contribute to their design of experiments and optimize the process parameters without an additional experimental process/cost. This research gap is addressed herein by developing a new and robust thermomechanical model of the 0. 3 wt.% Y2O3 composition of IN718 alloy for the first time in the literature. Therefore, the main and novel aim of this study is to develop an enhanced thermomechanical process model and investigate the effect of AM process parameters on the residual stress of the new ODS-modified Inconel 718 alloys (ODS-IN718) through benchmarking with the old one, i.e., IN718 alloy. To this end, a coupled thermomechanical FEM model is presented to analyze the L-PBF process of both IN718 and ODS-IN718 alloys. Although only one layer case is considered in most of the prior computational studies, the thermal exchange between the adjacent layers significantly affects the residual stress distribution in the real L-PBF process. Thus, as another novel aspect of this study, multi-layer single-track modeling approach of both IN718 and ODS-IN718 on the 316 stainless steel base plate is carefully implemented into the present thermomechanical model for making better physical reasoning of the residual stress distribution between adjacent layers. Also, the model is validated against the experimental melt pool dimensions and numerical results of several benchmark cases taken from the literature.

The remainder of this study is organized as follows. Section 2 presents the mathematical formulation of the coupled thermomechanical model. The governing equations, as well as the elastoplastic constitutive law, are presented. In Sect. 3, the numerical implementation and experimental and numerical verification have been discussed. The problem statement in terms of the computational domain, FEM model assumptions, the heat source model, and the thermophysical properties of IN718 and ODS-IN718 are provided. Section 4 demonstrates the thermal response of the products and validation of the thermal part in terms of the melt pool dimensions with experiments and numerical results from the literature. Then, it analyses the mechanical response of the products in terms of residual stress, and the effect of scan speed as a process parameter on the residual stress distribution is studied. Finally, the L-PBF produced IN718 and ODS-IN718 alloys were compared.

2 Mathematical formulation

L-PBF is a highly complex process that involves a wide range of thermomechanical phenomena. To simplify the modeling of the coupled thermomechanical L-PBF process and make it more tractable, certain assumptions can be made. It is important to note that these assumptions are simplifications and may not fully reflect the complexity of the L-PBF process. Nevertheless, they can be useful in creating a model that is easier to work with and that provides insights into the behavior of the process. In our study the following assumptions can be made.

(1) The base plate and powder bed are assumed to be homogeneous, isotropic, and continuum media. Particularly, the spherical powder particles are modeled as continuum solid elements.
(2) The thermomechanical simulation is conducted in two steps by using two equations. First, the thermal model calculates the temperature distribution. Then, the thermal response is used as an input to the mechanical model. The thermomechanical coupling is one way. Meaning the thermal strain is included in the mechanical model. Conversely, due to low impact, the effect of the mechanical model on the thermal model is not included.
(3) The material's thermophysical properties are temperature and phase dependent.
(4) The laser absorptivity coefficient and convection heat transfer coefficient between the powder bed and environment is considered constant.
(5) The latent heat generated in phase change is ignored, and the effect of phase change on stress is not considered.
(6) Fluid dynamics is not considered. Hence there is no melt pool flow and vaporization analysis.

2.1 Thermal model

The governing equations of the problem constitute the structural and thermal parts. Regarding the one way coupling in the present study, first, the thermal equation is solved. Then, the thermal solution is used in the mechanical equation. For the thermal part, the energy balance is applied. Due to the rapid changes in temperature during the L-PBF process, the energy equation must be solved transiently. In this study, the conduction, convection, and radiation mechanisms of heat transfer are considered. Equation (1) shows the governing transient energy equation in a volume Ω, in which $\dot{Q}_s$, ρ, c, T, and t are heat input per unit volume, density, specific heat, temperature, and time, respectively. The conduction heat flux vector is correlated with thermal gradient using the Fourier's law of heat conduction as in the first term in the right-hand side of Eq. (1). Also, $\mathbf{K}$ is the thermal conductivity tensor which is assumed with the equal terms for the x, y, and z directions for the homogenous media as Eq. (2).

$$\rho c \dot{T} = \nabla \cdot (\mathbf{K}\, \nabla T) + \dot{Q}_s \text{ , on } \Omega \text{ volume} \tag{1}$$

$$\mathbf{K} = \begin{bmatrix} k_x & 0 & 0 \\ 0 & k_y & 0 \\ 0 & 0 & k_z \end{bmatrix} \tag{2}$$

The heat input, $\dot{Q}_s$, is the supplied laser beam heat flux. Goldak's volumetric gaussian function is used as the heat source, stated with Eq. (3) [41]. In Eq. (3), P, μ, r, and (x, y, z) are laser power, lumped efficiency term or absorptivity, the radius of the laser beam, and the coordinates of the distances between surrounding points and heat source, respectively.

$$\dot{Q}_s = \frac{6\sqrt{3}P\mu}{\pi^{3/2} r_x r_y r_z} e^{\left[-\frac{3x^2}{r_x^2} - \frac{3y^2}{r_y^2} - \frac{3z^2}{r_z^2}\right]} \tag{3}$$

Note that time derivate of the heat source position is referred to as "laser scan speed" denoted by the symbol 'V' in the reminder the study. Assuming the isotropic thermal conductivity, convection and radiation boundary conditions are implemented as Eq. (4) in the exposed surface of the powder bed, S. In this equation the third and fourth terms are the convective and radiative heat loss. Also, k, q, h_{conv}, ε, σ and T_{amb} are the isotropic conductivity, input heat flux, convection heat transfer coefficient, emissivity, Stefan–Boltzmann constant, which is 5.67×10^{-8} W/m^2/K^4 [41], and the ambient temperature.

$$-kT_{,n_s} + q - h_{conv}\left(T - T_{amb}\right) - \varepsilon\sigma\left(T^4 - T_{amb}^4\right) = 0\text{, on } S \text{ surface with a normal axis } n_s \tag{4}$$

2.2 Mechanical model

For the structural part, the momentum balance equation, is applied as Eq. (5) in a volume Ω, in which $\mathbf{b}$ is the body force, $\boldsymbol{\sigma}$ is the stress tensor.

$$\nabla \cdot \boldsymbol{\sigma} + \mathbf{b} = \rho\ddot{\mathbf{u}} \quad \rightarrow \quad \nabla \cdot \boldsymbol{\sigma} = 0 \tag{5}$$

Since the powder bed dimensions are larger than the laser beam diameter, the L-PBF process could be considered quasi-static. This is because the time scale of mechanical deformation is much slower than that of thermal deformation. Hence, the right-hand side of Eq. (5) can be neglected. Additionally, since there is no body force in the L-PBF process, the relevant term cancels out. According to the elastoplastic constitutive law, there is a relationship between the stress tensor and the elastic strain tensor as shown in Eq. (6), where $\mathbf{C}_T$ is the fourth-order material tangent tensor. As can be seen, the thermomechanical coupling is included by the thermal strain in Eq. (6).

$$\boldsymbol{\sigma} = \mathbf{C}_T : (\varepsilon - \varepsilon^{th}) \tag{6}$$

The governing thermal and mechanical equations are discretized over the domain using FEM. The details of the FEM discretization are provided in detail in Appendix A.

Assuming the elastoplastic material, the nonlinear path-dependent constitutive equation needs to be solved incrementally to capture the history of all strains experienced by the material. Hence, it is an initial value problem that requires numerical integration. One approach is to directly solve the constrained problem such as the method used in [80]. In this study, the implicit elastic predictor (radial return mapping) method as a pseudo-time discretization algorithm is used for this goal. According to this method, we consider the elastic strain increment that corresponds to a pseudo-time increment. Then, the elastic trial strain and stresses are calculated. Next, the plastic strain is obtained and used to obtain the trial yield stress. Then, using yield criteria, it is checked if the deformation is elastic or not. If it is elastic, the elastic assumption of the trial state is valid and is the solution to the integration problem. Otherwise, the deformation is elastoplastic, and using the return mapping algorithm, the strain, and stresses are calculated in the new increment as described below.

The total strain increment is calculated as Eq. (7), where ε^e is the elastic strain, $\varepsilon^p$is the plastic strain, and ε^{th} is the thermal strain tensors. The total thermal strain is obtained by Eq. (8).

$$\Delta\varepsilon = \Delta\varepsilon^e + \Delta\varepsilon^p + \Delta\varepsilon^{th} \tag{7}$$

$$\Delta\varepsilon^{th} = \left(\alpha_T(T - T_{ref}) - \alpha_{initial}(T_{initial} - T_{ref})\right)\mathbf{I} \tag{8}$$

in which α_T and $\alpha_{initial}$ are the isotropic volumetric thermal expansion coefficient at the current temperature T and initial temperature $T_{initial}$, respectively. $T_{ref}$is the reference temperature used to define the thermal expansion coefficient, and $\mathbf{I}$ is the second-order identity tensor.

Given the total strain increment of $\Delta\boldsymbol{\varepsilon}^e$, the trial strain is calculated by addition of strain increment with the strain of the previous increment, n, as Eq. (9). The corresponding trial stress, $\boldsymbol{\sigma}^{\mathbf{tr}}$, the stress resultant from the elastic trial strain, which will be simply shown as $\boldsymbol{\varepsilon}^{tr}$, is obtained assuming the elastic constitutive law as Eq. (10) in which $\mathbf{C}_e$ is the elastic stiffness tensor.

$$\boldsymbol{\varepsilon}_{n+1}^{tr} = \boldsymbol{\varepsilon}_n^e + \Delta\boldsymbol{\varepsilon}^e \tag{9}$$

$$\boldsymbol{\sigma}^{tr} = \mathbf{C}_e : \boldsymbol{\varepsilon}^{tr} \tag{10}$$

Evaluating the trial stress, we should check if the deformation is in the elastic range. This is achieved by assessing yield surface. The yield function, f, is described by Eq. (11) for an isotropic linear hardening material with von Mises plasticity model, in which σ_{von}, σ_y are the equivalent von Mises stress and yield stress.

$$f\left(\boldsymbol{\sigma}, \Delta p\right) = \sigma_{von}\left(\boldsymbol{\sigma}, \Delta p\right) - \sigma_y = 0 \tag{11}$$

If the state of the material is on the boundary or inside the yield surface, $f \leq 0$, the deformation is elastic, and the algorithm is completed. Otherwise, a plastic correction step should be used to achieve the solution as follows: The plastic strain increment is obtained by the associated flow rule as Eq. (12):

$$\Delta\boldsymbol{\varepsilon}^p = \mathbf{n}_p \Delta p \tag{12}$$

in which Δp is the plastic multiplier which is obtained from consistency condition. Based on the consistency condition, during the plastic deformation the state of the material is always on the yield surface, $f = 0$, Generally, the plastic multiplier is calculated from Eq. (11) using the Newton–Raphson algorithm. In this study, we assume a perfect plastic material. Hence, there is no need to use the Newton–Raphson algorithm and plastic multiplier is the only unknown in Eq. (11). In Eq. (12), $\mathbf{n}_p$ is the flow direction tensor based on normality principle, obtained by Eq. (13). According to the normality principle, the plastic strain increment at the yield point is normal to the yield surface. In Eq. (13) $\boldsymbol{\sigma}_{dev}^{tr}$ is the deviatoric part of the trial stress tensor obtained by Eq. (14). Additionally, Eq. (15) shows σ_{von}^{tr}, the von Mises trial stress.

$$\mathbf{n}_p = \frac{3}{2}\frac{\boldsymbol{\sigma}_{dev}^{tr}}{\sigma_{von}^{tr}} \tag{13}$$

$$\boldsymbol{\sigma}_{dev}^{tr} = \boldsymbol{\sigma}^{tr} - \frac{1}{3}\mathbf{I}\left(\boldsymbol{\sigma}^{tr} : \mathbf{I}\right) \tag{14}$$

$$\sigma_{von}^{tr} = \sqrt{\frac{3}{2}\boldsymbol{\sigma}_{dev}^{tr} : \boldsymbol{\sigma}_{dev}^{tr}} \tag{15}$$

After solving the thermal equation and obtaining temperature, the thermal strain increment is calculated by Eq. (8) using the temperature in the current and previous increments. Additionally, the plastic strain increment is obtained using Eq. (12). Subtracting these strain increments from the total strain increment, the updated elastic strain increment and stress could be obtained by Eqs. (7) and (10), respectively.

2.3 Modelling of powder liquid and solid states

The governing equations stated in the previous section are solved by assuming three states of the material. In the beginning of the simulation, the base plate is assumed solid, and the built plate is in powder state. When the laser applies, the powder is heated and melts to liquid state. Then, as the laser moves away, the liquid metal loses heat and goes to solid state. Additionally, when the laser prints the next layer, the already solidified layer could melt again if its temperature goes higher than melting temperature. To capture all these phase changes an algorithm updates the phase status of the material at the beginning of each increment by comparing the temperature with T_{liquid}, and T_{Solid} using a user-defined subroutine. Figure 1a shows the algorithm used for the state update. Aside from phase update, the material properties of each state, used in the energy equation, specific heat, density, conductivity, and emissivity are assigned accordingly using other subroutines. Figure 1b

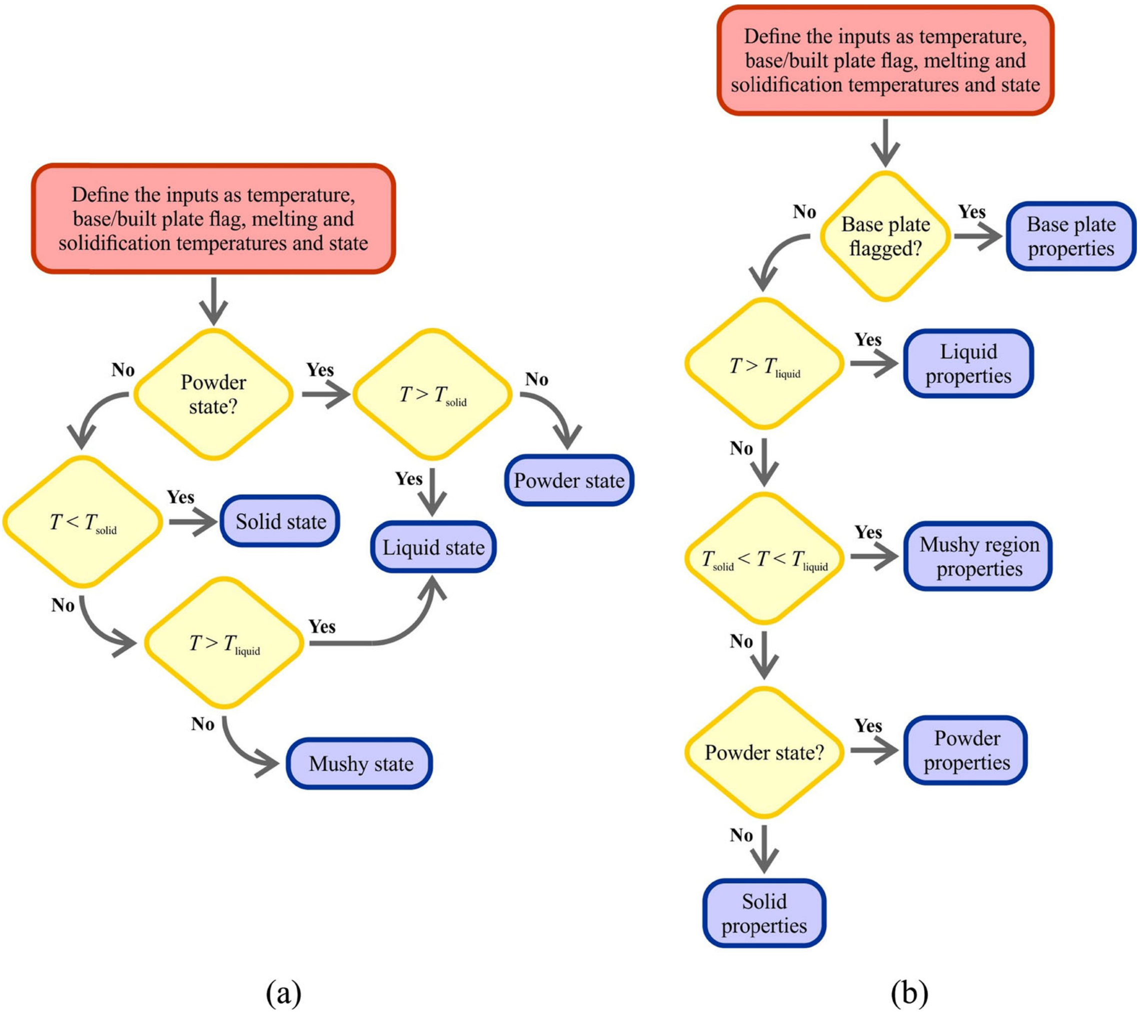

Fig. 1 Algorithm for assignment of **a** material state and **b** material properties

demonstrates the algorithm utilized for this implementation where the temperature of the element is used as the assessment criteria for properties assignment. For simplicity, the state of the material is assumed to be always solid for the base plate. Similarly, the updated states are used for the mechanical equation. In hypela2 subroutine the mechanical properties, elastic modulus, yield strength, Poisson's ratio, and thermal expansion coefficient are assigned to the solid state. The "element birth and death" is used for the structural analysis. For the powder and liquid states, a very small elastic modulus (1000 MPa) is assumed, and stress is set to zero to simulate the stress-releasing effect when the solid material is melted. Moreover, the hypela2 subroutine is used to implement the elastoplastic constitutive law, which was explained in the previous section.

To reduce computational cost and apply the layer-wise addition of powders the *uactive* subroutine is utilized to activate the built plate elements in each layer that laser is printing and deactivate the otherwise according to the time elapsed. The *uactive* subroutine is called at the beginning of each of the time increments before solving the governing equations. Figure 2 shows the flowchart of *uactive* subroutine. This subroutine first flags the base plate and built plate in the beginning. Then it activates the base plate for all the increments. For the built plate it compares the height of the element (Z_E) with the current layer height and activates the elements under the height of the current layer.

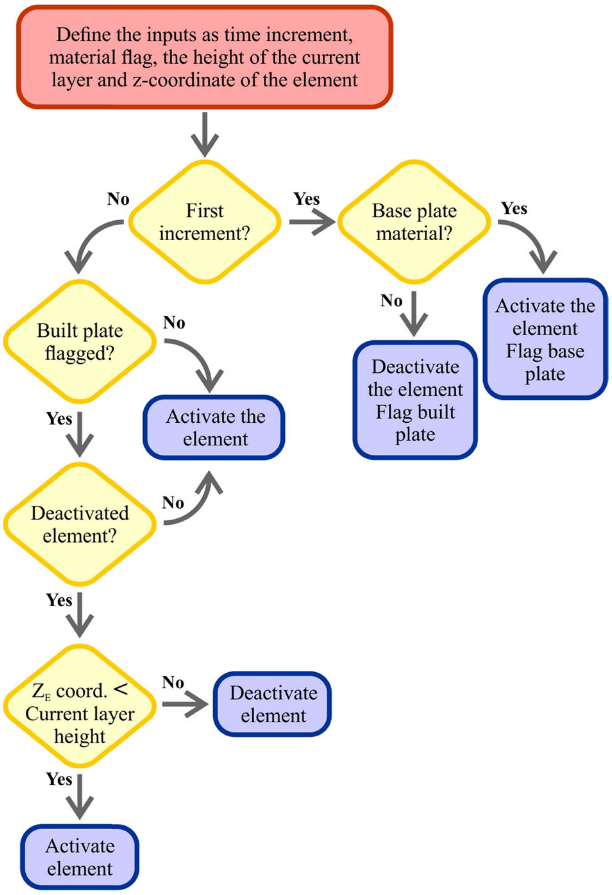

Fig. 2 Algorithm for activation of the elements

3 Numerical setup and implementation

A 3D model that has been utilized to simulate the L-PBF process. The base plate is considered a solid supporting structure. The downward movement of the base plate and powder bed for printing subsequent layers is modeled by considering the whole part stationary and adding layers over top. A layer-by-layer deposition of powder is modeled by adding a layer of powder as a continuum solid all at once on top of the base plate. The laser beam is simulated by applying a volumetric thermal heat flux supplying the energy for melting the powder. To model solid and liquid phases, the temperature of each point is compared with the melting temperature. The 3D nonlinear transient coupled thermomechanical FE model is implemented to simulate the L-PBF process of a mesoscale case study using MSC MARC software. Explicit time integration is employed in order to derive the fully discrete formulation. The Newton–Raphson algorithm is used to solve these nonlinear equations iteratively at each time step. The governing equations were numerically integrated over the finite elements using Gauss quadrature in spatial discretization. As discussed in the previous section, the nonlinear constitutive equation is solved incrementally using the implicit elastic predictor (radial return mapping) method, which serves as a pseudo-time discretization algorithm to handle the material's plasticity behavior.

Figure 3 demonstrates the computational domain geometry used for simulations with base plate dimensions of $w \times l \times h_B$ and powder bed dimensions of $w \times l \times h_P$, In Fig. 3 the red region, with $w_T \times l_T$ dimensions, indicates the track region, where the laser beam applies.

Discretizing the computational domain, a non-uniform coarse mesh is utilized for the base plate and built plate side regions to reduce the computational costs. A finer mesh is used for the track region of the built plate to capture the large gradients. This geometry will be used in the following sections, for different verification and main cases.

For the numerical simulations, the L-PBF process of a single-track three-layer case study with the geometry of $w = 0.55, w_T = 0.3, l = 1.3, l_T = 1, h_B = 0.18, h_P = 0.12$ mm is considered. As there are three

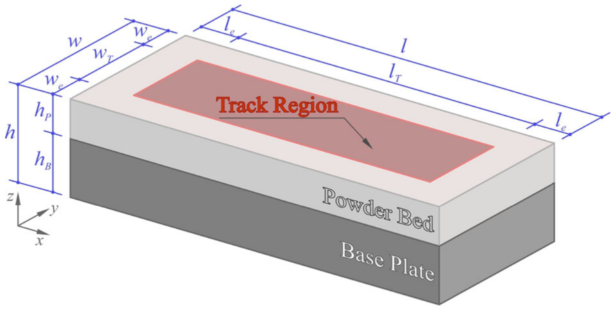

Fig. 3 The 3-dimensional representation of the computational domain

layers, the powder layer thickness becomes $h_P/3 = 40\mu$m for the simulations, which is consistent with the experiments. The initial and boundary conditions are the same as our validation benchmark case of Bayraktar and Demir [81]. The base plate is made of 316 stainless steels with material properties as conductivity of k =14 W/m/K, elastic modulus, $E = 195 \times 10^3$ MPa, Poisson's ratio of 0.3, yield strength of 205 MPa, $\alpha = 1.2 \times 10^{-6}$K, specific heat of c =500 (J/kg/K) and density of $\rho = 7700\,\mathrm{kg/m^3}$, For the built plate powder, we simulate the response of both ODS-IN718 alloy and pure IN718 alloy. Both materials' properties are given as a function of temperature in "Appendix B" for different solid, liquid, powder, and mushy phases. Here, the material properties of ODS-IN718 alloy are experimentally obtained through performing in-house mechanical testing (i.e., well justified in our previous study [76]) whereas the properties of pure IN718 alloy belong to a wrought material [82,83] rather than an additively manufactured one. Nevertheless, the material properties of wrought IN718 are very close to those of the additively manufactured counterpart reported in the literature. Accordingly, these properties were frequently utilized to perform AM process simulations in the literature [81,84,85]. Therefore, utilizing wrought material properties for our simulations is a valid and well-supported approach. Thus, we revisit these simulations for benchmarking with results of ODS-IN718 alloy.

For material properties of ODS-IN718, in-situ tensile tests were carried out at room temperature (RT), 700 °C, and 1000 °C using BESMAK BMT-E series and INSTRON 5582 universal testing machines according to ISO 6892-1 and ISO 6892-2 standards. Until the yield point, $7\times^{-5}\,\mathrm{s}^{-1}$ strain rate, and between yield and fracture points, $4 \times 10^{-4}\,\mathrm{s}^{-1}$ rate were used. Cylindrical samples along the axis perpendicular to the built direction were machined into the dog-boned tensile test samples with 4 mm gauge diameter and 20 mm gauge length, which is five times the diameter suggested by the ASTM E-8M standard for room temperature tests and ASTM E21-20 standard for high-temperature tests. It should be noted that 2 samples have been tested at room temperature where the results are repeatedly similar while 3 samples were tested at 700 °C and 1000 °C for each condition. On the other hand, Poisson's ratio was calculated by loading samples in elastic deformation region. The loading amount was selected as half of the yield strength of the material to guarantee that testing was applied in elastic deformation region. The details of the powder morphologies and mixing parameters have been provided in our previous study [76].

To elaborate on the strength difference of IN718 and ODS-IN718 at the high temperature, the ODS-IN718 alloy lacks the γ' and γ'' strengthening particles because it is just solutionized at 1050 C for 1 h after the additive manufacturing whereas the IN718 alloy was aged to obtain maximum strengthening [82,83]. Therefore, the lower yield strength of ODS-IN718 alloy at high temperatures in Fig. 16c is attributed to difference of the material processing conditions of these alloys. Besides, Li et al. [79] investigated the mechanical properties of pure IN718 alloys in solutionized condition at 700 C and reported the yield strength as ~750 MPa, which is lower than that of ODS-IN718 in this study. Hence, the properties shown in Figs. (B. 16 and 17) can be safely used for benchmarking the AM-induced residual stresses between the ODS-IN718 alloy and the pure one. Regarding the use of these properties as input to the simulations, recall that the material properties for each of the states (phases) are assigned using the algorithm in Fig. 1.

Table 1 shows the process parameters used in the numerical simulations as well as the experiments. We assume laser scan speeds in the range of 750–1200 mm/s and laser power in the range of 150–350 W.

To determine the grid independence of the results, different grids with different number of elements have been simulated and compared in terms of maximum temperature and displacement in the last increment that the laser applies on the powder bed. Figure 4 shows this maximum temperature and displacement using different grids. As evident in Fig. 4, increasing the number of elements causes negligible variations in the results after a

Table 1 Process parameters used in simulations

Properties	Value
Laser power, P (W)	150–350
Scan speed, V (mm/s)	750–1200
Wait time for recoater, t_{wait} (s)	0.01
Beam size, (m)	$r_x = r_y = r_z = 8.4 \times 10^{-5}$
Powder porosity	0.3
Powder absorptivity	0.2
Heat transfer coefficient (W/m^2 K)	25

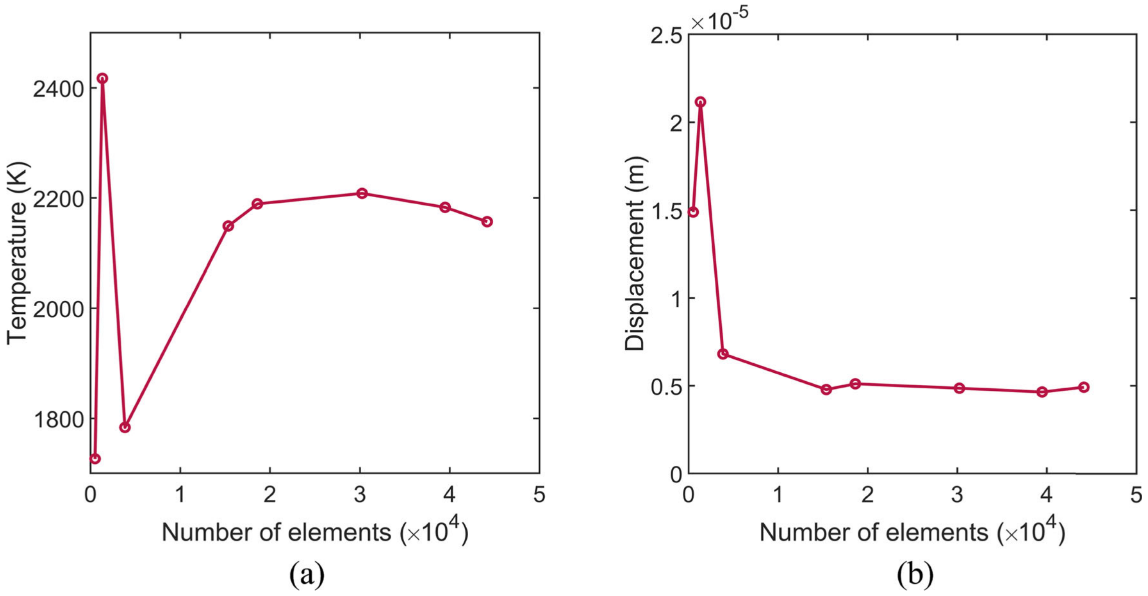

(a) (b)

Fig. 4 Mesh convergence results of **a** Maximum temperature and **b** displacement using different grids

specific number of elements. Considering the computational cost and accuracy, the grid with 30,240 elements with an element size of 16.7 × 16.7 × 40 μm^3 shows an error of 0.8% and 4% for the temperature and displacement, respectively and is selected for the future simulations. Also, the time step is set to 10^{-7}s.

4 Results and discussion

4.1 Numerical verification

The thermomechanical model is verified using three benchmark cases. In the first two cases, the thermal model is verified using the numerical finite element results from the study conducted by Luo et al. [34] and numerical and experimental results obtained by Le et al. [87] and Mahmood and Tariq [88]. Luo et al. [34] simulated the L-PBF process of the thermoelectric SnTe using the FEM model and validated their results with experiments. During this process, one layer of SnTe powder consisting of 5 hatches is printed on a SnTe substrate, using the laser power of P = 10W and scan speed of V = 300 mm/s. The geometrical variables shown in Fig. 4 used in this case study are as $w = 0.66, w_T = 0.26, l = 1.4, l_T = 1, h_B = 0.3, h_P = 0.025$ mm. A non-uniform mesh is used for the discretization with fine element size of 20 × 20 × 25 μm^3 in the track region. The hatch spacing is 40 μm and the powder layer thickness is 25 mm. The powder porosity of $\varphi = 0.5$, convection heat transfer coefficient of h =5 W/m^{2}K, laser beam radius of 50 μm, absorptivity coefficient of μ =0.3, a 2-dimensional Gaussian heat source, the melting/solidifying temperature and ambient temperatures of $T_{Solid} = T_{liquid} = 1078$ K and $T_{amb} = 298$ K are considered. The mechanical properties are $\nu = 0.3$, $\sigma_y = 75$ MPa and a temperature dependent elastic modulus provided in [34]. For thermal properties $\alpha = 20.4 \times 10^{-6}$ K^{-1} and density, specific heat, and conductivity of SnTe are considered temperature dependent as presented in [34]. The entire body

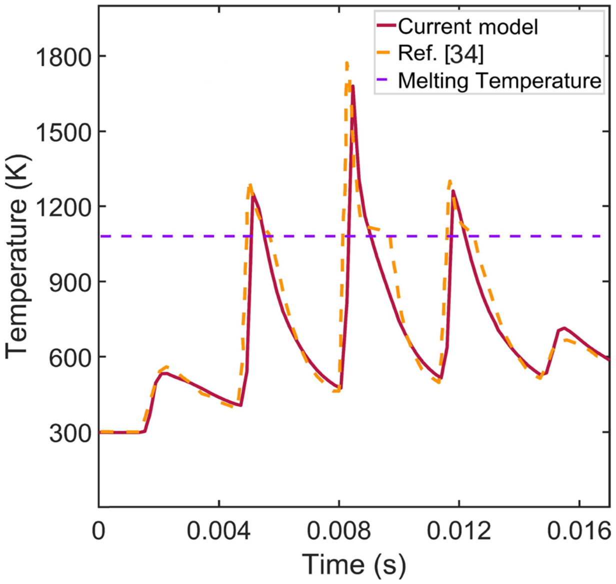

Fig. 5 Verification of the temperature variation of SnTe in the middle of the third scanned track at P = 10 W and V = 300 mm/s using the comparison between current model and Ref. [34]

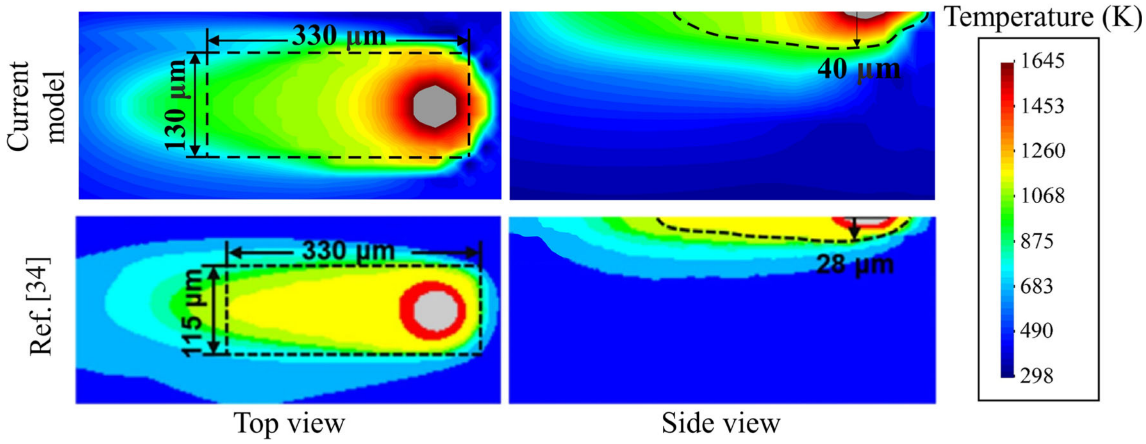

Fig. 6 Verification of temperature distribution and melt pool dimensions (dashed line) of SnTe when the laser beam is in the middle of the third scanned track at P = 10 W and V = 300 mm/s using the comparison between current model and ref [34]

has an initial temperature of $T_0 = 323\,\mathrm{K}$. Regarding boundary conditions, the bottom surface of the base plate, where it is attached to the ground, is considered fixed in all directions and free displacement for other surfaces. Also, the bottom face of the base plate has the fixed temperature of T = 298K. The convection boundary condition is considered for the top surface of the powder bed where it is exposed to the environment implemented as Eq. (4). Finally, all the other faces are considered adiabatic.

Figure 5 shows the comparison of the temperature variation in the middle of the third scanned track during the whole scanning and cooling process using our FEM model and the results from Luo et al. [34]. It is shown that the temperature variations are analogous throughout printing. However, there are instants where a relatively noticeable difference between the results is observed. This difference corresponds to the latent heat of phase transformation. Our model did not consider phase transformation, while it is considered in the reference study. Additionally, Fig. 6 shows the comparison of the melt pool dimensions obtained by our model with results of Luo et al. [34]. Here, the dashed black line in the contour plots represents the melt pool dimension. Eventually, this verification provides an accurate validation of our thermal model.

As a further step, the thermal model is verified using melt pool dimensions obtained numerically and experimentally from the literature for IN718. For this purpose, FEM simulations are conducted for the single-

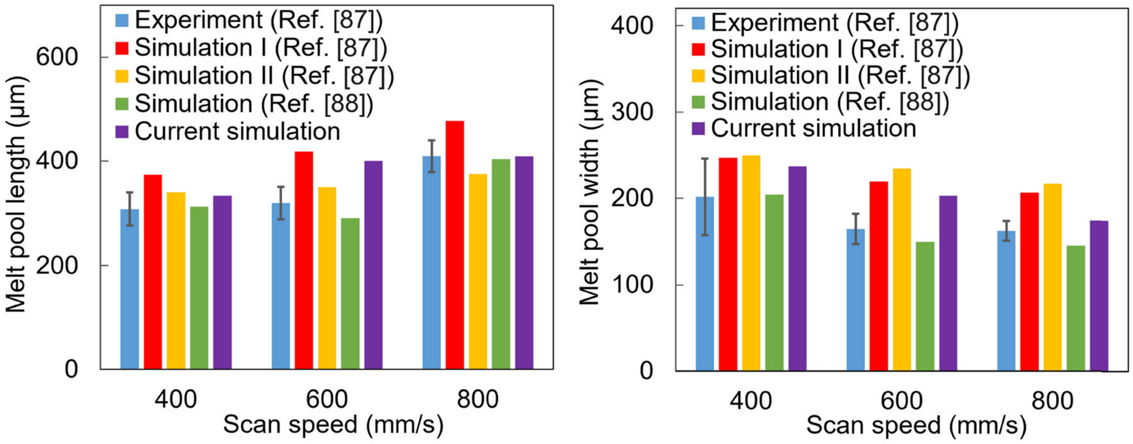

(a) (b)

Fig. 7 Verification of melt pool dimensions of IN718 at P = 180 W and V = 400, 600 and 800 mm/s using the comparison between current model and Refs. [87,88]

track L-PBF process of IN718 using laser power of P = 180 W and scan speeds of V = 400, 600 and 800 mm/s. The length and width of the melt pool are compared to those available in [87], where the authors validated their numerical results with their experimental data. Furthermore, the same results are compared with those reported in [88]. Figure 7 illustrates the comparison of the melt pool dimensions using the current model and literature. As can be seen, there is acceptable agreement between results. Both current simulations and experimental results show that increasing scan speed increases melt pool length and decreases pool width. Although the overall behavior is similar, the most consistent results for the length and width of the melt pool are obtained at a scanning speed of 800 mm/s. It is also important to emphasize that the current simulation results obtained for this speed are closer to the experimental results than all other reference simulations. Ultimately, our thermal model is verified with the numerical and experimental results in the literature.

In the next step, the thermomechanical model is validated using the numerical results of another case study in literature [81]. In this case study, the L-PBF process of printing a single layer of IN718 consisting of 10 hatches on a stainless-steel substrate is studied. The parameters are P = 160W and V = 1000 mm/s, $w = 1.8$, $w_T = 1$, $l = 1.8$, $l_T = 1$, $h_B = 0.32$, $h_P = 0.04$mm, $T_{amb} = 298$ K, h =25 W/m^{2}K, $T_{Solid} = 1523$ Kand $T_{liquid} = 1609$ K and $T_0 = 323$ K A non-uniform mesh with finer mesh size of 16.7× 16.7× 16.7 μm^3 in the powder bed area is considered. The hatch spacing of 110 μm, the powder layer thickness of 40 μm with φ =0.3, a 3-dimensional Gaussian heat source function implemented as Eq. (3), the laser beam radius of 50 μm and absorptivity of μ =0.3 are assumed. The temperature dependent thermophysical properties are provided in [81]. The boundary conditions are the same as the previous case study, except that radiation is also considered for the top layer and the temperature of the bottom face is T = 323 K.

Figure 8 shows the acceptable agreement between the current FEM model and numerical results from the literature in terms of the mean x (printing direction) and y (transverse direction) stress components of the final product over the whole domain. Hence, the thermomechanical model is also validated.

4.2 Thermomechanical analysis of ODS-IN718 alloys

4.2.1 Thermal characterization

In this section, the numerical simulations of the L-PBF process are verified with experiments. Since measuring the temperature during the L-PBF process is difficult experimentally, melt pool dimensions are used to validate thermal analysis. The explained single-track multilayer case of ODS-IN718 on the 316 L stainless steel base plate is used for the numerical model and experiments.

In this study, an ODS IN718 alloy was produced using 0.3 wt.%Y2O3 and 99.7 wt.% IN718 powders. The details of the powder morphologies and mixing parameters as well as the tensile curve have been provided in our previous study [76]. After mixing the powders, ODS-IN718 alloys were produced by laser powder bed fusion using EOS M 290 machine with a 40 μm layer thickness, 110μm hatch spacing and 67 ° rotation

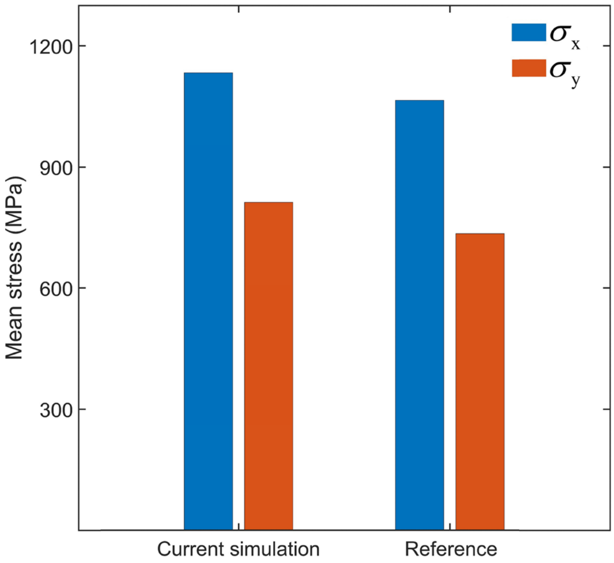

Fig. 8 Verification of the thermomechanical model using the comparison between mean stress in the final part produced using L-PBF obtained from current FEM model and reference [81]

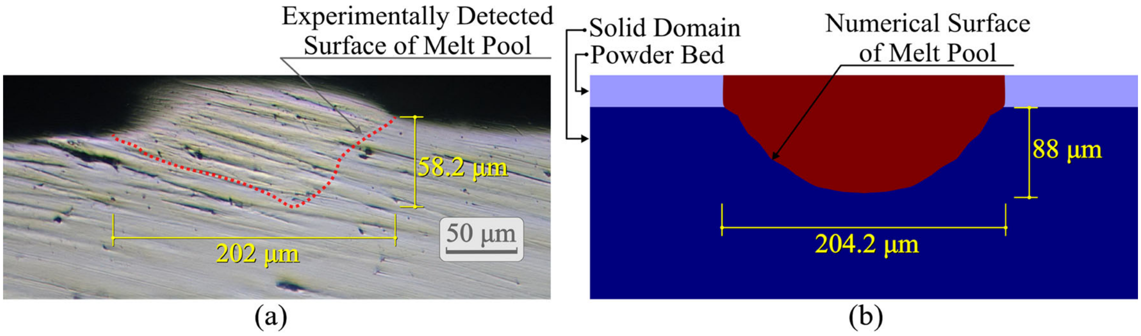

Fig. 9 Comparison of the melt pool dimensions obtained from simulations and experiments for depth and width at P = 350 W and V = 960 mm/s

strategy on a stainless-steel base plate in Argon atmosphere. To determine the optimum production parameters, power versus velocity parameter studies were conducted, as reported in [76]. Accordingly, the simulations were performed using our finite element model.

Figure 9 shows the cross-section of the melt pool predicted by simulations (yellow solid curve) which is compared with the experimental results (red dashed curve) for the process parameters: laser power of 350W and scan speed of 960 mm/s. The melt pool dimensions are compared based on the width and depth measurements shown in Fig. 9a, b, respectively. In terms of width, the numerical and experimental results are very close, with values of 202 µm and 204.2 µm, respectively, demonstrating strong correlation. However, in the depth direction, the results show a relatively larger deviation, indicating a less precise agreement between the two results. Figures 10 and 11 demonstrate the comparison of width and depth dimensions of melt pool between numerical and experimental results concerning varying laser power and scan speed values. As can be observed, the melt pool dimensions are increased in most cases for increasing value of the power in each fixed scan speed. This behavior can be attributed to the high fusion rate of the powder particles when higher energy is supplied which yields larger melt pool dimensions. Also, increasing velocity in a specific laser power causes a decrease in the melt pool dimensions in general. The reason might be that when the velocity increases, the available time for heat to diffuse decreases. Therefore, a smaller region gets heated and melts. For a quantitative comparison, the numerical melt pool dimensions provide an average error of 17% from the experimental melt pool dimensions for different laser scan speeds and laser powers. This error level can be attributed to the variability of the experimental measurements and the use of wrought IN718 material's thermal properties for

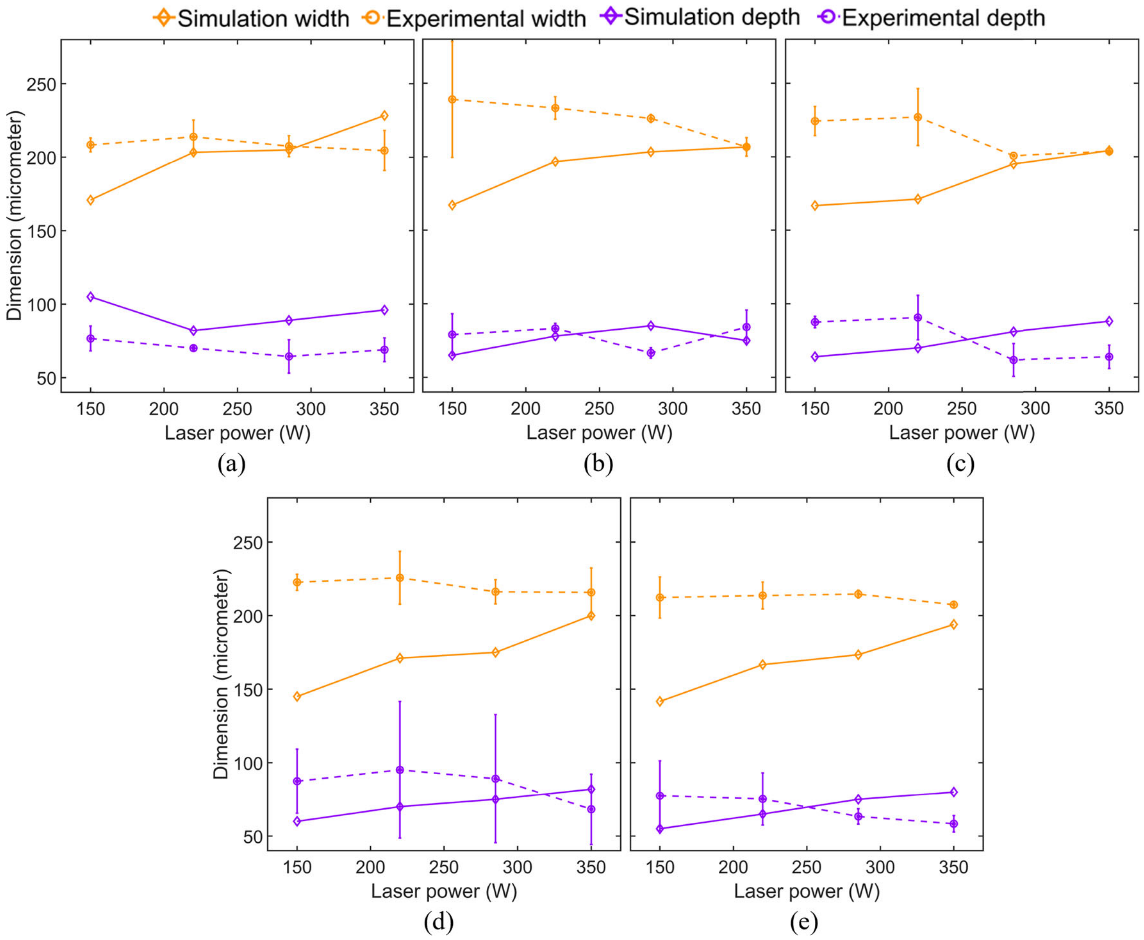

(a) (b) (c)

(d) (e)

Fig. 10 Comparison of numerical and experimental (with error bars) melt pool dimensions for varying laser power at different laser scan speeds: **a** V = 750 mm/s, **b** V=850 mm/s, **c** V = 960 mm/s **d** V = 1100 mm/s, **e** V=1200 mm/s

additively manufactured ODS-IN718 process simulations. Hence, there is an acceptable difference between experiments and simulations.

Determining the temperature variations of the L-PBF process plays a crucial role in predicting the quality of the final product since the temperature variation over time causes the emergence of residual stresses in the final built part. Figure 12 shows the melt pool shape and state distribution of ODS-IN718 around the laser beam while printing. A detailed inspection of Fig. 12 reveals that the temperature distribution is more compact in the front region of the moving heat source in the scan direction, which shows a higher temperature gradient. The reason is related to the lower thermal diffusion of the powder in the positive x-axis direction than the liquid or mushy phase in the trail region of the track. This difference in thermal behavior is critical as it affects the overall cooling rates and solidification patterns, which directly influence the microstructure and mechanical properties of the printed material. The highest peak temperature recorded is 1609 K at a specific point. The temperature decreases rapidly as the laser beam moves further from this point. These findings show that the energy density is no longer sufficient to melt the substrate, causing the stabilizing effect of the contact zone (penetration into the substrate) to diminish. As evident from Fig. 17c, the thermal conductivity of the liquid and mushy phases is higher than that of the powder phase, which leads to higher thermal diffusion. Similarly, the temperature gradient is less in the depth direction than the scanning, positive x-axis direction, and the perpendicular direction, y-direction. In this case, when the laser beam acts, it deals with the already solidified layers in the depth, z-direction, and the powders in the x and y front directions. As given in Fig. 17c, the conductivity of the solid is more than the powder. This difference highlights the importance of the material's thermal properties in the solidified layers, as they affect heat dissipation and the stability of the melt pool. Accordingly, the thermal diffusion would be more in the depth direction with the solid phase, leading

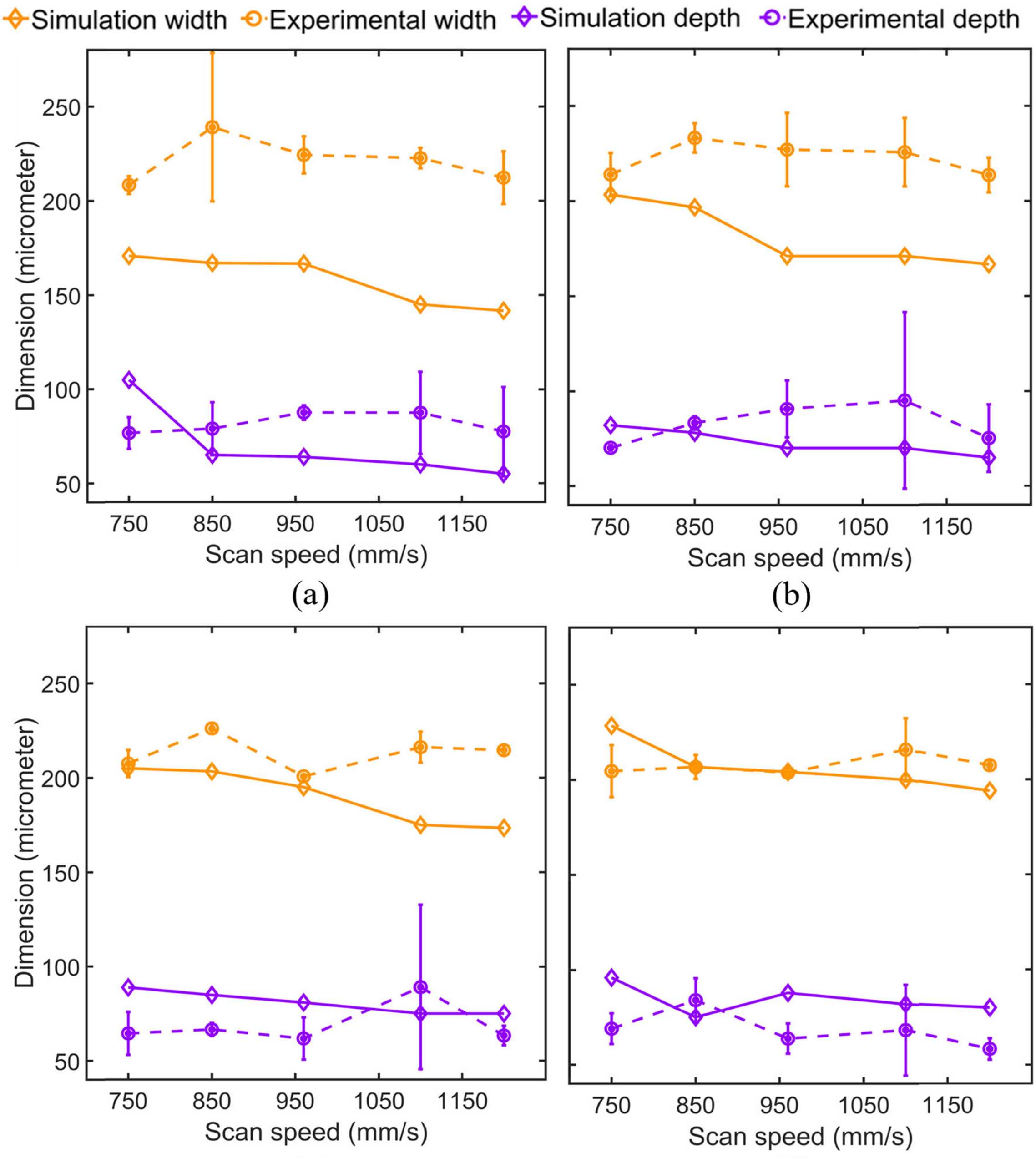

(a)

(b)

(c)

(d)

Fig. 11 Comparison of numerical and experimental (with error bars) melt pool dimensions for varying laser scan speeds at different laser power: **a** P = 150 W, **b** P = 220 W, **c** P = 285 W, **d** P = 350 W

to less temperature gradient in the depth direction in comparison with the positive x-direction and y-direction but more in comparison with the liquid trail direction (negative x-direction) with higher conductivity. This variation in thermal gradients underscores the anisotropic nature of heat transfer in additive manufacturing processes, which can significantly influence the final part's quality.

4.2.2 Residual stress assessment

It is well-known that high residual stresses can be observed after the L-PBF process when rapid cooling occurs. These high residual stresses are induced due to the rapid cyclic temperature changes in the vicinity of the laser

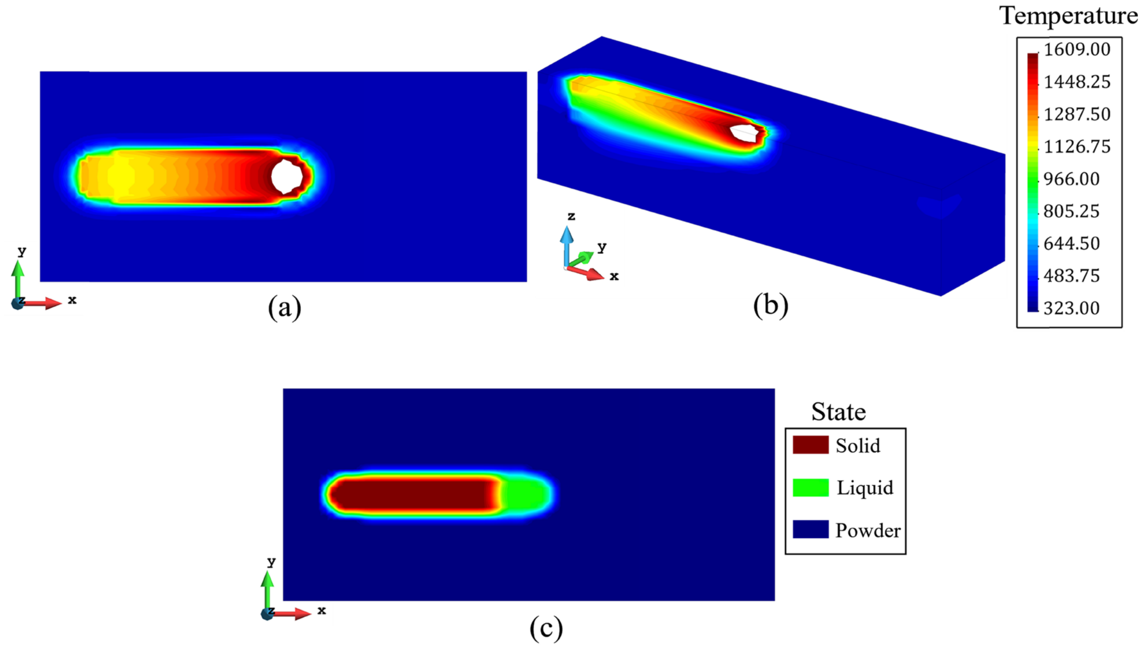

Fig. 12 Temperature distribution when the laser beam is in the middle of the third layer for ODS-IN718 at P = 150 W and V = 750 mm/s from **a** top view, **b** side view, and **c** state distribution

beam as observed in the previous part and could have a detrimental effect on the mechanical performance of the final product. Figure 13 demonstrates the components of residual stress and von Mises stress distribution of ODS-IN718 all over the base and built part in a sliced view after cooling to room temperature. As expected, there is a significant residual stress accumulation near the laser beam regions due to the high thermal gradients around the laser beam, observed in the previous section. Noticing the x component of the residual stress, the component in the printing direction, is higher than the y and z components. This response is in accordance with the reported observations in the literature [89,90]. Likewise, the x-component of stress is mainly positive, showing tensile stress, the magnitude of which is higher compared to that of compressive stress. This suggests that tensile stress is a determining damage factor in the L-PBF process. Here, tensile stress is higher in higher layers, while compressive stress is observed in the base plate. Furthermore, the y and z components of the stress indicate a higher magnitude at the beginning of the track. This might be because at the beginning of the printing, when the laser heat starts to be applied, the surrounding powder bed is at room temperature, so a higher temperature gradient is introduced to the powder bed resulting in a higher thermal strain. Consequently, higher residual stress would occur at the beginning as compared to the following instants when the laser heats the rest of the track. This also applies to the end of the track where the heat source gets off, and the thermal gradients increase again. Lastly, the von Mises stress has a behavior very similar to the x-component of stress, a high tensile stress concentrated mainly in the middle part of the upper layers.

Figure 14 shows the von Mises residual stress distribution for pure IN718 and ODS-IN718, respectively, in a sliced view for various scan speeds in a range of V = 750–1200 mm/s after cooling to room temperature. To examine the effect of scan speed as well as the impact of modifying IN718 with nano-oxides, stress distributions are presented with equal modified levels of presentation. As the scan speed increases, the stress is more concentrated in the higher layers. This suggests that better final product quality, in terms of residual stresses, could be achieved by increasing the scan speed. However, the regions with high stress at the lower layers and base plate get bigger. The reason for this apparently contradictory behavior is that, as explained in the previous sections, by increasing the laser scan speed, the amount of energy absorbed decreases, reducing the amount of temperature change and, consequently, thermal strains and residual stresses. Hence, increasing the laser scan speed decreases the induced tensile stress in the upper layers. Conversely, less absorbed energy for the lower layers causes the melt pool depth to decrease. This causes less remelting of the previous layers, smaller thermal affected regions, and consequently less stress relief work on the lower layers. In other words, the same mechanism that causes less accumulation of the residual stresses in upper layers causes less residual stress relief in lower layers at higher scan speeds. Comparing the ODS-IN718 and IN718 in Fig. 14, it can be

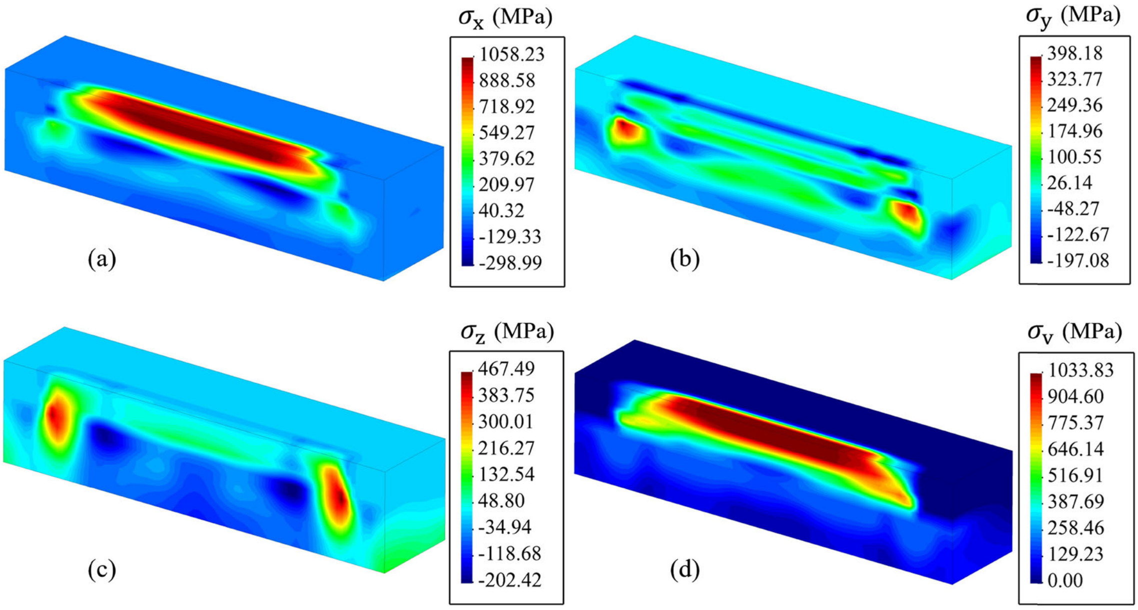

Fig. 13 Residual stress distribution of ODS-IN718 **a** x-component, σ_x **b** y-component, σ_y **c** z-component, σ_z and von Mises after cooling for P = 150 W and V = 750 mm/s when the whole model is cooled down to room temperature

noticed that the ODS-IN718 generally has less residual stress than pure IN718. This less stress can be explained using Fig. 16a, which shows that ODS-IN718 has less elastic modulus than IN718 at elevated temperatures. Since residual stresses start accumulating while cooling from melting temperature after solidification, the ODS-IN718 would have a lower elastic modulus, resulting in lower stiffness and, consequently, lower residual stress. This is particularly highlighted in the higher layers.

Investigating the history of the residual stress, Fig. 15 demonstrates the stress variation in the middle of the track in the first layer printed for both IN718 and ODS-IN718. First, the laser moves in the first layer, passes the specified location, and melts the powder. Then, following a rapid cooling, high thermal gradients are induced in the solidified location, leading to high residual stress as the first peak in Fig. 15. In fact, decreasing temperature causes volume shrinkage and consequently tensile stress in the x-component of stress in Fig. 15a. Afterwards, during the recoating time, the stress reaches a steady state. Later, the laser starts to print the second layer upon the first one. As the laser approaches the location above the specified location, it causes heat treatment in the previous location, relieving some stress. The rapid increase in temperature even causes compressive x-component stress in the pre-solidified specified location. Then, the laser moves away, and the cycle repeats but this time, it induces less stress than the first layer since the printing of the second layer has less thermal effect on the first layer. This result is also true for the y and z components of the stress in Figs. 15b, c for all scan speeds. Ultimately, as the repeating pattern of the fluctuating stress in Fig. 15 shows, printing the subsequent layers reduces the residual stress in the lower layers by heat treatment mechanism. This behavior can also be seen in the 3-dimensional stress distributions in Figs. 13 and 14, in which the residual stress is less in the lower layers compared to higher layers.

Comparing various scan speeds, the three peaks of all stress components associated with printing each of the three layers damp for most of the cases as the scan speed increases. As explained previously, increasing the scan speed would not necessarily lead to less final residual stress in the lower layers and base plate. Eventually, as can be seen in Fig. 15, the scan speed of V = 1100 mm/s has the least final von Mises stress in the middle of the lower layers compared to other scan speeds, indicating that the scan speed of V = 1100 mm/s is the optimal scan speed for P = 150 W in terms of the final residual stress in the middle lower part of the product where it is attached to the base plate.

Another important point is the effect of adding nano-oxide particles to IN718. As evident in Fig. 15, adding nano-oxides has different effects on the x, y, and z components of stress, but for the von Mises stress, it would lead to less stress throughout the whole printing process for all scan speeds. This improvement could also be generalized to the whole product, as seen in Fig. 14, where ODS-IN718 demonstrates more improvement than pure IN718 in the final von Mises stress distribution at all scan speeds. Focusing on the first peak of the

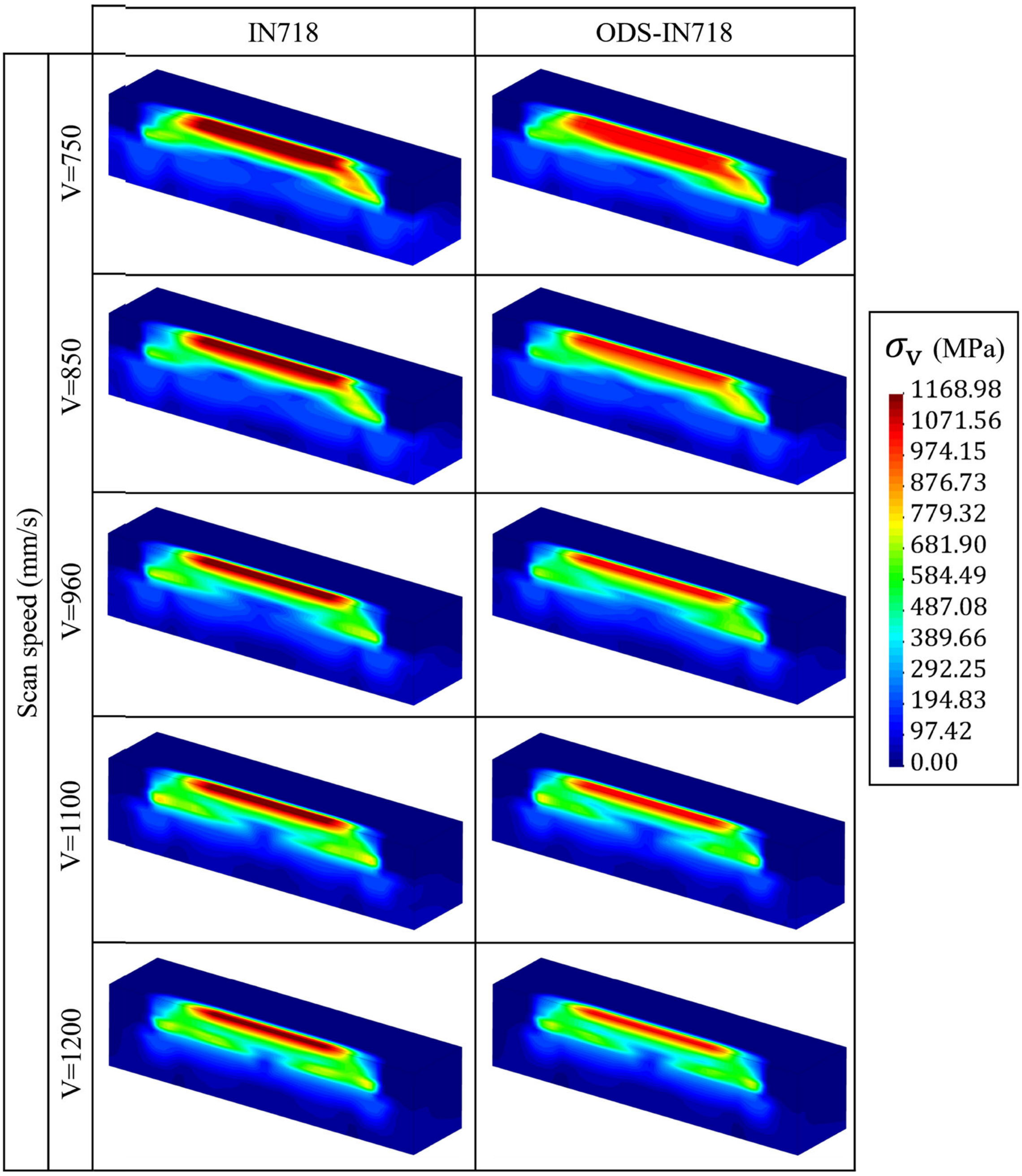

Fig. 14 The comparison between the von Mises, σ_v, residual stress distribution of IN718 and ODS-IN718 at $P = 150\,W$ for different laser scan speeds (when the whole model is cooled down to room temperature)

von Mises history plot, Fig. 15d, starting from the beginning until after printing the first layer, the residual stress reduction of ODS-IN718 compared to IN718 is more significant in lower scan speeds because more heat would be provided, and larger regions would have higher temperatures. In Fig. 16a, it is obvious that the difference between the elastic modulus of ODS-IN718 and that of IN718 increases at higher temperatures. Hence, by decreasing scan speed, the ODS-IN718 part would have larger regions with less elastic modulus and less residual stress. Later, at the second peak of the von Mises history plot, Fig. 15d, starting from printing the second layer until after printing the second layer, the temperature increases from room temperature to higher temperatures in the middle of the first layer. Noticing Fig. 16a, elastic modulus of the ODS-IN718 is higher than IN718 by 810 K, and then it gets lower. In other words, the ODS-IN718 would first have more stress and

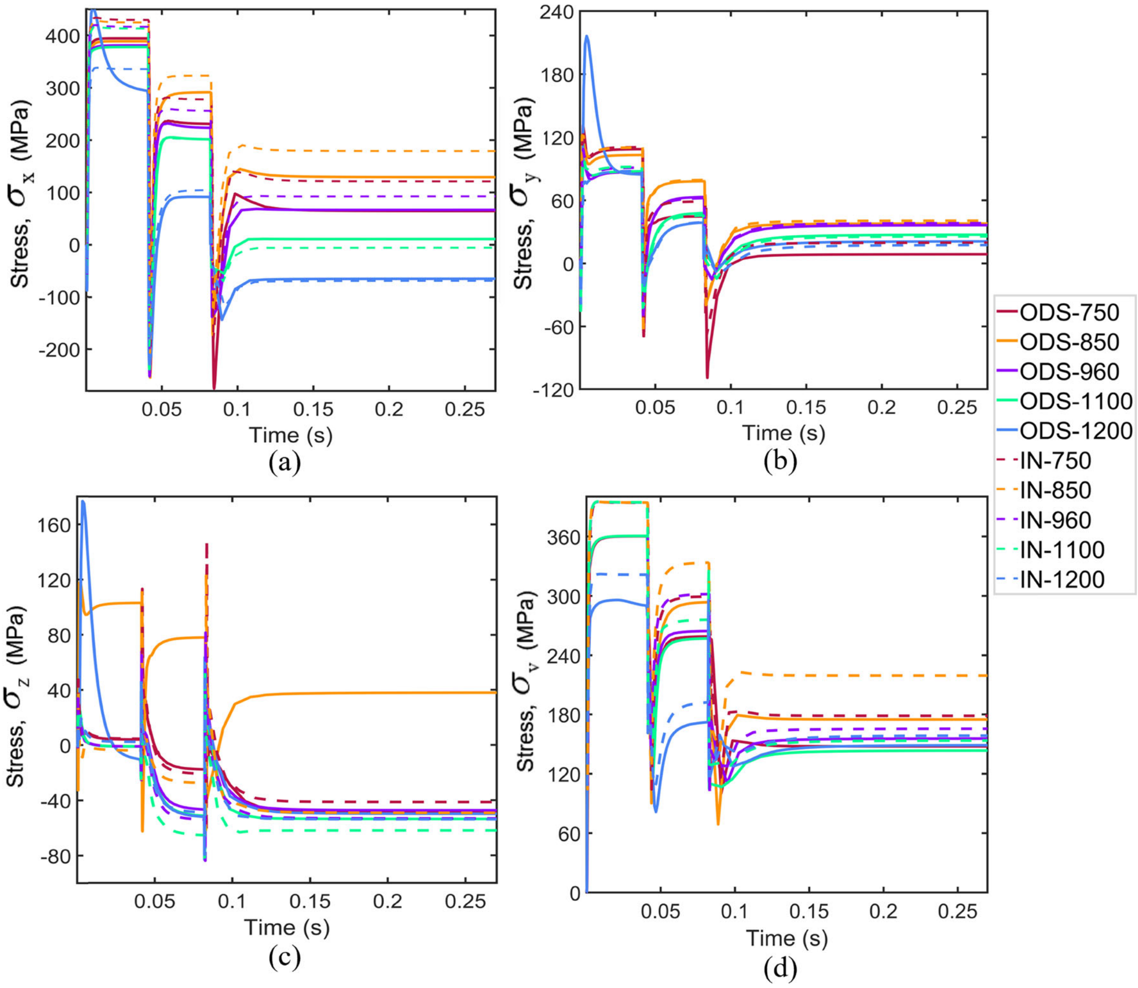

Fig. 15 Comparison between IN718 and ODS-IN718 variation of **a** x-component, σ_x , **b** y-component, σ_y , **c** z-component, σ_z, and **d** von Mises, σ_v, stress with time in the middle of the first track printed with P = 150 W and V = 750, 850, 960, 1100 and 1200 mm/s

then less stress in the middle of the first layer. Eventually, as Fig. 15d shows, there is the same stress difference between ODS-IN718 and IN718 in the second peak of the history plot as the first peak. This response suggests that the advantages of adding nanoparticles in pure IN718 are highlighted in lower scan speeds regarding the final residual stresses in the middle of the lower layers.

5 Concluding remarks

In this paper, a coupled transient thermomechanical FEM model is presented to study the L-PBF process of the IN718 and ODS-IN718 alloy. The novel aim of the study is to assess, for the first time, the effect of the process parameters on the residual stress and quality of the final product for the alloys strengthened by nano-oxide particles. Hence, a new thermomechanical model is implemented for the specific case of the 0.3 wt.% Y2O3 composition of IN718 alloy, addressing the need for predicting the behavior of nano-oxide dispersed alloys in additive manufacturing. Additionally, this study compares the thermomechanical responses of IN718 and ODS-IN718 for the first time.

For the validation of the thermal model, melt pool dimensions are compared with experimental results, and the temperature profile is verified by the numerical results from the literature. The impact of process parameters on melt pool dimensions is investigated with both numerical and experimental results. Thus, the melt pool dimensions increase as the power is increased at a constant laser scan speed as more energy is supplied to the powder bed. Conversely, melt pool dimensions decrease as the laser scan speed increases at a fixed power as less time is available for heat diffusion.

The thermomechanical model is validated against numerical results in the literature in terms of residual stresses. Furthermore, numerical thermomechanical simulations are conducted for various laser scan speeds, and the effect of laser scan speed on the residual stress of the final product is investigated. Afterward, the quality of the ODS-IN718 and pure IN718 products are compared. This analysis presented, for the first time, a detailed assessment of the influence of scan speed on residual stress for ODS-IN718 alloys. According to the results, temperature and stress variations follow a repetitive pattern over time corresponding to the printing of each layer. The residual stress induced after printing each layer is mainly tensile and has the highest magnitude in the printing direction. During the printing of subsequent layers, the laser beam provides heat to the previous layers as well. As a result, some previously induced tensile stress in pre-solidified layers is relieved. Thus, as the printing continues, the maximum residual stress moves to the upper layers. This observation highlights the importance of conducting a multilayer analysis in L-PBF process simulations to obtain more realistic estimates, addressing the limitations of the single layer modeling approach often used in prior studies.

It is observed that in the benchmark cases, increasing the laser scan speed decreases the volume of areas with high tensile residual stresses in the higher layers. However, the volume of regions with compressive stress increases at lower layers. Eventually, as the scan speed increases, the maximum residual stress concentrates in the higher layers. Additionally, the residual stress in the lower layers, where the built part is attached to the base plate, is the highest at two ends of the printing path and the lowest in the middle. The maximum residual stress at two ends of the first layer does not differ significantly with increasing scan speed. However, increasing the scan speed of the region with high residual stress extends to a wider length along the printing path.

A key finding of this study is that comparing the ODS-IN718 and pure IN718, the residual stress of the ODS-IN718 is generally less than pure IN718, especially for the above layers. In view of this finding, oxide-dispersed alloys offer the potential to improve the quality of additively manufactured parts. Also, the minimal residual stress of the ODS-IN718 in upper layers is a critical observation since the maximum residual stress of the part corresponds to these layers. Moreover, our study demonstrated that the improvement in residual stress caused by the change in material properties due to the presence of nano-oxide particles is more effective at lower scan speeds since more energy is available and larger regions with higher temperatures are obtained. As a result, the higher difference between the elastic modulus of ODS-IN718 and that of pure IN718 at higher temperatures will highlight the improvement in residual stress. Finally, this study lays the groundwork for future research into the optimization of AM processes for advanced materials such as ODS alloys. It should be noted that by implementing more accurate material properties, especially the exact thermal properties for ODS-IN718, the advantages of using the ODS-modified IN718 alloy would be highlighted even more. Furthermore, future studies may explore the implementation of other non-linear plasticity models to better account for temperature gradients.

Acknowledgements The financial support provided by the Scientific and Technological Research Council of Turkey (TUBITAK) under the Grant No. 219M500 is greatly acknowledged.

Author contribution E. Yousefimiab wrote the main manuscript text and performed simulations, and E. Yousefimiab and A. Kendibilir prepared the figures and performed the revisions. Y. Yalcin performed the experiments. C. Cardillo performed the literature survey of metamaterials and continuum mechanics. E. Aydogan and A. Kefal conceptualized idea and supervised the study. All authors reviewed the manuscript.

Data availibility

Funding

Declarations

Conflict of interest

Appendix A Finite element implementation

To discretize the mechanical model over the domain using FEM, Eq. (5) is multiplied by an arbitrary weighting function/virtual displacement and integrated over the whole domain. Applying the chain rule, then, employing Gauss's divergence theorem, Eq. (A.1), (weak form) is obtained for the equilibrium state. In Eq. (A. 1) $\mathbf{t}$ is the traction force vector on S surface.

$$\int_S \delta\mathbf{u}^T \mathbf{t} dS - \int_\Omega \sigma : \delta\varepsilon \, d\Omega = 0 \tag{A.1}$$

To formulate the problem with FEM, we need to assume that displacement field is correlated with nodal displacements vector, $\mathbf{u}^e$, and shape functions, $\mathbf{N}$ as $\mathbf{u} = \mathbf{N}\mathbf{u}^e$. The vector assumption of the displacement field necessitates that the stress and strain fields should be vectors as well. using vector form of the stress and strain, $\tilde{\sigma}$ and $\tilde{\varepsilon}$, Eq. (A.1) is re-written in Voigt notation. Then, implementing strain–displacement relation, $\tilde{\varepsilon} = \mathbf{B}\mathbf{u}^e$, and $\mathbf{u} = \mathbf{N}\mathbf{u}^e$ in Voigt notation of Eq. (A.1) rearranging and $\delta\mathbf{u}^e T$ being cancelled out, Eq. (A.2) is obtained. In Eq. (A.2), $\mathbf{f}^{in}$ and $\mathbf{f}^{ext}$ are the internal and external force vectors, respectively.

$$\delta\mathbf{u}^{eT}\left(\int_\Omega \mathbf{B}^T\tilde{\sigma} d\Omega - \int_S \mathbf{N}_S^T \mathbf{t} dS\right) = 0 \;\Rightarrow\; \underbrace{\delta\mathbf{u}^{eT}}_{\neq 0}\left(\mathbf{f}^{in} - \mathbf{f}^{ext}\right) = 0 \tag{A.2}$$

Next, we need to drive the incremental boundary value problem since the constitutive law is solved incrementally. Hence, we need to solve the incremental form of the finite element equilibrium equation, Eq. (A.2). We define the residual force vector, $\mathbf{r}$ as the unbalance force vector that we are trying to minimize. The residual force vector in the $k-1$th iteration is as Eq. (A.3). This equation is nonlinear because of the nonlinear constitutive law in the internal force vector. Thus, the Newton-Raphson scheme is implemented to solve it as Eq. (A.4). In each Newton–Raphson iteration, the linearized form of the incremental equilibrium, Eq. (A.4), is being solved. $\mathbf{K}_T$ is the global tangent stiffness matrix obtained from the linearization of Eq. (A.2), assembled from local element matrices in Eq. (A.5). In Eq. (A.5) local tangent stiffness matrix is obtained by numerical integration using Gauss points with the Jacobian J. Also, $\tilde{\mathbf{C}}_T$ is the second-order material tangent (material stiffness matrix) as given in Eq. (A.6), which can be extracted from the fourth-order material tensor of a perfectly plastic material, $\mathbf{C}_T = \mathbf{C}^e - \mathbf{C}^e : \mathbf{n}_p \otimes \mathbf{n}_p : \mathbf{C}^e \big/ \mathbf{n}_p : \mathbf{C}^e : \mathbf{n}_p$, according to the Voight notation. After obtaining $\Delta\mathbf{u}^{(k)}$ from Eq. (A.4) we apply newton correction, Eq. (A.7) to obtain the new displacement. Using the new displacement, strain is updated by $\tilde{\varepsilon} = \mathbf{B}\mathbf{u}^e$. Then using the constitutive integration, explained in Section 2. 2, stress and other state variables are updated. Then, the new internal force vector will be calculated, and the residual force vector will be updated. The Newton–Raphson iterations are repeated until the convergence criterion, Eq. (A.8), is satisfied.

$$\mathbf{r}^{(k-1)} = \mathbf{f}^{in}(\mathbf{u}_{n+1}^{(k-1)}) - \mathbf{f}_{n+1}^{ext} = 0 \tag{A.3}$$

$$\mathbf{K}_T \Delta\mathbf{u}^{(k)} = -\mathbf{r}^{(k-1)} \tag{A.4}$$

$$\mathbf{K}_T^e = \int_V \mathbf{B}^T \tilde{\mathbf{C}}_T \mathbf{B} dV = \sum_{i=1}^{n_{gp}} w_i J_i \mathbf{B}_i^T \tilde{\mathbf{C}}_T i \mathbf{B}_i \tag{A.5}$$

$$\tilde{\mathbf{C}}_T = \frac{\partial\tilde{\sigma}}{\partial\tilde{\varepsilon}_{n+1}} \tag{A.6}$$

$$\mathbf{u}_{n+1}^{(k)} = \mathbf{u}_{n+1}^{(k-1)} + \Delta\mathbf{u}^{(k)} \tag{A.7}$$

$$\left\| r^{(i)} \right\| \Big/ \left\| \mathbf{f}_{n+1}^{ext} \right\| \le e_{tol} \tag{A.8}$$

To implement FEM in thermal model, like mechanical part, the strong form of the energy equation, Eq. (1) is multiplied by an arbitrary weighting function/virtual temperature, integrated over the volumetric domain and the resulting weak form of the energy equation is obtained. Applying the chain rule and then the divergence theorem yields to the Eq. (A.9) where $\mathbf{q}_s$ is the conduction surface heat flux vector that satisfies heat conduction equilibrium, $\mathbf{q}_s = \mathbf{K}\nabla T$, on the surface S with normal vector, $\mathbf{n}_s$,

$$\int_\Omega \delta T \rho c \dot{T} d\Omega + \int_\Omega \nabla(\delta T)\cdot(\mathbf{K}\nabla T) d\Omega = \int_S \delta T\, \mathbf{q}_s \cdot \mathbf{n}_s dS + \int_\Omega \delta T\, \dot{Q}_s d\Omega \tag{A.9}$$

Likewise, temperature field is correlated with nodal temperatures, $\mathbf{T}^e$, and shape functions, $\mathbf{N}_{th}$ as $T = \mathbf{N}_{th}^T\mathbf{T}^e$. Accordingly, the temperature gradient and virtual temperature are correlated by $\nabla T = \nabla\mathbf{N}_{th}^T\mathbf{T}^e \equiv \mathbf{B}_{th}^T\mathbf{T}^e$ and $\delta T = \mathbf{N}_{th}^T\delta\mathbf{T}^e$. Replacing these terms in Eq. (A.9) we get Eq. (A.10). $\delta\mathbf{T}^{eT}$ being canceled out, we obtain Eq. (A.11), where specific energy storage stiffness, conduction stiffness matrices, surface flux and

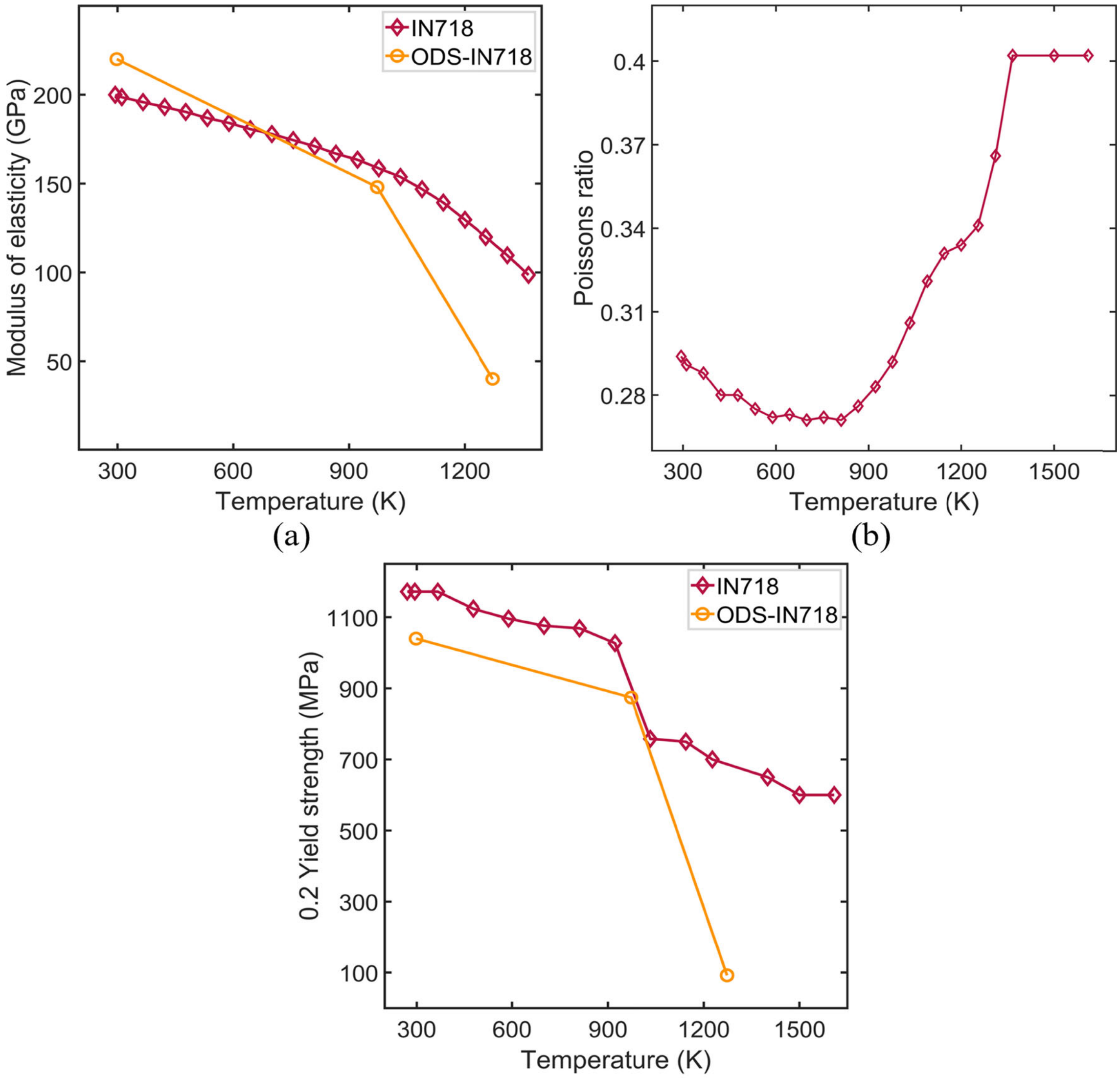

(a) (b) (c)

Fig. 16 Mechanical properties of IN718 and ODS-IN718: **a** modulus of elasticity, **b** Poisson's ratio of IN718, **c** yield strength

heat input force vectors are represented in Eq. (A.12). In Eq. (A.11) we use a backward Euler (implicit) time discretization scheme. Since the material properties are temperature dependent, a nonlinear system of algebraic equations is obtained that can be solved by the Newton–Raphson method. Additionally, in this study a maximum temperature change of 100 K is used as a tolerance between the temperature used to calculate the properties and the resulting temperature, to allow iterations as necessary.

$$\underbrace{\delta \mathbf{T}^{eT}}_{\neq 0}\left(\left(\int_\Omega \rho \mathbf{c}\mathbf{N}_{th}\mathbf{N}_{th}^T d\Omega\right)\dot{\mathbf{T}}^e + \left(\int_\Omega \mathbf{B}_{th}\mathbf{K}\mathbf{B}_{th}^T d\Omega\right)\mathbf{T}^e - \int_S \mathbf{N}_{th}\mathbf{q}_s^T\mathbf{n}_s dS - \int_\Omega \mathbf{N}_{th}\dot{Q}_s d\Omega\right) = 0 \tag{A.10}$$

$$\mathbf{C}^{th}\dot{\mathbf{T}}^e + \mathbf{K}^{th}\mathbf{T}^e = \mathbf{f}_s + \mathbf{f}_q \tag{A.11}$$

$$\mathbf{C}^{th} = \int_\Omega \rho c\, \mathbf{N}_{th}\mathbf{N}_{th}^T d\Omega \tag{A.12a}$$

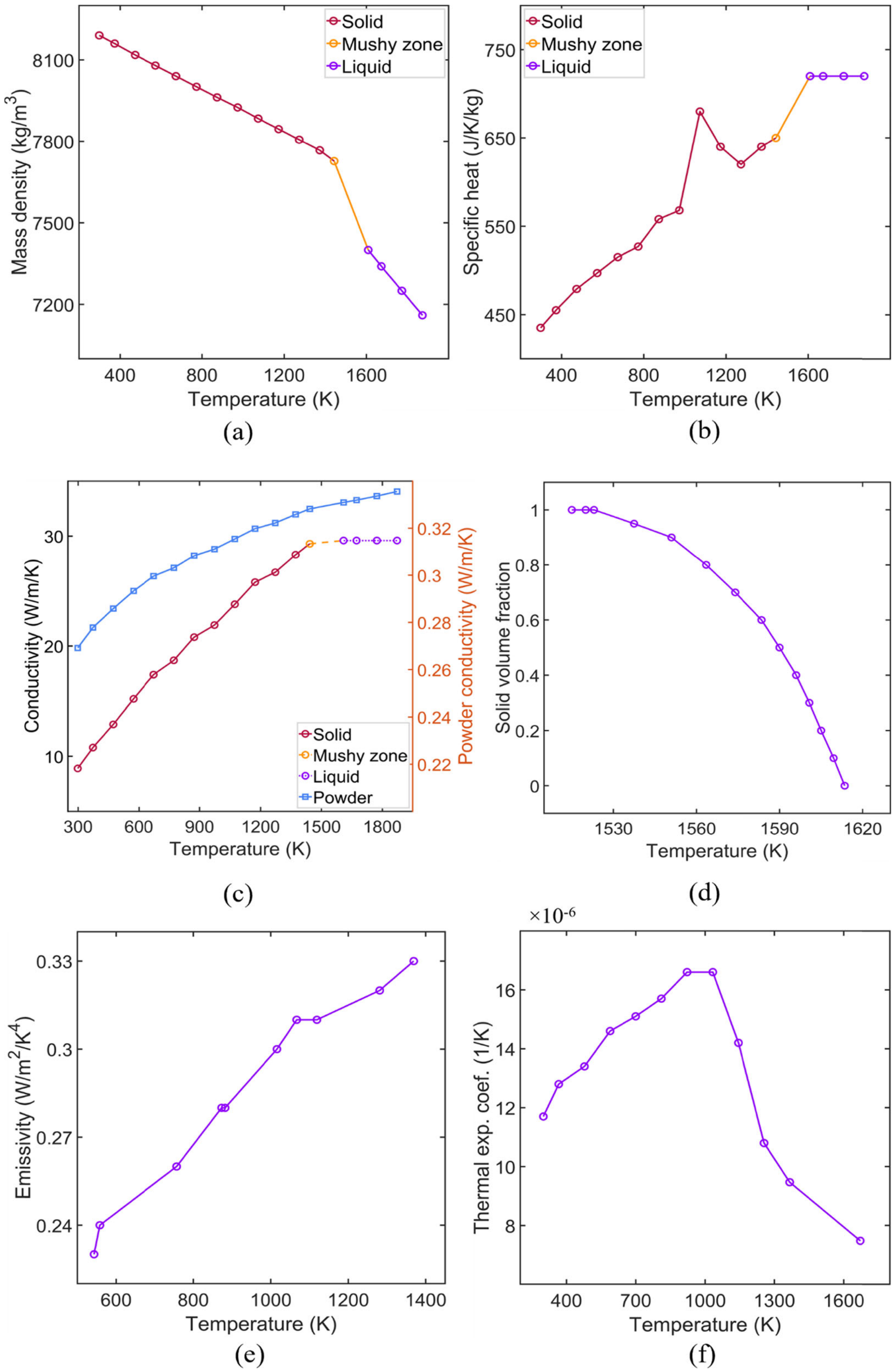

(a) (b)

(c) (d)

(e) (f)

Fig. 17 Thermal properties of IN718 and ODS-IN718: **a** density, **b** specific heat, **c** conductivity, **d** solid volume fraction, **e** emissivity, **f** thermal expansion coefficient

$$\mathbf{K}^{th} = \int_{\Omega} \mathbf{B}_{th}\mathbf{K}\mathbf{B}_{th}^{T} d\Omega \tag{A.12b}$$

$$\mathbf{f}_s = \int_{S} \mathbf{N}_{th}\mathbf{q}_s^{T}\mathbf{n}_s dS \tag{A.12c}$$

$$\mathbf{f}_q = \int_{\Omega} \mathbf{N}_{th}^{T}\dot{Q}_s \, d\Omega \tag{A.12d}$$

Appendix B Material properties

The thermophysical properties of the powder bed are provided in this section. Density, specific heat [71], emissivity [5] and isotropic thermal conductivity [90] of the powder are as follows. In these relations the s subscript represents the properties of the solid phase and φ, A_H, and ε_H are the powder porosity, porous area fraction of the powder, and emissivity of the powder surface vacancies. Also, k_f is the conductivity of surrounding Argon gas, taken as 0. 016, k_r is the radiation between powder particles obtained from $k_r = \frac{4}{3}\sigma T^3 D_p$. σ and D_p, are the Boltzmann constant, taken as 1.38×10^{-23} and the average diameter of the powder taken as 30 µm, respectively.

$$\rho_p = \rho_s (1 - \varphi) \tag{B.1}$$

$$c_p = c_s (1 - \varphi) \tag{B.2}$$

$$\varepsilon_p = A_H \varepsilon_H + (1 - A_H)\,\varepsilon_s \tag{B.3}$$

$$A_H = \frac{0.908\varphi^2}{1.908\varphi^2 - 2\varphi + 1} \text{ and } \varepsilon_H = \frac{\varepsilon_s\left[2 + 3.082\left(\frac{1-\varphi}{\varphi}\right)^2\right]}{\varepsilon_s\left[1 + 3.082\left(\frac{1-\varphi}{\varphi}\right)^2\right] + 1} \tag{B.4}$$

$$.k_p = k_f\left[\left(1 - \sqrt{1-\varphi}\right)\left(1 + \varphi\frac{k_r}{k_f}\right) + \sqrt{1-\varphi}\left(\frac{2}{1 - k_f/k_s}\left(\frac{1}{1 - \frac{k_f}{k_s}}\ln\frac{k_s}{k_f} - 1\right) + \frac{k_r}{k_f}\right)\right]. \tag{B.5}$$

In addition to the above formulations the temperature-dependent mechanical and thermophysical properties of the other phases are presented in Figs. 16 and 17.

References

1. Xia, M., Gu, D., Yu, G., Dai, D., Chen, H., Shi, Q.: Influence of hatch spacing on heat and mass transfer, thermodynamics and laser processability during additive manufacturing of Inconel 718 alloy. Int. J. Mach. Tools Manuf **109**, 147–157 (2016)
2. Bayat, M., Mohanty, S., Hattel, J.H.: A systematic investigation of the effects of process parameters on heat and fluid flow and metallurgical conditions during laser-based powder bed fusion of Ti6Al4V alloy. Int. J. Heat Mass Transf. **139**, 213–230 (2019)
3. Zhuang, J.R., Lee, Y.T., Hsieh, W.H., Yang, A.S.: Determination of melt pool dimensions using DOE-FEM and RSM with process window during SLM of Ti6Al4V powder. Opt. Laser Technol. **103**, 59–76 (2018)
4. Foroozmehr, A., Badrossamay, M., Foroozmehr, E., Golabi, S.I.: Finite element simulation of selective laser melting process considering optical penetration depth of laser in powder bed. Mater. Design **89**, 255–263 (2016)
5. Li, C., Fu, C.H., Guo, Y.B., Fang, F.Z.: A multiscale modeling approach for fast prediction of part distortion in selective laser melting. J. Mater. Process. Technol. **229**, 703–712 (2016)
6. Giorgio, I.: Lattice shells composed of two families of curved Kirchhoff rods: an archetypal example, topology optimization of a cycloidal metamaterial. Continuum Mech. Thermodyn. **33**(4), 1063–1082 (2021)
7. Giorgio, I., Ciallella, A., Scerrato, D.: A study about the impact of the topological arrangement of fibers on fiber-reinforced composites: some guidelines aiming at the development of new ultra-stiff and ultra-soft metamaterials. Int. J. Solids Struct. **203**, 73–83 (2020)
8. Ciallella, A., D'Annibale, F., Del Vescovo, D., Giorgio, I.: Deformation patterns in a second-gradient lattice annular plate composed of Spira mirabilis" fibers. Continuum Mech. Thermodyn. **35**(4), 1561–1580 (2023)
9. Abali, B.E., Barchiesi, E.: Additive manufacturing introduced substructure and computational determination of metamaterials parameters by means of the asymptotic homogenization. Continuum Mech. Thermodyn. **33**(4), 993–1009 (2021)
10. Aydin, G., Sarar, B.C., Yildizdag, M.E., Abali, B.E.: Investigating infill density and pattern effects in additive manufacturing by characterizing metamaterials along the strain-gradient theory. Math. Mech. Solids **27**(10), 2002–2016 (2022)

11. Aydin, G., Yildizdag, M.E., Abali, B.E.: Strain-gradient modeling and computation of 3-d printed metamaterials for verifying constitutive parameters determined by asymptotic homogenization. In: Analyses, Theoretical (ed.) Comput. Exp. Multiscale Mater., pp. 343–357. Springer International Publishing, Cham (2022)
12. Yildizdag, M. E., Tran, C. A., Barchiesi, E., Spagnuolo, M., dell'Isola, F., Hild, F.: A multi-disciplinary approach for mechanical metamaterial synthesis: a hierarchical modular multiscale cellular structure paradigm. In: State of the Art and Future Trends in Material Modeling, pp. 485–505 (2019)
13. Carcaterra, A., dell'Isola, F., Esposito, R., Pulvirenti, M.: Macroscopic description of microscopically strongly inhomogenous systems: a mathematical basis for the synthesis of higher gradients metamaterials. Arch. Ration. Mech. Anal. **218**, 1239–1262 (2015)
14. Turco, E., Giorgio, I., Misra, A., dell'Isola, F.: King post truss as a motif for internal structure of (meta)material with controlled elastic properties. R. Soc. Open Sci. **4**(10), 171153 (2017). https://doi.org/10.1098/rsos.171153
15. Alibert, J.J., Seppecher, P., Dell'Isola, F.: Truss modular beams with deformation energy depending on higher displacement gradients. Math. Mech. Solids **8**(1), 51–73 (2003)
16. Giorgio, I., Hild, F., Gerami, E., dell'Isola, F., Misra, A.: Experimental verification of 2D cosserat chirality with stretch-micro-rotation coupling in orthotropic metamaterials with granular motif. Mech. Res. Commun. **126**, 1–9 (2022). https://doi.org/10.1016/j.mechrescom.2022.104020
17. Giorgio, I., dell'Isola, F., Misra, A.: Chirality in 2D Cosserat media related to stretch-micro-rotation coupling with links to granular micromechanics. Int. J. Solids Struct. **202**, 28–38 (2020)
18. Giorgio, I., De Angelo, M., Turco, E., Misra, A.: A Biot-Cosserat two-dimensional elastic nonlinear model for a micromorphic medium. Continuum Mech. Thermodyn. **32**(5), 1357–1369 (2020). https://doi.org/10.1007/s00161-019-00848-1
19. Turco, E., Barchiesi, E., Causin, A., dell'Isola, F., Solci, M.: Kresling tube metamaterial exhibits extreme large-displacement buckling behavior. Mech. Res. Commun. **134**, 104202 (2023)
20. Turco, E., Barchiesi, E., Causin, A., dell'Isola, F., Solci, M.: Harnessing unconventional buckling of tube origami metamaterials based on Kresling pattern. Int. J. Solids Struct. 112925 (2024)
21. Ciallella, A., Giorgio, I., Barchiesi, E., Alaimo, G., Cattenone, A., Smaniotto, B., Vintache, A., D'Annibale, F., dell'Isola, F., Hild, F., Auricchio, F.: A 3D pantographic metamaterial behaving as a mechanical shield: experimental and numerical evidence. Mater. Design **237**(112554), 1–12 (2024)
22. Misra, A., Lekszycki, T., Giorgio, I., Ganzosch, G., Müller, W.H., dell'Isola, F.: Pantographic metamaterials show atypical poynting effect reversal. Mech. Res. Commun. **89**, 6–10 (2018). https://doi.org/10.1016/j.mechrescom.2018.02.003
23. dell'Isola, F., Lekszycki, T., Pawlikowski, M., Grygoruk, R., Greco, L.: Designing a light fabric metamaterial being highly macroscopically tough under directional extension: first experimental evidence. Z. Angew. Math. Phys. **66**, 3473–3498 (2015)
24. Golaszewski, M., Grygoruk, R., Giorgio, I., Laudato, M., Di Cosmo, F.: Metamaterials with relative displacements in their microstructure: technological challenges in 3D printing, experiments and numerical predictions. Continuum Mech. Thermodyn. **31**(4), 1015–1034 (2019). https://doi.org/10.1007/s00161-018-0692-0
25. Spagnuolo, M., Andreaus, U., Misra, A., Giorgio, I., Hild, F.: Mesoscale modeling and experimental analyses for pantographic cells: effect of hinge deformation. Mech. Mater. **160**, 103924 (2021)
26. Turco, E., Barchiesi, E., Giorgio, I., dell'Isola, F.: A Lagrangian Hencky-type non-linear model suitable for metamaterials design of shearable and extensible slender deformable bodies alternative to Timoshenko theory. Int. J. Non-Linear Mech. **123**, 1–19 (2020)
27. Hild, F., Misra, A., dell'Isola, F.: Multiscale DIC applied to pantographic structures. Exp. Mech. **61**(2), 431–443 (2021)
28. Barchiesi, E., dell'Isola, F., Hild, F.: On the validation of homogenized modeling for bi-pantographic metamaterials via digital image correlation. Int. J. Solids Struct. **208**, 49–62 (2021)
29. Yang, H., Ganzosch, G., Giorgio, I., Abali, B.E.: Material characterization and computations of a polymeric metamaterial with a pantographic substructure. ZAMP **69**(4), 1051–16 (2018). https://doi.org/10.1007/s00033-018-1000-3
30. De Angelo, M., Yilmaz, N., Yildizdag, M.E., Misra, A., Hild, F., dell'Isola, F.: Identification and validation of constitutive parameters of a Hencky-type discrete model via experiments on millimetric pantographic unit cells. Int. J. Non-Linear Mech. **153**, 104419 (2023)
31. Li, Y., Zhou, K., Tan, P., Tor, S.B., Chua, C.K., Leong, K.F.: Modeling temperature and residual stress fields in selective laser melting. Int. J. Mech. Sci. **136**, 24–35 (2018)
32. Peng, C.Q., Cai, Z.Y., Wang, R.C., Zhou, Z.H., Li, X.G., Cao, X.Y.: Finite element analysis of temperature and stress fields during selective laser melting process of Al-Mg-Sc-Zr alloy. Trans. Nonferrous Metals Soc. China **31**(10), 2922–2938 (2021)
33. Ahmad, B., van der Veen, S.O., Fitzpatrick, M.E., Guo, H.: Residual stress evaluation in selective-laser-melting additively manufactured titanium (Ti-6Al-4V) and inconel 718 using the contour method and numerical simulation. Addit. Manuf. **22**, 571–582 (2018)
34. Luo, C., Qiu, J., Yan, Y., Yang, J., Uher, C., Tang, X.: Finite element analysis of temperature and stress fields during the selective laser melting process of thermoelectric SnTe. J. Mater. Process. Technol. **261**, 74–85 (2018)
35. Gu, D., He, B.: Finite element simulation and experimental investigation of residual stresses in selective laser melted Ti-Ni shape memory alloy. Comput. Mater. Sci. **117**, 221–232 (2016)
36. Antony, K., Arivazhagan, N., Senthilkumaran, K.: Numerical and experimental investigations on laser melting of stainless steel 316L metal powders. J. Manuf. Process. **16**(3), 345–355 (2014)
37. Li, Y., Gu, D.: Thermal behavior during selective laser melting of commercially pure titanium powder: Numerical simulation and experimental study. Addit. Manuf. **1**, 99–109 (2014)
38. Marques, B.M., Andrade, C.M., Neto, D.M., Oliveira, M.C., Alves, J.L., Menezes, L.F.: Numerical analysis of residual stresses in parts produced by selective laser melting process. Procedia Manuf. **47**, 1170–1177 (2020)
39. Denlinger, E.R., Jagdale, V., Srinivasan, G.V., El-Wardany, T., Michaleris, P.: Thermal modeling of Inconel 718 processed with powder bed fusion and experimental validation using in situ measurements. Addit. Manuf. **11**, 7–15 (2016)
40. Kruth, J.P., Froyen, L., Van Vaerenbergh, J., Mercelis, P., Rombouts, M., Lauwers, B.: Selective laser melting of iron-based powder. J. Mater. Process. Technol. **149**(1–3), 616–622 (2004)

41. Parry, L., Ashcroft, I.A., Wildman, R.D.: Understanding the effect of laser scan strategy on residual stress in selective laser melting through thermo-mechanical simulation. Addit. Manuf. **12**, 1–15 (2016)
42. Arıso, Y.M., Criales, L.E., Özel, T.: Modeling and simulation of thermal field and solidification in laser powder bed fusion of nickel alloy IN625. Opt. Laser Technol. **109**, 278–292 (2019)
43. Bian, P., Shi, J., Liu, Y., Xie, Y.: Influence of laser power and scanning strategy on residual stress distribution in additively manufactured 316L steel. Opt. Laser Technol. **132**, 106477 (2020)
44. Marques, B.M., Andrade, C.M., Neto, D.M., Oliveira, M.C., Alves, J.L., Menezes, L.F.: Numerical analysis of residual stresses in parts produced by selective laser melting process. Procedia Manuf. **47**, 1170–1177 (2020)
45. Zinovieva, O., Romanova, V., Zinoviev, A., Nekhorosheva, O., Balokhonov, R.: Elastic properties of additively manufactured steel produced with different scan strategies. Int. J. Mech. Sci. **244**, 108089 (2023)
46. Zhou, J., Barrett, R.A., Leen, S.B.: Three-dimensional finite element modelling for additive manufacturing of Ti-6Al-4V components: effect of scanning strategies on temperature history and residual stress. J. Adv. Join. Process. **5**, 100106 (2022)
47. Giganto, S., Martínez-Pellitero, S., Barreiro, J., Leo, P., Castro-Sastre, M.Á.: Impact of the laser scanning strategy on the quality of 17–4PH stainless steel parts manufactured by selective laser melting. J. Market. Res. **20**, 2734–2747 (2022)
48. Zhou, L., Sun, J., Bi, X., Chen, J., Chen, W., Ren, Y., Niu, Y., Li, C., Qiu, W., Yuan, T.: Effect of scanning strategies on the microstructure and mechanical properties of Ti-15Mo alloy fabricated by selective laser melting. Vacuum **205**, 111454 (2022)
49. Zheng, Z., Jin, X., Bai, Y., Yang, Y., Ni, C., Lu, W.F., Wang, H.: Microstructure and anisotropic mechanical properties of selective laser melted Ti6Al4V alloy under different scanning strategies. Mater. Sci. Eng. A **831**, 142236 (2022)
50. Cao, L.: Mesoscopic-scale numerical investigation including the influence of scanning strategy on selective laser melting process. Comput. Mater. Sci. **189**, 110263 (2021)
51. Ravichander, B.B., Mamidi, K., Rajendran, V., Farhang, B., Ganesh-Ram, A., Hanumantha, M., Moghaddam, N.S., Amerinatanzi, A.: Experimental investigation of laser scan strategy on the microstructure and properties of Inconel 718 parts fabricated by laser powder bed fusion. Mater. Charact. **186**, 111765 (2022)
52. Natarajan, S.P., Vaudreuil, S., Chibane, H., Morandeau, A., Xavior, M.A., Cormier, J., Leroy, R., Duchosal, A.: Influence of heat treatment on the tool life while machining SLM Inconel 718 with reference to C&W Inconel 718. J. Manuf. Process. **83**, 192–202 (2022)
53. Yuan, Z., Chang, F., Chen, A., Li, F., Ma, R., Bai, J., Zheng, J.: Microstructure and properties of SLM-Hastelloy X alloy after different hot isostatic pressing+ heat treatment. Mater. Sci. Eng. A **852**, 143714 (2022)
54. Yang, X., Zhang, B., Bai, Q., Xie, G.: Correlation of microstructure and mechanical properties of Ti2AlNb manufactured by SLM and heat treatment. Intermetallics **139**, 107367 (2021)
55. Periane, S., Duchosal, A., Vaudreuil, S., Chibane, H., Morandeau, A., Xavior, M.A., Leroy, R.: Influence of heat treatment on the fatigue resistance of Inconel 718 fabricated by selective laser melting (SLM). Mater. Today Proc. **46**, 7860–7865 (2021)
56. Williams, R.J., Vecchiato, F., Kelleher, J., Wenman, M.R., Hooper, P.A., Davies, C.M.: Effects of heat treatment on residual stresses in the laser powder bed fusion of 316L stainless steel: Finite element predictions and neutron diffraction measurements. J. Manuf. Process. **57**, 641–653 (2020)
57. Panda, B.K., Sahoo, S.: Thermo-mechanical modeling and validation of stress field during laser powder bed fusion of AlSi10Mg built part. Results Phys. **12**, 1372–1381 (2019)
58. Giorgio, I.: A variational formulation for one-dimensional linear thermoviscoelasticity. Math. Mech. Complex Syst. **9**(4), 397–412 (2022)
59. Giorgio, I., Placidi, L.: A variational formulation for three-dimensional linear thermoelasticity with 'thermal inertia'. Meccanica 1–12 (2024)
60. Placidi, L., Barchiesi, E., dell'Isola, F., Maksimov, V., Misra, A., Rezaei, N., Timofeev, D.: On a hemi-variational formulation for a 2D elasto-plastic-damage strain gradient solid with granular microstructure. Math. Eng. **5**, 1–24 (2022)
61. Placidi, L., Timofeev, D., Maksimov, V., Barchiesi, E., Ciallella, A., Misra, A., dell'Isola, F.: Micro-mechano-morphology-informed continuum damage modeling with intrinsic 2nd gradient (pantographic) grain-grain interactions. Int. J. Solids Struct. **254**, 111880 (2022)
62. Placidi, L., Barchiesi, E., Misra, A.: A strain gradient variational approach to damage: a comparison with damage gradient models and numerical results. Math. Mech. Complex Syst. **6**(2), 77–100 (2018)
63. Abali, B.E., Klunker, A., Barchiesi, E., Placidi, L.: A novel phase-field approach to brittle damage mechanics of gradient metamaterials combining action formalism and history variable. ZAMM **101**(9), e202000289 (2021)
64. Placidi, L., Di Girolamo, F., Fedele, R.: Variational study of a Maxwell-Rayleigh-type finite length model for the preliminary design of a tensegrity chain with a tunable band gap. Mech. Res. Commun. **136**, 104255 (2024)
65. Bersani, A.M., Caressa, P., dell'Isola, F.: Approximation of dissipative systems by elastic chains: numerical evidence. Math. Mech. Solids **28**(2), 501–520 (2023)
66. Ciallella, A., Scerrato, D., Spagnuolo, M., Giorgio, I.: A continuum model based on Rayleigh dissipation functions to describe a Coulomb-type constitutive law for internal friction in woven fabrics. Z. Angew. Math. Phys. **73**(5), 209 (2022)
67. Ciallella, A., Pasquali, D., Głaszewski, M., D'Annibale, F., Giorgio, I.: A rate-independent internal friction to describe the hysteretic behavior of pantographic structures under cyclic loads. Mech. Res. Commun. **116**, 103761 (2021)
68. Fedele, R., Placidi, L., Fabbrocino, F.: A review of inverse problems for generalized elastic media: formulations, experiments, synthesis. Continuum Mech. Thermodyn. 1–41 (2024)
69. Abali, B.E.: Revealing the physical insight of a length-scale parameter in metamaterials by exploiting the variational formulation. Continuum Mech. Thermodyn. **31**(4), 885–894 (2019)
70. Fedele, R., Galantucci, L., Ciani, A.: Global 2D digital image correlation for motion estimation in a finite element framework: a variational formulation and a regularized, pyramidal, multi-grid implementation. Int. J. Numer. Meth. Eng. **96**(12), 739–762 (2013)
71. Waqar, S., Guo, K., Sun, J.: FEM analysis of thermal and residual stress profile in selective laser melting of 316L stainless steel. J. Manuf. Process. **66**, 81–100 (2021)

72. Xiao, Z., Chen, C., Zhu, H., Hu, Z., Nagarajan, B., Guo, L., Zeng, X.: Study of residual stress in selective laser melting of Ti6Al4V. Mater. Design **193**, 108846 (2020)
73. Tawfik, S.M., Nasr, M.N., El Gamal, H.A.: Finite element modeling for part distortion calculation in selective laser melting. Alex. Eng. J. **58**(1), 67–74 (2019)
74. Shrivastava, A., Kumar, S.A., Rao, S.: A numerical modeling approach for prediction of distortion in LPBF processed Inconel 718. Mater. Today Proc. **44**, 4233–4238 (2021)
75. Song, Q.S., Zhang, Y., Wei, Y.F., Zhou, X.Y., Shen, Y.F., Zhou, Y.M., Feng, X.M.: Microstructure and mechanical performance of ODS superalloys manufactured by selective laser melting. Opt. Laser Technol. **144**, 107423 (2021)
76. Yalcin, M.Y., Derin, B., Aydogan, E.: Development and additive manufacturing of oxide dispersion strengthened inconel 718: thermochemical and experimental studies. J. Alloys Compd. **914**, 165193 (2022)
77. Jia, H., Zhou, Z., Li, S.: A new strategy for additive manufacturing ODS steel using Y-containing gas atomized powder. Mater. Charact. **187**, 111876 (2022)
78. Shi, Y., Lu, Z., Yu, L., Xie, R., Ren, Y., Yang, G.: Microstructure and tensile properties of Zr-containing ODS-FeCrAl alloy fabricated by laser additive manufacturing. Mater. Sci. Eng. A **774**, 138937 (2020)
79. Li, M., Wang, L., Yang, H., Zhang, S., Lin, X., Huang, W.: Microstructure and mechanical properties of Y2O3 strengthened Inconel 625 alloy fabricated by selective laser melting. Mater. Sci. Eng. A **854**, 143813 (2022)
80. Areias, P., Rabczuk, T., Dias-da-Costa, D.: Element-wise fracture algorithm based on rotation of edges. Eng. Fract. Mech. **110**, 113–137 (2013)
81. Bayraktar, C., Demir, E.: A thermomechanical finite element model and its comparison to inherent strain method for powder-bed fusion process. Addit. Manuf. **54**, 102708 (2022)
82. Mills, K.C.: Recommended values of thermophysical properties for selected commercial alloys. Woodhead Publishing (2002)
83. High Temp Metals: Inconel 718 Tech data. https://www.hightempmetals.com/techdata/hitempInconel718data.php. Accessed 1 Sept 2023 (2015)
84. Wei, H.L., Mukherjee, T., Zhang, W., Zuback, J.S., Knapp, G.L., De, A., DebRoy, T.: Mechanistic models for additive manufacturing of metallic components. Prog. Mater Sci. **116**, 100703 (2021)
85. Khan, K., Mohan, L.S., De, A., DebRoy, T.: Rapid calculation of part scale residual stress-Powder bed fusion of stainless steel, and aluminum, titanium, nickel alloys. Addit. Manuf. **60**, 103240 (2022)
86. Denlinger, E.R., Gouge, M., Irwin, J., Michaleris, P.: Thermomechanical model development and in situ experimental validation of the Laser Powder-Bed Fusion process. Addit. Manuf. **16**, 73–80 (2017)
87. Le, T.N., Lo, Y.L., Lin, Z.H.: Numerical simulation and experimental validation of melting and solidification process in selective laser melting of IN718 alloy. Addit. Manuf. **36**, 101519 (2020)
88. Mahmood, M.A., Tariq, U.: A novel framework using FEM and machine learning models with experimental verification for inconel-718 rapid part qualification by laser powder bed fusion. Int. J. Adv. Manuf. Technol. **129**(3), 1567–1584 (2023)
89. Chen, C., Yin, J., Zhu, H., Xiao, Z., Zhang, L., Zeng, X.: Effect of overlap rate and pattern on residual stress in selective laser melting. Int. J. Mach. Tools Manuf **145**, 103433 (2019)
90. Chen, Y., Chen, H., Chen, J., Xiong, J., Wu, Y., Dong, S.: Numerical and experimental investigation on thermal behavior and microstructure during selective laser melting of high strength steel. J. Manuf. Process. **57**, 533–542 (2020)

Chapter 9

Coupled Flexoelectric-Photovoltaic Phenomena in Nanoscale Materials

Chapter abstract

This chapter introduces an extensive variational framework for describing the combined flexoelectric and photovoltaic effects in nanoscale materials, especially $BaTiO_3$ thin plates. By incorporating mechanical, electrical, and photonic variables, the model accounts for the complex interaction between strain gradients, polarization, and light-driven photocurrents. The formulation of internal energy includes higher-order gradient contributions, with carefully derived tensor symmetries using principles of continuum mechanics and Noether's theorem. Adapting the theory to thin plates through Kirchhoff–Love kinematics provides simplified governing equations that consider curvature-induced flexoelectric and photovoltaic influences, along with dynamic elements like inertial effects. Closed-form solutions for clamped square and circular plates subjected to uniform transverse and oscillatory loads demonstrate that flexoelectric and photonic interactions decrease the effective bending modulus while boosting curvature-driven polarization and photocurrent. For example, the model forecasts under the oscillatory loading, $q(x, y, t) = 1000 \sin(100t)$ Pa, a time-averaged energy output of around 3.7e-5 J for a 10 mm circular plate, whereas an optimized setup can achieve up to 0.011 J, highlighting the system energy harvesting capability. Analytical forecasts strongly align with experimental results, confirming the theoretical validity of the framework and practical significance for developing MEMS-based sensors and nanoscale energy harvesters.

Coupled Flexoelectric–Photovoltaic Phenomena in Nanoscale Materials: Variational Modeling and Analytical Solutions for Advanced Energy Harvesting

Koffi Enakoutsa
Department of Mathematics
University of California, Los Angeles (UCLA)
Los Angeles, CA 90095, USA
`koffi@math.ucla.edu`

Christian Cardillo
Department of Civil Engineering and Architecture (DICAR)
University of Catania
Catania 95123, Italy
`christian.cardillo@phd.unict.it`

Daria Scerrato
Department of Mechanical and Aerospace Engineering (DIMA)
University of Rome "La Sapienza"
Rome 00194, Italy
`daria.scerrato@uniroma1.it`

Abstract

This work presents a comprehensive variational framework for modeling coupled flexoelectric and photovoltaic phenomena in nanoscale materials, with a focus on $\mathrm{BaTiO_3}$ thin plates. By integrating mechanical, electrical, and photonic interactions, the model captures the complex interaction between strain gradients, polarization, and light-induced photocurrents. The internal energy formulation incorporates higher-order gradient terms, with rigorously derived tensor symmetries using continuum mechanics and Noether's theorem. Specializing the theory to thin plates via Kirchhoff–Love kinematics yields reduced governing equations that account for curvature-induced flexoelectric and photovoltaic effects, including dynamic terms such as inertial contributions. Closed-form solutions for clamped square and circular plates under uniform transverse and oscillatory loadings reveal that flexoelectric and photonic couplings reduce the effective bending modulus while enhancing curvature-driven polarization and photocurrent. For instance, under oscillatory loading $q(x, y, t) = 1000\,\mathrm{N/m^2}\sin(100t)$, the model predicts a time-averaged energy output of approximately 3.7×10^{-5} J for a 10 mm circular plate, while a more optimized configuration achieves up to 0.011 J, underscoring the potential of such systems for energy harvesting. Analytical predictions show strong agreement with experimental data [11, 12], establishing both the theoretical rigor and practical relevance of the framework for the design of multifunctional MEMS-based sensors and nanoscale energy harvesters.

Keywords: Flexoelectric-photovoltaic coupling, Variational modeling, Higher-gradient continuum, Multiphysics energy harvesting, Nanoscale mechanics.

1 Introduction

The discovery of flexoelectricity, the generation of electric polarization in response to strain gradients, has significantly advanced our understanding of electromechanical coupling in dielectric materials, particularly at the nanoscale [1, 2]. In contrast to piezoelectricity, which requires non-centrosymmetric crystal structures, flexoelectricity is a universal property observed in all dielectrics. This universality makes it particularly significant for nanoscale systems, where pronounced strain gradients arise due to size effects [3, 7]. Initial studies focused on theoretical frameworks and experimental validation in materials such as barium titanate ($\mathrm{BaTiO_3}$) and other perovskites, where mechanical deformations were shown to induce substantial polarization [8, 35]. These findings have incentivized interest in flexoelectricity for applications in sensors, actuators, and energy harvesting devices, where nanoscale dimensions enhance the coupling between mechanical strain gradients and electric fields [5, 31].

In parallel, photovoltaic effects in ferroelectric and perovskite materials have drawn increasing attention for their capacity to generate photocurrents under illumination, offering potential for solar energy conversion and optoelectronic devices [12, 13]. Notably, the bulk photovoltaic effect, observed in noncentrosymmetric materials, produces voltages above the band gap, making materials such as $\mathrm{BaTiO_3}$ ideal for photovoltaic applications [4,6]. Recent advances have highlighted the role of nanoscale structures, such as thin films and nanoparticles, in enhancing photovoltaic efficiency due to increased surface-to-volume ratios and localized electric fields [57, 60]. However, conventional photovoltaic models typically neglect mechanical interactions, limiting their scope in multifunctional devices that operate under simultaneous mechanical and photonic stimuli [15, 16].

The convergence of flexoelectric and photovoltaic effects has led to the emergence of photo-flexoelectric coupling, where light-induced currents enhance polarization through strain gradients, creating new pathways for versatile nanoscale devices [10, 58]. This coupling is particularly significant in thin plates and films, where curvature-induced effects amplify electrical and photovoltaic responses [17, 36]. Despite its potential, there remains a lack of unified models capable of consistently describing the interaction among mechanical, electrical, and photonic fields [33, 62]. This framework is essential for the design of integrated devices for sensing, actuation, and energy harvesting. Addressing this gap requires a variational framework that accounts for higher-order gradient effects and provides analytical solutions for practical geometries, enabling applications in high-sensitivity sensors, energy harvesters, and optoelectronic actuators [59, 63]. The mathematical foundations for strain gradient elasticity were strengthened by Eremeyev and dell'Isola. In particular, in [64, 65], they provided a rigorous variational-analytic treatment of dilatational strain gradient elasticity, including the existence and uniqueness of weak solutions in Lipschitz domains. This work underpins the use of higher-order gradient terms and Sobolev space formulations in continuum mechanics. Advanced continuum formulations using higher gradients have been extensively developed in recent decades. Fedele et al. [66] present a broad review of second- and third-gradient elastic models, emphasizing non-standard boundary conditions and inverse problem techniques, which support our adoption of higher-order energy and constraint terms. Third-gradient variational formulations, including edge and wedge force treatments, are detailed in [67–69], providing critical mathematical tools for formulating natural boundary conditions in our plate model. Earlier contributions [70–74] offer a Piola-based derivation of equilibrium equations for second-gradient bodies, reinforcing the variational structure used in our strain-gradient energy density. The incorporation of higher-gradient terms in continuum models, such as strain gradients, polarization gradients, and curvature-dependent effects, significantly enriches the predictive capabilities of mechanical theories, especially at micro- and nanoscale levels. However, this added accuracy comes at the cost of increased computational and mathematical complexity. Specifically, higher-gradient theories typically involve governing equations of fourth or even sixth order, which demand numerical techniques beyond standard finite element methods (FEM). Classical FEM schemes, which rely on continuity of the displacement field only, are insufficient to handle the required inter-element continuity of derivatives. As a result, the implementation of such models requires specialized numerical strategies, including mixed formulations, non-conforming finite elements, isogeometric analysis, or weak enforcement techniques (e.g., penalty or Nitsche methods) for higher-order continuity [75–78, 80, 81, 86]. The development and application of such tailored approaches is essential to faithfully capture the physical behavior predicted by higher-gradient models, particularly in systems involving flexoelectricity, photonic coupling, and thin-plate mechanics. In this context, our analytical results can serve as benchmarks for future numerical implementations and validations.

The goal of this paper is to develop a comprehensive variational model that captures the coupled behavior of the flexoelectric, photovoltaic, and photoflexoelectric effects in nanoscale materials. Our formulation includes the effects of strain, strain gradients, polarization, and photocurrent, extending prior flexoelectric models [18, 19] to account for photonic contributions. The limitation of conventional models restricts the design of multifunctional devices that harness mechanical and photonic stimuli, particularly on thin plates where curvature effects dominate [29, 30]. By extending the flexoelectric model of [20] to include photovoltaic and photoflexoelectric terms, this work provides a unified framework to predict and optimize device performance, with applications in MEMS, energy harvesting, and sensing [37, 38]. The variational approach is pivotal in this context, as it facilitates the robust modeling of coupling interactions among phenomena of diverse natures within a unified framework. For example, earlier variational work on layered structures that combine electric and mechanical interaction has demonstrated the power of mixed formulations with Lagrange multipliers in capturing through-thickness interactions. Notably, Maurini et al. [39] developed a variational model for layered beams that accurately predicts transverse stresses, electric fields, and constitutive coefficients in sandwich configurations. The dynamic flexo-piezo coupling in nanobeams has been carefully studied by Malikan and Eremeyev [40], who developed a variational model for visco–piezo–flexoelectric nanobeams, revealing how combined mechanical, electrical and flexoelectric effects influence dynamic responses at the nanoscale. Recently, there has been a steady focus on broadening variational methods to encompass complex continua. Cosserat et al. [41] formulate Dirac structures and Lie algebroids variationally, opening pathways to handle multiphysical couplings within continuum frameworks. Similarly, Giorgio et al. [42, 43] demonstrate how a variational principle can be successfully applied to linear thermoviscoelasticity, blending mechanical and dissipative thermal effects. Furthermore, Grillo and Di Stefano [44] introduced an a posteriori variational framework for volumetric growth, deriving growth laws via virtual-work formulations—paralleling our approach to deriving coupled flexoelectric–photovoltaic equations. In their follow-up study [45], they critically compared growth law formulations, emphasizing how variational consistency and boundary treatment shape material responses —concepts crucial to our handling of polarization and photocurrent boundary conditions. This formulation can be easily integrated with mass transport equations, as shown in both biological [46–48] and civil [49, 50] applications. In addition, Placidi et al. developed a variational 2D damage model with strain gradient and Karush-Kuhn-Tucker boundary conditions [52–54], offering methodological insights directly applicable to our treatment of strain, polarization gradients, and photocurrent boundary constraints. These contributions reinforce the suitability of our variational treatment of coupled flexoelectric and photovoltaic effects and support the theoretical foundations of our higher-gradient plate model. Additionally, this formulation is the theoretical base for the finite element method and, as such, inherently provides powerful tools for achieving robust numerical simulations with a strong mathematical basis. For example, in [55], a coupled variational approach is presented that integrates mechanics, thermodynamics, and electromagnetism through the implementation of FEM, echoing our multiphysics modeling approach. [56] features a non-linear variational FE model for rods with embedded piezoelectric actuators.

This study employs a variational approach to derive, starting from the internal energy density, the governing equations, and the boundary conditions of a flexoelectric-photovoltaic system, incorporating higher-order gradient effects. Tensor symmetries are justified using continuum mechanics and Noether's theorem, ensuring thermodynamic consistency [21–24]. The model is reduced for a thin plate under Kirchhoff–Love kinematics, resulting in coupled equations for displacement, polarization, and photocurrent [25, 26]. Closed-form analytical solutions are provided for clamped square and circular plates subjected to uniform transverse loading. These solutions reveal the curvature-driven generation of polarization and photocurrent and quantify how the coupling reduces the effective bending modulus [27, 28]. An application to a MEMS-scale energy harvesting device demonstrates a power output of 0.101 W under realistic loading and illumination conditions [82, 106], showcasing the practical relevance of the model. Piezoelectric materials have been extensively studied in the context of smart rods and plates (see, e.g., [98–103]). Although less research on flexoelectric devices is available [104], the insights gained from piezoelectric smart devices can be applied similarly to this emerging technology.

Architectured second-gradient models for beams and plates have been actively explored recently. For example, Barchiesi et al. [79, 83–85], following the pioneer work [87], derived 1D and 2D continuum limits from pantographic microstructures, producing richer constitutive laws involving both curvature and elongation gradients —an approach closely analogous to the higher-order terms in our flexoelectric–photovoltaic plate model. On the modeling front, Misra et al. [88, 89] proposed a geometrically non-linear micromorphic continuum derived from granular microstructure via variational homogenization, paralleling our efforts to derive reduced plate models via Kirchhoff–Love kinematics. Furthermore, Abali and Yang [90] show energy-based methods to model generalized materials, reinforcing the foundational techniques that underlie our theoretical structure. Abali and Barchiesi [91] demonstrate asymptotic homogenization to extract gradient continuum parameters from metamaterial microstructures, supporting our reduction and parameter derivation in flexoelectric-photovoltaic plates. Experimental techniques aimed at extracting these higher-order parameters are discussed in [92–94].

Recent advances in multiscale modeling highlight the critical importance of integrating uncertainty quantification and data-driven techniques alongside traditional deterministic methods. In particular, Soize presents a detailed review of probabilistic learning methods on manifolds [95], demonstrating how surrogate models built from limited datasets can effectively capture multiscale variability and stochastic homogenization effects. These methods, grounded in geometric statistics and stochastic inference, are especially relevant for materials with microscale heterogeneity [96, 97], a key factor in flexoelectric and photovoltaic coupling. Although our current approach is deterministic and variational, such techniques offer a compelling path forward for robust model calibration, sensitivity analysis, and design under uncertainty in nanoscale energy-harvesting structures.

The paper is structured as follows. In Section 2, the internal energy density is defined incorporating the terms related to flexoelectric, photovoltaic, and photo-flexoelectric phenomena. In Section 3, the symmetries of constitutive tensors using continuum mechanics and variational principles are justified. The mechanical, polarization, and photocurrent governing equations are derived via variational methods, in Sect. 4. Section 5 presents the reduced governing equations for a thin plate under Kirchhoff–Love kinematics, while Sect. 6 provides closed-form solutions for a clamped square plate, highlighting curvature-driven effects. Closed-form solutions for a clamped circular plate are presented in Sect. 7. Engineering applications in energy harvesting, strain sensing, and optoelectronic actuation are detailed in Sect. 8.

This research connects theoretical mechanics to nanotechnology, offering both a robust mathematical foundation and design-oriented tools for the next generation of high-performance multifunctional nanoscale devices [105, 106].

2 Extended Energy Density

The internal energy density, $\mathcal{W}$, extends the previous flexoelectric model proposed in [20] by also incorporating purely photovoltaic and cross-coupled photo-flexoelectric contributions, thereby capturing the combined effects of strain gradients, polarization, and light-induced charge dynamics. The resulting expression reads:

$$\begin{aligned}\mathcal{W} =&\frac{1}{2}C_{ijkl}D_{ij}D_{kl} + \frac{1}{2}\chi_{ij}P_iP_j + \epsilon_{ijk}P_iD_{jk} + G_{ijklm}D_{ij}D_{kl,m} + \frac{1}{2}H_{ijklmn}D_{ij,k}D_{lm,n}\\ &+ K_{ijkl}P_iD_{jk,l} + a_{ij}P_{i,j} + \frac{1}{2}b_{ijkl}P_{i,j}P_{k,l} + d_{ijkl}P_{i,j}D_{kl} + g_{ijk}P_iP_{k,j}\\ &+ \frac{1}{2}\kappa_{ij}J_iJ_j + \eta_{ij}P_iJ_j + \xi_{ijkl}J_iD_{jk,l} + \gamma_{ijk}J_iD_{jk},\end{aligned} \tag{1}$$

where:

- $D_{ij} = \frac{1}{2}(u_{i,j} + u_{j,i})$ is the strain tensor, with u_i as displacement;
- P_i is the polarization vector;
- J_i stands for the photo-electric displacement, defined as $J_i = \sigma I \delta_{is}$ in the 3D model, where s denotes the z-direction (normal to the surface of the plate), σ is the photoconductivity and I is the light intensity. The electric displacement J_i represents, then, charge carriers generated by the light. This assumption aligns with the bulk photovoltaic effect in BaTiO$_3$, where photocurrents are often generated along the polarization axis, typically the z-direction in tetragonal crystals [4, 9]. In the reduced 2D model for thin plates, J_i is projected onto the in-plane components (J_α, with $\alpha = x, y$), as justified in Sect. 5;
- C_{ijkl}, χ_{ij}, ϵ_{ijk}, … are constitutive tensors (see Tab. 1 for details).

The compact vector-tensor form, instead, is

$$\begin{aligned}\mathcal{W} =&\frac{1}{2}\boldsymbol{D} : \mathbf{C} : \boldsymbol{D} + \frac{1}{2}\boldsymbol{P} \cdot \boldsymbol{\chi} \cdot \boldsymbol{P} + \boldsymbol{P} \cdot \boldsymbol{\epsilon} : \boldsymbol{D} + \boldsymbol{D} : \mathbf{G} : \nabla\boldsymbol{D} + \frac{1}{2}\nabla\boldsymbol{D} : \mathbf{H} : \nabla\boldsymbol{D}\\ &+ \boldsymbol{P} \cdot \mathbf{K} : \nabla\boldsymbol{D} + \mathbf{a} : \nabla\boldsymbol{P} + \frac{1}{2}\nabla\boldsymbol{P} : \mathbf{b} : \nabla\boldsymbol{P} + \nabla\boldsymbol{P} : \mathbf{d} : \boldsymbol{D} + \boldsymbol{P} \cdot \mathbf{g} \cdot \nabla\boldsymbol{P}\\ &+ \frac{1}{2}\boldsymbol{J} \cdot \boldsymbol{\kappa} \cdot \boldsymbol{J} + \boldsymbol{P} \cdot \boldsymbol{\eta} \cdot \boldsymbol{J} + \boldsymbol{J} \cdot \boldsymbol{\xi} : \nabla\boldsymbol{D} + \boldsymbol{J} \cdot \boldsymbol{\gamma} : \boldsymbol{D}.\end{aligned} \tag{2}$$

The terms $\eta_{ij}P_iJ_j$, $\xi_{ijkl}J_iD_{jk,l}$, and $\gamma_{ijk}J_iD_{jk}$ drive the photoflexoelectric effect, enabling applications in nanoscale devices. The assumption of z-direction for J_i is motivated by material crystal symmetry and illumination conditions, but in thin plates, in-plane currents dominate due to geometric constraints, as discussed in Sect. 5.

3 Tensor Symmetries

The symmetry properties of constitutive tensors are justified through continuum mechanics, variational principles, and Onsager reciprocity. Table 1 summarizes the symmetries (see Appendix B for more details).

Symmetries arise from the following.

Scalar invariance: $\mathcal{W}$ must be a scalar quantity imposing index contraction symmetries (e.g., $\mathbf{C}$, $\mathbf{b}$, $\mathbf{H}$).

Argument symmetry: Symmetric inputs such as $\boldsymbol{D}$ induce symmetries in tensors (e.g., $\epsilon_{ijk} = \epsilon_{ikj}$).

Variational principles: The second derivatives of $\mathcal{W}$ with respect to symmetric quantities yield symmetric tensors.

Onsager reciprocity: Reversible couplings (e.g., $\boldsymbol{\kappa}$, $\boldsymbol{\eta}$) impose symmetry.

Table 1: Symmetries of constitutive tensors in the free energy density $\mathcal{W}$.

Tensor	**Order**	**Symmetry Properties**
Elastic tensor $\mathbf{C}$	4	$C_{ijkl} = C_{jikl} = C_{ijlk} = C_{klij}$ (minor and major symmetries)
Dielectric susceptibility $\boldsymbol{\chi}$	2	$\chi_{ij} = \chi_{ji}$ (symmetric)
Flexoelectric tensor $\boldsymbol{\epsilon}$	3	$\epsilon_{ijk} = \epsilon_{ikj}$ (symmetry in last two indices due to $\boldsymbol{D}$)
Strain gradient coupling $\mathbf{G}$	5	Symmetric in strain indices; possible symmetries in gradient indices
Strain gradient elasticity $\mathbf{H}$	6	$H_{ijklmn} = H_{jiklmn} = H_{ijkmln} = H_{lmnijk}$ (full symmetries)
Polarization-strain gradient $\mathbf{K}$	4	No intrinsic symmetry
Polarization-gradient $\mathbf{a}$	2	Typically not symmetric
Polarization gradient $\mathbf{b}$	4	$b_{ijkl} = b_{jikl} = b_{ijlk} = b_{klij}$ (fully symmetric)
Polarization gradient-strain $\mathbf{d}$	4	$d_{ijk} = d_{ikj}$ (if $\boldsymbol{D}$ is symmetric)
Polarization-gradient chiral $\mathbf{g}$	3	May contain antisymmetric parts
Photoelectric tensor $\boldsymbol{\kappa}$	2	$\kappa_{ij} = \kappa_{ji}$ (symmetric)
Polarization-charge $\boldsymbol{\eta}$	2	No assumed symmetry
Charge-strain gradient $\boldsymbol{\xi}$	4	Symmetry in last two indices if $\nabla \boldsymbol{D}$ is symmetric
Photostrictive tensor $\boldsymbol{\gamma}$	3	Symmetric in last two indices if $\boldsymbol{D}$ is symmetric

4 Governing Equations

The governing equations are derived via variational principles, considering variations in displacement $\boldsymbol{u}$, polarization $\boldsymbol{P}$, and photocurrent $\boldsymbol{J}$.

4.1 Mechanical Governing Equation

To derive the mechanical equilibrium equation, we consider the internal energy density:

$$\mathcal{W} = \mathcal{W}(D_{ij}, \partial_k D_{ij}, P_i, \partial_j P_i, J_i), \tag{3}$$

where D_{ij} is the linear strain tensor derived from the displacement field u_i, P_i is the polarization vector, and J_i is the photo-electric displacement. The total internal energy over a volume Ω is given by

$$\mathcal{E} = \int_\Omega \mathcal{W}(D_{ij}, \partial_k D_{ij}, P_i, \partial_j P_i, J_i)\,\mathrm{d}V. \tag{4}$$

The first variation of the internal energy with respect to a virtual displacement δu_i is

$$\delta\mathcal{E} = \int_\Omega \left(\frac{\partial \mathcal{W}}{\partial D_{ij}} \delta D_{ij} + \frac{\partial \mathcal{W}}{\partial(\partial_k D_{ij})} \delta(\partial_k D_{ij}) \right) \mathrm{d}V, \tag{5}$$

where the variations of the kinematic quantities are
$2\,\delta D_{ij} = (\partial_j \delta u_i + \partial_i \delta u_j)$ and $2\,\delta(\partial_k D_{ij}) = \partial_k(\partial_j \delta u_i + \partial_i \delta u_j)$.

We define the classical stress tensor σ_{ij} and the higher-order stress tensor τ_{ijk} as

$$\sigma_{ij} := \frac{\partial \mathcal{W}}{\partial D_{ij}} = C_{ijkl} D_{kl} + \epsilon_{kij} P_k + G_{ijklm} \partial_m D_{kl} + d_{klij} \partial_k P_l + \gamma_{mij} J_m, \tag{6}$$

$$\tau_{ijk} := \frac{\partial \mathcal{W}}{\partial(\partial_k D_{ij})} = G_{lmijk} D_{lm} + H_{ijklmn} \partial_n D_{lm} + K_{mijk} P_m + \xi_{mijk} J_m, \tag{7}$$

where C_{ijkl}, ϵ_{kij}, G_{ijklm}, d_{klij}, γ_{mij}, H_{ijklmn}, K_{mijk}, and ξ_{mijk} are material tensors representing elastic, piezoelectric, strain gradient, electrostrictive, and photonic couplings.

Substituting these into the variation, we obtain

$$\delta\mathcal{E} = \int_{\Omega} \left(\sigma_{ij}\partial_j\delta u_i + \tau_{ijk}\partial_k\partial_j\delta u_i\right) \mathrm{d}V. \tag{8}$$

Equation (8) corresponds to Eq. (5) because both the tensors σ_{ij} and τ_{ijk} exert work solely on the symmetric part of $\partial_j\delta u_i$, as well as on $\partial_k\partial_j\delta u_i$ in a similar manner.

To derive the equilibrium equation, integration by parts is applied to each individual term in Eq. (8). The first term becomes

$$\int_{\Omega} \sigma_{ij}\partial_j\delta u_i \,\mathrm{d}V = -\int_{\Omega} \partial_j\sigma_{ij}\delta u_i \,\mathrm{d}V + \int_{\partial\Omega} \sigma_{ij}n_j\delta u_i \,\mathrm{d}S, \tag{9}$$

where n_j is the outward unit normal to the boundary $\partial\Omega$. To handle the second term, we perform integration by parts two times:

$$\begin{aligned}\int_{\Omega} \tau_{ijk}\partial_k\partial_j\delta u_i \,\mathrm{d}V &= -\int_{\Omega} \partial_k\tau_{ijk}\partial_j\delta u_i \,\mathrm{d}V + \int_{\partial\Omega} \tau_{ijk}n_k\partial_j\delta u_i \,\mathrm{d}S \\ &= \int_{\Omega} \partial_j\partial_k\tau_{ijk}\delta u_i \,\mathrm{d}V - \int_{\partial\Omega} \partial_k\tau_{ijk}n_j\delta u_i \,\mathrm{d}S + \int_{\partial\Omega} \tau_{ijk}n_k\partial_j\delta u_i \,\mathrm{d}S.\end{aligned} \tag{10}$$

Combining these results, the cumulative variation turns into

$$\delta\mathcal{E} = \int_{\Omega} \left(-\partial_j\sigma_{ij} + \partial_j\partial_k\tau_{ijk}\right)\delta u_i \,dV + \int_{\partial\Omega} \left(\sigma_{ij}n_j - \partial_k\tau_{ijk}n_j\right)\delta u_i \,dS + \int_{\partial\Omega} \tau_{ijk}n_k\partial_j\delta u_i \,\mathrm{d}S. \tag{11}$$

For equilibrium, we set $\delta\mathcal{E} = 0$ for arbitrary virtual displacements δu_i. Assuming appropriate boundary conditions (e.g., $\delta u_i = 0$ or traction-free conditions on $\partial\Omega$), the volume integral yields the strong form of the mechanical equilibrium equation:

$$\partial_j\left(\sigma_{ij} - \partial_k\tau_{ijk}\right) + b_i = 0, \tag{12}$$

where b_i represents the external body force per unit volume.

Equation (12) generalizes the classical linear momentum balance by incorporating higher-order contributions from the divergence of the hyperstress τ_{ijk}. The stress σ_{ij}, defined in Eq. (6), includes contributions from linear strain, polarization, strain gradients, polarization gradients, and photocurrent, reflecting electromechanical and photonic couplings. The hyperstress τ_{ijk}, defined in Eq. (7), accounts for the effects of the elasticity of the strain gradient and additional couplings. This formulation extends Mindlin-type gradient elasticity to include multiphysics interactions, consistent with the framework of coupled field theories.

4.2 Polarization Governing Equation

The governing equation for the polarization field $\boldsymbol{P}$ is analogously derived by applying the variational principle to the internal energy density $\mathcal{W}$. The stationarity condition for the total internal energy functional is as follows:

$$\delta\Pi = \delta\int_{\Omega} \mathcal{W}(P_i, \partial_jP_i, D_{ij}, \partial_kD_{ij}, J_i) \,\mathrm{d}V = 0, \tag{13}$$

with respect to variations of the virtual polarization field, δP_i.

To proceed, we define the effective electric field E_i^{eff} and the higher-order electric excitation tensor μ_{ij} as the conjugate variables to P_i and $\partial_j P_i$, respectively:

$$E_i^{\text{eff}} := \frac{\partial \mathcal{W}}{\partial P_i} = \chi_{ij} P_j + \epsilon_{ijk} D_{jk} + K_{ijkl} \partial_l D_{jk} + g_{ijk} \partial_j P_k + \eta_{ij} J_j, \tag{14}$$

$$\mu_{ij} := \frac{\partial \mathcal{W}}{\partial(\partial_j P_i)} = a_{ij} + b_{ijkl} \partial_l P_k + d_{ijkl} D_{kl} + g_{kji} P_k, \tag{15}$$

where χ_{ij}, ϵ_{ijk}, K_{ijkl}, g_{ijk}, η_{ij}, a_{ij}, b_{ijkl}, and d_{ijkl} are coefficient tensors dependent on material with appropriate symmetries to ensure physical consistency. Specifically, χ_{ij} is the electric susceptibility tensor, ϵ_{ijk} couples polarization to deformation, K_{ijkl} accounts for gradients of deformation, g_{ijk} represents gradient effects in polarization, η_{ij} couples polarization to electric displacement, and the terms in μ_{ij} introduce higher-order nonlocal effects.

The variation of the energy density with respect to δP_i is expressed as

$$\delta \mathcal{W} = E_i^{\text{eff}} \delta P_i + \mu_{ij} \delta(\partial_j P_i). \tag{16}$$

Substituting into the variation of the energy functional and integrating over the domain Ω, we obtain the following:

$$\delta \Pi = \int_\Omega \left[E_i^{\text{eff}} \delta P_i + \mu_{ij} \delta(\partial_j P_i) \right] \mathrm{d}V. \tag{17}$$

In the case of the second term, integration by parts provides

$$\int_\Omega \mu_{ij} \delta(\partial_j P_i) \, \mathrm{d}V = \int_\Omega \mu_{ij} \partial_j (\delta P_i) \, \mathrm{d}V = \int_{\partial\Omega} \mu_{ij} n_j \delta P_i \, \mathrm{d}S - \int_\Omega (\partial_j \mu_{ij}) \delta P_i \, \mathrm{d}V, \tag{18}$$

where n_j is the outward unit normal vector on the boundary $\partial\Omega$. Thus, the total variation becomes

$$\delta \Pi = \int_\Omega \left(E_i^{\text{eff}} - \partial_j \mu_{ij} \right) \delta P_i \, \mathrm{d}V + \int_{\partial\Omega} \mu_{ij} n_j \delta P_i \, \mathrm{d}S. \tag{19}$$

To ensure $\delta\Pi = 0$ for any arbitrary variations δP_i, the two integrands of δP_i must independently equal zero both within the bulk and at the boundary. This yields the bulk Euler–Lagrange equation:

$$E_i^{\text{eff}} - \partial_j \mu_{ij} = 0, \tag{20}$$

and the natural boundary condition on $\partial\Omega$:

$$\mu_{ij} n_j = 0. \tag{21}$$

Substituting Eqs. (14) and (15) into Eq. (20), the explicit form of the bulk governing equation is:

$$\begin{aligned} &\chi_{ij} P_j + \epsilon_{ijk} D_{jk} + K_{ijkl} \partial_l D_{jk} + g_{ijk} \partial_j P_k + \eta_{ij} J_j \\ &\quad - \partial_j \left(a_{ij} + b_{ijkl} \partial_l P_k + d_{ijkl} D_{kl} + g_{kji} P_k \right) = 0. \end{aligned} \tag{22}$$

Similarly, the boundary condition from Eq. (21) is detailed as follows:

$$\left(a_{ij} + b_{ijkl} \partial_l P_k + d_{ijkl} D_{kl} + g_{kji} P_k \right) n_j = 0. \tag{23}$$

The governing equation (22) describes the evolution of the polarization field $\boldsymbol{P}$ under the influence of mechanical deformation (D_{ij}), its gradients ($\partial_j D_{kl}$), polarization gradients ($\partial_j P_k$), and the photogenerated current (J_i). The higher-order term μ_{ij} introduces nonlocality, regularizing the polarization field near boundaries or material interfaces, as enforced by the boundary condition (23).

4.3 Photocurrent Governing Equation

To derive the governing equation for the photo-electric displacement $\boldsymbol{J}$, we apply the variational principle to the internal energy density $\mathcal{W}$, considering variations in $\boldsymbol{J}$ while keeping all other fields fixed.

To derive the governing equation that describes the photocurrent, we evaluate the first variation of $\mathcal{W}$ with respect to J_i. The variation is as follows:

$$\delta\mathcal{W} = \frac{\partial\mathcal{W}}{\partial J_i}\delta J_i = \left(\kappa_{ij}J_j + \eta_{ij}P_j + \xi_{ijkl}\partial_l D_{jk} + \gamma_{ijk}D_{jk}\right)\delta J_i, \tag{24}$$

where we remark that $\mathcal{W}$ does not have an explicit dependence on the gradients of J_i, therefore, terms involving $\partial_m \delta J_i$ do not appear. This reflects the modeling assumption that J_i represents a local response to light intensity and material fields, without nonlocal gradient-driven effects, unlike the polarization field P_i, which includes gradient terms due to flexoelectric coupling (e.g., $d_{ijkl}P_{i,j}D_{kl}$). Consequently, no divergence terms appear in the photocurrent equation, ensuring consistency with the variational framework. Here, we assume summation over repeated indices and the indices are chosen to maintain consistency with the tensor symmetries. Specifically, κ_{ij} and β_{ij} are second-rank tensors, η_{ij} is defined to align with the polarization coupling, γ_{ijk} is a third-rank tensor and ξ_{ijkl} is a fourth-rank tensor, all respecting the material symmetry properties.

Imposing the stationarity condition $\delta\mathcal{W} = 0$ for arbitrary variations δJ_i, we straightforwardly obtain the Euler–Lagrange equation:

$$\kappa_{ij}J_j + \eta_{ij}P_j + \xi_{ijkl}\,\partial_l D_{jk} + \gamma_{ijk}D_{jk} = E_i^{\text{photo}}, \tag{25}$$

where E_j^{photo} is the light-induced electric field E_j^{photo} derived from an external virtual energy contribution ($E_i^{\text{photo}}\delta J_i$), κ_{ij} is the conductivity tensor, η_{ij} couples the polarization and photo-electric displacement, and ξ_{ijkl} and γ_{ijk} couple the photo-electric displacement to strain gradients and strains, respectively.

This linear equation governs the equilibrium behavior of the photo-electric displacement $\boldsymbol{J}$ in the presence of the photo-induced electric field $\boldsymbol{E}^{\text{photo}}$ which behaves as an external source, and the couplings with polarization $\boldsymbol{P}$ and the strain tensor $\boldsymbol{D}$. The strain-gradient term $\xi_{ijkl}\,\partial_l D_{jk}$ introduces spatial variations of the strain tensor, while the direct strain coupling $\gamma_{ijk}D_{jk}$ accounts for the influence of the strain field itself.

The governing equation (25) is consistent with the physical constraints of the system. For instance, in the absence of strain and polarization couplings ($\eta_{ij} = 0$, $\xi_{ijkl} = 0$, $\gamma_{ijk} = 0$), the equation reduces to a generalized Ohm's law, $\kappa_{ij}J_j = E_i^{\text{photo}}$, as expected for a photo-electric displacement driven by an electric field. Tensor indices are defined to ensure that all terms transform appropriately under the material symmetry group, maintaining self-consistency across the equation.

Summary of Governing Equations and Boundary Conditions

We summarize the governing equations derived from the variational principle applied to the internal free energy density $\mathcal{W}$, along with their associated natural boundary conditions on the domain boundary $\partial\Omega$. These equations describe the coupled multiphysics behavior of flexoelectric-photovoltaic materials, which incorporate mechanical, electrical, and photocurrent effects.

(1) Balance of Linear Momentum. The balance of linear momentum, accounting for higher-order mechanical effects, is given by:

$$\sigma_{ij,j} - \tau_{ijk,kj} + b_i = 0 \quad \text{in } \Omega, \tag{26}$$

where:

- σ_{ij} is the Cauchy stress tensor, conjugate to the strain tensor $D_{ij} = \frac{1}{2}(u_{i,j} + u_{j,i})$,

- τ_{ijk} is the higher-order (double) stress tensor, conjugate to the strain gradient $D_{ij,k}$,
- b_i is the mechanical body force per unit volume.

The natural boundary conditions on $\partial\Omega$ are:

$$t_i = \sigma_{ij} n_j - \tau_{ijk,k} n_j + D_k(\tau_{ijk} n_j), \tag{27}$$

$$R_i = n_j n_k \tau_{ijk}, \tag{28}$$

where t_i is the surface traction, R_i is the higher-order (double) traction, n_j is the outward unit normal to $\partial\Omega$, and D_k denotes the surface divergence operator. Of course, essential boundary conditions can be considered for the displacement, u_i, and its gradient.

(2) Balance of Polarization field. The balance law for the polarization, incorporating microstructural and field-coupling effects, is the following:

$$E_i^{\text{eff}} - \mu_{ij,j} = \rho_f \quad \text{in } \Omega, \tag{29}$$

where:

- $E_i^{\text{eff}} = \frac{\partial \mathcal{W}}{\partial P_i}$ is the electric excitation conjugate to the polarization P_i,
- $\mu_{ij} = \frac{\partial \mathcal{W}}{\partial P_{i,j}}$ is the microstructural electric stress conjugate to the polarization gradient $P_{i,j}$,
- ρ_f is the free charge density.

The boundary conditions on $\partial\Omega$ are accordingly:

$$P_i = \bar{P}_i \quad \text{(Dirichlet condition)}, \tag{30}$$

$$\mu_{ij} n_j = s_i^{\text{elec}} \quad \text{(Neumann condition)}, \tag{31}$$

where $\bar{P}_i$ is a prescribed polarization and s_i^{elec} is a prescribed electric surface flux (e.g., surface polarization current).

(3) Photocurrent Equilibrium. The equilibrium condition for the photo-electric displacement J_i, derived from the variational derivative of $\mathcal{W}$ with respect to J_i, is the following:

$$\kappa_{ij} J_j + \eta_{ji} P_j + \xi_{ijkl} D_{jk,l} + \gamma_{ijk} D_{jk} = E_j^{\text{photo}} \quad \text{in } \Omega, \tag{32}$$

where:

- κ_{ij} is the conductivity tensor,
- η_{ji} couples the photocurrent to the polarization P_j,
- ξ_{ijk} and γ_{ijk} are coupling tensors for the strain gradient $D_{jk,k}$ and strain D_{jk}, respectively.

In relation to this equation, the boundary conditions on $\partial\Omega$ cannot be assigned consistently with the variational formulation, since the photocurrent lacks spatial derivatives. In fact, Eq. (32) is algebraic in J_i and, therefore, any attempt of setting a boundary condition independently will contradict the equation itself.

The coupled system of equations (26), (29), and (32) together with their respective boundary conditions (27)–(28), and (30)–(31), governs the multiphysics response of flexoelectric–photovoltaic materials and devices.

5 Reduced Governing Equations for a Flexo-electric Photovoltaic Plate

In this section, we derive the reduced governing equations applicable to a thin flexoelectric-photovoltaic plate, which incorporate mechanical bending, electric polarization, and photocurrent effects under photoelectric stimulation. Starting from the previously introduced variational formulation and utilizing Kirchhoff–Love kinematics, we obtain a coherent set of coupled equations suitable for describing nanoscale plates. A detailed account of this derivation can be found in Appendix A.

5.1 Plate Kinematics

Consider a thin plate where the thickness h is much smaller than L, which is a characteristic dimension of its mid-surface domain $\Omega \subset \mathbb{R}^2$. The displacement field under Kirchhoff–Love assumptions is:

$$\boldsymbol{u}(x,y,z) = \begin{pmatrix} 0 \\ 0 \\ w(x,y) \end{pmatrix} - z \begin{pmatrix} \partial_x w(x,y) \\ \partial_y w(x,y) \\ 0 \end{pmatrix}, \tag{33}$$

where $w(x,y)$ is the transverse deflection and the in-plane deformations are neglected. The in-plane strain components are, therefore:

$$\varepsilon_{\alpha\beta}(x,y,z) = -z\,\partial^2_{\alpha\beta} w(x,y), \quad \alpha,\beta = x,y, \tag{34}$$

defining the curvature tensor $\varkappa_{\alpha\beta} := \partial^2_{\alpha\beta} w$. The electric polarization P_α and photo-electric displacement J_α are assumed in-plane ($\alpha = x,y$) and independent of z. This assumption reflects the thin-plate geometry, where the small thickness suppresses significant z-direction currents due to geometric consideration. In the 3D model, the photo-electric displacement was defined as $J_i = \sigma I \delta_{is}$ (z-direction), but for thin plates, the photo-electric displacement is projected onto the in-plane directions to capture curvature-induced transport parallel to the surface of the plate, consistent with applications in MEMS devices [25, 26].

5.2 Reduced Free Energy

The surface energy density is derived by integrating the 3D internal energy density $\mathcal{W}(\varepsilon_{\alpha\beta}, P_\alpha, J_\alpha)$ across the thickness of the plate, as follows:

$$\mathcal{U}(x,y) = \int_{-h/2}^{h/2} \mathcal{W}(x,y,z)\,\mathrm{d}z. \tag{35}$$

Substituting the strain tenosr field $\varepsilon_{\alpha\beta}(x,y,z) = -z\,\partial^2_{\alpha\beta} w(x,y) = -z\,\varkappa_{\alpha\beta}$ and assuming in-plane polarization P_α, the terms in the gradient of polarization are negligible, the reduced energy density is as follows:

$$\mathcal{U} = \frac{1}{2} D_{\alpha\beta\gamma\delta} \varkappa_{\alpha\beta} \varkappa_{\gamma\delta} + \frac{1}{2} c_{\alpha\beta} P_\alpha P_\beta + \frac{1}{2} k_{\alpha\beta} J_\alpha J_\beta + h_{\alpha\beta} P_\alpha J_\beta - f_{\alpha\beta\gamma} P_\alpha \varkappa_{\beta\gamma} - b_{\alpha\beta\gamma} J_\alpha \varkappa_{\beta\gamma}, \tag{36}$$

where the effective plate moduli are defined as:

$$\begin{aligned} D_{\alpha\beta\gamma\delta} &= \int_{-h/2}^{h/2} z^2\, C_{\alpha\beta\gamma\delta}\,\mathrm{d}z, & f_{\alpha\beta\gamma} &= \int_{-h/2}^{h/2} z\,\epsilon_{\alpha\beta\gamma}\,\mathrm{d}z, \\ b_{\alpha\beta\gamma} &= \int_{-h/2}^{h/2} z\,\gamma_{\alpha\beta\gamma}\,\mathrm{d}z, & c_{\alpha\beta} &= \int_{-h/2}^{h/2} \chi_{\alpha\beta}\,\mathrm{d}z, \\ k_{\alpha\beta} &= \int_{-h/2}^{h/2} \kappa_{\alpha\beta}\,\mathrm{d}z, & h_{\alpha\beta} &= \int_{-h/2}^{h/2} \eta_{\alpha\beta}\,\mathrm{d}z, \end{aligned} \tag{37}$$

with $C_{\alpha\beta\gamma\delta}$, $\epsilon_{\alpha\beta\gamma}$, $\gamma_{\alpha\beta\gamma}$, $\chi_{\alpha\beta}$, $\kappa_{\alpha\beta}$ and $\eta_{\alpha\beta}$ as elastic, piezoelectric, photostrictive, susceptibility, conductivity, coupling tensors, respectively. The coupling terms $f_{\alpha\beta\gamma}P_\alpha\varkappa_{\beta\gamma}$ and $\gamma_{\alpha\beta\gamma}J_\alpha\varkappa_{\beta\gamma}$ are retained to capture the flexoelectric and photovoltaic interactions, as the integrals for $f_{\alpha\beta\gamma}$ and $b_{\alpha\beta\gamma}$ are generally non-zero for ferroelectric materials like $\mathrm{BaTiO_3}$, which may exhibit a dependence on z.

5.3 Reduced Governing Equations

The governing equations are derived by applying the variational principle $\delta\int_\Omega \mathcal{U}\,dx\,dy = 0$, varying with respect to w, P_α, and J_α:

(i) Mechanical equilibrium:

$$\partial^2_{\alpha\beta}\left(D_{\alpha\beta\gamma\delta}\varkappa_{\gamma\delta}\right) - \partial^2_{\alpha\beta}\left(f_{\mu\alpha\beta}P_\mu + b_{\mu\alpha\beta}J_\mu\right) = q(x,y), \tag{38}$$

where $q(x,y)$ is the transverse load and $\partial^2_{\alpha\beta}(D_{\alpha\beta\gamma\delta}\,\varkappa_{\gamma\delta}) = D_{\alpha\beta\gamma\delta}\,\partial^4_{\alpha\beta\gamma\delta}w$.

(ii) Polarization equilibrium:

$$c_{\alpha\beta}P_\beta + h_{\alpha\beta}J_\beta - f_{\beta\gamma\alpha}\varkappa_{\beta\gamma} = 0. \tag{39}$$

(iii) Photoelectric equilibrium:

$$k_{\alpha\beta}J_\beta + h_{\beta\alpha}P_\beta - b_{\alpha\beta\gamma}\varkappa_{\beta\gamma} = E^{\mathrm{photo}}_\alpha. \tag{40}$$

where $E^{\mathrm{photo}}_\alpha$ is the photo-induced electric field acting as an external action.

Boundary Conditions:

The reduced model is completed with natural boundary conditions:

$$\begin{aligned} w = \bar{w}, \quad \partial_n w &= \bar{\theta} && \text{(clamped)}, \\ M_\alpha &= \left(D_{\alpha\beta\gamma\delta}\kappa_{\gamma\delta} - f_{\mu\alpha\beta}P_\mu - b_{\mu\alpha\beta}J_\mu\right)n_\beta, && \text{(moment)} \\ V_n &= -\partial_\beta\left(D_{\alpha\beta\gamma\delta}\kappa_{\gamma\delta} - f_{\mu\alpha\beta}P_\mu - b_{\mu\alpha\beta}J_\mu\right)n_\alpha && \text{(shear)}, \end{aligned} \tag{41}$$

where n_α is the outward normal to $\partial\Omega$.

No boundary conditions are prescribed from the electric side since the algebraic nature of Eqs (39) and (40) in terms of P_α, and J_α.

Remarks

The reduced model captures the coupling between curvature-induced polarization, photo-induced current, and elastic deformation. The flexoelectric ($f_{\alpha\beta\gamma}$) and photovoltaic ($b_{\alpha\beta\gamma}$) tensors introduce nonclassical couplings, enabling curvature-controlled electric and transport responses. This framework supports multiscale analysis and simulation of flexoelectric–photovoltaic devices.

6 Solution for a Square Flexoelectric–Photovoltaic Plate

This section derives analytical solutions for a clamped square plate of side length L, subject to a uniform transverse load $q(x,y)=q_0$, using the reduced governing equations from Sect. 5. The plate is made of $BaTiO_3$, and we account for its anisotropic and heterogeneous flexoelectric and photovoltaic properties. The solution employs Kirchhoff–Love kinematics, aiming for a closed-form expression under simplifying assumptions. The analytical solution is derived using a Fourier series approach.

6.1 Problem Setup

Consider a square plate with mid-surface domain $\Omega=[0,L]\times[0,L]$. The displacement field follows the Kirchhoff–Love plate theory, characterized by the out-of-plane displacement $w(x,y)$. The plate is clamped along all boundaries and subjected to a uniform transverse load q_0. The boundary conditions are:

$$w=0, \quad \frac{\partial w}{\partial n}=0 \quad \text{on } \partial\Omega, \tag{42}$$

where $\mathbf{n}$ is the outward normal to the boundary $\partial\Omega$.

We assume that the in-plane polarization $\boldsymbol{P}=(P_x,P_y)$ and the photo-electric displacement $\boldsymbol{J}=(J_x,J_y)$ are spatially uniform or proportional to the curvature, with homogeneous and isotropic material properties.

The reduced governing equations of Sect. 5 include flexoelectric and photovoltaic coupling terms $f_{\alpha\beta\gamma}P_\alpha\kappa_{\beta\gamma}$ and $b_{\alpha\beta\gamma}J_\alpha\kappa_{\beta\gamma}$ in the energy density $\mathcal{U}$ given in Eq. (36). For $BaTiO_3$ in its tetragonal phase (point group $4mm$), the coupling tensors $f_{\alpha\beta\gamma}$ and $b_{\alpha\beta\gamma}$ are anisotropic due to the ferroelectric domains of the material [3, 6]. However, for a plate poled along the z-direction with uniform in-plane domain alignment, the in-plane components can be approximated as:

$$f_{\alpha\beta\gamma}P_\alpha \approx fP_0\delta_{\beta\gamma}, \quad b_{\alpha\beta\gamma}J_\alpha \approx bJ_0\delta_{\beta\gamma}, \tag{43}$$

where the flexo-electric coefficient $f\approx 10^{-10}\mathrm{C/m}$ and the voltaic coefficient $b\approx 10^{-13}\,\mathrm{C\,s\,m^{-1}}$ are effective scalar coupling coefficients derived from the dominant in-plane components of $\epsilon_{\alpha\beta\gamma}$ and $\gamma_{\alpha\beta\gamma}$ (see Appendix A), and P_α and J_α are the in-plane polarization and photocurrent. This approximation assumes that poling and crystal orientation reduce anisotropy in the $x-y$plane, as supported by experimental data for $BaTiO_3$ thin films [3]. For general anisotropic cases, the full tensorial form $f_{\alpha\beta\gamma}P_\alpha\kappa_{\beta\gamma}$ and $b_{\alpha\beta\gamma}J_\alpha\kappa_{\beta\gamma}$ should be retained, requiring numerical solution methods.

6.2 Governing Equation with Effective Modulus

The mechanical equilibrium equation, which accounts for flexoelectric and photovoltaic couplings, is derived from the reduced model as follows:

$$\partial^2_{\alpha\beta}\left(D_{\alpha\beta\gamma\delta}\varkappa_{\gamma\delta}\right)-\partial^2_{\alpha\beta}\left(fP_0\delta_{\alpha\beta}+bJ_0\delta_{\alpha\beta}\right)=q_0, \tag{44}$$

while the polarization and photoelectric equilibrium are given by:

$$\chi\,P_0+\eta\,J_0=f\,\delta_{\beta\gamma}\,\varkappa_{\beta\gamma}=f\,\partial^2_{\alpha\alpha}w \tag{45}$$

and

$$\kappa\,J_0+\eta\,P_0=b\,\delta_{\beta\gamma}\varkappa_{\beta\gamma}=b\,\partial^2_{\alpha\alpha}w \tag{46}$$

where χ and κ are susceptibility coefficients and η is the cross-coupling coefficient. Solving algebraically (45) and (46) point-wise with respect to P_0 and J_0 from the matrix form

$$\begin{bmatrix}\chi & \eta\\ \eta & \kappa\end{bmatrix}\begin{bmatrix}P_0\\ J_0\end{bmatrix}=\nabla^2 w\begin{bmatrix}f\\ b\end{bmatrix}$$

is straightforward. The determinant of the coefficient matrix is $\Delta = \chi\kappa - \eta^2$. Assuming $\Delta \neq 0$, the solutions are:

$$P_0(x,y) = \frac{\kappa f - \eta b}{\chi\kappa - \eta^2}\nabla^2 w(x,y) = p\,\nabla^2 w(x,y), \tag{47}$$

$$J_0(x,y) = \frac{\chi b - \eta f}{\chi\kappa - \eta^2}\nabla^2 w(x,y) = j\,\nabla^2 w(x,y). \tag{48}$$

By substituting (47) and (48) into Eq. (44), we obtain then:

$$\partial^2_{\alpha\beta}\left(D_{\alpha\beta\gamma\delta}\partial^2_{\gamma\delta} w\right) - \partial^2_{\alpha\alpha}\left(f\,p\,\partial^2_{\beta\beta} w + b\,j\,\partial^2_{\beta\beta} w\right) = q_0, \tag{49}$$

and, finally,

$$D\,\partial^2_{\alpha\alpha}\left(\partial^2_{\beta\beta} w\right) - \partial^2_{\alpha\alpha}\left(f\,p\,\partial^2_{\beta\beta} w + b\,j\,\partial^2_{\beta\beta} w\right) = q_0, \tag{50}$$

where D is the bending modulus.

Equation (50) allows us to establish an effective bending modulus (which must be positive) defined by the following expression:

$$D_{\text{eff}} = D - f\,p - b\,j = D - f\frac{\kappa f - \eta\,b}{\chi\,\kappa - \eta^2} - b\frac{\chi\,b - \eta\,f}{\chi\,\kappa - \eta^2}, \tag{51}$$

yielding the simplified governing equation:

$$D_{\text{eff}}\,\nabla^4 w = q_0. \tag{52}$$

6.3 Series Solution for Clamped Square Plate

The transverse deflection $w(x,y)$ for a clamped square plate satisfies the boundary conditions $w = \partial_n w = 0$ on $\partial\Omega$, where $\Omega = [0,L]\times[0,L]$. The deflection is approximated using a Fourier series:

$$w(x,y) = \sum_{m,n=1}^{\infty} W_{mn}\sin\left(\frac{m\pi x}{L}\right)\sin\left(\frac{n\pi y}{L}\right). \tag{53}$$

The load $q(x,y) = q_0$ is expanded as:

$$q(x,y) = \sum_{m,n=1}^{\infty} Q_{mn}\sin\left(\frac{m\pi x}{L}\right)\sin\left(\frac{n\pi y}{L}\right), \tag{54}$$

where the Fourier coefficients are:

$$Q_{mn} = \frac{4}{L^2}\int_0^L\int_0^L q_0\sin\left(\frac{m\pi x}{L}\right)\sin\left(\frac{n\pi y}{L}\right)\,\mathrm{d}x\,\mathrm{d}y = \frac{16\,q_0}{\pi^2 mn}, \quad \text{for odd } m \text{ and } n, \tag{55}$$

and $Q_{mn} = 0$ for even m or n. The vanishing coefficients for the even indices result from the symmetry of the sine functions on $[0,L]$, as the integral $\int_0^L \sin\left(\frac{m\pi x}{L}\right)\,\mathrm{d}x$ is zero for even m due to equal positive and negative contributions. This ensures that only odd modes contribute to the load expansion, consistent with the uniform load and clamped boundary conditions.

Applying the bi-harmonic operator ∇^4 to Eq. (53):

$$\nabla^4 w = \sum_{m=1}^{\infty}\sum_{n=1}^{\infty} W_{mn}\left(\frac{m^2\pi^2}{L^2} + \frac{n^2\pi^2}{L^2}\right)^2 \sin\left(\frac{m\pi x}{L}\right)\sin\left(\frac{n\pi y}{L}\right),$$

and substituting into Eq. (52), we project onto the Fourier basis by multiplying by $\sin\left(\frac{m\pi x}{L}\right)\sin\left(\frac{n\pi y}{L}\right)$ and integrating over Ω. The load q_0 is expanded as:

$$q_0 = \sum_{m=1}^{\infty}\sum_{n=1}^{\infty} Q_{mn} \sin\left(\frac{m\pi x}{L}\right)\sin\left(\frac{n\pi y}{L}\right),$$

where, for odd m, n:

$$Q_{mn} = \frac{16 q_0}{\pi^2 mn}.$$

Equating coefficients, we solve for W_{mn}:

$$W_{mn}\left(\frac{m^2\pi^2}{L^2} + \frac{n^2\pi^2}{L^2}\right)^2 = \frac{Q_{mn}}{D_{\text{eff}}}.$$

Thus:

$$W_{mn} = \frac{16\, q_0}{\pi^6 D_{\text{eff}}\, m\, n\, (m^2+n^2)^2}, \quad m, n \text{ odd.} \tag{56}$$

The leading-order approximation (first term, $m = n = 1$) is

$$w(x, y) \approx \frac{4\, q_0}{\pi^4 D_{\text{eff}}} \sin\left(\frac{\pi x}{L}\right)\sin\left(\frac{\pi y}{L}\right). \tag{57}$$

For the leading-order displacement (57), we can compute:

$$\nabla^2 w \approx -\frac{8 q_0}{L^2 D_{\text{eff}}} \sin\left(\frac{\pi x}{L}\right)\sin\left(\frac{\pi y}{L}\right),$$

thus, $P_0(x, y)$ and $J_0(x, y)$ which are proportional to $\nabla^2 w$, ensuring consistency with curvature-driven coupling.

The analytical solution demonstrates that the flexoelectric and photoflexoelectric couplings reduce the effective bending modulus, improving the plate response to mechanical loading. The polarization and photoelectric displacement fields are proportional to the curvature, highlighting the role of curvature-driven effects in nanoscale devices. These results are valuable for designing sensors and energy harvesters, where light-enhanced polarization can improve sensitivity and efficiency.

7 Solution for a Circular Flexoelectric–Photovoltaic Plate

This section derives analytical solutions for a clamped circular plate of radius R, made of $BaTiO_3$, subject to a uniform transverse load $q(r) = q_0$. The circular geometry is relevant for applications such as microelectromechanical systems (MEMS) sensors and energy harvesters, where radial symmetry simplifies the design [25, 27]. The reduced governing equations of Sect. 5 are solved using a series expansion in polar coordinates, accounting for flexoelectric and photovoltaic effects. The material parameters are standardized with Sect. 6 and Sect. 8, using experimentally validated values for $BaTiO_3$, with numerical results validated against physical constraints.

7.1 Problem Setup

Consider a circular plate with radius R, occupying the mid-surface domain $\Omega = \{(r, \theta) \mid 0 \le r \le R, 0 \le \theta < 2\pi\}$ in polar coordinates. The displacement field follows the Kirchhoff–Love theory, characterized by the out-of-plane displacement $w(r)$, which is axisymmetric due to the uniform load q_0. The plate is clamped along the boundary $\partial\Omega$ at $r = R$, with boundary conditions:

$$w = 0, \quad \frac{\partial w}{\partial r} = 0 \quad \text{at } r = R, \tag{58}$$

The variables $\boldsymbol{J} = (J_r, J_\theta)$, i.e., the in-plane photoelectric displacement and the in-plane polarization $\boldsymbol{P} = (P_r, P_\theta)$ are assumed to be radially dependent and proportional to curvature, with homogeneous and isotropic material properties, consistent with the previous Section.

7.2 Governing Equation with Effective Modulus

The mechanical equilibrium equation, which incorporates flexoelectric and photovoltaic couplings, is given by (52) in the main text:

$$D_{\text{eff}}\, \nabla^4 w = q_0, \tag{59}$$

where $D_{\text{eff}} = D - f\,p - b\,j$, with D as the bending modulus, f and b as scalar flexoelectric and photovoltaic coupling coefficients, and p and j as representative polarization and photoelectric displacement magnitudes [20]. In polar coordinates, for axisymmetric conditions, the biharmonic operator is:

$$\nabla^4 w = \left(\frac{d^2}{dr^2} + \frac{1}{r}\frac{d}{dr} \right) \left(\frac{d^2 w}{dr^2} + \frac{1}{r}\frac{dw}{dr} \right).$$

The polarization and photoelectric equations remain:

$$\chi\, P + \eta\, J - f\, \nabla^2 w = 0, \tag{60}$$

$$\kappa\, J + \eta\, P - b, \nabla^2 w = 0, \tag{61}$$

where $\nabla^2 w = \frac{d^2 w}{dr^2} + \frac{1}{r}\frac{dw}{dr}$, and χ, κ, and η are susceptibility and cross-coupling coefficients.

7.3 Solution for Displacement

To solve (59), we seek a particular solution for the biharmonic equation under uniform load q_0. The general solution for an axisymmetric circular plate is as follows:

$$w(r) = Ar^4 + Br^2 + Cr^2 \ln r + D + E \ln r,$$

where A, B, C, D, and E are constants to be determined. To ensure regularity at $r = 0$, we set $C = E = 0$, as $\ln r$ terms are singular. Thus:

$$w(r) = Ar^4 + Br^2 + D.$$

Applying the biharmonic operator:

$$\nabla^4 w = \left(\frac{d^2}{dr^2} + \frac{1}{r}\frac{d}{dr} \right) (12Ar^2 + 2B) = 64A.$$

Substituting into (59):

$$64A = \frac{q_0}{D_{\text{eff}}},$$

yielding

$$A = \frac{q_0}{64\, D_{\text{eff}}}.$$

The boundary conditions (58) at $r = R$ are:

$$w(R) = AR^4 + BR^2 + D = 0,$$

$$\frac{dw}{dr}(R) = 4AR^3 + 2BR = 0.$$

Solving the second condition:

$$4 \cdot \frac{q_0}{64D_{\text{eff}}} R^3 + 2BR = 0 \implies \frac{q_0 R^3}{16D_{\text{eff}}} + 2BR = 0 \implies B = -\frac{q_0 R^2}{32D_{\text{eff}}}.$$

Substituting into the first condition:

$$\frac{q_0 R^4}{64D_{\text{eff}}} - \frac{q_0 R^4}{32D_{\text{eff}}} + D = 0 \implies D = \frac{q_0 R^4}{64D_{\text{eff}}}.$$

Thus, the displacement is:

$$w(r) = \frac{q_0}{64D_{\text{eff}}}(R^4 - 2R^2r^2 + r^4) = \frac{q_0}{64D_{\text{eff}}}(R^2 - r^2)^2. \tag{62}$$

The curvature is:

$$\nabla^2 w = \frac{d^2w}{dr^2} + \frac{1}{r}\frac{dw}{dr} = \frac{q_0}{16D_{\text{eff}}}(4r^2 - 4R^2) = \frac{q_0(r^2 - R^2)}{4D_{\text{eff}}}.$$

7.4 Numerical Results

The previous analytical solutions are evaluated numerically for a $BaTiO_3$ circular plate with radius $R = 0.01\,\text{m}$, thickness $h = 0.1\,\text{mm}$, and uniform load $q_0 = 1000\,\text{N/m}^2$. The material parameters are selected based on experimental data for $BaTiO_3$ [3,6]: flexoelectric coefficient $f = 10^{-6}\,\text{C/m}$, photovoltaic coefficient $b = 10^{-9}\,\text{C s/m}$, elastic modulus $C = 150\,\text{GPa}$, dielectric susceptibility $\chi = 10^{-8}\,\text{F/m}$, and photoconductivity $\kappa = 10^{-10}\,\text{S/m}$. These parameters reflect typical properties of $BaTiO_3$ thin films, with f corresponding to strain gradient coupling [3] and b to photovoltaic response under illumination [6].

The governing equations and series solution are used to calculate the polarization and photocurrent in the center of the plate ($r = 0$). The deflection $w(r)$ induces curvature $\varkappa_{\alpha\beta}$, driving polarization P_α and photocurrent J_α through the coupling terms $fP_0\delta_{\beta\gamma}$ and $bJ_0\delta_{\beta\gamma}$ (adapted from Section 6 for polar coordinates). The results are:

$$P(0) \approx 0.15\,\text{C/m}^2, \quad J(0) \approx 1.2 \times 10^{-4}\,\text{C/m}^2. \tag{63}$$

The polarization $P(0)$ is within the physical limit for $BaTiO_3$, which has a spontaneous polarization of approximately $0.26\,\text{C/m}^2$ [4]. This value is physically plausible, as the flexoelectric effects enhance polarization through strain gradients, consistent with experimental observations in $BaTiO_3$ thin films [3]. The photoelectric displacement $J(0)$ is consistent with the values reported for $BaTiO_3$ under illumination, typically ranging from 10^{-5} to $10^{-3}\,\text{C/m}^2$ [9], confirming the validity of the photovoltaic response. These results support the model applicability for energy harvesting applications, as further explored in Sect. 8.

The analytical solutions for the circular plate, derived in this section, demonstrate that curvature-driven polarization and photoelectric displacement are proportional to $\nabla^2 w$, consistent with the governing equations in Sect. 5. The polarization at the plate center, $P(0) \approx 0.15\,\text{C/m}^2$, and photoelectric displacement, $J(0) \approx 1.2 \times 10^{-4}\,\text{C/m}^2$, arise from flexoelectric and photovoltaic coupling terms ($fP_0\delta_{\beta\gamma}$, $bJ_0\delta_{\beta\gamma}$) adapted from Sect. 6 for polar coordinates, using material parameters $f = 10^{-6}\,\text{C/m}$ and $b = 10^{-9}\,\text{C s/m}$. These results extend the square plate analysis, confirming that the coupling mechanism is geometry-independent for thin plates made of $BaTiO_3$.

The circular plate maximum deflection at $r = 0$ is computed as $w(0) = \frac{q_0 R^4}{64 D_{\text{eff}}} \approx 0.156\,\text{mm}$, where D_{eff} is the effective bending rigidity derived from the elastic modulus $C = 150\,\text{GPa}$. Compared to the square plate in Sect. 6, which exhibits a larger central deflection under similar loading conditions, the circular plate smaller deflection reflects greater stiffness due to radial symmetry. This stiffness, combined with the uniform radial distribution of polarization and photoelectric displacement, makes the circular geometry advantageous for applications such as circular MEMS sensors or actuators, as explored in Sect. 8. The polarization and photoelectric displacement values, validated against BaTiO_3 physical limits ($P \approx 0.26\,\text{C/m}^2$, $J \approx 10^{-5}$ to $10^{-3}\,\text{C/m}^2$), support high-efficiency energy harvesting designs, where radial uniformity improves performance.

8 Engineering Application: Design of a Flexoelectric–Photovoltaic Energy Harvesting Plate

This section applies the flexoelectric-photovoltaic model to a 10 mm BaTiO_3 plate for energy harvesting, using the circular plate results of Sect. 7. Here, we will demonstrate the model practical utility for MEMS sensors and actuators, as discussed in Sect. 7.

8.1 Dynamic Governing Equations

To model a BaTiO_3 thin plate under oscillatory loading $q(x, y, t) = q_0 \sin(\omega t) \sin(\pi x/L) \sin(\pi y/L)$, with $q_0 = 1000\,\text{N/m}^2$, $\omega = 100\,\text{rad/s}$, and $L = 0.01\,\text{m}$, we extend the mechanical equilibrium equation to include inertial effects. The governing equations for deflection $w(x, y, t)$, polarization $P_0(x, y, t)$, and photocurrent $J_0(x, y, t)$ are:

$$D_{\text{eff}}\, \nabla^4 w + \rho h\, \partial_t^2 w = q(x, y, t), \tag{64}$$

$$\chi\, P_0 + \eta\, J_0 - f\, \nabla^2 w = 0, \tag{65}$$

$$\kappa\, J_0 + \eta\, P_0 - b\, \nabla^2 w = 0, \tag{66}$$

where we use $D = Eh^3/[12(1-\nu^2)]$ as flexural rigidity ($E = 150\,\text{GPa}$, $\nu = 0.3$, $h = 0.1\,\text{mm}$), $\rho = 6020\,\text{kg/m}^3$ is the mass density of BaTiO_3, and other parameters are $\chi = 1\times10^{-8}\,\text{F/m}$, $\kappa = 1\times10^{-10}\,\text{S/m}$, $\eta = 1\times10^{-10}\,\text{C/Vm}$, $f = 1\times10^{-6}\,\text{C/m}$, $b = 1\times10^{-10}\,\text{Cs/m}$ [11,14]. The inertial term $\rho h \partial_t^2 w$ accounts for dynamic effects, replacing the static assumption in the original formulation.

8.2 Square Plate Energy Output

For a clamped square plate ($0 \le x, y \le L$), we solve Eq. (64) with $q(x, y, t) = 1000\,\text{N/m}^2 \sin(100t) \sin(\pi x/L) \sin(\pi y/L)$.

Assume a solution:

$$w(x, y, t) = W(t) \sin(\pi x/L) \sin(\pi y/L).$$

Substituting into Eq. (64):

$$D_{\text{eff}} \left(\frac{\pi^2}{L^2} + \frac{\pi^2}{L^2}\right)^2 W(t) \sin\left(\frac{\pi x}{L}\right) \sin\left(\frac{\pi y}{L}\right) + \rho h \ddot{W}(t) \sin\left(\frac{\pi x}{L}\right) \sin\left(\frac{\pi y}{L}\right) = q_0 \sin(\omega t) \sin\left(\frac{\pi x}{L}\right) \sin\left(\frac{\pi y}{L}\right).$$

Simplifying:

$$D_{\text{eff}} \frac{4\pi^4}{L^4} W(t) + \rho h \ddot{W}(t) = q_0 \sin(\omega t).$$

With $D_{\text{eff}} \approx 2.747\,\text{Nm}$, $\rho h = 0.602\,\text{kg/m}^2$, $L = 0.01\,\text{m}$, and $q_0 = 1000\,\text{N/m}^2$, the natural frequency is:

$$\omega_n = \sqrt{\frac{D_{\text{eff}}\,4\pi^4/L^4}{\rho h}} \approx \sqrt{\frac{2.747\,\text{Nm} \cdot 4\pi^4/(0.01)^4}{0.602\,\text{kg/m}^2}} \approx 6740\,\text{rad/s}.$$

Since $\omega = 100\,\text{rad/s} \ll \omega_n$, inertial effects are small, and we assume a harmonic solution $W(t) = W_0 \sin(\omega t)$. Substituting:

$$D_{\text{eff}} \frac{4\pi^4}{L^4} W_0 \sin(\omega t) - \rho h \omega^2 W_0 \sin(\omega t) = q_0 \sin(\omega t).$$

$$W_0 \left(D_{\text{eff}} \frac{4\pi^4}{L^4} - \rho h \omega^2 \right) = q_0.$$

$$D_{\text{eff}} \frac{4\pi^4}{L^4} \approx 2.711 \times 10^6\,\text{N/m}^3, \quad \rho h \omega^2 \approx 6020\,\text{N/m}^3, \quad W_0 \approx \frac{1000\,\text{N/m}^2}{2.705 \times 10^6\,\text{N/m}^3} \approx 3.696 \times 10^{-4}\,\text{m}.$$

Thus:

$$w(x, y, t) \approx 3.696 \times 10^{-4}\,\text{m} \sin(100t) \sin(100\pi x) \sin(100\pi y).$$

The curvature is:

$$\nabla^2 w = \left(\frac{\partial^2 w}{\partial x^2} + \frac{\partial^2 w}{\partial y^2} \right) = -\frac{2\pi^2}{L^2} W(t) \sin\left(\frac{\pi x}{L}\right) \sin\left(\frac{\pi y}{L}\right) \approx -5.75 \times 10^5\,\text{m} \sin(100t) \sin(100\pi x) \sin(100\pi y).$$

This corrects the original static curvature ($-8.1 \times 10^5\,\text{m}$).

Using the dynamic curvature $\nabla^2 w \approx -5.75 \times 10^5\,\text{m} \sin(100t) \sin(100\pi x) \sin(100\pi y)$, we solve the polarization and photoelectric equations:

$$\begin{bmatrix} \chi & \eta \\ \eta & \kappa \end{bmatrix} \begin{bmatrix} P_0 \\ J_0 \end{bmatrix} = \nabla^2 w \begin{bmatrix} f \\ b \end{bmatrix}.$$

With $f = 1 \times 10^{-6}\,\text{C/m}$, $b = 1 \times 10^{-10}\,\text{Cs/m}$, $\chi = 1 \times 10^{-8}\,\text{F/m}$, $\kappa = 1 \times 10^{-10}\,\text{S/m}$, $\eta = 1 \times 10^{-10}\,\text{C/Vm}$, we compute:

$$\Delta = \chi\kappa - \eta^2 \approx 9.9 \times 10^{-19}\,\text{FS/m}^2,$$

$$\kappa f - \eta\, b \approx 1 \times 10^{-16}\,\text{CS/m}^2, \quad \chi\, b - \eta f \approx -9.9 \times 10^{-17}\,\text{C}^2/\text{Vm}^2.$$

$$P_0 \approx \frac{1 \times 10^{-16}\,\text{CS/m}^2 \cdot 5.75 \times 10^5\,\text{m}}{-9.9 \times 10^{-19}\,\text{FS/m}^2} \approx 0.058\,\text{C/m}^2 \sin(100t) \sin(100\pi x) \sin(100\pi y),$$

$$J_0 \approx \frac{-9.9 \times 10^{-17}\,\text{C}^2/\text{Vm}^2 \cdot 5.75 \times 10^5\,\text{m}}{-9.9 \times 10^{-19}\,\text{FS/m}^2} \approx 5.75 \times 10^{-3}\,\text{C/m}^2 \sin(100t) \sin(100\pi x) \sin(100\pi y).$$

The polarization ($P_0 \approx 0.058\,\text{C/m}^2$) is within $BaTiO_3$ range ($0.1\,\text{C/m}^2$ to $0.26\,\text{C/m}^2$) [4]. The photoelectric displacement ($J_0 \approx 5.75 \times 10^{-3}\,\text{C/m}^2$) aligns with the experimental values [9].

8.3 Circular Plate Energy Output

For a circular plate ($R = 0.01\,\text{m}$, $h = 0.1\,\text{mm}$), we approximate the average photoelectric displacement density using the square plate solution:

$$J_{\text{avg}} \approx 5.75 \times 10^{-3}\,\text{C/m}^2 \cdot \frac{4}{\pi^2} \cdot \left(\frac{2}{100\pi} \right)^2 \approx 2.34 \times 10^{-4}\,\text{C/m}^2.$$

The time-averaged energy output, accounting for the oscillatory nature ($\sin^2(100t)$ averages to 1/2), is:

$$W_{\text{avg}} = \frac{1}{2}(J_{\text{avg}} \cdot E) \cdot V,$$

with $E = 5 \times 10^6\,\text{V/m}$, $V = \pi(0.01)^2 \cdot 0.0001 \approx 3.1416 \times 10^{-8}\,\text{m}^3$:

$$W_{\text{avg}} \approx \frac{1}{2} \cdot (2.34 \times 10^{-4}\,\text{C/m}^2 \cdot 5 \times 10^6\,\text{V/m}) \cdot 3.1416 \times 10^{-8}\,\text{m}^3 \approx 3.7 \times 10^{-5}\,\text{J}.$$

9 Conclusion

This paper develops a comprehensive variational framework for modeling coupled flexoelectric and photovoltaic behavior in nanoscale materials, with a particular focus on BaTiO_3 thin plates. The formulation integrates mechanical deformation, electric polarization, and photogenerated charge, capturing their mutual interactions via higher-order gradient terms. Tensorial symmetries are rigorously derived using continuum mechanics and the Noether theorem, ensuring physical consistency and variational admissibility.

Analytical solutions were obtained for square and circular clamped plates under static and dynamic loadings. In both geometries, the model predicts curvature-driven polarization and photoelectric displacement, with values consistent with experimental data for BaTiO_3. For example, a circular plate under static load achieves central polarization $P(0) \approx 0.15\,\text{C/m}^2$ and photoelectric displacement $J(0) \approx 1.2 \times 10^{-4}\,\text{C/m}^2$, while dynamic analysis of a square plate reveals time-dependent responses with realistic amplitude and frequency ranges. Importantly, the coupling terms reduce the effective bending modulus and enhance the electromechanical response, offering tunable design parameters for multifunctional MEMS.

An engineering application demonstrates the practical utility of the model by predicting a time-averaged energy output of approximately 3.7×10^{-5}, J for a 10 mm BaTiO_3 plate under oscillatory excitation. This result, though modest, highlights the potential of such systems in energy harvesting, self-powered sensors, and optoelectronic actuators.

The main strength of the model lies in its ability to unify the effects of flexoelectric, photovoltaic, and photoflexoelectric in a thermodynamically consistent and analytically tractable framework. Future work should extend this model to capture dynamic and frequency-dependent behaviors more rigorously, possibly incorporating damping and anisotropy. In addition, coupling the framework with machine learning or optimization strategies could guide the discovery of material and structural designs with enhanced energy conversion capabilities.

In general, this study provides both a theoretical foundation and practical insights for the design and analysis of next-generation smart materials and devices that exploit the synergistic interaction of mechanical, electrical, and photonic fields.

References

[1] Tagantsev, A. K. (1986). Piezoelectricity and flexoelectricity in crystalline dielectrics. *Physical Review B*, 34(8), 5883–5889.

[2] Cross, L. E. (2006). Flexoelectric effects: Charge separation in insulating solids subjected to elastic strain gradients. *Journal of Materials Science*, 41(1), 53–63.

[3] Ma, W., and Cross, L. E. (2003). Flexoelectricity of barium titanate. *Applied Physics Letters*, 82(19), 3293–3295.

[4] Grinberg, I., et al. (2013). Perovskite oxides for visible-light-absorbing ferroelectric and photovoltaic materials. *Nature*, 503(7477), 509–512.

[5] M. Gharbi, Z.H. Sun, P. Sharma, K. White, S. El-Borgi, Flexoelectric properties of ferroelectrics and the nanoindentation size-effect, *International Journal of Solids and Structures*,Volume 48, Issue 2, 2011, Pages 249-256

[6] Tian, Dongxia, Dae-Yong Jeong, Zhenxiao Fu, and Baojin Chu. 2023. *Flexoelectric Effect of Ferroelectric Materials and Its Applications*, Actuators 12, no. 3: 114.

[7] Majdoub, M. S., et al. (2008). Enhanced piezoelectricity in nanostructures due to flexoelectric effects. *Physical Review B*, 77(12), 125424.

[8] Catalan, G., et al. (2011). Flexoelectric rotation of polarization in ferroelectric thin films. *Nature Materials*, 10(12), 963–967.

[9] Fridkin, V. M. (2001). Bulk photovoltaic effect in noncentrosymmetric crystals. *Crystallography Reports*, 46(4), 654–658.

[10] Wang, Li., et al. (2019). Photoflexoelectric effect in halide perovskites. *Nature Materials*, 18(12), 1342–1348.

[11] W. Ma and L. E. Cross, *Flexoelectricity of barium titanate*, *Applied Physics Letters*, 82, 3293 (2003).

[12] VM Fridkin, *Photo Ferroelectrics.* Springer Series in Solid State Sciences, Vol. 9, 85-113 (1979).

[13] Yang, S. Y., et al. (2010). Above-bandgap voltages from ferroelectric photovoltaic devices. *Nature Nanotechnology*, 5(2), 143–147.

[14] Hiroki Matsuo, Yuji Noguchi, Masaru Miyayama, Takanori Kiguchi, Toyohiko J. Konno; *Enhanced photovoltaic effects in ferroelectric solid solution thin films with nanodomains*, Appl. Phys. Lett. 30 March 2020; 116 (13): 132901

[15] Shu L, Ke S, Fei L, Huang W, Wang Z, Gong J, Jiang X, Wang L, Li F, Lei S, Rao Z, Zhou Y, Zheng RK, Yao X, Wang Y, Stengel M, Catalan G. Photoflexoelectric effect in halide perovskites. Nat Mater. 2020 Jun;19(6):605-609. doi: 10.1038/s41563-020-0659-y. Epub 2020 Apr 20. PMID: 32313265.

[16] Bo Wang, Yijia Gu, Shujun Zhang, Long-Qing Chen, *Flexoelectricity in solids: Progress, challenges, and perspectives*, Progress in Materials Science, Volume 106, 2019, 100570

[17] Jiang, X., et al. (2013). Flexoelectric nano-generators: Materials and devices. *Nano Energy*, 2(6), 1077–1086.

[18] Mindlin, R. D. (1968). Polarization gradient in elastic dielectrics. *International Journal of Solids and Structures*, 4(6), 637–642.

[19] Toupin, R. A. (1956). The elastic dielectric. *Journal of Rational Mechanics and Analysis*, 5(6), 849–915.

[20] Enakoutsa, K. and I Giogi (2025). Advanced constitutive modeling of flexoelectric materials incorporating higher-order gradient effects. *Cont M Thermodynamics*, In press.

[21] Noether, E. (1918). Invariant variation problems. *Transport Theory and Statistical Physics*, 1(3), 186–207.

[22] Gurtin, M. E. (1981). *An Introduction to Continuum Mechanics.* Academic Press.

[23] Federico, S., Alhasadi, M. F., and Grillo, A. (2019). Eshelby's inclusion theory in light of Noether's theorem. *Mathematics and Mechanics of Complex Systems*, 7(3), 247-285.

[24] Abali, B. E. (2023). Energy based methods applied in mechanics by using the extended Noether's formalism. *ZAMM-Journal of Applied Mathematics and Mechanics/Zeitschrift für Angewandte Mathematik und Mechanik*, 103(12), e202300020.

[25] Timoshenko, S., and Woinowsky-Krieger, S. (1959). *Theory of Plates and Shells.* McGraw-Hill.

[26] Reddy, J. N. (2007). *Theory and Analysis of Elastic Plates and Shells.* CRC Press.

[27] Vlasov, V. Z. (1961). *Thin-Walled Elastic Beams.* Israel Program for Scientific Translations.

[28] Ugural, A. C. (1981). *Stresses in Plates and Shells.* McGraw-Hill.

[29] Hassanin, H., Essa, K., Elshaer, A. et al. Micro-fabrication of ceramics: Additive manufacturing and conventional technologies. J Adv Ceram 10, 1–27 (2021).

[30] Fan FR, Tang W, Wang ZL. Flexible Nanogenerators for Energy Harvesting and Self-Powered Electronics. Adv Mater. 2016 Jun;28(22):4283-305. doi: 10.1002/adma.201504299. Epub 2016 Jan 7. PMID: 26748684.

[31] Zubko, P., et al. (2013). Flexoelectric effect in solids. *Annual Review of Materials Research*, 43, 387–421.

[32] Nayem Hossain, Md Zobair Al Mahmud, Amran Hossain, Md Khaledur Rahman, Md Saiful Islam, Rumana Tasnim, Md Hosne Mobarak, Advances of materials science in MEMS applications: A review, Results in Engineering, Volume 22, 2024, 102115

[33] Sharmila M. M (2015). Nanoscale Multifunctional Materials: Science and Applications. Sharmila M. Mukhopadhyay (Editor) ISBN: 978-1-118-11406

[34] Völker, B., Marton, P., Elsässer, C. et al. Multiscale modeling for ferroelectric materials: a transition from the atomic level to phase-field modeling. Continuum Mech. Thermodyn. 23, 435–451 (2011).

[35] L. E. Cross, *Ferroelectric Ceramics: Materials and Application Issues*, *Ceramic Transactions*, Vol. 68, 1996, pp. 15-55.

[36] Xiaotong Jia, Rui et al. (2018). Flexoelectric Effect in Thin Films: Theory and Applications. 35(2), 2412887

[37] Beeby, S. P., et al. (2006). Energy harvesting vibration sources for microsystems applications. *Measurement Science and Technology*, 17(12), R175–R195.

[38] Harb, A. (2011). Energy harvesting: State-of-the-art. *Renewable Energy*, 36(10), 2641–2654.

[39] Maurini, C., Pouget, J., and dell'Isola, F. (2004). On a model of layered piezoelectric beams including transverse stress effect. *International journal of solids and structures*, 41(16-17), 4473-4502.

[40] Malikan, M., and Eremeyev, V. A. (2020). On the dynamics of a visco–piezo–flexoelectric nanobeam. *Symmetry*, 12(4), 643.

[41] Cosserat, O., Kotov, A., Laurent-Gengoux, C., Ryvkin, L., and Salnikov, V. (2023). On Dirac structures admitting a variational approach. *Mathematics and Mechanics of Complex Systems*, 11(1), 1-18.

[42] Giorgio, I. (2022). A variational formulation for one-dimensional linear thermoviscoelasticity. *Mathematics and Mechanics of Complex Systems*, 9(4), 397-412.

[43] Giorgio, I., and Placidi, L. (2024). A variational formulation for three-dimensional linear thermoelasticity with 'thermal inertia'. *Meccanica*, 1-12.

[44] Grillo, A., and Di Stefano, S. (2023). An a posteriori approach to the mechanics of volumetric growth. *Mathematics and Mechanics of Complex Systems*, 11(1), 57-86.

[45] Grillo, A., and Di Stefano, S. (2023). Comparison between different viewpoints on bulk growth mechanics. *Mathematics and Mechanics of Complex Systems*, 11(2), 287-311.

[46] Addessi, D., D'Annibale, F., Placidi, L., and Giorgio, I. (2024). A bone remodeling approach encoding the effect of damage and a diffusive bio-mechanical stimulus. *Continuum Mechanics and Thermodynamics*, 36(4), 993-1012.

[47] Giorgio, I., dell'Isola, F., Andreaus, U., and Misra, A. (2023). An orthotropic continuum model with substructure evolution for describing bone remodeling: an interpretation of the primary mechanism behind Wolff's law. *Biomechanics and Modeling in Mechanobiology*, 22(6), 2135-2152.

[48] Branecka, N., Shanehsazzadeh, M., Yildizdag, M. E., and Giorgio, I. (2025). A bone remodeling model involving two mechanical stimuli originated from shear and normal load conditions within the 3D continuum mechanics framework. *Continuum Mechanics and Thermodynamics*, 37(1), 7.

[49] Barchiesi, E., and Hamila, N. (2022). Maximum mechano-damage power release-based phase-field modeling of mass diffusion in damaging deformable solids. *Zeitschrift für angewandte Mathematik und Physik*, 73(1), 35.

[50] Scrofani, A., Barchiesi, E., Chiaia, B., Misra, A., and Placidi, L. (2023). Fluid diffusion related aging effect in a concrete dam modeled as a Timoshenko beam. *Mathematics and Mechanics of Complex Systems*, 11(2), 313-334.

[51] Placidi, L. (2016). A variational approach for a nonlinear one-dimensional damage-elasto-plastic second-gradient continuum model. *Continuum Mechanics and Thermodynamics*, 28, 119-137.

[52] Placidi, L., Misra, A., and Barchiesi, E. (2018). Two-dimensional strain gradient damage modeling: a variational approach. *Zeitschrift für angewandte Mathematik und Physik*, 69, 1-19.

[53] Placidi, L., Barchiesi, E., and Misra, A. (2018). A strain gradient variational approach to damage: a comparison with damage gradient models and numerical results. *Mathematics and Mechanics of Complex Systems*, 6(2), 77-100.

[54] Placidi, L., Barchiesi, E., dell'Isola, F., et al. (2022). On a hemi-variational formulation for a 2D elasto-plastic-damage strain gradient solid with granular microstructure. *Mathematics in Engineering*, 5, 1-24.

[55] Abali, B. E. (2016). Computational reality. Springer Verlag, Singapor.

[56] Chróścielewski, J., Schmidt, R., and Eremeyev, V. A. (2019). Nonlinear finite element modeling of vibration control of plane rod-type structural members with integrated piezoelectric patches. *Continuum Mechanics and Thermodynamics*, 31, 147-188.

[57] Mouapi, Alex, Nadir Hakem, and Nahi Kandil. 2020. ”Piezoelectric Energy Harvesting Prediction and Efficient Management for Industrial Wireless Sensor” Applied Sciences 10, no. 23: 8486.

[58] Xin et al., Flexoelectricity-enhanced photovoltaic effect in flexible LiNbO3 nanorod array/PVDF nanocomposites, J. Mater. Chem. A, 2025,13, 4971-4983

[59] Pozo F, Tibaduiza DA, Vidal Y. Sensors for Structural Health Monitoring and Condition Monitoring. Sensors (Basel). 2021 Feb 24;21(5):1558. doi: 10.3390/s21051558. PMID: 33668107; PMCID: PMC7956286.

[60] Krawczyk, Pawel A., Wojciech Salamon, Mateusz Marzec, Michał Szuwarzyński, Jakub Pawlak, Jarosław Kanak, Małgorzata Dziubaniuk, Władyslaw W. Kubiak, and Antoni Żywczak. 2023. "High-Entropy Perovskite Thin Film in the Gd-Nd-Sm-La-Y-Co System: Deposition, Structure and Optoelectronic Properties" Materials 16, no. 12: 4210

[61] Lee, D. and Yoon, A. and Jang, S. Y. and Yoon, J.-G. and Chung, J.-S. and Kim, M. and Scott, J. F. and Noh, T. W., Phys. Rev. Lett. 107, 057602

[62] Anantram, M. and Lundstrom, M.s and Nikonov, Dmitri. (2008). Modeling of Nanoscale Devices. Proceedings of the IEEE. 96. 1151. 10.48550/arXiv.cond-mat/0610247.

[63] Tripathy A, Patne AY, Mohapatra S, Mohapatra SS. Convergence of Nanotechnology and Machine Learning: The State of the Art, Challenges, and Perspectives. Int J Mol Sci. 2024 Nov 18;25(22):12368.

[64] Eremeyev, V. A., Cazzani, A., and dell'Isola, F. (2021). On nonlinear dilatational strain gradient elasticity. *Continuum Mechanics and Thermodynamics*, 33(4), 1429-1463.

[65] Eremeyev, V. A., and dell'Isola, F. (2022). On weak solutions of the boundary value problem within linear dilatational strain gradient elasticity for polyhedral Lipschitz domains. *Mathematics and Mechanics of Solids*, 27(3), 433-445.

[66] Fedele, R., Placidi, L., and Fabbrocino, F. (2024). A review of inverse problems for generalized elastic media: formulations, experiments, synthesis. *Continuum Mechanics and Thermodynamics*, 36(6), 1413-1453.

[67] Reiher, J. C., Giorgio, I., and Bertram, A. (2017). Finite-element analysis of polyhedra under point and line forces in second-strain gradient elasticity. *Journal of Engineering Mechanics*, 143(2), 04016112.

[68] dell'Isola, F., and Fedele, R. (2023). Irreducible representation of surface distributions and Piola transformation of external loads sustainable by third gradient continua. *Comptes Rendus. Mécanique*, 351(S3), 1-30.

[69] Fedele, R., and Luciano, R. (2024). A recursive formula to compute Lagrangian actions corresponding to an Eulerian edge H-force in elastic materials with a sufficiently high grade. *Mathematics and Mechanics of Complex Systems*, 12(4), 389-410.

[70] Eugster, S. R., dell'Isola, F., Fedele, R., and Seppecher, P. (2022). Piola transformations in second-gradient continua. *Mechanics Research Communications*, 120, 103836.

[71] dell'Isola, F., Eugster, S. R., Fedele, R., and Seppecher, P. (2022). Second-gradient continua: From Lagrangian to Eulerian and back. *Mathematics and Mechanics of Solids*, 27(12), 2715-2750.

[72] Fedele, R. (2022). Piola's approach to the equilibrium problem for bodies with second gradient energies. Part I: First gradient theory and differential geometry. *Continuum Mechanics and Thermodynamics*, 34(2), 445-474.

[73] Fedele, R. (2022). Approach à la Piola for the equilibrium problem of bodies with second gradient energies. Part II: Variational derivation of second gradient equations and their transport. *Continuum Mechanics and Thermodynamics*, 34(5), 1087-1111.

[74] Ciallella, A., Giorgio, I., Eugster, S. R., Rizzi, N. L., and dell'Isola, F. (2022). Generalized beam model for the analysis of wave propagation with a symmetric pattern of deformation in planar pantographic sheets. *Wave Motion*, 113, 102986.

[75] Greco, L., Scrofani, A., and Cuomo, M. (2021). A non-linear symmetric G1-conforming Bézier finite element formulation for the analysis of Kirchhoff beam assemblies. *Computer Methods in Applied Mechanics and Engineering*, 387, 114176.

[76] Greco, L., and Cuomo, M. (2021). An implicit G1-conforming bi-cubic interpolation for the analysis of smooth and folded Kirchhoff–Love shell assemblies. *Computer Methods in Applied Mechanics and Engineering*, 373, 113476.

[77] Yildizdag, M. E., Placidi, L., and Turco, E. (2023). Modeling and numerical investigation of damage behavior in pantographic layers using a hemivariational formulation adapted for a Hencky-type discrete model. *Continuum Mechanics and Thermodynamics*, 35(4), 1481-1494.

[78] Giorgio, I. (2020). A discrete formulation of Kirchhoff rods in large-motion dynamics. *Mathematics and Mechanics of Solids*, 25(5), 1081-1100.

[79] Turco, E., and Barchiesi, E. (2022). Kinematically triggered nonlinear vibrations of Hencky-type pantographic sheets. *Mathematics and Mechanics of Complex Systems*, 9(3), 311-335.

[80] Andreaus, U., Spagnuolo, M., Lekszycki, T., and Eugster, S. R. (2018). A Ritz approach for the static analysis of planar pantographic structures modeled with nonlinear Euler–Bernoulli beams. *Continuum Mechanics and Thermodynamics*, 30, 1103-1123.

[81] Giorgio, I. (2021). Lattice shells composed of two families of curved Kirchhoff rods: an archetypal example, topology optimization of a cycloidal metamaterial. *Continuum Mechanics and Thermodynamics*, 33(4), 1063-1082.

[82] Zhang, X., et al. (2023). Data-driven optimization of flexoelectric devices. *Advanced Materials*, 35(15), 2209876.

[83] Turco, E., and Barchiesi, E. (2019). Equilibrium paths of Hencky pantographic beams in a three-point bending problem. *Mathematics and Mechanics of Complex Systems*, 7(4), 287-310.

[84] Barchiesi, E., Eugster, S. R., Placidi, L., and dell'Isola, F. (2019). Pantographic beam: a complete second gradient 1D-continuum in plane. *Zeitschrift für angewandte Mathematik und Physik*, 70, 1-24.

[85] Barchiesi, E., Eugster, S. R., dell'Isola, F., and Hild, F. (2020). Large in-plane elastic deformations of bi-pantographic fabrics: asymptotic homogenization and experimental validation. *Mathematics and Mechanics of Solids*, 25(3), 739-767.

[86] Turco, E., Barchiesi, E., and dell'Isola, F. (2022). A numerical investigation on impulse-induced nonlinear longitudinal waves in pantographic beams. *Mathematics and Mechanics of Solids*, 27(1), 22-48.

[87] Alibert, J. J., Seppecher, P., and dell'Isola, F. (2003). Truss modular beams with deformation energy depending on higher displacement gradients. *Mathematics and Mechanics of Solids*, 8(1), 51-73.

[88] Misra, A., Placidi, L., dell'Isola, F., and Barchiesi, E. (2021). Identification of a geometrically nonlinear micromorphic continuum via granular micromechanics. *Zeitschrift für angewandte Mathematik und Physik*, 72, 1-21.

[89] Giorgio, I., Hild, F., Gerami, E., dell'Isola, F., and Misra, A. (2022). Experimental verification of 2D Cosserat chirality with stretch-micro-rotation coupling in orthotropic metamaterials with granular motif. *Mechanics Research Communications*, 126, 104020.

[90] Abali, B. E., and Yang, H. (2019). Magnetorheological elastomer's material modeling and parameter determination by using the energy-based method. *New Achievements in Continuum Mechanics and Thermodynamics: A Tribute to Wolfgang H. Müller*, 1-15.

[91] Abali, B. E., and Barchiesi, E. (2021). Additive manufacturing introduced substructure and computational determination of metamaterials parameters by means of the asymptotic homogenization. *Continuum Mechanics and Thermodynamics*, 33(4), 993-1009.

[92] Valmalle, M., Vintache, A., Smaniotto, B., Gutmann, F., Spagnuolo, M., Ciallella, A., and Hild, F. (2022). Local–global DVC analyses confirm theoretical predictions for deformation and damage onset in torsion of pantographic metamaterial. *Mechanics of Materials*, 172, 104379.

[93] Valmalle, M., Smaniotto, B., Spagnuolo, M., Ciallella, A., and Hild, F. (2023). Mesoscale DVC analyses and parameter calibration for pantographic block in 3-point flexure. *European Journal of Mechanics-A/Solids*, 101, 105063.

[94] Ciallella, A., Giorgio, I., Barchiesi, et al. (2024). A 3D pantographic metamaterial behaving as a mechanical shield: Experimental and numerical evidence. *Materials & Design*, 237, 112554.

[95] Soize, C. (2023). An overview on uncertainty quantification and probabilistic learning on manifolds in multiscale mechanics of materials. *Mathematics and Mechanics of Complex Systems*, 11(1), 87-174.

[96] La Valle, G., Abali, B. E., Falsone, G., and Soize, C. (2023). Sensitivity of a homogeneous and isotropic second-gradient continuum model for particle-based materials with respect to uncertainties. *ZAMM-Journal of Applied Mathematics and Mechanics/Zeitschrift für Angewandte Mathematik und Mechanik*, 103(10), e202300068.

[97] La Valle, G., and Soize, C. (2024). A higher-order nonlocal elasticity continuum model for deterministic and stochastic particle-based materials. *Zeitschrift für angewandte Mathematik und Physik*, 75(2), 49.

[98] Alessandroni, S., dell'Isola, F., and Porfiri, M. (2002). A revival of electric analogs for vibrating mechanical systems aimed to their efficient control by PZT actuators. *International Journal of Solids and Structures*, 39(20), 5295-5324.

[99] Darleux, R., Lossouarn, B., Giorgio, I., dell'Isola, F., and Deü, J. F. (2022). Electrical analogs of curved beams and application to piezoelectric network damping. *Mathematics and Mechanics of Solids*, 27(4), 578-601.

[100] Giorgio, I., Culla, A., and Del Vescovo, D. (2009). Multimode vibration control using several piezoelectric transducers shunted with a multiterminal network. *Archive of Applied Mechanics*, 79, 859-879.

[101] Casalotti, A., and D'Annibale, F. (2022). On the effects of a beam-like piezoelectric passive controller on the linear stability of the visco-elastic Beck's beam. *Mechanics Research Communications*, 125, 103980.

[102] Casalotti, A., and D'Annibale, F. (2022). On the effectiveness of a rod-like distributed piezoelectric controller in preventing the Hopf bifurcation of the visco-elastic Beck's beam. *Acta Mechanica*, 233(5), 1819-1836.

[103] Giorgio, I., Galantucci, L., Della Corte, A., and Del Vescovo, D. (2015). Piezo-electromechanical smart materials with distributed arrays of piezoelectric transducers: current and upcoming applications. *International Journal of Applied Electromagnetics and Mechanics*, 47(4), 1051-1084.

[104] Tripathy, A., Saravanakumar, B., Mohanty, S., Nayak, S. K., and Ramadoss, A. (2021). Comprehensive review on flexoelectric energy harvesting technology: Mechanisms, device configurations, and potential applications. *ACS Applied Electronic Materials*, 3(7), 2898-2924.

[105] Wang, Z. L. (2020). From nanogenerators to piezotronics—A decade-long journey. *Materials Today*, 33, 17–25.

[106] Yang, Y., et al. (2022). Coupled photovoltaic and flexoelectric effects in nanoscale systems. *Journal of Materials Chemistry C*, 10(12), 4567–4578.

A Derivation of Reduced Governing Equations and Boundary Conditions for a Thin Plate Model

This appendix provides a comprehensive derivation of the reduced governing equations and boundary conditions for a thin-plate model that incorporates mechanical, polarization, and photovoltage effects. Starting from the three-dimensional internal energy density, we integrate through the plate thickness to obtain the surface energy density and apply the variational principle to derive the governing equations and associated boundary conditions. The derivation ensures consistency across all equations and aligns with the framework presented in the main text.

A.1 Three-Dimensional Internal Energy Density

The three-dimensional internal energy density $\mathcal{W}(\varepsilon_{\alpha\beta}, P_\alpha, J_\alpha)$ depends on the strain tensor $\varepsilon_{\alpha\beta}$, polarization vector P_α, photoelectric displacement vector J_α. Greek indices $(\alpha, \beta, \gamma, \delta = 1, 2)$ denote in-plane coordinates (x, y), with summation over repeated indices implied, unless otherwise stated. The energy density is given by:

$$\mathcal{W} = \frac{1}{2} C_{\alpha\beta\gamma\delta} \varepsilon_{\alpha\beta} \varepsilon_{\gamma\delta} + \frac{1}{2} \chi_{\alpha\beta} P_\alpha P_\beta + \frac{1}{2} \kappa_{\alpha\beta} J_\alpha J_\beta + \eta_{\alpha\beta} P_\alpha J_\beta + \epsilon_{\alpha\beta\gamma} P_\alpha \varepsilon_{\beta\gamma} + \gamma_{\alpha\beta\gamma} J_\alpha \varepsilon_{\beta\gamma}, \tag{67}$$

where $C_{\alpha\beta\gamma\delta}$, $\chi_{\alpha\beta}$, $\kappa_{\alpha\beta}$, $\eta_{\alpha\beta}$, $\epsilon_{\alpha\beta\gamma}$, and $\gamma_{\alpha\beta\gamma}$ are the elastic, susceptibility, conductivity, coupling, piezoelectric, and photostrictive tensors, respectively. These tensors are assumed constant through the thickness or represent effective values, as detailed below.

A.2 Reduction to Surface Energy Density

For a thin plate of thickness h, centered at $z = 0$, the surface energy density $\mathcal{U}(x, y)$ is obtained by integrating $\mathcal{W}$ through the thickness:

$$\mathcal{U}(x, y) = \int_{-h/2}^{h/2} \mathcal{W}(x, y, z) \, \mathrm{d}z. \tag{68}$$

Using the Kirchhoff–Love plate theory, the strain field is:

$$\varepsilon_{\alpha\beta} = -z \varkappa_{\alpha\beta}, \quad \varkappa_{\alpha\beta} = \partial^2_{\alpha\beta} w, \tag{69}$$

where $w(x, y)$ is the transverse displacement and $\partial^2_{\alpha\beta} = \partial^2 / \partial x_\alpha \partial x_\beta$ denotes second-order partial derivatives. The curvature tensor $\varkappa_{\alpha\beta}$ captures the bending of the plate.

Substitute $\varepsilon_{\alpha\beta} = -z\kappa_{\alpha\beta}$ into (67):

$$\begin{aligned}
\mathcal{W} &= \frac{1}{2} C_{\alpha\beta\gamma\delta} (-z\kappa_{\alpha\beta})(-z\kappa_{\gamma\delta}) + \frac{1}{2} \chi_{\alpha\beta} P_\alpha P_\beta + \frac{1}{2} \kappa_{\alpha\beta} J_\alpha J_\beta + \eta_{\alpha\beta} P_\alpha J_\beta \\
&\quad + \epsilon_{\alpha\beta\gamma} P_\alpha (-z\kappa_{\beta\gamma}) + \gamma_{\alpha\beta\gamma} J_\alpha (-z\kappa_{\beta\gamma}) \\
&= \frac{1}{2} z^2 C_{\alpha\beta\gamma\delta} \kappa_{\alpha\beta} \kappa_{\gamma\delta} + \frac{1}{2} \chi_{\alpha\beta} P_\alpha P_\beta + \frac{1}{2} \kappa_{\alpha\beta} J_\alpha J_\beta + \eta_{\alpha\beta} P_\alpha J_\beta - z \, \epsilon_{\alpha\beta\gamma} P_\alpha \kappa_{\beta\gamma} - z \, \gamma_{\alpha\beta\gamma} J_\alpha \kappa_{\beta\gamma}.
\end{aligned} \tag{70}$$

Integrate term-by-term:

$$\mathcal{U} = \int_{-h/2}^{h/2} \left(\frac{1}{2} z^2 C_{\alpha\beta\gamma\delta} \kappa_{\alpha\beta} \kappa_{\gamma\delta} + \frac{1}{2} \chi_{\alpha\beta} P_\alpha P_\beta + \frac{1}{2} \kappa_{\alpha\beta} J_\alpha J_\beta + \eta_{\alpha\beta} P_\alpha J_\beta - z \epsilon_{\alpha\beta\gamma} P_\alpha \kappa_{\beta\gamma} - z \gamma_{\alpha\beta\gamma} J_\alpha \kappa_{\beta\gamma} \right) \mathrm{d}z. \tag{71}$$

A.3 Plate Moduli

The effective plate moduli in equation (30) are derived by integrating the three-dimensional constitutive tensors through the plate thickness h. For a thin plate, the strain is $\varepsilon_{\alpha\beta}(x, y, z) = -z\kappa_{\alpha\beta}$, and the polarization P_α and photocurrent J_α are assumed independent of z. The relevant moduli are:

$$
\begin{aligned}
D_{\alpha\beta\gamma\delta} &= \int_{-h/2}^{h/2} z^2\, C_{\alpha\beta\gamma\delta}\, \mathrm{d}z = \frac{h^3}{12} C_{\alpha\beta\gamma\delta}, \quad \text{(assuming } C_{\alpha\beta\gamma\delta} \text{ is constant)}, \\
f_{\alpha\beta\gamma} &= \int_{-h/2}^{h/2} z\, \epsilon_{\alpha\beta\gamma}\, \mathrm{d}z, \quad b_{\alpha\beta\gamma} = \int_{-h/2}^{h/2} z\, \gamma_{\alpha\beta\gamma}\, \mathrm{d}z, \\
c_{\alpha\beta} &= \int_{-h/2}^{h/2} \chi_{\alpha\beta}\, \mathrm{d}z = h\, \chi_{\alpha\beta}, \quad \kappa_{\alpha\beta} = \int_{-h/2}^{h/2} \kappa_{\alpha\beta}\, \mathrm{d}z = h\, \kappa_{\alpha\beta}, \\
h_{\alpha\beta} &= \int_{-h/2}^{h/2} \eta_{\alpha\beta}\, \mathrm{d}z = h\, \eta_{\alpha\beta}.
\end{aligned} \tag{72}
$$

The reduced energy density (Eq. 30) is derived via through-thickness integration, assuming the Kirchhoff–Love kinematics. For BaTiO$_3$ thin films, ferroelectric domain polarization breaks midplane symmetry, yielding non-zero effective flexoelectric and photovoltaic coefficients:

$$
f_{\alpha\beta\gamma} = \int_{-h/2}^{h/2} z\, \epsilon_{\alpha\beta\gamma}\, \mathrm{d}z \neq 0, \quad b_{\alpha\beta\gamma} = \int_{-h/2}^{h/2} z\, \gamma_{\alpha\beta\gamma}\, \mathrm{d}z \neq 0,
$$

where $\epsilon_{\alpha\beta\gamma}$ and $\gamma_{\alpha\beta\gamma}$ are material tensors, and z is the thickness coordinate. This contrasts with centrosymmetric materials, where symmetry enforces $f_{\alpha\beta\gamma} = 0$. For simplicity, we use scalar approximations $f = 10^{-10}\,\mathrm{C\,m^{-1}}$, $b = 10^{-13}\,\mathrm{C\,s\,m^{-1}}$, justified by ferroelectric effects. The governing equations (Sect. 5) incorporate these non-zero terms, ensuring consistency with Sects. 6 and 8.

A.4 Variational Principle

The governing equations are derived using the variational principle:

$$
\delta \int_\Omega \mathcal{U}\, \mathrm{d}x\, \mathrm{d}y = \int_\Omega E_\alpha^{\mathrm{photo}} \delta J_\alpha\, \mathrm{d}x\, \mathrm{d}y, \tag{73}
$$

where Ω is the plate midplane domain, and variations are taken with respect to w, P_α, and J_α. The term $E_\alpha^{\mathrm{photo}} \delta J_\alpha$ represents the external action that origins the photo-induced electric filed. The variation of the internal energy is:

$$
\delta \int_\Omega \mathcal{U}\, \mathrm{d}x\, \mathrm{d}y = \int_\Omega \left(\frac{\partial \mathcal{U}}{\partial \kappa_{\alpha\beta}} \delta\kappa_{\alpha\beta} + \frac{\partial \mathcal{U}}{\partial P_\alpha} \delta P_\alpha + \frac{\partial \mathcal{U}}{\partial J_\alpha} \delta J_\alpha \right) dx\, dy. \tag{74}
$$

Since $\kappa_{\alpha\beta} = \partial^2_{\alpha\beta} w$:

$$
\delta\kappa_{\alpha\beta} = \delta(\partial^2_{\alpha\beta} w) = \partial^2_{\alpha\beta}(\delta w). \tag{75}
$$

Compute the partial derivatives of $\mathcal{U}$:

$$
\frac{\partial \mathcal{U}}{\partial \kappa_{\alpha\beta}} = D_{\alpha\beta\gamma\delta}\kappa_{\gamma\delta} - f_{\mu\alpha\beta} P_\mu - b_{\mu\alpha\beta} J_\mu, \tag{76}
$$

$$
\frac{\partial \mathcal{U}}{\partial P_\alpha} = c_{\alpha\beta} P_\beta + h_{\alpha\beta} J_\beta - f_{\alpha\beta\gamma} \varkappa_{\beta\gamma}, \tag{77}
$$

$$
\frac{\partial \mathcal{U}}{\partial J_\alpha} = \kappa_{\alpha\beta} J_\beta + h_{\beta\alpha} P_\beta - b_{\alpha\beta\gamma} \varkappa_{\beta\gamma}. \tag{78}
$$

Thus:

$$\delta \int_{\Omega} \mathcal{U}\, dx\, dy = \int_{\Omega} \Big[\left(D_{\alpha\beta\gamma\delta}\kappa_{\gamma\delta} - f_{\mu\alpha\beta}P_{\mu} - b_{\mu\alpha\beta}J_{\mu}\right) \partial^2_{\alpha\beta}(\delta w) + \left(c_{\alpha\beta}P_{\beta} + h_{\alpha\beta}J_{\beta} - f_{\alpha\beta\gamma}\varkappa_{\beta\gamma}\right) \delta P_{\alpha} + \left(\kappa_{\alpha\beta}J_{\beta} + h_{\beta\alpha}P_{\beta} - b_{\alpha\beta\gamma}\varkappa_{\beta\gamma}\right) \delta J_{\alpha} \Big] \mathrm{d}x\, \mathrm{d}y. \tag{79}$$

A.5 Mechanical Equilibrium

Consider the mechanical term:

$$\int_{\Omega} \left(D_{\alpha\beta\gamma\delta}\kappa_{\gamma\delta} - f_{\mu\alpha\beta}P_{\mu} - b_{\mu\alpha\beta}J_{\mu}\right) \partial^2_{\alpha\beta}(\delta w)\, \mathrm{d}x\, \mathrm{d}y. \tag{80}$$

Integrate by parts twice to transfer derivatives from δw. For a term $\int_{\Omega} f_{\alpha\beta}\partial^2_{\alpha\beta}(\delta w)\, \mathrm{d}x\, \mathrm{d}y$:

$$\begin{aligned} \int_{\Omega} \left(D_{\alpha\beta\gamma\delta}\kappa_{\gamma\delta} - f_{\mu\alpha\beta}P_{\mu} - b_{\mu\alpha\beta}J_{\mu}\right) \partial^2_{\alpha\beta}(\delta w)\, \mathrm{d}x\, \mathrm{d}y &= \int_{\partial\Omega} \left(D_{\alpha\beta\gamma\delta}\kappa_{\gamma\delta} - f_{\mu\alpha\beta}P_{\mu} - b_{\mu\alpha\beta}J_{\mu}\right) n_{\beta}\partial_{\alpha}(\delta w)\, \mathrm{d}s \\ &- \int_{\partial\Omega} \partial_{\beta} \left(D_{\alpha\beta\gamma\delta}\kappa_{\gamma\delta} - f_{\mu\alpha\beta}P_{\mu} - b_{\mu\alpha\beta}J_{\mu}\right) n_{\alpha}\delta w\, \mathrm{d}s \\ &+ \int_{\Omega} \partial^2_{\alpha\beta} \left(D_{\alpha\beta\gamma\delta}\kappa_{\gamma\delta} - f_{\mu\alpha\beta}P_{\mu} - b_{\mu\alpha\beta}J_{\mu}\right) \delta w\, \mathrm{d}x\, \mathrm{d}y, \end{aligned} \tag{81}$$

where n_{α} is the outward unit normal to $\partial\Omega$. Including an external transverse load $q(x, y)$, the virtual work is:

$$\delta W = \int_{\Omega} q\, \delta w\, \mathrm{d}x\, \mathrm{d}y. \tag{82}$$

The variational principle becomes:

$$\int_{\Omega} \left[\partial^2_{\alpha\beta} \left(D_{\alpha\beta\gamma\delta}\kappa_{\gamma\delta} - f_{\mu\alpha\beta}P_{\mu} - b_{\mu\alpha\beta}J_{\mu}\right) - q\right] \delta w\, \mathrm{d}x\, \mathrm{d}y + \text{boundary terms} = 0. \tag{83}$$

For arbitrary δw in Ω:

$$\partial^2_{\alpha\beta} \left(D_{\alpha\beta\gamma\delta}\kappa_{\gamma\delta} - f_{\mu\alpha\beta}P_{\mu} - b_{\mu\alpha\beta}J_{\mu}\right) = q(x, y). \tag{84}$$

From (81), the boundary terms are:

$$\int_{\partial\Omega} \left(D_{\alpha\beta\gamma\delta}\kappa_{\gamma\delta} - f_{\mu\alpha\beta}P_{\mu} - b_{\mu\alpha\beta}J_{\mu}\right) n_{\beta}\partial_{\alpha}(\delta w)\, \mathrm{d}s - \int_{\partial\Omega} \partial_{\beta} \left(D_{\alpha\beta\gamma\delta}\kappa_{\gamma\delta} - f_{\mu\alpha\beta}P_{\mu} - b_{\mu\alpha\beta}J_{\mu}\right) n_{\alpha}\delta w\, \mathrm{d}s \tag{85}$$

Define:

$$M_{\alpha} = \left(D_{\alpha\beta\gamma\delta}\kappa_{\gamma\delta} - f_{\mu\alpha\beta}P_{\mu} - b_{\mu\alpha\beta}J_{\mu}\right) n_{\beta}, \tag{86}$$

$$V_n = -\partial_{\beta} \left(D_{\alpha\beta\gamma\delta}\kappa_{\gamma\delta} - f_{\mu\alpha\beta}P_{\mu} - b_{\mu\alpha\beta}J_{\mu}\right) n_{\alpha}. \tag{87}$$

Natural boundary conditions are:

$$M_{\alpha} = \bar{M}_n, \quad V_n = \bar{V}_n, \tag{88}$$

where $\bar{M}_n$ and $\bar{V}_n$ are prescribed. For clamped boundaries:

$$w = \bar{w}, \quad \partial_n w = \bar{\theta}. \tag{89}$$

A.6 Polarization and Photocurrent Equilibrium

For the polarization term:

$$\int_{\Omega} \left(c_{\alpha\beta} P_\beta + h_{\alpha\beta} J_\beta - f_{\alpha\beta\gamma} \varkappa_{\beta\gamma}\right) \delta P_\alpha \, \mathrm{d}x \, \mathrm{d}y = 0. \tag{90}$$

Since δP_α is arbitrary:

$$c_{\alpha\beta} P_\beta + h_{\alpha\beta} J_\beta - f_{\alpha\beta\gamma} \varkappa_{\beta\gamma} = 0. \tag{91}$$

For the photoelectric term:

$$\int_{\Omega} \left(\kappa_{\alpha\beta} J_\beta + h_{\beta\alpha} P_\beta - b_{\alpha\beta\gamma} \varkappa_{\beta\gamma}\right) \delta J_\alpha \, \mathrm{d}x \, \mathrm{d}y = 0, \tag{92}$$

yielding

$$\kappa_{\alpha\beta} J_\beta + h_{\beta\alpha} P_\beta - b_{\alpha\beta\gamma} \varkappa_{\beta\gamma} = E_\beta^{\text{photo}}. \tag{93}$$

B Derivation of Tensor Symmetries

This appendix provides a rigorous derivation of the symmetry properties of the constitutive tensors in the internal energy density $\mathcal{W}$ for a flexoelectric-photovoltaic material model, as presented in Table 1 of the main text. The energy density $\mathcal{W}$ is a scalar function that encapsulates mechanical, electrical, and photonic interactions, defined as:

$$\begin{aligned}
\mathcal{W} = {} & \frac{1}{2} C_{ijkl} D_{ij} D_{kl} + \frac{1}{2} \chi_{ij} P_i P_j + \epsilon_{ijk} P_i D_{jk} + G_{ijklm} D_{ij} \partial_m D_{kl} + \frac{1}{2} H_{ijklmn} \partial_k D_{ij} \partial_n D_{lm} \\
& + K_{ijkl} P_i \partial_l D_{jk} + a_{ij} \partial_j P_i + \frac{1}{2} b_{ijkl} \partial_j P_i \partial_l P_k + d_{ijkl} \partial_j P_i D_{kl} + g_{ijk} P_i \partial_j P_k \\
& + \frac{1}{2} \kappa_{ij} J_i J_j + \eta_{ij} P_i J_j + \xi_{ijkl} J_i \partial_l D_{jk} + \gamma_{ijk} J_i D_{jk},
\end{aligned} \tag{94}$$

where $D_{ij} = \frac{1}{2}(u_{i,j} + u_{j,i})$ is the symmetric strain tensor, $\partial_k D_{ij}$ is the strain gradient, P_i is the polarization vector, $\partial_j P_i$ is the polarization gradient, and J_i is the photoelectric displacement. The tensors C_{ijkl}, χ_{ij}, ϵ_{ijk}, G_{ijklm}, H_{ijklmn}, K_{ijkl}, a_{ij}, b_{ijkl}, d_{ijkl}, g_{ijk}, κ_{ij}, η_{ij}, ξ_{ijkl} and γ_{ijk} are constitutive tensors that govern material response.

The symmetry properties of these tensors are derived from three key principles: (i) $\mathcal{W}$ is a scalar, requiring invariance under coordinate transformations; (ii) the symmetry of input arguments, such as $D_{ij} = D_{ji}$; and (iii) variational principles and Onsager reciprocity, which ensure thermodynamic consistency and symmetry in reversible couplings. Each tensor symmetry is demonstrated in the following, ensuring consistency with the variational framework used to derive the governing equations in the main text.

B.1 Elastic Tensor C

The elastic tensor **C**, of order 4, appears in the quadratic term $\frac{1}{2} C_{ijkl} D_{ij} D_{kl}$, representing the elastic energy. Since the strain tensor is symmetric ($D_{ij} = D_{ji}$), we consider the effect of index swapping:

$$\frac{1}{2} C_{ijkl} D_{ij} D_{kl} = \frac{1}{2} C_{ijkl} D_{ji} D_{lk} = \frac{1}{2} C_{jikl} D_{ij} D_{kl}, \tag{95}$$

implying $C_{ijkl} = C_{jikl}$, which establishes minor symmetry in the first two indices. Similarly, since $D_{kl} = D_{lk}$,

$$\frac{1}{2}C_{ijkl}D_{ij}D_{kl} = \frac{1}{2}C_{ijkl}D_{ij}D_{lk} = \frac{1}{2}C_{ijlk}D_{ij}D_{kl}, \tag{96}$$

yielding $C_{ijkl} = C_{ijlk}$, confirming the minor symmetry in the last two indices. For major symmetry, since $\mathcal{W}$ is a scalar, the quadratic form must be invariant under swapping of the index pairs (ij) and (kl):

$$C_{ijkl}D_{ij}D_{kl} = C_{klij}D_{kl}D_{ij}. \tag{97}$$

Relabeling indices, this implies $C_{ijkl} = C_{klij}$. Furthermore, the elastic energy is positive definite, and the second derivative of $\mathcal{W}$ with respect to the strain tensor,

$$\frac{\partial^2 \mathcal{W}}{\partial D_{ij} \partial D_{kl}} = C_{ijkl}, \tag{98}$$

is symmetric in $(ij) \leftrightarrow (kl)$, reinforcing $C_{ijkl} = C_{klij}$. Thus, $\mathbf{C}$ exhibits both minor symmetries $(C_{ijkl} = C_{jikl} = C_{ijlk})$ and major symmetry $(C_{ijkl} = C_{klij})$.

B.2 Dielectric Susceptibility $\boldsymbol{\chi}$

The dielectric susceptibility tensor $\boldsymbol{\chi}$, of order 2, governs the dielectric energy term $\frac{1}{2}\chi_{ij}P_iP_j$. As a scalar, $\mathcal{W}$ requires the quadratic form to be invariant under index swapping:

$$\chi_{ij}P_iP_j = \chi_{ji}P_jP_i = \chi_{ji}P_iP_j, \tag{99}$$

since $P_iP_j = P_jP_i$. This implies $\chi_{ij} = \chi_{ji}$. Additionally, in the variational framework, the electric excitation is defined as:

$$E_i^{\text{eff}} = \frac{\partial \mathcal{W}}{\partial P_i} = \chi_{ij}P_j + \text{other terms}, \tag{100}$$

and the second derivative,

$$\frac{\partial^2 \mathcal{W}}{\partial P_i \partial P_j} = \chi_{ij}, \tag{101}$$

is symmetric $(\chi_{ij} = \chi_{ji})$ due to the commutativity of partial derivatives, confirming that χ is a symmetric second-rank tensor.

B.3 Polarization-Strain Tensor $\boldsymbol{\epsilon}$

The tensor $\boldsymbol{\epsilon}$, of order 3, appears in the coupling term $\epsilon_{ijk}P_iD_{jk}$. Since the strain tensor is symmetric $(D_{jk} = D_{kj})$, we evaluate:

$$\epsilon_{ijk}P_iD_{jk} = \epsilon_{ijk}P_iD_{kj} = \epsilon_{ikj}P_iD_{jk}, \tag{102}$$

implying $\epsilon_{ijk} = \epsilon_{ikj}$. This symmetry in the last two indices arises because the strain tensor symmetry constrains the tensor ϵ to produce the same energy contribution regardless of the order of j and k. This is consistent with the variational derivation of the stress tensor $\sigma_{ij} = \frac{\partial \mathcal{W}}{\partial D_{ij}}$, which includes $\epsilon_{kij}P_k$, where the symmetry in ij due to D_{ij} enforces consistency in the coupling.

B.4 Strain Gradient Coupling G

The strain gradient coupling tensor **G**, of order 5, appears in $G_{ijklm} D_{ij} \partial_m D_{kl}$. Since $D_{ij} = D_{ji}$ and $D_{kl} = D_{lk}$, we have:

$$G_{ijklm} D_{ij} \partial_m D_{kl} = G_{jikl} D_{ji} \partial_m D_{kl} = G_{jikl} D_{ij} \partial_m D_{kl}, \tag{103}$$

implying $G_{ijklm} = G_{jikl}$. Similarly,

$$G_{ijklm} D_{ij} \partial_m D_{kl} = G_{ijlk} D_{ij} \partial_m D_{lk} = G_{ijlk} D_{ij} \partial_m D_{kl}, \tag{104}$$

yielding $G_{ijklm} = G_{ijlk}$. Thus, **G** is symmetric in the strain indices (ij) and (kl). The gradient index m may exhibit additional symmetries in isotropic materials (e.g., proportional to δ_{im}), but the general form does not mandate further symmetries, as $\partial_m D_{kl}$ is not inherently symmetric.

B.5 Strain Gradient Elasticity H

The strain gradient elasticity tensor **H**, of order 6, governs the quadratic term $\frac{1}{2} H_{ijklmn} \partial_k D_{ij} \partial_n D_{lm}$. Since $\partial_k D_{ij} = \partial_k D_{ji}$, we evaluate:

$$H_{ijklmn} \partial_k D_{ij} \partial_n D_{lm} = H_{jiklmn} \partial_k D_{ji} \partial_n D_{lm} = H_{jiklmn} \partial_k D_{ij} \partial_n D_{lm}, \tag{105}$$

implying $H_{ijklmn} = H_{jiklmn}$. Similarly, $\partial_n D_{lm} = \partial_n D_{ml}$ gives:

$$H_{ijklmn} \partial_k D_{ij} \partial_n D_{lm} = H_{ijlmn} \partial_k D_{ij} \partial_n D_{ml} = H_{ijlmn} \partial_k D_{ij} \partial_n D_{lm}, \tag{106}$$

yielding $H_{ijklmn} = H_{ijmln}$. For major symmetry, the quadratic form requires:

$$H_{ijklmn} \partial_k D_{ij} \partial_n D_{lm} = H_{klmnij} \partial_n D_{lm} \partial_k D_{ij}, \tag{107}$$

implying $H_{ijklmn} = H_{klmnij}$. The second derivative,

$$\frac{\partial^2 \mathcal{W}}{\partial(\partial_k D_{ij}) \partial(\partial_n D_{lm})} = H_{ijklmn}, \tag{108}$$

is symmetric in $(ijk) \leftrightarrow (lmn)$, confirming full symmetries. These symmetries ensure that the strain gradient energy is positive definite and consistent with the variational derivation of the hyperstress $\tau_{ijk} = \frac{\partial \mathcal{W}}{\partial(\partial_k D_{ij})}$.

B.6 Polarization-Strain Gradient K

The tensor **K**, of order 4, appears in $K_{ijkl} P_i \partial_l D_{jk}$. Since neither P_i nor $\partial_l D_{jk}$ is inherently symmetric, no general symmetry is imposed:

$$K_{ijkl} P_i \partial_l D_{jk} \neq K_{ikjl} P_i \partial_l D_{kj}, \tag{109}$$

unless specific material symmetries (e.g., isotropy) enforce constraints. This lack of symmetry is consistent with the coupling role in the polarization equilibrium equation, where **K** contributes to the effective electric field without requiring index symmetry.

B.7 Polarization-Gradient a

The tensor **a**, of order 2, appears in $a_{ij}\partial_j P_i$. Since the polarization gradient $\partial_j P_i$ is not symmetric, we have the following.

$$a_{ij}\partial_j P_i \neq a_{ji}\partial_i P_j, \tag{110}$$

indicating that **a** is typically not symmetric unless material symmetry (e.g. isotropy, where $a_{ij} \propto \delta_{ij}$) imposes $a_{ij} = a_{ji}$. This is reflected in the polarization governing equation, where $\partial_j a_{ij}$ contributes to non-local effects without symmetry constraints.

B.8 Polarization Gradient b

The tensor **b**, of order 4, governs the quadratic term $\frac{1}{2}b_{ijkl}\partial_j P_i \partial_l P_k$. Since $\partial_j P_i \partial_l P_k = \partial_j P_i \partial_k P_l$, we have:

$$b_{ijkl}\partial_j P_i \partial_l P_k = b_{ijlk}\partial_j P_i \partial_k P_l = b_{ijlk}\partial_j P_i \partial_l P_k, \tag{111}$$

implying $b_{ijkl} = b_{ijlk}$. Similarly, $\partial_j P_i \partial_k P_l = \partial_i P_j \partial_k P_l$ gives $b_{ijkl} = b_{jikl}$. For major symmetry:

$$b_{ijkl}\partial_j P_i \partial_l P_k = b_{klij}\partial_l P_k \partial_j P_i, \tag{112}$$

yielding $b_{ijkl} = b_{klij}$. The second derivative,

$$\frac{\partial^2 \mathcal{W}}{\partial(\partial_j P_i)\partial(\partial_l P_k)} = b_{ijkl}, \tag{113}$$

is symmetric, confirming the full symmetry ($b_{ijkl} = b_{jikl} = b_{ijlk} = b_{klij}$). This ensures that the polarization gradient energy is positive definite and consistent with the variational derivation of the electric excitation tensor μ_{ij}.

B.9 Polarization Gradient-Strain d

The tensor **d**, of order 4, appears in $d_{ijkl}\partial_j P_i D_{kl}$. Since $D_{kl} = D_{lk}$,

$$d_{ijkl}\partial_j P_i D_{kl} = d_{ijlk}\partial_j P_i D_{lk} = d_{ijlk}\partial_j P_i D_{kl}, \tag{114}$$

implying $d_{ijkl} = d_{ijlk}$. This symmetry in the last two indices arises from the strain tensor symmetry and is consistent with the variational contribution to the electric excitation $\mu_{ij} = \frac{\partial \mathcal{W}}{\partial(\partial_j P_i)}$.

B.10 Polarization-Gradient Chiral g

The tensor **g**, of order 3, appears in $g_{ijk}P_i\partial_j P_k$. Since neither P_i nor $\partial_j P_k$ is symmetric, no inherent symmetry is required:

$$g_{ijk}P_i\partial_j P_k \neq g_{ikj}P_i\partial_k P_j, \tag{115}$$

allowing **g** to contain antisymmetric parts, especially in chiral materials where non-centrosymmetric properties may introduce such behavior. This is reflected in the polarization governing equation, where **g** contributes to gradient effects without symmetry constraints.

B.11 Photoelectric Tensor $\boldsymbol{\kappa}$

The photoelectric tensor $\boldsymbol{\kappa}$, of order 2, governs the quadratic term $\frac{1}{2}\kappa_{ij}J_iJ_j$. Since $\mathcal{W}$ is a scalar,

$$\kappa_{ij}J_iJ_j = \kappa_{ji}J_jJ_i = \kappa_{ji}J_iJ_j, \tag{116}$$

implying $\kappa_{ij} = \kappa_{ji}$. Additionally, the Onsager reciprocity for reversible transport processes ensures symmetry, as does the second derivative:

$$\frac{\partial^2\mathcal{W}}{\partial J_i \partial J_j} = \kappa_{ij} = \kappa_{ji}, \tag{117}$$

confirming that κ is symmetric, consistent with its role in the photoelectric equilibrium equation.

B.12 Polarization-Charge Tensor $\boldsymbol{\eta}$

The tensor $\boldsymbol{\eta}$, of order 2, appears in $\eta_{ij}P_iJ_j$. Since P_i and J_j are independent vectors,

$$\eta_{ij}P_iJ_j \neq \eta_{ji}P_jJ_i, \tag{118}$$

indicating no inherent symmetry unless imposed by material properties. This is reflected in the coupled polarization and photoelectric equations, where $\boldsymbol{\eta}$ facilitates cross-coupling without requiring symmetry.

B.13 Charge-Strain Gradient Tensor $\boldsymbol{\xi}$

The tensor $\boldsymbol{\xi}$, of order 4, appears in $\xi_{ijkl}J_i\partial_l D_{jk}$. Since $\partial_l D_{jk} = \partial_l D_{kj}$,

$$\xi_{ijkl}J_i\partial_l D_{jk} = \xi_{ikjl}J_i\partial_l D_{kj} = \xi_{ijkl}J_i\partial_l D_{jk}, \tag{119}$$

implying $\xi_{ijkl} = \xi_{ijlk}$. This symmetry in the last two indices arises from the strain gradient symmetry and is consistent with the photoelectric equilibrium equation.

B.14 Photostrictive Tensor $\boldsymbol{\gamma}$

The tensor $\boldsymbol{\gamma}$, of order 3, appears in $\gamma_{ijk}J_iD_{jk}$. Since $D_{jk} = D_{kj}$,

$$\gamma_{ijk}J_iD_{jk} = \gamma_{ikj}J_iD_{kj}, \tag{120}$$

implying $\gamma_{ijk} = \gamma_{ikj}$. This symmetry in the last two indices is due to the strain tensor symmetry and aligns with the variational derivation of the photoelectric governing equation.

B.15 Consistency with Variational Framework

The symmetries derived above ensure that $\mathcal{W}$ is a well-defined scalar potential, consistent with the variational principle $\delta \int_\Omega \mathcal{W}\,\mathrm{d}V = 0$, used to derive the governing equations (mechanical, polarization, and photoelectric phenomena) in the main text. For example, the symmetry of $\mathbf{C}$, $\boldsymbol{\chi}$, $\mathbf{b}$, and $\boldsymbol{\kappa}$ ensures positive definiteness of the quadratic terms, while the symmetries of $\boldsymbol{\epsilon}$, $\mathbf{G}$, $\mathbf{H}$, $\mathbf{d}$, $\boldsymbol{\xi}$, and $\boldsymbol{\gamma}$ reflect the symmetric nature of the strain tensor D_{ij}. The lack of symmetry in $\mathbf{K}$, $\mathbf{a}$, and $\boldsymbol{\eta}$ allows flexibility for anisotropic or non-centrosymmetric materials, and the potential antisymmetry in $\mathbf{g}$ accommodates chiral effects. These properties collectively ensure thermodynamic consistency and compatibility with the boundary conditions derived in the main text.

Chapter 10

Conclusions

The works collected in this thesis illustrate a coherent journey from the modeling of specific dissipation phenomena in cementitious materials to the broader application of advanced continuum mechanics and multiphysics approaches to other complex systems, ranging from biological tissues to porous media, advanced manufacturing, and nanoscale energy harvesting.

The starting point is the development of enhanced Timoshenko beam models tailored for concrete-like materials, where microcrack-induced dissipation plays a central role. These contributions demonstrate how incorporating micromorphic kinematics and friction-based mechanisms enables an accurate and physically consistent representation of hysteresis, cyclic energy loss, and micro–macro interactions. The finite element simulations validate these models against experimental data, providing a robust foundation for the predictive design of more durable and resilient cementitious structures.

Building on this methodological core, the modeling strategies extend naturally to other materials and phenomena. In the biomechanics domain, similar constitutive modeling and parametric analysis strategies are employed to investigate corneal mechanics in health and disease. The coupling of shear wave elastography with finite element simulations highlights the potential of physics-based models to improve diagnostic accuracy and guide personalized treatment planning in ophthalmology.

The research also explores fluid flow in fractured porous media, where instability phenomena such as viscous fingering are investigated experimentally and quantitatively analyzed. This work reflects the same guiding principle: using targeted experiments, combined with mechanical modeling, to unveil the fundamental parameters that govern complex system behavior.

In advanced manufacturing, the thermomechanical modeling of additive manufacturing processes for nanoparticle-reinforced superalloys exemplifies the predictive power of coupled simulations for optimizing process parameters, reducing residual stresses, and improving component performance.

Finally, the exploration of coupled flexoelectric-photovoltaic effects in nanoscale materials brings the continuum mechanics approach to the frontier of multifunctional material design. By uniting mechanical, electrical, and photonic effects in a single variational framework, this work points toward innovative energy harvesting devices and multifunctional sensors.

Across these diverse applications, a common methodological and conceptual thread emerges: the rigorous integration of constitutive modeling, variational principles, and computational simulation, often complemented by experimental validation. This synergy enables both the in-depth understanding of specific materials and the generalization of methods to other contexts.

The findings not only deepen the theoretical foundations of continuum and multiphysics modeling but also open concrete pathways for application. Potential outcomes include improved civil infrastructure through better material design, enhanced diagnostic tools in medicine, optimized manufacturing workflows, and novel nanoscale devices for sustainable energy. In this way, the research achieves a dual impact, contributing to the scientific understanding of complex material behavior while providing tangible benefits in engineering and technology. In summary, *this thesis has shown that a single, well-structured modeling philosophy, rooted in continuum mechanics, enriched with targeted microstructural descriptors, and expressed through variational principles, can transcend material classes, physical scales, and application domains.* From microcrack friction in concrete beams to viscoelastic relaxation in the cornea, from viscous fingering in fractured rocks to residual stress control in additive manufacturing, and from multiphysics coupling in nanostructures to functional energy harvesting, the same conceptual tools have proven adaptable and predictive. This unifying approach not only advances our scientific understanding of complex material behavior but also lays the groundwork for practical solutions across civil, biomedical, environmental, manufacturing, and nanotechnological engineering, demonstrating that, with the proper framework, the boundaries between disciplines can be bridged.

The research presented in this thesis demonstrates that a unified modeling framework, grounded in continuum mechanics, enriched with microstructural descriptors, and implemented through variational formulations, can effectively capture the complex mechanical, dissipative, and multiphysics phenomena exhibited by a broad range of materials. By following a progression from specific case studies in cementitious elements to increasingly generalized treatments of heterogeneous and functional materials, the work establishes a conceptual bridge between seemingly disparate domains.

In the case of cement-based materials, the enhanced Timoshenko beam models incorporating micromorphic descriptors for microcrack sliding have provided both predictive accuracy and physical interpretability for cyclic dissipation. These developments not only align with experimental evidence but also offer practical tools for structural assessment and material design. The same principles of internal variables and multi-scale coupling have proven equally effective in the study of soft tissues, such as the cornea, where viscoelastic and anisotropic effects govern diagnostic and therapeutic outcomes. Likewise, the framework has been adapted to model multiphase fluid transport in fractured porous media, thermomechanical behavior in metal additive manufacturing, and coupled flexoelectric-photovoltaic effects in nanostructures, demonstrating the remarkable versatility of the approach.

The results underscore several key findings: i) Internal variables associated with microstructural kinematics offer a systematic route to embed dissipation and nonlinearity without sacrificing mathematical rigor; ii) Variational principles provide a natural and consistent foundation for integrating mechanical, thermal, fluid, and electromechanical effects; iii) The cross-domain adaptability of the methodology enables knowledge transfer from one field to another, accelerating model development and validation.

Future work will build upon these achievements in several directions. First, the cementitious material models will be extended to account for evolving microcrack density, enabling damage-coupled dissipation descriptions suitable for long-term fatigue and seismic analysis. Second, in biomedical applications, the corneal models will be personalized using patient-specific imaging and inverse identification techniques, with the goal of improving diagnostic precision and treatment planning. Third, in the context of porous media and fluid transport, coupling with reactive transport models will be pursued to address environmental and energy applications such as CO_2 sequestration. Fourth, in additive manufacturing, the framework will be expanded to include phase-field models for defect prediction and mitigation. Finally, at the nanoscale, the coupled flexoelectric-photovoltaic theory will be integrated into multi-physics simulation environments for the design of MEMS-based sensors and energy harvesters.

In conclusion, this work not only advances the modeling of each individual material system studied but also validates the concept that a single, coherent set of principles can illuminate the behavior of complex, multiscale, multiphenomenon materials across engineering and applied science. This paradigm of unification holds significant promise for both fundamental research and industrial innovation.

Chapter 11

List of Publications

1. Aretusi, G., **Cardillo, C.**, Salvatori, A., Bednarczyk, E., & Fedele, R. (2024). A simple extension of Timoshenko beam model to describe dissipation in cementitious elements. *Zeitschrift für angewandte Mathematik und Physik*, **75**(5), 166.

2. Aretusi, G., **Cardillo, C.**, Terranova, L. M., & Bednarczyk, E. (2024). A dissipation model for concrete based on an enhanced Timoshenko beam. *Networks and Heterogeneous Media*, **19**(2), 700–723.

3. Terranova, L. M., **Cardillo, C.**, & Aretusi, G (2025) An enhanced beam model incorporating a hysteresis-based solid friction damping mechanism for cementitious materials. *Continuum Mechanics and Thermodynamics*, **37**, 2

4. Mazinani, P., **Cardillo, C.**, & Mosaddegh, P. (2025). Evaluating corneal biomechanics using shear wave elastography and finite element modeling: sensitivity analysis and parametric optimization. *Continuum Mechanics and Thermodynamics*, **37**(1), 12.

5. Mazinani, P., & **Cardillo, C.** (2025). Shear wave velocity and finite element modeling for understanding keratoconus biomechanics: Comparison with healthy cornea. *Mathematics and Mechanics of Solids*,
DOI: 10.1177/10812865251347512.

6. Zadehkabir, A., Mazinani, P., Vamerzani, B. Z., **Cardillo, C.**, Saffari, H., & Hosseinalipour, S. M. (2025). Experimental study of fluid displacement and viscous fingering in fractured porous media: effect of viscosity ratio. *Continuum Mechanics and Thermodynamics*, **37**(2), 29.

7. Yousefimiab, E., Kendibilir, A., Yalcin, Y., **Cardillo, C.**, Aydogan, E., & Kefal, A. (2025). Thermomechanical process modelling and simulation for additive manufacturing of nanoparticle dispersed Inconel 718 alloys. *Continuum Mechanics and Thermodynamics*, **37**(1), 11.

8. Enakoutsa, K., **Cardillo, C.**, Scerrato, D. (2025) Coupled Flexoelectric-Photovoltaic Phenomena in Nanoscale Materials: Variational Modeling and Analytical Solutions for Advanced Energy Harvesting, *Mathematics and Mechanics of Solids*, DOI: 10.1177/10812865251390452

Acknowledgements

I would like to express my deepest gratitude to all those who have supported and guided me throughout this doctoral journey. First and foremost, I must tip my hat to my supervisor, Prof. Ivan Giorgio, whose invaluable guidance has proven as essential to this research as a compass to a ship captain. However, I confess his patience in the face of my scholarly wanderings has been tested with the persistence of a saint and the fortitude of a man who has made peace with the fact that enlightenment, like a fine wine, cannot be rushed, no matter how vigorously one might shake the bottle.

I am equally grateful to my co-supervisor, Prof. Roberto Fedele, for his insightful contributions, thoughtful discussions, and collaborative spirit. His unique perspective and expertise have greatly enriched this thesis and broadened my understanding of the field.

I am compelled to acknowledge Dr. Ewa Bednarczyk, whose co-supervision during my research period in Poland proved as indispensable as it was illuminating: for without her guidance, I might have wandered the labyrinthine corridors of academic inquiry with all the purpose of a tourist in Warsaw armed only with a map of Krakow.

My heartfelt thanks go to Prof. Francesco dell'Isola, whose exceptional teaching and mentorship laid the foundation for my academic pursuits. His passion for knowledge and dedication to student success have been a constant source of inspiration.

I would also like to acknowledge Prof. Massimo Cuomo for his administrative support and guidance throughout the doctoral program. His efforts in facilitating the academic and administrative aspects of my PhD journey have been invaluable.

This research was supported by M&MoCS research center, for which I am grateful.